

Infrared

Aspects of

Dark

Matter

Phenomenology





FACULTÉ
DES SCIENCES



UNIVERSITÉ LIBRE DE BRUXELLES

Infrared Aspects of Dark Matter Phenomenology

thèse présentée par Jérôme VANDECASTEELE

en vue de l'obtention du grade académique de docteur en physique

Année académique 2020-2021

Sous la direction du Professeur Michel TYTGAT, promoteur
Service de Physique Théorique

Jury de thèse :

Barbara CLERBAUX (Université libre de Bruxelles, Président)
Laura LOPEZ-HONOREZ (Université libre de Bruxelles, Secrétaire)
Malcolm FAIRBAIRN (King's College London)
Nathan GOLDMAN (Université libre de Bruxelles)
Josef PRADLER (Österreichische Akademie der Wissenschaften)



Infrared Aspects of Dark Matter Phenomenology

Jérôme Vandecasteele

Résumé en français

Bien que représentant plus d'un quart de la distribution en énergie de notre Univers ainsi que la majorité (84%) de la masse de celui-ci, la nature de la matière noire n'a pas encore été percée à ce jour. Dans cette thèse, il sera supposé que la matière noire est une nouvelle particule élémentaire, stable et dont la connexion (hors interactions gravitationnelles) avec le secteur visible est réalisée grâce à une autre particule, le médiateur. Au sein de ces lignes, la matière noire sera supposée être un fermion de Dirac et le médiateur un boson (vecteur ou scalaire), ce dernier étant choisi comme étant plus léger que la matière noire. Cette thèse propose d'explorer les aspects infrarouges de la production de la matière noire dans l'Univers primordial, le potentiel de détection d'une importante classe de candidats dits "freeze-in", caractérisés par de très faibles interactions avec le Modèle Standard, auprès des expériences de détection directe et l'effet des auto-interactions de la matière noire sur son comportement superfluide dans les régions de haute densité de matière noire (halos, capture par des astres compacts) asymétrique. Sous ces hypothèses, premièrement, une étude exhaustive des différents mécanismes de production de la matière noire est réalisée, illustrée dans un modèle où le médiateur est un photon du secteur caché, issu d'un nouveau groupe de jauge $U(1)$, qui mélange de façon cinématique avec le photon du Modèle Standard. En particulier, de nouveaux canaux de production sont mis en avant, nommément *freeze-in from mediator* et *sequential freeze-in*. Ceux-ci correspondent à des scénarios où la matière noire est très faiblement couplée au Modèle Standard, n'atteint jamais l'équilibre avec celui-ci dans l'Univers primordial et est produit petit à petit par des annihilations de médiateurs (en équilibre ou non avec le Modèle Standard). Il est ensuite montré que pour l'important et très attractif cas d'une matière noire milli-chargée (ainsi que pour des scénarios où le médiateur n'est pas plus massif que 40 méga-electronvolt), l'expérience de détection indirect Xenon1T contraint aujourd'hui l'espace des paramètres de la phase de freeze-in de ces modèles, et est, dans cette région de l'espace des paramètres, la contrainte la plus importante. Une réinterprétation des limites sur les interactions indépendantes du spin matière noire – nucléon est par ailleurs nécessaire, détaillée et validée. Dans la seconde partie de la thèse, l'effet des auto-interactions dans les scénarios de matière noire asymétrique est exploré. Sous l'hypothèse qu'un halo (galactique ou non) de matière noire atteint l'équilibre thermodynamique à très basse température (comparée à sa masse) et développe donc un potentiel chimique fini, des interactions matière noire – matière noire au voisinage de la surface de Fermi peut entraîner la formation de condensats, de transitions de phase du milieu et dès lors modifier drastiquement l'équation d'état du halo. Un système d'équations auto-consistant pour les condensats est présenté et résolu numériquement. Ensuite, la thermodynamique du système de gaz interagissant est explorée. Finalement, les interactions gravitationnelles sont considérées et les configurations auto-gravitantes, prenant en compte l'ensemble des auto-interactions, sont déterminées et leurs aspects phénoménologiques sont explorés.

Infrared Aspects of Dark Matter Phenomenology

Jérôme Vandecasteele

Summary in English

Even though dark matter represents more than a quarter of the energy budget of our Universe and the majority (84%) of its mass, the nature of dark matter has not yet been unravelled. In this thesis, it will be assumed that dark matter is a new elementary particle, stable and whose connection (on top of gravitational interactions) with the visible sector is realized through another particle, the mediator. In this thesis, dark matter will be assumed to be a Dirac fermion and the mediator will be a boson (either vector or scalar). This thesis proposes to explore infrared aspects of the production of dark matter in the primeval Universe, aspects of detection of the important class of feebly coupled “freeze-in” candidates at direct detection experiments and aspects of condensed matter physics such as superfluidity in region of high dark matter density (halos or inside compact objects such as neutron stars). Under these hypothesis, we will first detail an exhaustive study of the possible thermal mechanism of dark matter production, illustrated in a model where the mediator is a dark photon, arising from a new $U(1)'$ gauge group, which kinematically mixes with the Standard Model photon. In particular, new production channels are put forward, namely the *freeze-in from mediator* and *sequential freeze-in*. They correspond to scenarios where dark matter is very feebly coupled to the Standard Model, do not reach equilibrium with the visible sector thermal bath in the Early Universe and are slowly produced by mediator annihilations (in-equilibrium or not with the Standard Model). It is then showed that for the popular case of a millicharged dark matter (and for scenarios in which the mediator mass is not bigger than 40 mega electronvolt), the direct detection experiment XENON1T constrains today the freeze-in parameter space of such models and is the strongest constraint overall for such candidates. A recast of the bounds on spin-independent dark matter–nucleon interactions was needed and we validate our procedure against other recast. In the second part of this thesis, the effects of self-interactions in asymmetric dark matter scenarios are explored. Under the hypothesis that a dark matter halo reaches thermodynamic equilibrium at very low temperature (compared to its mass) and develops a finite chemical potential, dark matter– dark matter interactions at the vicinity of the Fermi surface can lead to the formation of condensates, to phase transitions and therefore modify drastically the equation of state of the halo. A self-consistent set of equations for the condensates is presented and solved numerically. The thermodynamics of the interacting dark matter cloud is also explored. Finally, gravitational interactions are considered and self-gravitating configurations of halos, taking into account self-interactions, are determined and their phenomenological aspects is explored.

What you will find in this thesis

My PhD began in September 2017 and ended in September 2021. The first year was dedicated to continuing my master thesis project, which led to the publication of the following two articles [1, 2]

- S. Colucci, B. Fuks, F. Giacchino, L. Lopez Honorez, M. H. G. Tytgat and **J. Vandecasteele**, *Top-philic Vector-Like Portal to Scalar Dark Matter*, *Phys. Ref. D* **98** (2018) 035002, [1804.05068]
- S. Colucci, F. Giacchino, M. H. G. Tytgat and **J. Vandecasteele**, *Radiative corrections to vectorlike portal dark matter*, *Phys. Ref. D* **98** (2018) 115029, [1805.10173]

Although this project can be seen as sharing some overall features with the rest of my thesis, it is far enough removed from my more recent work that discussing it would require introducing many new concepts and thus many additional chapters. I took instead the decision to briefly summarize our findings in Appendix A, with a focus on the results obtained from the full phenomenological study of the DM candidates of [1]. The two articles are self-contained and the phenomenology of the top-philic vector-like portal to scalar dark matter was partially described in the thesis [3].

The second year of my PhD was then devoted to two projects within the framework of the kinetic mixing portal to dark matter. Two articles have been published [4, 5]

- T. Hambye M. H. G. Tytgat, **J. Vandecasteele** and L. Vanderheyden *Dark matter direct detection is testing freeze-in*, *Phys. Ref. D* **98** (2018) 035002, [1807.05022]
- T. Hambye M. H. G. Tytgat, **J. Vandecasteele** and L. Vanderheyden *Dark matter from dark photons : a taxonomy of dark matter production*, *Phys. Ref. D* **98** (2018) 095018, [1908.09864]

These projects are discussed in details in the Part I of my thesis and many aspects of these two papers have been expanded, updated and explained more deeply.

In the last two years, in the addition to the thesis writing process, I focused my attention on the study of in-medium effects on the behaviour of degenerate dark matter. This project is discussed in Part II of my thesis. The project is still ongoing and will be the object of an upcoming article [6]

- R. Garani M. H. G. Tytgat and **J. Vandecasteele** *A theory of condensed dark matter, In preparation* [21xx.xxxxx]

Even though the results are not yet published, there has been many cross checks and we are confident in our findings.

Acknowledgements

First and foremost, I would like to thank Michel Tytgat, my advisor, for shaping the physicist that I became after almost seven years of teaching, mentoring and close collaboration. Looking back to the start of my PhD, I can now see how much I improved under his supervision beyond anything I could have imagined.

I would also like to thank Barbara Clerbaux, Malcolm Fairbairn, Nathan Goldman, Laura Lopez-Honorez and Josef Pradler who all accepted to be in my jury. I am very grateful that they were willing to read, question and validate my work.

I have been very lucky to collaborate with Benjamin, Federica, Laura and Stefano in the earliest stages of my PhD. Thomas and Laurent were the perfect companions to explore the richness of the dark photon phenomenology. Finally, the majority of the last two years of my PhD were spent working alongside Raghu and it has been plain fun.

The permanent staff of the Service de Physique Théorique, composed of Jean-Marie Frère, Peter Tinyakov, Michel Tytgat, Thomas Hambye and Laura Lopez-Honorez has always been a bottomless pit of physics insight that I wish I could tap forever! I thank them for the formative lectures, interesting seminars, relentless questions during journal clubs, discussions, sailing trips, end of the year parties and everything else. I also thank Isabelle and Sarah for their invaluable help in navigating the administrative mazes that I encountered. In this research group, I have crossed path with many, many great physicists and might have stolen from all of them a bit of their knowledge of physics. Many thanks to Aritra, Armando, Camilo, Chaimae, Daniele, Deanna, Federica, Iason, Julian, Laurent, Lucien, Marco, Matteo, Mikhail, Quentin, Raghu, Rupert, Sam, Xunjie, Yoann and Yongchao.

From the very start of the bachelor up to the end of the PhD, which amounts to ten (!) years, with Antoine, Bilal, Laurent, and Tanguy, we all shared the same path and I am very happy that we accomplished this journey together. I can only feel sad that our paths have already started to diverge.

I say thank you to my South-West of France friends : Arthur, Arthur, Cédric, Delphine, Elya, Hugo, Laurine, Marius, Romain, not forgetting Oggy & Joséphine. Many thanks to Laurine for her beautiful front page.

Last but not least, I would like to thank my mom and Simran. For everything.

Contents

1	Introduction	1
1.1	Dark matter seen in the Milky Way	1
1.2	A hint on the nature of dark matter?	3
1.3	The Boltzmann equation for dark matter production	6
1.4	A few words on portal models	11
I	A spin one portal	14
2	Kinetic Mixing Portal to Dark Matter	15
2.1	The model	15
2.2	Mixing, diagonalization	16
2.3	UV completions of photon-dark photon mixing	18
3	The mesa diagram of the dark matter relic density	21
3.1	Interplay between the visible and hidden sector	21
3.2	Phase diagram of dark matter production	25
3.3	Freeze-in: regimes Ia and Ib	29
3.3.1	Regima Ia	29
3.3.2	Regime Ib	30
3.4	Sequential freeze-in: regime II	31
3.5	Reannihilation: regimes IIIa and IIIb	32
3.6	Secluded freeze-out: regimes IVa and IVb	34
3.7	Freeze-out: regimes Va and Vb	34
3.8	The parameter space of DM candidates	36
4	Inclusion of thermal effects	39
4.1	On-shell production	39
4.2	Self-energy	41
4.3	Dark photon abundance	44
4.4	Impact on Dark Matter Production	46
5	Constraints	51
5.1	Constraints on Dark Photons	51
5.1.1	Cosmological constraints	54
5.1.2	Stars, supernovae constraints	55
5.1.3	$\gamma \leftrightarrow \gamma'$ transitions	56
5.1.4	Colliders and beam dump experiments	57
5.1.5	The dark photon as a mediator for feebly coupled DM set by freeze-in	58
5.2	Constraining kinetic mixing portal DM	58
5.2.1	Astrophysical and cosmological constraints of CHAMP DM	59

5.3	A particular look at direct detection constraints	59
5.3.1	With a light mediator	59
5.3.2	Freeze-in <i>vs</i> direct detection	62
5.3.3	Probing self-interacting dark matter	66
5.4	Can dark stars shine bright?	67
5.4.1	Spontaneous symmetry breaking at high density	68
II	A spin zero portal	70
6	Self-interacting asymmetric dark matter	71
6.1	Context and motivation	71
6.1.1	DM capture in NS	72
6.1.2	Signatures of DM capture in compact objects	73
6.2	Density effects	74
6.2.1	The scalar condensate at finite density	75
6.2.2	Bardeen–Cooper–Schrieffer superfluidity	77
6.2.3	Superfluid dark matter in neutron stars : first steps	80
7	A theory of condensed dark matter	83
7.1	The consistent system of gap equations	83
7.2	Solutions of the gap equations	87
7.2.1	The gaps $\tilde{\Delta}_-$ with heavy mediators	88
7.2.2	The gaps $\tilde{\Delta}_-$ with light mediators	91
8	Thermodynamics, phase transition and dark matter clouds	93
8.1	Thermodynamics, phase transition	94
8.2	Building clouds	98
8.2.1	Free, degenerate DM halos	99
8.2.2	The Tremain-Gunn bounds	100
8.2.3	Beyond Tremain-Gunn with self interactions	101
9	General conclusions and perspectives	107
A	A spin 1/2 portal	111
B	Dark photon emission rate	115
C	Obtaining the gap equations	117
C.1	The free energy of an interacting gas	117
C.2	Quasiparticle dispersion relations	120
C.3	The gap equations at zero temperature	120
C.3.1	Dirac algebra and derivatives	120
C.3.2	Useful integrals	121
C.3.3	The gap equations for $\tilde{\Delta}_\eta, \tilde{\kappa}$	122
C.4	First corrections to the gap equations	122
C.5	Derivation from projectors	123
C.6	Numerical methods for solving the gap equations	125
C.6.1	Gap	125
C.6.2	An approximated solution to the gap equation	126
C.6.3	Condensate - gap coupled system	126

List of Figures

1.1	Rotation curve of the Milky Way	2
1.2	Composite picture of the collision of two cluster of galaxies	3
1.3	Illustration of the core/cusp problem in DDO 154	5
1.4	Freeze-out and freeze-in in a DM toy model	9
1.5	Schematic representation of infrared dominated freeze-in.	11
2.1	Coupling structure of the kinetic mixing portal	17
3.1	Feynman diagrams for the relevant processes of DM and dark photon production. . .	22
3.2	Illustration of the 3 connections between the 3 sectors	23
3.3	Pictorial representation of the 9 DM production regimes of the millicharged DM with a light dark photon scenario.	24
3.4	Contours of the DM relic density for $m_{\text{DM}} = 3$ GeV and $m_{\gamma'} = 1$ GeV.	26
3.5	Contours of the DM relic density for $m_{\text{DM}} = 100$ GeV and $m_{\gamma'} = 10$ GeV.	28
3.6	Parameter space of regime Ia, Ib and II.	30
3.7	Effects of the interferences between the s -channel exchange of a photon and a dark photon in the $\epsilon - \delta$	35
3.8	The parameter space of DM candidates in the kinetic mixing portal	36
4.1	Illustration of thermal effects	41
4.2	Dispersion relation for the transverse and longitudinal photon modes	43
4.3	Dark photon production in the Early Universe	45
4.4	Impact of the dark photon abundance on the DM abundance	46
4.5	Non-thermal spectrum of dark photons after their freeze-in production	47
4.6	Contours of the DM relic density for $m_{\text{DM}} = 3$ GeV and $m_{\gamma} = 1$ GeV with the thermal effects on the dark photon production taken into account.	48
4.7	Contours of the DM relic density for $m_{\text{DM}} = 100$ GeV and $m_{\gamma} = 10$ GeV with the thermal effects on the dark photon production taken into account.	49
4.8	Parameter space of regime Ia, Ib and II but with the thermal effects on dark photon production taken into account.	50
5.1	Non-exhaustive summary of current constraints on the dark photon mass and its kinetic mixing parameter with the SM photon	53
5.2	Illustration of the direct detection recast procedure.	61
5.3	Recasted direct detection exclusion limits.	63
5.4	Comparison between the light mediator recast of the WIMP exclusion limit of PandaX-II of 2017 with the dedicated 2018 light mediator analysis of PandaX-II . .	64
5.5	Self-interacting dark matter candidates that are tested by direct detection.	66
6.1	Diagrammatic representations of the scalar condensate and Cooper pairing.	76
6.2	Condensate as a function of Fermi momentum k_F for different values of the effective coupling constant.	77

7.1	Normalization of the gap $\tilde{\Delta}_-$ at the Fermi momentum with $g = 4$	88
7.2	Normalization of the gap $\tilde{\Delta}_-$ at the Fermi momentum with $m_\phi = 10^{1.5}$	89
7.3	Coupling dependence of the gap $\tilde{\Delta}_-$ (k_F) in the ultra relativistic limit.	89
7.4	Shape function of $\tilde{\Delta}_-$ for $g = 4$ and $m_\phi/m = 30$	90
7.5	Normalization of the gap $\tilde{\Delta}_-$ in the light mediator regime.	92
8.1	Binding energy per particle as a function of density for different coupling C_ϕ^2	95
8.2	Maxwell construction of the physical equation of state.	96
8.3	Phase diagram in the density–coupling plane.	98
8.4	Phase diagrams in the pressure–inverse coupling plane.	98
8.5	DM halo mass–radius relationship for a free degenerate gas of fermions.	100
8.6	Equation of state $P(\rho)$ of the liquid phase and the bag model approximation.	102
8.7	DM halo mass–radius relationship for a self-interacting degenerate gas of fermions that is dominated by the condensate.	103
A.1	Parameter space of the thermal candidates of the model of Eq. (A.1) in the $m_T/m_S - 1$ and m_S plane. The colour code gives the Yukawa coupling. The dotted lines correspond to the parameter space of the thermal candidates coupling predominantly to the up quark, for which mass effects in the final state are negligible.	112
A.2	Summary of constraints on the thermal DM candidates of the model of Eq. (A.1) in the $m_T/m_S - 1$ and m_S plane (color shaded regions). Viable candidates lie within the white region.	113
A.3	Feynman diagrams depicting the main channels for the production of S and T at colliders.	114
A.4	LHC constraints on the top-philic scalar DM thermal candidates in the $m_S - m_T$ plane.	114

List of Tables

1.1	Classification of portal models	12
4.1	Summary of the transverse photon and dark photon couplings in a plasma	42
5.1	Details on the recast procedure of a few DM candidates	63
8.1	Benchmark candidates that can reproduce a DM halo with $M = 10^8 M_\odot$ and $R = 1$ kpc, which is representative of DM halos in dwarf galaxies.	104

Chapter 1

Introduction

In this first Chapter, we will discuss the historical evidences of dark matter (**DM**) (Section 1.1) and motivate some particular DM scenario (Section 1.2). As a stepping stone for the rest of the thesis, we will describe the basics of DM production in the Early Universe (Section 1.3) and provide a few elements of DM model building (Section 1.4).

1.1 Dark matter seen in the Milky Way

From a scientific point of view, it is incredibly exciting to be surprised and therefore to seek new knowledge. As of today, not all puzzles in our Universe have been solved and, perhaps, much has yet to be unravelled. One particular unsolved puzzle is that of the Dark Matter (**DM**) problem. One is allowed to wonder about its possible solutions which, unlike the Standard model (**SM**) of fundamental interactions, is necessarily outside of the experimentally-backed knowledge of today. This problem came to light by astrophysical observations at the scales of galaxy clusters of the motions of bright objects (namely, galaxies) back in the 30's [7, 8]. After extracting the velocity dispersion of the luminous objects that are all thought to be gravitationally bound to each other, the *total* gravitational mass can be inferred by use of the virial theorem¹. It was found that the luminous mass accounts for only a small fraction of the total gravitational mass and that galaxy clusters can be dominated by a form of non-luminous mass². Let us now make an (almost) anachronic comment. The SM provides non-luminous matter (*i.e.* electrically neutral) in the form of neutrons and neutrinos³. With a lifetime of about 15 minutes, it is clear that free neutrons are not suitable for taking the role of a cosmologically stable dark matter. Neutrinos, on the other hand, have characteristics that might be shared with dark matter. If their mass is of about 100 electron-Volt, the expected abundance from their production in the Early Universe would be a factor 5 more than luminous matter [9], which would allow for DM dominated clusters, for example. However, many observations of the neutrino mass from the large scale structure of the Universe [10] or more recent direct experiments [11] and Early Universe physics studies [12] rule out completely this possibility⁴. Nonetheless, it is interesting to keep in mind that DM could be an elementary particle. Further study of the DM puzzle by Vera Rubin cemented the dark matter problem and provided beautiful galaxy rotations curves [14] through which the discrepancy between the luminous and gravitational total mass becomes very clear. An interesting feature of galactic rotation curves is that they allow

¹This theorem states that in an in-equilibrium system of gravitationally bound objects, the average (over all objects) kinetic energy (K) and the average gravitational potential (U) are related. If the velocity distribution is isotropic and all objects have the same mass, the relation takes the simple form $K = -U/2$.

²We stress that this statement has the underlying assumption that the low acceleration limit of the theory of gravity can be well approximated by Newton's laws of motion at cluster scales.

³Interestingly, both the neutron and (electron-)neutrino were discovered also in the 30's.

⁴A stable hexaquark bound state *uuddss* has also been in recent years theorized to be a possible DM candidate [13].

for a very straightforward understanding of the problem, as we will see below.

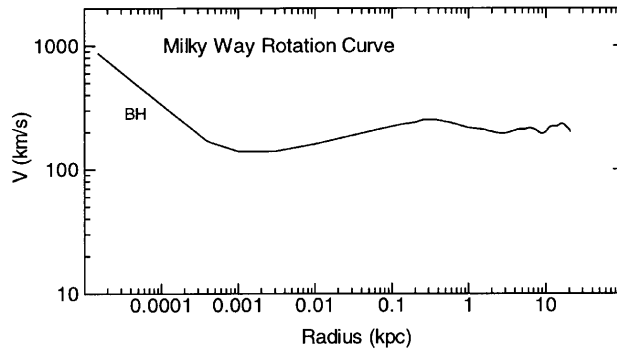


Figure 1.1: Rotation curve of the Milky Way, adapted from [15].

In Fig. 1.1, we reproduce Fig. 1b of [15], which gives the rotation velocity of the Milky Way as a function of radius. At very low radii, the rotation velocity decreases and at higher radius, it flattens, up to the very outskirts of our Galaxy. We mention that more recent studies confirmed that flatness of the rotation curve up to 50 kpc [16]. For a test mass in a circular orbit of radius r around an object of mass M , its velocity is given by

$$v = \sqrt{GM(r)/r} \quad (1.1)$$

where $M(r)$ is the enclosed mass within the radius r . Let us now focus on the inner most regions of our Galaxy (see “BH” on Fig. 1.1). In those regions, the mass is dominated by the super massive black hole located at the center of the Milky Way and therefore $M(r)$ can be approximated by a point mass at $r = 0$. If $M(r)$ is independent of r , $v \propto 1/\sqrt{r}$ and the rotational velocity decreases, as can be seen on the Figure up to 1 pc. Given the Milky Way characteristics, the majority of the luminous mass lies within 5 kpc of the center [17] and we should therefore observe the same $v \propto 1/\sqrt{r}$ behaviour at larger radii if the luminous mass is equal to the total gravitational mass. As is evident from Fig. 1.1, the rotation curve is flat. One concludes that the gravitational mass is bigger than the luminous mass. The plateau observed at large radii ($r > 5$ kpc) is therefore a gravitational evidence for the presence of DM in our galaxy. In addition, since $v \sim \text{constant}$, this means that $M(r) \propto r$ and that the density of non-luminous matter should grow as r^{-2} at large radii. A standard parametrization for the DM halo density profile is that of the Navarro-Frenk-White (NFW) profile [18]

$$\rho_{\text{NFW}}(r) = \rho_0 \left[\frac{r}{R_s} \left(1 + \frac{r}{R_s} \right)^2 \right]^{-1} \quad (1.2)$$

for R_s the scale radius and ρ_0 the DM density at $r = R_s$. For $r \gg R_s$, $\rho_{\text{NFW}} \propto r^{-3}$. For $r \ll R_s$, the halo behaves instead as $\rho_{\text{NFW}} \propto r^{-1}$. For $r \approx R_s$, the transition between the small and large r regimes can provide a range of r such that the profile behaves as $\propto r^{-2}$ and the DM halo profile can reproduce, for instance, the flat rotation curve of the Milky Way if R_s is chosen appropriately.

Even though we only illustrated one gravitational evidence for DM in one galaxy, we mention that one finds the same behaviour of the rotation curve in many other galaxies [14, 15], a similar effect on the velocity dispersion in dwarf galaxies [19] and galaxy clusters [20, 21]. For a wider overview of gravitational evidences for DM observed across many epochs of our Universe, see the following non-exhaustive list of much more exhaustive reviews about DM [22, 23, 24, 25]. We finally stress that these works, as we have done explicitly in Eq. (1.1), assume that the theory of gravity

behaves as General Relativity (**GR**) would behave at cluster scales, for instance. A competing explanation is that of MODified Newtonian Dynamics (MOND) [26] which foregoes GR. Some particular successes of this paradigm is the reproduction of the galactic rotation curves without DM and the Tully-Fischer relation [27, 28], which is an empirical relation between the luminous mass of a spiral galaxy and its rotation velocity at large radius. This relation has been known to be a shortcoming of DM [29, 30].

1.2 A hint on the nature of dark matter?

Until now, we have discussed in very broad terms the DM puzzle and have been extremely laconic as to what *is* DM. We have argued that DM could be a manifestation of the breakdown of GR at galaxy scales. A richer possibility is that DM is a new particle, *i.e* that does not belong to the SM. It could be an elementary, point-like particle or a composite state arising from some non-abelian dark gauge theory. In the following of this thesis, we will assume DM to be an elementary particle. Owing to many efforts across many decades made towards the understanding of the nature of DM, many informations are available as to what DM is *not*. Interestingly, there exists also indirect hints that points to DM having some particular properties. As we will use these indications to motivate our study of some particular aspects of DM models, we will now describe the most relevant observations.

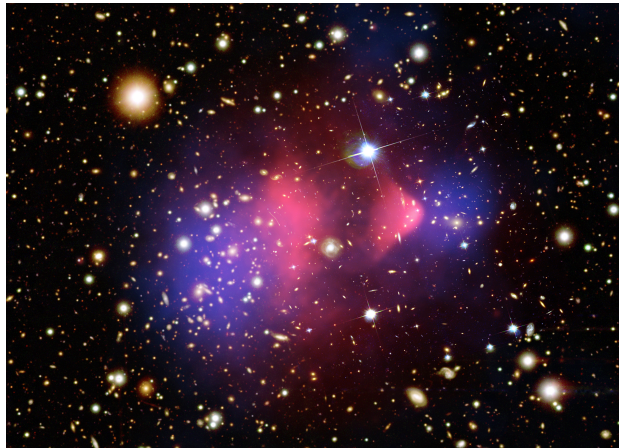


Figure 1.2: Composite picture of the collision of two cluster of galaxies. Credit: X-ray: NASA/CXC/CfA/M.Markevitch et al.; Optical: NASA/STScI; Magellan/U.Arizona/D.Clowe et al.; Lensing Map: NASA/STScI; ESO WFI; Magellan/U.Arizona/D.Clowe et al.

In Fig. 1.2, we give a composite picture of the so-called “Bullet Cluster”. This image depicts the aftermath of a collision between 2 clusters of galaxies. In pink is given the X-ray map made by the Chandra X-ray observatory which corresponds to emission from hot gas. The pink regions can therefore be used as a proxy for the luminous matter. The white/orange bright points with diffraction spikes are foreground nearby stars and the other objects are background galaxies [31]. In blue is given the inferred density of matter by gravitational lensing [31, 32]. The blue regions are invisible in both the optical and X-ray bands, dominate the mass distribution of the clusters and are a proxy for the dark matter. The leftmost cluster travels from right to left and the rightmost cluster travels from left to right. The scale of the collision is of about 2 Mpc. As can be seen, the luminous (and, for our purpose, *interacting*) matter trails behind the DM, whereas the luminous matter was hosted inside the DM halo before collision. We conclude that as the cluster collided, the halos of DM passed unimpeded through each other whereas the luminous matter in the form of hot

gas slowed down due to friction by electromagnetic interactions. On top of being a visually striking evidence for DM, this image gives us the information that DM interacts very differently from the SM. This statement can be made quantitative by setting an upper bound on the self-interaction cross section of DM, *i.e.* a limit on the efficiency of the $\text{DM} + \text{DM} \rightarrow \text{DM} + \text{DM}$ process [33]. For a comprehensive review of the physics used to put such a bound, see for example [34]. We only quote here the typical upper limit

$$\sigma/m \leq 1 \text{ cm}^2/\text{g} \tag{1.3}$$

where σ is the DM–DM scattering cross section, m the DM mass and the relative velocity between DM particles is set to be about $v \sim 1000 \text{ km/s}$. For reference, this figure is of the order of the scattering cross section of processes such as $np \rightarrow np$ [34]. We also mention that such analyses can be performed on other cluster collisions and similar bounds have been found [35].

Using the Bullet Cluster, we have argued that DM should be *collisionless*. However, there exists many shortcomings of this paradigm and we now aim at describing the *core-cusp problem* in galaxies. We mention that this particular problem has also been identified in the Milky Way satellites [36] and clusters [37]. We mention also that there exists other issues of DM at small scales such as the related *diversity problem* [38, 39] and the *missing satellites* and *too-big-to-fail problems* [40, 41]. These problems have been identified by comparing astrophysical observations of dwarf galaxies, galaxies and cluster of galaxies to many body cosmological simulation of DM. The initial condition for the DM distribution is inferred by the measurements of the Cosmic Microwave Background (**CMB**) [42]. It is then evolved by using GR until today. The distribution of DM obtained from these cosmological simulations shows that the inner profile of the DM halos, which will ultimately host for instance galaxies, is cuspy, hence the inner slope $\propto r^{-1}$ of the NFW profile of Eq. (1.2). As an aside comment, we mention that these simulations provide another evidence for the existence of DM. They reproduce admirably well the large scale, filament-like, structure of our Universe [43]. More importantly, DM is actually required for the Universe to look as it looks on the largest scales. If one does not consider DM and evolves the density perturbations of the SM plasma inferred by CMB anisotropies⁵ up to today, the Universe would be permeated by a slightly inhomogeneous (at roughly the 10% level) distribution of matter [44], whereas clearly today the inhomogeneities are of order 1 (*i.e.* there regions of matter and region of emptiness). In more familiar term, this argues that DM acts as the seed of the structures of the Universe.

⁵Typically, the temperature perturbations are $\delta T/T \sim \delta\rho/\rho \sim 10^{-5}$ for ρ the energy density of matter at CMB decoupling.

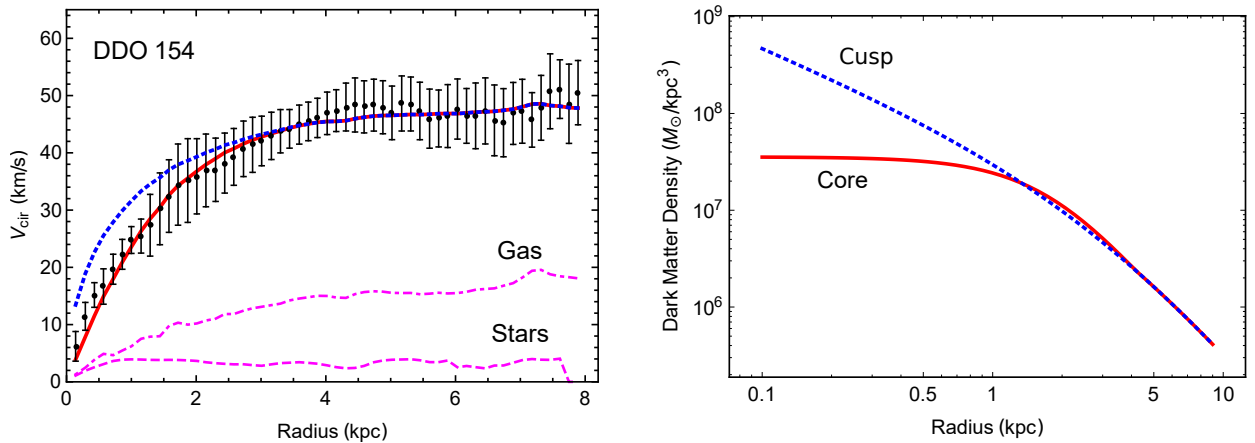


Figure 1.3: Right : dark matter density profile. Left : Rotation curve for the galaxy DDO 154. The black dots are data points, the pink dashed and dot-dashed curve are the contribution to the circular velocity from gas and stars. In dashed blue is given the rotation curve of the cuspy DM profile and in solid red is given the one obtained from the cored profile. Taken from [34].

In order to unveil a hint on the nature of DM, let us now visualize the core-cusp problem through the measured rotation curve of the galaxy DDO 154, see Fig. 1.3 (left, data points, from [34]). Like the Milky Way, this galaxy exhibits a plateau in its circular velocity at large radii. Using the NFW profile of Eq. (1.2), we can then fit the two free parameters ρ_0 and R_s , see Eq. (1.2), in order to obtain the DM halo profile that hosts this galaxy. On the right of Fig. 1.3 is given the best fit for the NFW profile to this rotation curve⁶ (blue dashed line). The rotation curve expected from this cuspy profile is then reported on the left (dashed blue) and the asymptotic velocity matches very well the data. However, at small radii, below 1 kpc, there exists a strong discrepancy between observations and expectations from the best fit cuspy profile. We observe that a cored profile (solid red) provides a much better fit to the data in the inner regions of the galaxy, in stark contrast with what is expected from collisionless DM. It is endearing to find in the same Figure both an evidence for DM ($v_{\text{cir}} \sim \text{constant}$ at big radii) and a shortcoming of the collisionless DM paradigm.

However, this begs the question of how to obtain a cored profile as in Fig. 1.3. The cuspieness of DM halo profile is inferred from collisionless DM-only simulations. However, baryon feedback – for instance in the form of star formations, outflows of visible matter from SN shock – might change the DM distribution at such small scales [45]⁷. There exists also the interesting possibility that this shortcoming of DM at small scales is giving us a hint about DM interactions. To reiterate, if Fig. 1.3, through measurements of the rotation velocities, shows strong gravitational evidences of DM when looking at large radii, it could also very well tell us at small radii that DM might be far from collisionless. As this topic will be touched upon in the remainder of this thesis, let us detail this statement. It has been put forward that DM self-interactions might be a possible resolution to the small scale crisis of collisionless DM [46]. If one simply looks at the upper bound on the DM self-interaction cross section we quoted in Eq. (1.3), there is much room for allowing DM to self-interact since this cross section is as high as what can be found in nuclear processes. In a DM halo, the inner part of the DM halo is colder than the outer parts, owing to smaller velocities. Through DM–DM interactions, the high velocity component can kick the low velocity one to higher orbits, effectively depleting the number of DM particle at the core. At those scales, the DM relative velocity is of

⁶We mention that the NFW profile parameters (ρ_0, R_s) are found to be highly correlated in simulations. In Fig. 1.3, the NFW parameters have been chosen under this constraint. Putting aside this constraint, it is possible to find a ρ_0 and a R_s that gives a better fit.

⁷We mention that the other problems of DM at small scales named above can also be alleviated by the same considerations [45].

about $v \sim 200$ km/s and a self-interaction cross section of $0.1 \text{ cm}^2/\text{g} < \sigma/m < 10 \text{ cm}^2/\text{g}$ makes the energy transfer efficient enough in order to alleviate the core-cusp problem.

In this section, we have discussed about some aspects of DM that are relevant today, but DM can have a very rich history. In the following Section, we will discuss the puzzle of DM in the very Early Universe.

1.3 The Boltzmann equation for dark matter production

If one rewinds the history of our Universe far back enough, they will reach a hot and dense thermal bath of in-equilibrium particles. If DM is an elementary particle, nothing forbids it to also reach equilibrium and, of course, nothing forbids it from not reaching equilibrium with the SM thermal bath. However, one thing that is extremely desirable from theoretical arguments would be that the relic abundance of DM was set by its elementary interactions with other particles in the very Early Universe. In this section, we aim at building the tools for describing DM production by the SM thermal bath in the Early Universe. Most of the first part of this thesis will be dedicated to this question and many results will be built on what will be shortly described.

In order to reach the observed DM relic abundance, one should start from a certain amount of DM particles that is argued to be natural⁸ and then use DM number changing processes provided by the DM interactions. Those number changing processes arise from relativistic effects in quantum mechanics and they can be incorporated in the equation governing the evolution of the phase space density⁹ $f(p^\mu, x^\mu)$ (the Liouville equation) by considering a collision term [9]

$$\hat{L}[f] = C[f] \tag{1.4}$$

where \hat{L} is the Liouville operator and C contains terms that either add or subtract particles. Note that for the case under study, the particles are considered free in a time-dependent background and only occasionally interact with another particle. Generally, solving the Liouville equation is extremely difficult and we will now justify a few approximations. We will assume that the system is infinite but with a finite density of particles and spatially homogeneous, isotropic but time-dependent, as is expected from the Early Universe. Therefore, the phase space density can only depend on time and the modulus of the impulsion (or, equivalently, the energy E). In addition, we are not interested in a very fine grained description of the system but would simply like to obtain the number density of DM particles, which we write n . The density of particles is of course related to the phase space density by $n(t) = g \int d^3p / (2\pi)^3 f(E, t)$ for g the number of internal degrees of freedom of the particle of the system (assuming a 1 species system). Upon integrating over all momenta, the Liouville equation is rewritten as [9]

$$\frac{dn}{dt} + 3\frac{\dot{a}}{a}n = \frac{g}{(2\pi)^3} \int d^3p C[f] \frac{d^3p}{E} \tag{1.5}$$

where $a = a(t)$ is an arbitrary scale that is stretched by the expansion of the Universe and whose time evolution is governed by cosmology. A few comments are in order. Setting the collision term to 0, we see that the evolution of the number density is proportional to $n \propto 1/a^3$, which is consistent with the dilution of the average number density expected when a 3 dimensional box of size a gets stretched from all sides. On the right hand side resides a quantity that can be computed by the

⁸For example, an equilibrium amount if the DM is in equilibrium with the SM thermal bath in the Early Universe or a negligible amount if reheating proceed in majority in the visible sector.

⁹The phase space density gives the probability $f(p, q) dpdq$ that the system is found in the phase space volume $dpdq$.

tools of Quantum Field Theory (**QFT**) and which is related to the cross sections of the processes that change the number density n [47].

Before solving the Boltzmann equation we need to provide some necessary cosmological ingredients in order to know the time evolution of $a(t)$ in Eq. (1.5). At the largest scales, the Universe is observed to be filled by an homogeneous and isotropic energy density. This motivates the description of our Universe by the maximally symmetric Friedmann–Lemaître–Robertson–Walker metric, which only depends on an unknown dimensionless function of time $a(t)$ dubbed the scale factor. Given an energy distribution, the metric can be a solution to Einstein’s field equations if $a(t)$ is chosen accordingly. Under our current knowledge of cosmology, our Universe started as a very high temperature bath, hence radiation at some temperature T . For each relativistic particle in the bath with g degrees of freedom, their contribution to the energy density ρ is

$$\rho = \mathcal{R} \frac{\pi^2}{30} g T^4 \quad (1.6)$$

where \mathcal{R} is 1 for bosons and 7/8 for fermions. They will also contribute to the number density n

$$n = \mathcal{N} \frac{\zeta(3)}{\pi^2} g T^3 \quad (1.7)$$

where $\zeta(3) \approx 1.2$ and \mathcal{N} is 1 for bosons and 3/4 for fermions. In the non-relativistic limit, a species of mass m at temperature T has

$$n \stackrel{T \ll m}{\approx} g \left(\frac{mT}{2\pi} \right)^{3/2} \exp(-m/T) \quad (1.8)$$

and $\rho = mn$. Let us now take the particle content of the SM and set the initial temperature of the thermal bath to some T . The fluid that permeates the Universe has total energy density which is simply the sum of all the individual ρ given by Eq. (1.6) and pressure $P = \rho/3$. This sets the stress-energy tensor in the Einstein’s field equation and one can now solve them in order to find the solution $a(t)$ *i.e.* the expansion of the Universe. For our purposes, we give $H = \dot{a}/a$ the Hubble parameter in a radiation dominated era

$$H = 1.66 \sqrt{g_*} T^2 / M_{\text{Planck}} \quad (1.9)$$

where g_* is the effective number of relativistic degrees of freedom (see for example [48]) and $M_{\text{Planck}} = 1.22 \times 10^{19}$ GeV.

Let us now look at a toy model of DM in order to understand its possible production in the Early Universe. We will assume that the DM has some interactions with, say, the electrons of the SM thermal bath. We will also assume that the DM is much heavier than the electron. At lowest order in the coupling, the leading DM number changing processes are depletion into electrons $\text{DM} + \text{DM} \rightarrow e^+ e^-$ and creation by electrons $e^+ e^- \rightarrow \text{DM} + \text{DM}$. Within this picture, the Boltzmann equation for the number density of DM particles in the Early Universe is given by

$$\frac{dn_{\text{DM}}}{dt} + 3Hn_{\text{DM}} = - \langle \sigma v \rangle_{\text{DM} + \text{DM} \rightarrow e^+ e^-} n_{\text{DM}}^2 + \langle \sigma v \rangle_{e^+ e^- \rightarrow \text{DM} + \text{DM}} n_{e^\pm, \text{eq}}^2 \quad (1.10)$$

where we introduced the Hubble parameter H . On the right hand side, the first term corresponds to the DM depletion process. It is proportional to the square of the DM number density n_{DM} since it involves 2 DM particles in the initial states. The second term corresponds to the creation process. It is instead proportional to the square of the equilibrium densities of electron since an e^\pm pair is in the initial state and we assume the SM thermal bath to be at equilibrium. We mention that

σ corresponds to the cross section of the process and $\langle\sigma v\rangle$ is the *thermally averaged* cross section [47]. In order to solve numerically¹⁰ the Boltzmann equation, we would need in principle to model the DM–electron interactions by the exchange of some particles, for example the photon if the DM has a small electric charge, in order to compute the thermally averaged cross section. Since such endeavours will be taken in Chapter 3 with the appearance of a very rich phenomenology, we will restrict ourselves here to a simple expression for the cross section, in line with our DM *toy-model*. We choose to consider the following temperature dependent form of the thermally averaged annihilation cross section

$$\langle\sigma v\rangle_{\text{DM}+\text{DM}\rightarrow e^+e^-} = \frac{\alpha_D^2}{4m_{\text{DM}}^2 + T^2} \quad (1.11)$$

and the reverse process is simply obtained by adding an extra factor of $(n_{\text{DM}}^{\text{eq}}/n_{e^-}^{\text{eq}})^2$ by definition of the thermally averaged cross section. Here, $\alpha_D \equiv g_D^2/4\pi$ where g_D is the strength of the interaction between the DM and electrons. At high temperature, $T \gg m_{\text{DM}}$, we expect the cross section to behave as $1/s$, where \sqrt{s} is the energy in the center of mass frame. In a thermal bath at temperature T , particles typically have a kinetic energy of order T , hence our choice of this specific high T behaviour. However, at low temperature, $T \lesssim m_{\text{DM}}$, the rest mass dominates the energy budget of the interaction and we choose the cross section to become constant. Additional factors of suppression due to kinematics or phase-space have been neglected. This form of the cross section encompasses the main features of the thermally averaged cross section of a typical DM model.

We will first detail the processes through which DM reaches equilibrium with the SM, as it will be important in Part I of the manuscript. Starting from an in-equilibrium thermal bath of SM particles at temperature T , DM will be said to have reached equilibrium with the SM thermal bath if its phase space density is close to an equilibrium density $f_{\text{DM}} \sim f^{\text{eq}}$. Through interactions with the SM particles, the DM can inherit the same impulsion distribution (kinetic equilibrium) as the bath if scatterings $\text{DM} + e^\pm \rightarrow \text{DM} + e^\pm$ are “fast” (to be made more precise later). Similarly, the total number of DM particles can become comparable to the equilibrium number (chemical equilibrium) if annihilation processes $\text{DM} + \text{DM} \rightarrow e^+e^-$ are also fast. Note that chemical equilibrium will ensure kinetic equilibrium but the reverse is not true. We will say that DM chemical equilibrium with the SM thermal bath is reached at time t if, on average, every DM particle has interacted once with the thermal bath during that time. Also, we would like to know if DM reaches equilibrium before the temperature drops below its mass, point after which annihilation processes are highly suppressed by the kinematics. In mathematical terms, DM reaches equilibrium with the SM if

$$\Gamma/H|_{T=m_{\text{DM}}} = \left. \frac{\langle\sigma v\rangle_{e^+e^-\leftrightarrow\text{DM}+\text{DM}} n^{\text{eq}}}{H} \right|_{T=m_{\text{DM}}} \lesssim 1 \quad (1.12)$$

where Γ is the rate of interactions and $1/H$ is a proxy for the age of the Universe¹¹. From the condition of Eq. (1.12), we can thus find the coupling $\alpha_{D,\text{th}}$ in Eq. (1.11) such that DM reaches equilibrium before $T = m_{\text{DM}}$, *i.e.* such that the DM–SM interactions are fast with respect to the expansion of the Universe. We find that for the DM candidate with a mass of 1 GeV, the critical coupling is

$$\alpha_{D,\text{th}} = 4 \times 10^{-9} \quad (1.13)$$

¹⁰It is possible to obtain analytical solutions to the Boltzmann equation, which can be very useful for estimating easily and accurately the relic abundance of DM. However, since the first part of the thesis will be focused on the numerical solutions of a system of Boltzmann equation, we will not detail them. See [9] for a canonical description of these approximations.

¹¹In the radiation era, the age of the Universe is given by $t_{\text{Univ}} = 1/2H$.

Any larger coupling will lead to thermalization before $T = m_{\text{DM}}$ and any smaller coupling would not lead to equilibration between the DM and the thermal sector. One interesting consequence is that if one takes $\alpha_D > \alpha_{D,\text{th}}$, the Boltzmann equation of Eq. (1.10) can be solved with $n_{\text{DM}} = n_{\text{DM}}^{\text{eq}}$ as initial condition. For $\alpha_D < \alpha_{D,\text{th}}$, it would depend on the post-inflation abundance of DM, which we will assume in the following to be 0.

We now have everything at hand to use Eq. (1.11) in Eq. (1.10) and obtain, given a couple $(m_{\text{DM}}, \alpha_D)$, the relic abundance of DM. It is convenient to introduce the comoving DM number density¹² (also called yield) $Y_{\text{DM}} = n_{\text{DM}}/s$ for s the total entropy¹³ and $z = m_{\text{DM}}/T$ the inverse temperature as the evolution parameter. Throughout the thesis, we will describe the abundance of DM in those terms.

In Fig. 1.4 (left) is given $Y(z)$ for different values of the coupling α_D for a DM candidate of $m_{\text{DM}} = 1$ GeV.

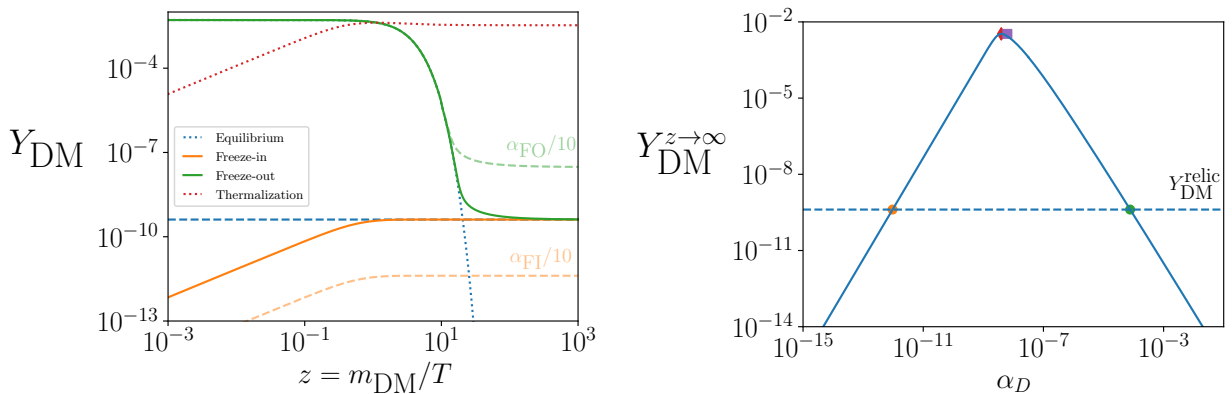


Figure 1.4: Left: DM abundance as a function of inverse temperature. The solid green (orange) curve represents the evolution of the abundance of a DM candidate set by freeze-out (freeze-in). In dotted red is given $Y(z)$ for the case where DM thermalizes and drops out of equilibrium at the same time. The dashed blue curve corresponds to the observed DM relic abundance. Right : The pyramid of the relic abundance of the DM toy-model, Eq. (1.11), as a function of DM–electron coupling. The dashed blue curve corresponds to the observed DM relic abundance. The highlighted points corresponds to freeze-out, freeze-in (green, orange), thermalization (red) and estimation of thermalization (violet, Eq. (1.12))

The dashed blue horizontal line corresponds to the observed relic abundance of DM [42] expressed in terms of the yield, $Y_{\text{DM}}^{\text{relic}} = 4.09 \times 10^{-9} (\text{GeV}/m_{\text{DM}})$. The dotted blue line corresponds to the equilibrium yield of DM. As T drops below m_{DM} , DM creation processes are suppressed and only DM depletion processes happen, hence the drop in the equilibrium DM abundance.

In Fig. 1.4 (left), the green lines give the DM abundance as a function of time for the case of two coupling such that $\alpha_D \gg \alpha_{D,\text{th}}$. At high temperature (early time, low z), the DM abundance follows the equilibrium curve. At $T < m_{\text{DM}}$, the abundance drops rapidly as annihilation processes become more frequent than creation processes. This suppression is dubbed “Boltzmann suppression”. As the abundance drops, annihilation processes become less efficient and, at low temperature (late time, high z), the DM abundance becomes constant. This processes is known as *freeze-out*. Through freeze-out, one is able to reproduce the observed DM abundance. In our toy-model, we find that

¹²The benefit of using this variable is that it is not diluted by the expansion of the Universe, whereas n is.

¹³More precisely, $s = 2\pi^2/45 \times \mathcal{R}T^3$ for each species in the thermal bath.

the coupling required to obtain the observed relic abundance for a 1 GeV DM candidate through freeze-out is

$$\alpha_{D,\text{FO}} = 8 \times 10^{-5} \quad (1.14)$$

which is much higher than $\alpha_{D,\text{th}}$. The abundance of the candidate with $\alpha = \alpha_{D,\text{FO}}$ is given as the green solid line in Fig. 1.4. The dashed green line corresponds to $\alpha = \alpha_{D,\text{FO}}/10$. With a smaller coupling, annihilations are less efficient and DM decouples from the thermal bath earlier, hence with a higher abundance.

In Fig. 1.4 (left), the orange lines give the DM abundance as a function of time for the case of two coupling such that $\alpha_D \ll \alpha_{D,\text{th}}$. Starting with the assumption that a negligible DM abundance is created at the end of inflation, at high temperature (early time, low z), the DM abundance is very small when compared to the equilibrium value. DM is then slowly produced by $e^+e^- \rightarrow \text{DM} + \text{DM}$ annihilations and its abundance grows with time. At high T , the DM “creation rate”, see the right hand side of Eq. (3.11), is constant and therefore $Y \propto z$. As the Universe cools down below $T = m_{\text{DM}}$, e^\pm annihilations into DM is kinematically suppressed and DM production stops. This process is known as *freeze-in*. As freeze-out, freeze-in is a possible mechanism for producing DM in the early Universe. In our toy-model, we find that the coupling required to obtain the right relic abundance for a 1 GeV DM candidate through freeze-in is

$$\alpha_{D,\text{FI}} = 9 \times 10^{-13} \quad (1.15)$$

which is much lower than $\alpha_{D,\text{th}}$. The abundance of the candidate with $\alpha = \alpha_{D,\text{FI}}$ is given as the orange solid line in Fig. 1.4. The dashed orange line corresponds to $\alpha = \alpha_{D,\text{FI}}/10$. With a smaller coupling, production is less efficient DM reaches therefore a smaller abundance.

In Fig. 1.4 (left), the dotted red line corresponds to the on-set of thermalization. For this particular coupling, we see that DM reaches equilibrium and drops out of equilibrium at the same time. If the coupling was lower, the abundance would be smaller. In the same vein, if the coupling was higher, the abundance would be smaller due to annihilations after reaching equilibrium. We find that

$$\alpha_{D,\text{crit}} = 6 \times 10^{-9} \quad (1.16)$$

which is very close to the estimation of $\alpha_{D,\text{th}}$ of Eq. (1.13).

Those observations have been summarized on the right of Fig. 1.4, in the so-called “pyramid”. The solid blue line corresponds to the relic abundance as a function of the coupling α_D . The dashed blue line corresponds to the observed DM relic density. For small couplings, the abundance is $\propto \alpha_D^2$. This is the freeze-in regime, where the abundance is proportional to the production cross section. For higher couplings, the abundance is instead $\propto \alpha_D^{-2}$. This corresponds to the freeze-out regime, for which the abundance is inversely proportional to the annihilation cross section. The solid blue line crosses the horizontal lines in two points, hence within this toy-model there indeed exist two possible DM production mechanisms. The green dot corresponds to freeze-out and the orange dot to freeze-in. At intermediate coupling, where the abundance is the highest, the red diamond corresponds to the critical coupling $\alpha_{D,\text{crit}}$ and the violet square to $\alpha_{D,\text{th}}$.

Since freeze-in will be discussed at length in Part I of the thesis, let us explore it in more detail. As can be seen from the left of Fig. 1.4, most of the DM is produced at low temperature. This is typical for a freeze-in that proceeds through renormalizable interactions¹⁴. In Fig. 1.5 we give (left)

¹⁴For a review of the phenomenology of freeze-in DM, see [49].

the contributions to the total relic abundance of a DM candidate being frozen-in by annihilations during different time range of the Early Universe. The label of each sector corresponds to the integration domain of the Boltzmann equation. On the right is given $Y(z)$ in arbitrary units where the corresponding time range is shaded in the same color (from red corresponding to hot and early to blue corresponding to cold and late). As can be easily seen, most of the production happens around $z \sim 1$ since the Universe is the oldest and stops for lower temperature, due to Boltzmann suppression.

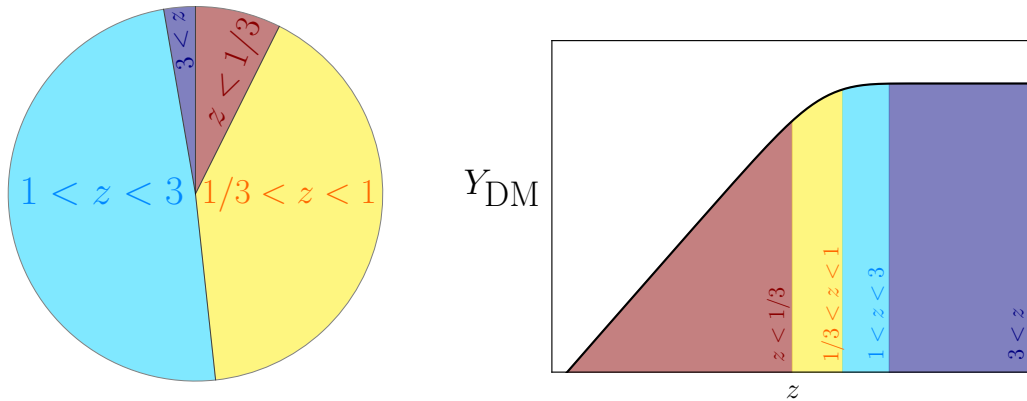


Figure 1.5: Schematic representation of infrared dominated freeze-in.

For higher dimensional operators, the freeze production is instead typically UV-dominated [50]. Interplays between both type of freeze-in is nonetheless possible [51].

As a final comment, let us mention one particular DM candidate : the Weakly Interacting Massive Particle (**WIMP**). Even though this is not transparent from our discussion of the freeze-out mechanism, a stable weak scale particle (*i.e.* a particle with either electroweak interactions or with interactions of the same strength) reproduces correctly the observed DM relic density by freeze out [52, 53]. This is especially surprising since the gauge group $SU(2)_L$ has *a priori* no relation to cosmology at all. Nonetheless, this so-called “miracle” has led to numerous searches by experimental collaboration and is still, to this day, a very useful benchmark for DM physics.

1.4 A few words on portal models

Even though Eq. (1.11) helped us greatly in understanding the dynamics of DM production in the Early Universe, it is not enough for the purpose of DM phenomenology. The Standard Model of elementary particles has proved that the Universe can be quite exquisitely understood by constructing a renormalizable theory that consists of gauge groups, elementary fermions and a complex scalar. In the following, we will say of all the particles that are described by the SM that they belong to the “visible” sector. We will also assume that the DM is described by similar ingredients. This will allow us to go beyond the simple toy-model of Eq. (1.11) by specifying the interactions that DM has with all the SM. Necessarily, this also put forth the idea that the DM could belong to a “dark” or “hidden” sector, which, on top of the DM, comprises of other new elementary particles. This dark sector could possibly be as complicated as the visible sector or fix all the shortcomings of the SM by being the cause of, say, the neutrino masses, inflation, matter-antimatter asymmetry and perhaps other puzzles that are yet to be unveiled. Out of all the parameters of the dark sector,

a great deal would be essentially¹⁵ free¹⁶ and this would make a global study of the dark sector extremely challenging. However, there is the hope that only a handful of the unknown dark sector parameters are relevant for a given question.

In that vein, this thesis proposes to study, in detail, simple DM models within the so-called “portal” structure [54]. Simplicity will be enforced by considering a small amount of new particles with a corresponding small amount of new parameters. The portal will be realized by an interaction that links the visible to the hidden sector. This will be done by considering a particle, the mediator, which could either belong to the dark sector or to the visible sector (in which case the only new particle is the DM). Finally, this theory should respect the principles of Lorentz and gauge invariance, be renormalizable and not jeopardize DM stability over the lifetime of the Universe. Interestingly, these requirements allow for a general classification of portal interactions [55, 56]. In Table. 1.1, we have adapted Table 2.1 of [3], which gives some representative interactions structure between a SM singlet DM candidate and a mediator.

DM	Mediator	Channel	Portal interactions
S	Φ	s	$\lambda_S S^2 \Phi^\dagger \Phi$
ψ	S	s	$gS\bar{\psi}\psi + S \leftrightarrow H$ mixing
V^μ	Φ	s	$\lambda_V V^\mu V_\mu \Phi^\dagger \Phi$
ϕ	V^μ	s	$V^\mu \left[g_\phi (\phi^* (i\partial_\mu \phi) - \phi (i\partial_\mu \phi^*)) + \sum_{f,i} \bar{f}_i \gamma_\mu (g_{f,i}^V - g_{f,i}^A \gamma_5) f_i \right]$
ψ	V^μ	s	$V^\mu \left[(\bar{\psi} (g_\psi^V - g_\psi^A \gamma_5) \psi) + \sum_{f,i} \bar{f}_i \gamma_\mu (g_{f,i}^V - g_{f,i}^A \gamma_5) f_i \right]$
ψ	Φ	t	$\sum_i (g_f^i \bar{\psi} \Phi_i^* f_{R,i} + \text{h.c.})$
S	Ψ	t	$\sum_i (y_f^i S \bar{\Psi}_i f_{R,i} + \text{h.c.})$

Table 1.1: Classification of portal models, adapted from [3]. S is a real scalar, Φ a complex scalar, ψ and Ψ have spin 1/2 and V^μ spin 1.

The index i runs across the three generations of a SM fermion f , which can be either a lepton or quark. Let us now comment on the physics of such simplified DM models.

We first focus on the first 3 row. When the mediator is a complex scalar Φ , the SM scalar can play the role of the mediator. However, when the mediator is a real scalar S , it is necessary to introduce mixing between S and H in order for the DM to couple to the visible sector. If Φ is not H , a $\Phi - H$ mixing should also be added. Note that we have omitted one possibility from the Table, a ψ DM candidate with a complex scalar Φ charged under a non-abelian group and interacting through a Yukawa interaction $g\bar{\psi}\Phi\psi$ (with appropriate representations). In these models, the DM therefore interacts with the SM through the “Higgs portal”. In Part II of this thesis, we will focus on the $\psi - S$ interaction of the second row.

In the fourth and fifth row, DM interacts with the SM through a vector mediator. We have considered both vector and axial couplings. In Part I of this thesis, we will explore at length the

¹⁵One combination of parameters can be fixed by asking the relic density of DM to be what is observed. The other parameters might be constrained by observations but generally the parameter space of a dark sector that contains a few particles is gigantic.

¹⁶The SM has about 20 parameters that needs to be measured.

phenomenology associated with a model akin to the fermionic case.

The last two rows exhibit t -channel mediators. Necessarily, the mediator and the SM fermions would need to have the same quantum numbers and thus only the sum over generations is present. We chose to present an interaction with right-handed SM fermions, left handed being treated in the same way. If ψ is a Majorana fermion, this structure is reminiscent of neutralino DM where Φ would be the superpartner of f [52]. In the last row, the spin of the DM and mediator are flipped. It is noteworthy that the features of the t -channel $S - \Psi$ are very different from those of the $\psi - \Phi$ model, even if from a model building perspective one simply has exchanged the role of the DM and mediator. In particular, a full phenomenological study of a top-philic candidate was the subject of the first year of the PhD. As explained before the introduction, this project is quite different from the two other subjects that were treated during the thesis. We therefore made the choice to only briefly discuss the top-philic scenario in Appendix A and instead refer the reader to the two (self-contained) articles [1, 2].

Even though only 1 DM particle and 1 mediator is considered, it is seen that the structures in which the mediator interacts with SM fermions might have many different free couplings, possibly one for each different generations, each different lepton and each different quark. Since it would complicate greatly the picture, it is common to focus on only one SM fermion, with models therefore dubbed as “lepto-philic” or “top-philic” for example. It is interesting to note that for the vector mediator cases, there exists one possibility to reduce the number of couplings drastically. The mediator V^μ could simply inherit the hypercharge of the SM fermions by mixing with the Y boson, see Chapter 2.

In this brief introduction to the puzzle that is DM, we first motivated its existence. The DM relic density should be set in the Early Universe by its elementary interactions and we sketched two possible mechanisms : freeze-out and freeze-in. We then argued that studying DM by using simple, minimal, renormalizable DM models will allow us to obtain insight into its characteristics, even if they are not the true, underlying theory of DM interactions. We now have in hand the majority of the ingredients that are required to start understanding the aspects of DM phenomenology that are described in this thesis. In the following Chapters, we will study two different DM models, on two fronts. In the first Part, we will mainly focus on describing the DM production mechanisms in a simple DM model and assess its discovery potential. In the second Part, we will treat an as simple DM model but focus on DM self-interactions in a medium.

Part I

A spin one portal

Chapter 2

Kinetic Mixing Portal to Dark Matter

In this Chapter, we will treat the case of a local broken $U(1)'$ extension of the SM containing a fermionic DM candidate and the associated massive gauge boson as mediator with the visible particles. This widely popular model (see the reviews [57, 58, 59]) is the direct extension of an old scenario where dark matter was assumed to be electrically charged [60]. This short Chapter aim at understanding the degrees of freedom and couplings of the model. In the subsequent Chapters, we will treat the problem of DM production in the Early Universe and then detail the possibility of detecting such DM candidates at earth-based direct detection experiment, within the context of the model presented here.

2.1 The model

Owing to few new arbitrary parameters, kinetic mixing portal models are theoretically attractive and extensive studies of their parameter space have revealed a stunning range of phenomena that show relevance throughout our Universe's history. Any family of particles charged under this $U(1)'$ will provide a natural stable DM candidate as its lightest particle, by charge conservation [61, 62, 63, 64, 65]. Even if the abelian group is broken through the Stückelberg or Brout-Englert-Higgs mechanisms, many degrees of freedom can nevertheless be stable. The lightest fermion will stay stable, again due to charge conservation. Assuming a completely secluded dark sector, the now massive gauge boson could also be stable if no decay channel into dark sector fermions are kinematically open. For a $U(1)'$ extension of the SM, where we seek for the gauge boson to act as a mediator, there exists very few possibilities. Coupling of DM to the SM could arise if visible matter is also charged under the gauge group. A possible realisation of such cases would be to simply give a small electric charge to the DM, making it therefore “mini-charged”. Another one would be to gauge the anomaly-free global symmetry $U(1)_{B-L}$ of the SM and charge DM under it. The only other renormalizable possibility is mixing, either kinetic or through a mass term, of the $U(1)'$. The example that will be most relevant for this work will be mixing with the hypercharge $U_Y(1)$.

The relevant part of the lagrangian describing a fermionic DM candidate, charged under a $U(1)'$ which mixes both kinematically and by mass mixing is the following

$$\begin{aligned} \mathcal{L} \supset & i\bar{\chi}\not{D}\chi - m_{\text{DM}}\bar{\chi}\chi - \frac{1}{4}B'^{\mu\nu}B'_{\mu\nu} + \frac{1}{2}m_{\gamma'}^2 B'^{\mu}B'_{\mu} \\ & - \frac{\hat{\epsilon}}{2}B^{\mu\nu}B'_{\mu\nu} + \hat{\delta}m_{\gamma'}^2 B^{\mu}B'_{\mu} + \dots \end{aligned} \tag{2.1}$$

where χ , the DM, is a Dirac fermion of mass m_{DM} charged under the new $U(1)'$ but not the SM. It couples with charge e' to the new gauge boson B'_μ . We write its field strength as $B'_{\mu\nu}$ and its mass $m_{\gamma'}$. The dark sector is then coupled to the SM through a kinetic mixing term with a small mixing angle $\hat{\epsilon}$ [66] and a small mass mixing $\hat{\delta}$. It thus comprises of 2 new particles, a DM candidate and a mediator, and 5 new parameters that are the DM mass m_{DM} , the kinetic and mass mixing parameters $\hat{\epsilon}, \hat{\delta}$, the dark charge e' and mass of the dark photon $m_{\gamma'}$. In the following, we will describe the interactions preferably through the dark fine structure constant $\alpha' \equiv e'^2/4\pi$ and the parameter $\kappa = \hat{\epsilon} \cos \theta_W e'/e$, that corresponds to the milli-electric charge of the DM if $m_{\gamma'} \rightarrow 0$. The dark photon mass can arise either through the Stückelberg [67] or Brout-Englert-Higgs mechanism [68, 69] and the dots in Eq. (2.1) would contain the relevant scalar sector¹.

2.2 Mixing, diagonalization

Provided the mixings are small, it is possible to treat them as good-old interaction terms in any perturbative computation, see Eq. (4.1). However we would like to read off the couplings of the DM and SM fermions to the dark photon and hypercharge boson directly. We will thus here proceed to the diagonalization of the kinetic and mass terms and identify the propagating degrees of freedom. First, we apply a non unitary transformation to the $U(1)'$ gauge boson

$$B'^\mu = \tilde{B}'^\mu - \hat{\epsilon} B^\mu \leftrightarrow B'_\mu = \tilde{B}'_\mu - \hat{\epsilon} B_\mu \quad (2.2)$$

which pushes the kinetic mixing into a mass mixing between B_μ and \tilde{B}'_μ

$$\begin{aligned} \mathcal{L} \rightarrow & -\frac{1}{4} \tilde{B}'^{\mu\nu} \tilde{B}'_{\mu\nu} + \frac{1}{2} m_{\gamma'}^2 \tilde{B}'^\mu \tilde{B}'_\mu - (\hat{\epsilon} - \hat{\delta}) m_{\gamma'}^2 B^\mu \tilde{B}'_\mu \\ & - ie' \bar{\chi} \gamma^\mu \chi (\tilde{B}'_\mu - \hat{\epsilon} B_\mu), \end{aligned} \quad (2.3)$$

where higher orders terms $\mathcal{O}(\hat{\epsilon}^2)$, $\mathcal{O}(\hat{\epsilon}\hat{\delta})$ have been neglected.

In the limit $m_{\gamma'} = 0$, the $B_\mu - \tilde{B}'_\mu$ system is diagonal and we identify B with the hypercharge boson, \tilde{B}' with the dark photon. SM particles interactions are untouched and couple only to the massless photon and the massive Z boson, defined as $B^\mu = \cos \theta_W A_0^\mu - \sin \theta_W Z_0^\mu$, $W_\mu^3 = \sin \theta_W A_0^\mu + \cos \theta_W Z_0^\mu$ where θ_W is the weak angle and we denote the standard SM fields by the subscript 0. In turn, χ possesses a small coupling to the hypercharge boson: it interacts with the SM photon A_0^μ , has the milli-electric charge $\kappa = \epsilon e'/e$, where $\epsilon = \hat{\epsilon} \cos \theta_W$ and couples to the Z -boson with strength $-e' \epsilon \tan \theta_W$. In the $m_{\gamma'} = 0$ limit, the dark photon \tilde{B}'^μ does not couple at all to SM fields and only couples to χ through the dark charge e' [70, 71]. If $m_{\gamma'} \neq 0$, the same conclusions as above can be reached if we restrict ourselves to $\hat{\delta} = \hat{\epsilon}$. For both of these special cases ($m_{\gamma'} = 0$ or $\hat{\epsilon} = \hat{\delta}$), one could in principle rotate the $B_\mu - \tilde{B}'_\mu$ system by an arbitrary angle, which would leave the kinetic terms and the (trivial) mass matrix untouched. In turn, the interaction terms will be modified and, for example, any electrically charged SM fermions would now couple to the 2 massless gauge bosons. However, since the physics of any real process is not impacted, we simply choose the basis where the SM fermions couple only to the hypercharge boson B .

If $m_{\gamma'} \neq 0$, the mass matrix must be diagonalized. Couplings of the dark photon with the SM fields arise from the mass mixing

$$-(\hat{\epsilon} - \hat{\delta}) m_{\gamma'}^2 \tilde{B}'_\mu B^\mu \equiv -(\epsilon - \delta) m_{\gamma'}^2 \tilde{B}'_\mu (A_0^\mu - \tan \theta_W Z_0^\mu), \quad (2.4)$$

¹In some particular cases, the scalar sector of the BEH mechanism can become relevant for aspects of the production phases. In this thesis, the scalar sector will be ignored but a few details can be found in [5].

where $\delta = \hat{\delta} \cos \theta_W$. In order to diagonalize the mass terms of the $\tilde{B}' - A_0 - Z_0$ system, we perform the following orthogonal transformation on the A_0 and \tilde{B} fields

$$A'^{\mu} = \tilde{B}'^{\mu} - (\epsilon - \delta) A_0^{\mu} \quad \text{and} \quad A^{\mu} = A_0^{\mu} + (\epsilon - \delta) \tilde{B}'^{\mu} \quad (2.5)$$

The kinetic and mass terms become diagonal

$$\begin{aligned} \mathcal{L} \rightarrow & -\frac{1}{4} A'^{\mu\nu} A'_{\mu\nu} - \frac{1}{4} A^{\mu\nu} A_{\mu\nu} + \\ & + \frac{1}{2} m_{\gamma'}^2 A'^{\mu} A'_{\mu} + (\epsilon - \delta) m_{\gamma'}^2 \tan \theta_W Z_0^{\mu} A'_{\mu} + \frac{1}{2} m_{Z_0}^2 Z_0^{\mu} Z_{0,\mu} \end{aligned} \quad (2.6)$$

up to a $A' - Z_0$ mass splitting, which will always be negligible in this thesis. The dark photon A' has mass $m_{A'} = m_{\gamma'}$ and the Z boson Z_0 has its SM mass m_{Z_0} , while the photon A remains massless. If the mass mixing with the Z_0 boson cannot be neglected, for example if $(\epsilon - \delta) m_{\gamma'}^2$ is not small compared to the Z_0 mass m_{Z_0} , one should instead rotate the three fields \tilde{B} , A_0 and Z_0 together and the mixing angles take more complicated expressions [72].

The interaction term between χ , \tilde{B}' and B in Eq. (2.3) becomes, in this eigenmass basis,

$$e' \bar{\chi} \gamma^{\mu} \chi (\tilde{B}'_{\mu} - \hat{e} B_{\mu}) \equiv e' \bar{\chi} \gamma^{\mu} \chi (A'_{\mu} - \delta A_{\mu} + \epsilon \tan \theta_W Z_{\mu}^0) \quad (2.7)$$

and the dark matter χ has a millicharge $-\delta e'$ and also couples to the massive gauge bosons, A' and Z_0 . In a similar fashion, the SM fields ψ that possesses an electric charge will inherit a “dark millicharge” $-(\epsilon - \delta)$ with respect to the dark photon A'

$$e \bar{\psi} \gamma^{\mu} \psi A_{0\mu} \equiv e \bar{\psi} \gamma^{\mu} \psi (A_{\mu} - (\epsilon - \delta) A'_{\mu}). \quad (2.8)$$

In Fig. 2.1 is given a summary of the coupling structure of the model

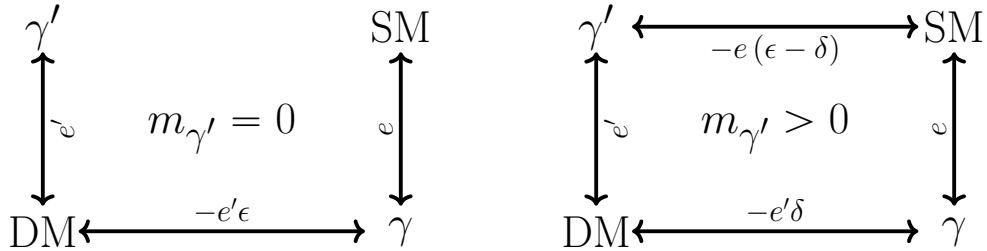


Figure 2.1: Representation of the active and inactive couplings between the fermion χ (DM) and the electrically charged ψ 's (SM). On the left the dark photon is massless and the basis of Eq. (2.3) is shown. On the right, the dark photon has a non zero mass and the couplings between the different sectors are that of the basis of Eq. (2.6), for which the kinetic and mass mixing have been rotated away.

A few comments on models with a massive dark photon are in order. The most studied case of a fermion charged under a kinematically mixed broken $U(1)'$ are models with no mass mixing term, $\delta = 0$. In these models, DM exclusively couples to the dark photon and the dark photon

couples to the SM. On the other hand, if $\epsilon = 0$ but $\delta \neq 0$, DM couples to both the photon and the dark photon². If $\epsilon = \delta$, one recovers the coupling structure of the massless theory but where DM self-interacts through both a Coulomb and Yukawa interaction. In this limit, the massive dark photon does not couple at all to the SM. For arbitrary values of ϵ and δ , DM–SM interactions proceed through the exchange of 2 different particles – the massless photon and the massive dark photon – which have different couplings. This can give rise to interesting behaviours of the cross sections in their s - or t - channel. For example, through the choice of the sign of $\epsilon - \delta$, it is possible for DM–SM scattering amplitudes to interfere either constructively or destructively. In summary, if δ is non-zero, DM is also millicharged even when the dark photon is massive.

2.3 UV completions of photon-dark photon mixing

Such models can be seen through the lens of a UV perspective. The SM could be a low-energy approximation of a more complicated theory whose degrees of freedom could, for example, solve the baryon asymmetry problem and other shortcomings of the SM. A particularly well motivated scenario is that of string theory where, among other successes, one sees gravity emerging from microphysics. A photon–dark photon kinetic mixing can be generated in string theory setup [73] and small values of $\epsilon \sim 10^{-6} - 10^{-12}$ can be argued to be natural. Other UV completions that provide an origin of the mixing parameters exist. The kinetic mixing between the $U(1)_Y$ and $U(1)'$ can be generated at the one-loop level by heavy fermions charged under both gauge group. If the high energy theory contains 2 fermions f and f' , of masses $m < m'$, with the charge assignment (e, e') and $(e, -e')$ under $U(1)_Y, U(1)'$ respectively then, after integrating out those heavy fermions, a kinetic mixing is generated and is of strength [66]

$$\epsilon = \frac{ee'}{6\pi^2} \log \frac{m'}{m} \quad (2.9)$$

This can be generalized to an arbitrary number of fermions charged under both $U(1)$ with the only condition that the sum of the product of each fermion charge with dark charge is 0 [74], to ensure that the sum of the new contributions to vacuum polarization is UV finite. It is also possible for one of the gauge group to be non-abelian [75, 76] and the mixing term would then be of the form

$$\frac{\epsilon}{M} \text{Tr}(\Phi G_{\mu\nu}) F^{\mu\nu} \quad (2.10)$$

where G is the field-strength tensor of a dark non-abelian group and Φ a “dark Higgs” field in, for this case, the adjoint. As a result of the kinetic mixing after spontaneous symmetry breaking, all massive dark gauge bosons would then couple to the electromagnetic current. From naturalness perspectives, the ratio $\langle \Phi \rangle / M$ could provide some additional suppression of the mixing parameter.

As for the mass mixing δ , it can easily arise from the Stückelberg mechanism³ [77, 78, 79]. In that case, the mass of the dark photon comes from the following term that is added to the lagrangian⁴

$$-\frac{1}{2} (\partial_\mu \sigma + m_{\gamma'} (B'_\mu + \delta B_\mu))^2 \quad (2.11)$$

²If the mass mixing is between the Z boson and the dark photon, it would be referred to as “dark Z ”.

³It is seen that the parameters ϵ and δ can arise from very different physics and this naturally begs the question if the limit $\epsilon = \delta$ is ever motivated on theoretical grounds.

⁴Had we chosen the second term in the bracket to be $m_Z (B_\mu + \delta B'_\mu)$ and $\delta \gg 1$, B'_μ would instead be called Z' and would have been of mass $\delta m_Z \gg m_Z$ [80].

One may recover this particular term from a spontaneous symmetry breaking mechanism as follows. Let Φ be a complex scalar with charges e_Φ and δe_Φ under $U(1)'$ and $U(1)_Y$ respectively. Let its potential be such that it develops a non-zero vacuum expectation value v_Φ , with radial and angular (Goldstone) excitations denoted H and σ . A dark photon mass $m_{\gamma'} = e_\Phi v_\Phi$ and an hypercharge boson mass $m_Y = \delta e_\Phi v_\Phi$ are therefore induced. It is then just a matter of decoupling H by taking the vev v_Φ to infinity (and hence the H mass also), the charge e_Φ to 0 while keeping the production $e_\Phi v_\Phi$ fixed to the desired dark photon mass $m_{\gamma'}$. After these manipulations, the scalar sector simply reduces to Eq. (2.11).

Interestingly, from UV considerations, it is possible to generate couplings of the massless dark photon to the SM fermions [81, 82]. However, they will necessarily appear only through higher dimensional operators, $\dim \mathcal{O} > 4$, which might provide interests in considering them to be naturally feeble. At dimension 5 and 6, one can write the following interactions

$$\mathcal{L}_{\dim>4} = \frac{e'}{2\Lambda_5} \bar{\psi}^i \sigma_{\mu\nu} \left(\mathcal{D}_M^{ij} + i\gamma_5 \mathcal{D}_E^{ij} \right) \psi^j F'^{\mu\nu} + \frac{e'}{2\Lambda_6^2} \bar{\psi}^i \gamma_\mu \left(\mathcal{R}_r^{ij} + i\gamma_5 \mathcal{R}_a^{ij} \right) D_\nu \psi^j F'^{\mu\nu} + \text{h.c.} \quad (2.12)$$

where the Λ 's are some UV scales, H is the field of the scalar of the SM and the i, j indices track flavors. The Lorentz generators $\sigma_{\mu\nu} = i/2[\gamma_\mu, \gamma_\nu]$ have been introduced and D_μ is the covariant derivative for the ψ field. \mathcal{D}_M and \mathcal{D}_E are the magnetic and electric dark dipole moment, respectively. For the latter, because of the γ_5 factor, the UV completion would necessarily need to break CP symmetry. In the last two terms, \mathcal{R}_r is related to the charge radius of the SM fermions and \mathcal{R}_a is the anapole⁵.

Since our study is of phenomenological nature, we will thus mostly work with the renormalizable model of Eq. (2.1). Naturalness aspects and the possible origin of the relevant terms will not be studied. As the kinetic and mass mixing terms do not break any symmetry of the lagrangian, they therefore could (should) be included in the theory, irrespectively of their theoretical attractiveness.

⁵For an application to DM phenomenology and further interpretations, see [83].

Chapter 3

The mesa diagram of the dark matter relic density

In contrast to our knowledge of the thermal history of the SM thermal bath through CMB and Big Bang Nucleosynthesis (**BBN**) observables, many scenarios are possible when it comes to a dark sector abundance evolution with respect to time. As compared to the WIMP traditional lore, many assumptions such as kinetic, chemical equilibrium or initial abundances can be relaxed, with, possibly, the appearance of new signatures in experiments. In this Chapter, we will describe the possible DM thermal production mechanisms in the Early Universe that can account for the DM relic abundance in the model of Eq. (2.1) by going beyond the WIMP scenario. In particular, many new regimes of DM production discovered in [5] will be shown to exist and the feeblest coupled regimes will be studied in details, see Sections 3.3 and 3.4. Of particular interest is that these new regimes will be a generic feature of portal model such as the kinetic mixing portal and the results of this Chapter can be readily applied to other scenarios, therefore expanding the phenomenology of already well studied models. The study of the possible DM production mechanisms in the kinetic mixing portal will pave the way for looking at these new DM candidates from a point of view of their detection possibility, which we will discuss in Chapter 5.

3.1 Interplay between the visible and hidden sector

The SM thermal population at temperature T will produce and deplete the DM and dark photon dark sector population through their connections, with the relevant Feynman diagrams shown in Fig. (3.1). Fig. (3.1a), (3.1b) describe SM–DM interaction whose strength is set by the millicharge κ . Lepton–dark photons interactions are given in diagrams (c–e), representing Compton scattering, pair annihilation and coalescence respectively, all governed by the mixing parameter ϵ . Quarks will have additional diagrams involving gluons. Finally, DM can also be produced and depleted through its connection with the dark photon, proportionally to the dark fine structure constant α' . An important assumption that can be relaxed is that the particles composing the dark sector populations need not to be in chemical equilibrium with the SM or between themselves. All in all, when going beyond the WIMP case, the parameter space of the simple model of Eq. (2.1) can span orders of magnitude in couplings and interesting phenomenology arises.

All the possible mechanisms of in- and out-of-equilibrium DM production through the SM and Dark Sector (**DS**) interactions of this model are depicted by the triangle diagrams of Fig. 3.2. As we will describe in the following, there are critical values of the couplings below which some connections drops out of relevance (dashed line), above which sectors reach equilibrium (double sided arrow) or start slowly producing particles (single arrow), leading to very different DM production history

for each corner of the parameter space.

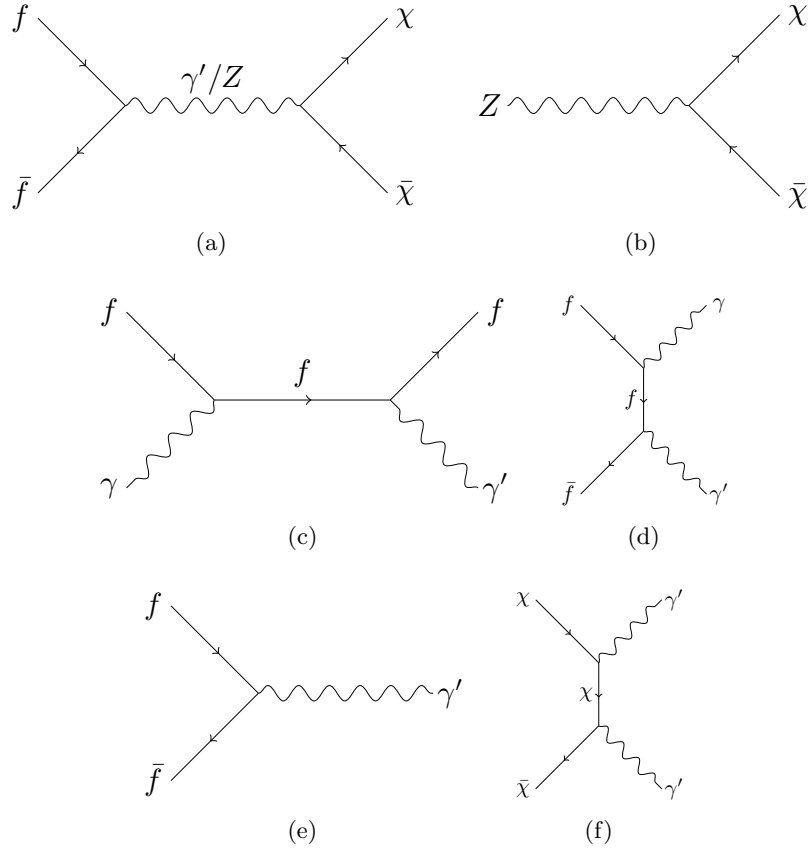


Figure 3.1: Feynman diagrams for the relevant processes of DM and dark photon production. The reverse processes would correspond to depletion of the corresponding population.

One can then use the illustration of Fig. 3.2 to understand the matter and coupling structure of this model. Each blob corresponds to a given particle sector and each of those possess connections to the others through one of three combination of the two lagrangian couplings. As many models share a similar picture, many of the results that we will obtain throughout this Chapter can be readily applied to those and thus can expand their phenomenology.

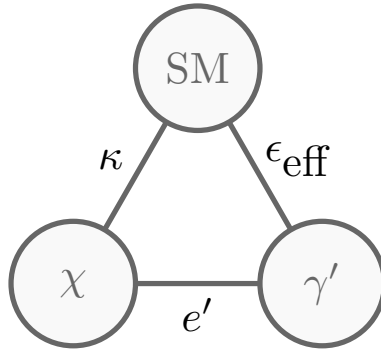


Figure 3.2: Illustration of the 3 connections (lines) between the 3 sectors (blob). The label of each line corresponds to the relevant coupling dictating the strength of interactions between two blobs. In the massless dark photon limit (or for scenarios where $\epsilon_{\text{eff}} \sim 0$, see Chapter 4), the SM – γ' connection is severed.

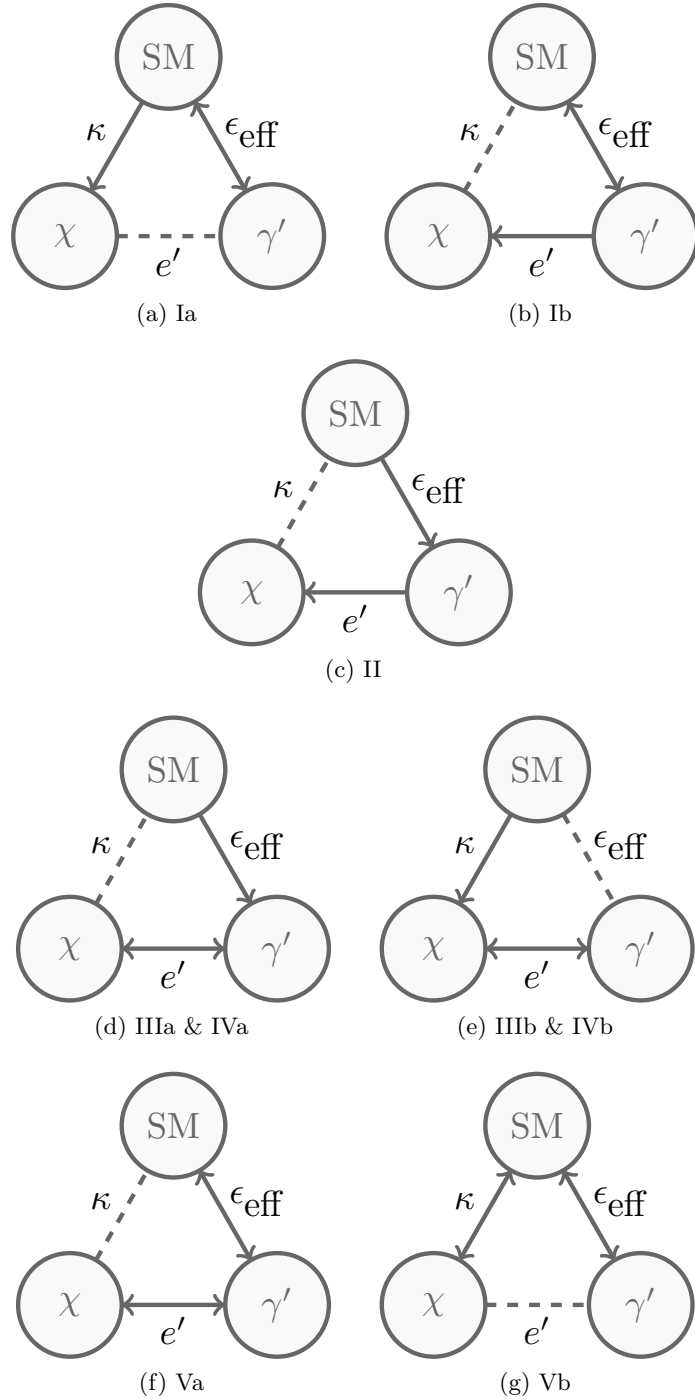


Figure 3.3: Pictorial representation of the 9 DM production regimes of the millicharged DM with a light dark photon scenario. A double sided arrow indicates equilibrium between two populations, a single sided arrow depicts a slow, out-of-equilibrium production of one population to another and a dashed line means that the connection between two population is negligible. Each row represents a different dynamical mechanism and those are : freeze-in (I), sequential freeze-in (II), re-annihilation (III), secluded freeze-out (IV) and freeze-out (V). Note that the diagrams for re-annihilation and secluded freeze-out are identical.

3.2 Phase diagram of dark matter production

To avoid complicating the DM production discussion, we will, in a first time, neglect the thermal effects that arise specifically in models with dark photons. As far as Fig. 3.2 is concerned, this amounts for the effective in-medium mixing ϵ_{eff} (which arise due to modifications of Eq. (2.8) when the photon becomes massive, for example due to thermal effects) to be approximated by $\epsilon_{\text{eff}} = \epsilon$. Thermal corrections are relegated to Chapter 4, as is the correct determination of the parameter space of the model. In this Chapter, we thus aim to give a qualitative description of the different mechanisms and to clarify the relevant physics that can be important for other models.

Within our framework, the DM relic abundance will depend on 4 dark sector parameters (DM mass, dark photon mass and a choice of two out of the three connectors α' , κ , ϵ). By fixing the masses, one can plot the abundance of DM as contours in, for example, the $\kappa - \alpha'$ plane. Imposing the constraint to reproduce the observed relic abundance will yield a line in this plane and navigating within it will imply that interactions could either become relevant or drop-out of relevance, showing the interplay between each different production mechanisms.

In the following we will focus in the “light mediator” limit of the model, $m_{\gamma'} < m_{\text{DM}}$. This condition forbids the mediator to decay into DM, thus only allowing the DM abundance to be set by $2 \rightarrow 2$ processes. By the same token, at temperature $T \sim m_{\text{DM}}$, DM annihilations into γ' will not be Boltzmann suppressed and $\text{DM} + \text{DM} \rightarrow \gamma' + \gamma'$ will therefore participate in the dynamics of the production of DM, with interesting consequences. The DM production phases in the range $m_{\gamma'} > m_{\text{DM}}$ has been explored by other works [84, 85].

The phase diagram of DM production will be inferred from the solutions of the set of Boltzmann equations that governs the evolution of the three sector populations as a function of time (or, equivalently, the SM temperature). The abundance of DM and dark photons will be written as the comoving yields $Y_{\text{DM},\gamma'} = n_{\text{DM},\gamma'}/s$, where s is the total entropy density of both sectors and $n_{\text{DM}} = n_{\chi} + n_{\bar{\chi}}$ the number density of DM particles. It is assumed that the SM population is in equilibrium with itself at high temperature and dominates the evolution of the Universe, therefore $Y_{\text{SM}}(t) = Y_{\text{SM}}^{\text{eq}}(T_{\text{SM}})$.

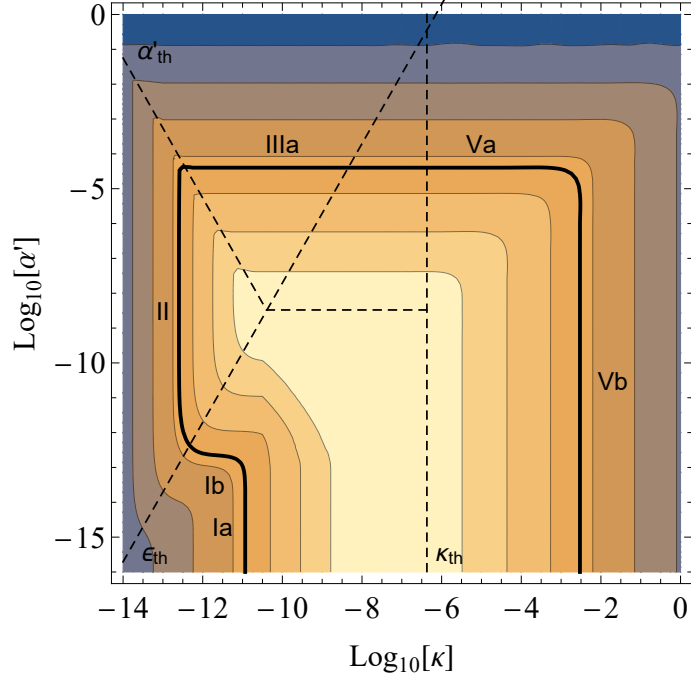


Figure 3.4: Contours of the DM relic density in the plane of the SM–DM connection (κ , horizontal axis) and DM– γ' connection (α' , vertical axis) for $m_{\text{DM}} = 3$ GeV and $m_{\gamma'} = 1$ GeV. The continuous line corresponds to the observed DM relic density, the blue (yellow) regions correspond to under (over) abundance of DM and the dashed lines correspond to the critical couplings for which equilibrium between two population is reached. On this diagram can be seen the various production regime (thermal effects neglected) that lead to the observed relic abundance. In this case, there are 6 different production regimes through 4 dynamical mechanism : freeze-in (Ia and Ib), sequential freeze-in (II), reannihilation (IIIa), freeze-out (Va and Vb)

Taking into account all DM and γ' number changing processes, the resulting system of Boltzmann equations is¹

$$\begin{aligned}
zHs \frac{dY_{\text{DM}}}{dz} &= \langle \sigma_{\text{DM} \rightarrow \text{SM}} v \rangle [(n_{\text{DM}}^{\text{eq}})^2 - n_{\text{DM}}^2] \\
&+ \langle \Gamma_{\text{DM} \rightarrow \text{SM}}^D \rangle \frac{n_Z^{\text{eq}}}{(n_{\text{DM}}^{\text{eq}})^2} [(n_{\text{DM}}^{\text{eq}})^2 - n_{\text{DM}}^2] \\
&+ \langle \sigma_{\gamma' \rightarrow \text{DM}} v \rangle n_{\gamma'}^2 - \langle \sigma_{\text{DM} \rightarrow \gamma'} v \rangle n_{\text{DM}}^2,
\end{aligned} \tag{3.1}$$

$$\begin{aligned}
zHs \frac{dY_{\gamma'}}{dz} &= \langle \sigma_{\gamma' \rightarrow \text{SM}} v \rangle n_{\text{SM}}^{\text{eq}} [n_{\gamma'}^{\text{eq}} - n_{\gamma'}] \\
&+ \langle \sigma_{\text{DM} \rightarrow \gamma'} v \rangle n_{\text{DM}}^2 - \langle \sigma_{\gamma' \rightarrow \text{DM}} v \rangle n_{\gamma'}^2,
\end{aligned} \tag{3.2}$$

with H being the Hubble parameter and the inverse SM temperature $z = m_{\text{DM}}/T$ being the evolution parameter. On the left hand side are all the factors contributing to the dilution of the number density by the expansion of the Universe, through the Hubble rate H . On the right hand-side

¹Written in this form, kinetic equilibrium at temperature T of the DM and of the γ' populations is assumed. This might not necessarily be true in the feebly coupled limit of the model. Nevertheless, as we assume all of the dark sector particles to be created from the SM bath, the impulsion distribution of those particles can be shown to be close to a Maxwell-Boltzmann distribution at T_{SM} [86]. Sometimes, this assumption can fail, see Fig. 4.5 and text.

are all DM and γ' number changing processes. Taking the first line as an example, the positive term corresponds to an annihilation of 2 SM particles into a $\chi - \bar{\chi}$ pair, therefore increasing the DM yield. For convenience, the factor of 2 has been absorbed in the definition of Y_{DM} . The negative term describes DM annihilations into SM particles, therefore reducing the DM yield. The second line of the first equation corresponds to Z decays $Z \rightarrow \text{DM} + \text{DM}$ and coalescence of DM particles into a Z boson, $\text{DM} + \text{DM} \rightarrow Z$. In the second equation, the dark photon yield can be changed by similar processes and similar terms are found. It is interesting to note that in the first line the number density of dark photons $n_{\gamma'}$ do not come squared, since, say, $e^+e^- \rightarrow \gamma'\gamma$ is less suppressed by the tiny kinetic mixing ϵ than $e^+e^- \rightarrow \gamma'\gamma'$, which comes with an additional ϵ^2 factor.

We have implicitly grouped all the relevant SM \leftrightarrow DM and SM \leftrightarrow γ' channels in the various cross sections σ and decay rate Γ , the subscript only indicating if the process is DM or γ' number changing. For ease, we will express the production cross-section in terms of production rates. Note that rates describe both the production processes and their reverse. The production rate are defined as follows

$$\gamma_{\text{SM}\leftrightarrow\text{DM}}^{\text{eq}} = \langle \sigma_{\text{DM}\rightarrow\text{SM}} v \rangle (n_{\text{DM}}^{\text{eq}})^2 + \langle \Gamma_{\text{SM}\rightarrow\text{DM}}^D \rangle n_{\text{SM}}^{\text{eq}} \quad (3.3)$$

and

$$\gamma_{\text{SM}\leftrightarrow\gamma'}^{\text{eq}} = \langle \sigma_{\gamma'\rightarrow\text{SM}} v \rangle n_{\text{SM}}^{\text{eq}} n_{\gamma'}^{\text{eq}}. \quad (3.4)$$

In writing Eq. (3.1–3.2), we have implicitly assumed that the shape of the impulsion distribution of the dark sector particles can be accurately described by the SM temperature. However, the hidden sector can thermalize within itself at a temperature $T' < T_{\text{SM}}$ and the set of Boltzmann equations needs to be complemented by an equation describing the energy transfer from visible to hidden sector, which will determine T' as a function of time. Such scenario will be encountered when discussing the reannihilation regimes in Section 3.5 and the set of Boltzmann equations describing a thermalized hidden sector will be explained there.

Even though the right hand side of the Boltzmann equations may involve many terms, only a few of them will be operative in a given production mechanism, *i.e.* for a given range of couplings. It is very instructive to first delimit the regions of thermalization between each sector in the parameter space. Assuming that if every particle of a reservoir scattering once off of the particles of another one leads to thermalization, the criteria for DM-SM equilibrium at time T is thus²

$$\left. \frac{\Gamma_{\text{SM}\leftrightarrow\text{DM}}}{H} \right|_{T \sim m_{\text{DM}}} \gtrsim 1, \quad (3.5)$$

with $\Gamma_{\text{SM}\leftrightarrow\text{DM}} = \gamma_{\text{SM}\leftrightarrow\text{DM}}^{\text{eq}}/n_{\text{DM}}^{\text{eq}}(z)$ the rate of collision of a DM particle with the SM thermal bath and $1/H$ is a proxy for the Universe age. For our purpose, this criteria is evaluated at a time such that DM reaches equilibrium before its production finishes. Considering the processes depicted in Fig. 3.1a, the criterion of Eq. (3.5) can be evaluated numerically and it is found that DM-SM thermalization is reached for millicharge above

$$\kappa \gtrsim \kappa_{\text{th}} \equiv 3.8 \times 10^{-7} \left(\frac{m_{\text{DM}}}{\text{GeV}} \right)^{1/2}, \quad (3.6)$$

²By writing this, it is implicitly assumed that Γ do not possess any resonant behaviour close to $T \sim m_{\text{DM}}$. In that case, one should instead solve the Boltzmann equation and check for which coupling does Y_{DM} reach an equilibrium value, see Eq. (4.18). This criteria is valid for a monotonically increasing rate until $T \sim m_{\text{DM}}$ and which then decreases rapidly, due to the Boltzmann suppression of SM + SM \rightarrow DM + DM processes.

For the two DM masses used as benchmark points, this critical coupling is exhibited in Figs. 3.4 and 3.5 as the vertical dashed line.

In turn, we also need to know when thermalization between the SM and the dark photons occurs (Fig. 3.1 c & d) albeit at the time of DM production, $T \sim m_{\text{DM}}$,

$$\frac{\Gamma_{\text{SM} \leftrightarrow \gamma'}}{H} \Big|_{T \sim m_{\text{DM}}} \gtrsim 1, \quad (3.7)$$

and we derive the following condition of the mixing parameter

$$\epsilon \gtrsim \epsilon_{\text{th}} \equiv 4.1 \times 10^{-8} \left(\frac{m_{\text{DM}}}{\text{GeV}} \right)^{1/2}, \quad (3.8)$$

with $\Gamma_{\text{SM} \leftrightarrow \gamma'} = \gamma_{\text{SM} \leftrightarrow \gamma'}^{\text{eq}} / n_{\gamma'}^{\text{eq}}(z)$. It is represented as the diagonal dashed line “ ϵ_{th} ” in Figs. 3.4 and 3.5. It must be noted that thermal effects will change drastically the numerical value and dependence on the DM mass of ϵ_{th} in Eq. (3.8).

Finally, it is possible for the dark sector to thermalize with itself and not with the SM. Either one of the two processes $\text{DM} + \text{DM} \rightarrow \gamma' \gamma'$ or $\gamma' \gamma' \rightarrow \text{DM} + \text{DM}$ can lead to equilibrium, depending on which one is dominant. Even though they are determined by the same coupling, the number density of targets will determine the dominant process. In other words, when comparing $\Gamma_{\text{DM} + \text{DM} \rightarrow \gamma' \gamma'}$ and $\Gamma_{\gamma' \gamma' \rightarrow \text{DM} + \text{DM}}$ to H , one has to include the abundance of target particles created, which are not necessarily in equilibrium. We will defer the discussion of this condition to Section 3.5 where it will play an important role.

We now turn to the detailed discussion of each regimes, using Fig. 3.4 as illustration.

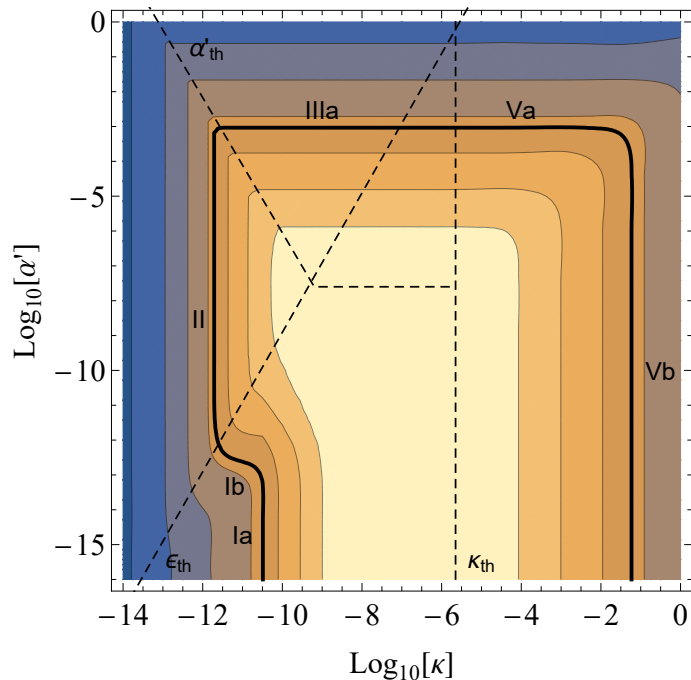


Figure 3.5: Same representation as Fig. 3.4 but with the choice $m_{\text{DM}} = 100 \text{ GeV}$ $m_{\gamma'} = 10 \text{ GeV}$. The overall picture is similar to that of Fig. 3.4 and the various production mechanisms can be understood in the same way.

3.3 Freeze-in: regimes Ia and Ib

The first regime under scrutiny (regime Ia) is a phase of the freeze-in mechanism of DM production and corresponds to the slow production of DM by SM through out-of-equilibrium processes $SM \rightarrow DM$, see Fig. (3.3 a). It has been originally studied in [87] and has been widely applied to DM phenomenology since then. The coupling that governs the production is κ and it is taken to be $\kappa \ll \kappa_{\text{th}}$. In this regime, α' is assumed to be too small for $\gamma' \rightarrow DM$ to have any impact.

3.3.1 Regima Ia

The set of Boltzmann equation reduces to its simplest possible form

$$\text{Regime Ia : } \quad zHs \frac{dY_{\text{DM}}}{dz} \approx \gamma_{\text{SM} \leftrightarrow \text{DM}}^{\text{eq}}(z). \quad (3.9)$$

with $Y_{\text{DM}} \ll Y^{\text{eq}}$. For a given DM mass, the production will be dependent on κ and a given DM relic abundance will thus be represented by a vertical contour in the phase diagram of Fig. 3.4. The thick black line corresponds to the observed DM relic abundance

$$Y_{\text{DM}}^{\text{relic}} = 4.09 \times 10^{-10} \left(\frac{\text{GeV}}{m_{\text{DM}}} \right) \quad (3.10)$$

Even though the production processes dictated by α' are taken to be negligible, there exists a small impact of dark photons on the cosmology. For small α' and κ required by freeze-in, $\kappa \sim 10^{-10}$, we have that $\epsilon > \epsilon_{\text{th}}$ (see Eq. (3.8)), *i.e.* $SM \leftrightarrow \gamma'$ process are in equilibrium. Therefore, the number of relativistic degrees of freedom in the thermal bath is modified and the expansion rate is increased by a factor $g'_{\gamma}/g_{\star}^{\text{SM}} = 2/g_{\star}^{\text{SM}} \sim 10^{-2}$ at high temperatures. We neglect this small effect in our analysis.

In Fig. 3.6 κ_{Ia} is shown as a function of m_{DM} , *i.e.* the millicharge required to reproduce the observed relic abundance through the Ia regime (green line). As the dark photon mass has very little impact on the kinematics, the Ia parameter space is effectively the same as for the $m_{\gamma'} = 0$ case, see [71]. Let us comment on the shape of the freeze-in from SM line as a function of the DM mass. If the DM mass is much higher than any SM particles, $m_{\text{DM}} \gg m_{\text{top}}$, DM freeze-in will stop at $T = m_{\text{DM}}/3 \gg m_{\text{top}}$ and the production cross section at those temperature will go as $\langle \sigma_{\text{SM} \rightarrow \text{DM}v} \rangle \sim \kappa^2/T^2 \sim \kappa^2/m_{\text{DM}}^2$. This means, recalling $\gamma^{\text{eq}} = (n_{\text{DM}}^{\text{eq}})^2 \langle \sigma_{\text{SM} \rightarrow \text{DM}v} \rangle \sim T^6/T^2 \sim m_{\text{DM}}^4$, that dY_{DM}/dz will go as $1/m_{\text{DM}}$ for the late time production. Assuming that the production proceeded during the entire lifetime of the Universe with the late time production (constant) rate, then $Y \sim z_f/m_{\text{DM}}$ with the end of production time $z_f = 1/3$. Since the relic abundance of DM is given by $\Omega_{\text{DM}} = m_{\text{DM}}Y_{\text{DM}}$, in this regime, Ω_{DM} is independent of m_{DM} and κ_{Ia} is also independent of m_{DM} , as is seen by the plateau in Fig. 3.6. Once m_{DM} drops below $m_Z/2$, the $Z \rightarrow \text{DM} + \text{DM}$ production channel opens. The Z decay rate into a DM pair is proportional to κ , see Eq. (2.7), but is nevertheless more efficient at producing DM than $2 \rightarrow 2$ processes, owing to less suppression by SM couplings. Keeping the DM relic abundance constant, this amounts to have to reduce the efficiency of DM production, *i.e.* reducing the millicharge κ , hence the dip. Through decays of Z , for a fixed coupling, the yield of DM particles produced will always be the same, as long as $m_{\text{DM}} < m_Z/2$. Therefore, assuming that all of the DM produced is by Z decays, if the DM mass is taken to be smaller, to keep $\Omega_{\text{DM}} = m_{\text{DM}}Y_{\text{DM}}$ fixed, one should take a comparatively higher κ , hence $\kappa_{\text{Ia}} \propto 1/m_{\text{DM}}$ in this regime. This is exactly what happens for $1 \text{ GeV} < m_{\text{DM}} < m_Z/2$, as can be seen on Fig. 3.6. In more details, Eq. (3.9) can be integrated and, assuming that all of the

production is done at the latest time possible, the number of DM particles created at time z is approximatively given by

$$Y_{\text{DM}}(z) \propto \sum_i \frac{(n_i^{\text{eq}})^2 \langle \sigma_{\text{SM}_i \rightarrow \text{DM}v} \rangle}{Hs} \Big|_{T=\max\{T, m_i, m_{\text{DM}}\}}, \quad (3.11)$$

where we sum over all the possible channels. One obtains the relic abundance of DM, $\Omega_{\text{DM}} = m_{\text{DM}} \times Y_{\text{DM}}$, when $z \rightarrow \infty$.

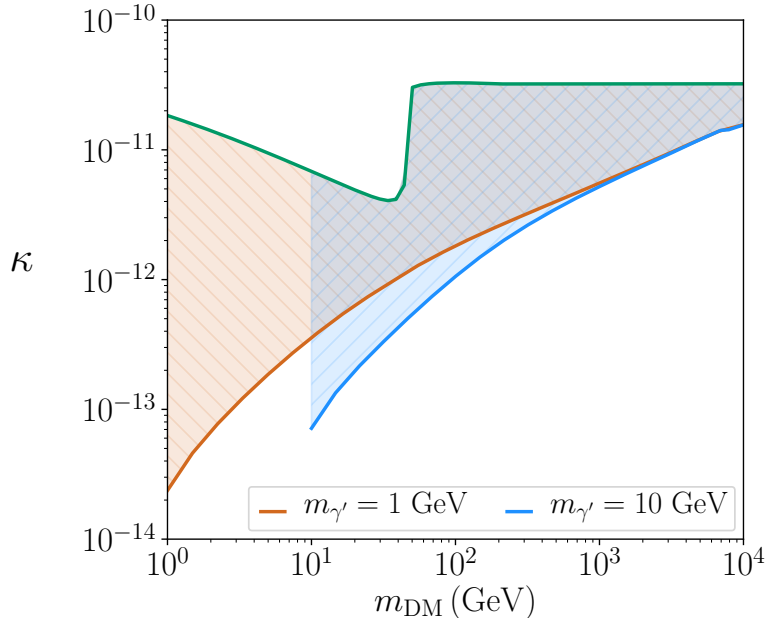


Figure 3.6: Millicharge κ required for a DM candidate of mass m_{DM} to account for the observed relic density through freeze-in from SM (regime Ia, green line), freeze-in from mediators (regime Ib, shaded area) and sequential freeze-in (regime II, orange (blue) line for $m_{\gamma'} = 1$ (10) GeV). It is seen from the Figure that more feebly coupled candidates exist below the freeze-in line.

3.3.2 Regime Ib

We now describe the regime Ib of the freeze-in phase, see Fig. (3.3 b). In the $\kappa - \alpha'$ plane, keeping κ fixed and increasing α' will make ϵ decrease. Therefore, starting from a region of the parameter space in which the dark photons have temperature $T_{\gamma'} = T$ and increasing α' , one reaches at some point an α' such that the dark photons drop out-of-equilibrium, $\epsilon < \epsilon_{\text{th}}$. However, before this happens, there can exist a value of α' large enough for the thermal dark photons to create dominantly the DM through a $\gamma' \rightarrow \text{DM}$ freeze-in³. In this case, the abundance depends only on α' , see the horizontal line “Ib” in Fig. 3.4. In a similar fashion to what has been discussed for regime Ia, the Boltzmann equation will involve only a DM production term from dark photons.

$$\text{Regime Ib :} \quad zHs \frac{dY_{\text{DM}}}{dz} \approx \gamma_{\gamma' \leftrightarrow \text{DM}}^{\text{eq}}, \quad (3.12)$$

³To the best of our knowledge, this regime has previously been briefly discussed in [88], there called “inverse annihilation”, and in [89], within a Higgs portal model.

with $\gamma_{\gamma' \leftrightarrow \text{DM}}^{\text{eq}} = \langle \sigma_{\gamma' \rightarrow \text{DM}} v \rangle (n_{\gamma'}^{\text{eq}})^2$. The DM abundance can be approximated as before by

$$Y_{\text{DM}}(z) = c_{\gamma'} \frac{(n_{\gamma'}^{\text{eq}})^2(z) \langle \sigma_{\gamma' \rightarrow \text{DM}} v \rangle}{Hs} \Big|_{T=\max\{T, m_{\text{DM}}\}}, \quad (3.13)$$

with $c_{\gamma'} = \mathcal{O}(1)$.

The α' required to produce all of the dark matter from γ' is

$$\alpha'_{\text{Ib}} = 2.5 \times 10^{-13} \left(\sqrt{g_*(m_{\text{DM}})} g_{*,S}(m_{\text{DM}}) \right)^{1/2}, \quad (3.14)$$

where the g factor comes from the dependence on Hs of Eq. (3.13). We have here assumed that $\epsilon > \epsilon_{\text{th}}$, meaning that the dark photon sector is in equilibrium with the SM thermal bath.

In Fig. 3.6, we assume that for every point in the shaded area, α' is fixed to a value that reproduces the relic abundance. Those regions therefore corresponds to the range of κ where the assumptions of regime Ib are valid, *i.e.* $\epsilon > \epsilon_{\text{th}}$. As can be clearly seen, in this regime, smaller values of κ are reached as compared to the standard freeze-in picture, $\kappa_{\text{Ib}} < \kappa_{\text{Ia}}$, and many new DM candidates are possible.

3.4 Sequential freeze-in: regime II

As we proceed along the Ib regime in Fig. 3.4, κ reaches values so small that the resulting ϵ drops below ϵ_{th} (oblique dashed line). The dark photons therefore are out of equilibrium at the time of DM production. As a result, Eq. (3.12) is not valid any more because the dark photon yield is not at its equilibrium value, $Y_{\gamma'}(z) < Y_{\gamma'}^{\text{eq}}$. This precludes the appearance of a new dynamical mechanism for DM production.

Within this corner of the $\kappa - \alpha'$ plane, none of the connectors allow any of the 3 sectors to thermalize between themselves. Nevertheless, we will now see that the slow production of γ' from the Standard Model and the subsequent slow production of DM by these out-of-equilibrium dark photons can successfully reproduce the DM relic abundance. We have dubbed this new dynamical mechanism of DM production “sequential freeze-in” and labelled it as regime II in Fig. 3.4.

This regime is thus described by the following coupled set of Boltzmann equations⁴

$$\underline{\text{Regime II}} : \quad zHs \frac{dY_{\gamma'}}{dz} \approx \gamma_{\text{SM} \leftrightarrow \gamma'}^{\text{eq}}, \quad (3.15)$$

$$zHs \frac{dY_{\text{DM}}}{dz} \approx \gamma_{\gamma' \leftrightarrow \text{DM}}, \quad (3.16)$$

where $\gamma_{\gamma' \leftrightarrow \text{DM}} = \langle \sigma_{\gamma' \leftrightarrow \text{DM}} v \rangle (n_{\gamma'})^2$, with $n_{\gamma'}$ determined by the first Boltzmann equation⁵. As the DM production rate is suppressed by a $(n_{\gamma'}/n_{\gamma'}^{\text{eq}}(z))^2$ factor, one should expect that this regime will lead us towards higher couplings.

⁴Note that, in principle, it is possible to choose a small enough ϵ such that $Y_{\gamma'} \leq Y_{\text{DM}}^{\text{relic}}$ and in this case, γ' depletion terms might need to be taken into account. We have checked a posteriori that it is never the case for the dark matter candidates and therefore neglect such terms.

⁵Here, we assume that, up to a normalization factor, the dark photons have an equilibrium distribution of momentum and therefore use the integrated Boltzmann equation for the DM production. However, when the γ' are produced non-relativistically, this assumption fails and departures from Maxwell-Boltzmann statistics can be important [86, 90]. Also, see Fig. 4.5 and the associated text.

The coupling dependence of this regime is readily understood by looking at the production terms of the Boltzmann equation

$$Y_{DM} \propto n_{\gamma'}^2 \times \langle \sigma_{\gamma' \rightarrow DM} v \rangle \propto \epsilon^4 \times \alpha'^2 \sim \kappa^4 \quad (3.17)$$

Therefore, in the sequential freeze-in regime, the relic density is solely determined by κ and is represented as the vertical line “II” in the phase diagram of Fig. 3.4.

We can estimate the millicharge κ_{II} for a given DM candidate by approximating it as the point at which regime Ib dominates and the dark photons are just about to drop out of equilibrium, *i.e.* $\epsilon = \epsilon_{th}$ and $\alpha' = \alpha'_{Ib}$. For example, in the case of Fig. 3.4, this gives

$$\kappa_{II} = \epsilon_{th} \sqrt{\frac{\alpha'_{Ib}}{\alpha}} \simeq 10^{-13} \ll \kappa_{Ia}, \quad (3.18)$$

with good agreement with the numerical solutions of the Boltzmann equations.

As in regime Ib, the sequential freeze-in mechanism is characterized by an extremely feeble SM-DM connection, orders of magnitude weaker than the ordinary freeze-in millicharge κ_{Ia} . Sequential freeze-in also leads to significantly stronger self-interactions than in the Ib regime, $\alpha' \gg \alpha'_{Ib}$.

In Fig. 3.6, where we have depicted the millicharge as a function of the DM mass, the bottom solid orange line correspond to κ_{II} for the parameters of Fig. 3.4. Overall, this picture is typical for model with relatively light mediators that can be summarized by similar triangle diagrams as in Fig. (3.3). As previously mentioned, thermal corrections have a big impact on the details of the parameter space but the main conclusions drawn from Fig. 3.6 are still valid.

As can be seen in Fig. 3.6 κ_{II} tends to κ_{Ia} at high mass, making the standard freeze-in Ia the dominant production mechanism throughout the κ – α' small coupling regions. It can be understood as being due to the fact that more massive DM candidates are produced at higher temperatures and thus earlier times, allowing dark photons to thermalize with SM only for comparatively larger mixing. As ϵ_{th} gets bigger, the corresponding line in Fig. 3.4 moves towards the bottom right, making the turn from Ib to II occur at larger and larger κ , until it reaches κ_{Ia} , thus making the Ib and II regime disappear.

3.5 Reannihilation: regimes IIIa and IIIb

As we follow regime II towards larger and larger α' , it is possible for the dark fine structure constant α' to allow for DM- γ' equilibrium, albeit at a colder temperature than the SM, since $Y_{\gamma',DM} \ll Y_{\gamma',DM}^{eq}$. This signals the onset of another dynamical mechanism of DM production, called reannihilation [71].

As explained in [71], once the dark sector thermalizes at $T' < T$, the DM production enters its reannihilation regime if, while DM is freezing-out in the dark sector at $T' < m_{DM}$, SM production of dark sector particles is still efficiently injecting energy into the dark sector.

Within the 3 connections–3 populations picture, there are two different ways for reannihilation to appear. Either the SM $\rightarrow \gamma'$ interactions transfers efficiently energy into the dark sector or the SM \rightarrow DM connection does so. We respectively call these regimes IIIa and IIIb, see Figs. 3.3d, 3.3e for the diagrams active in this regime and the topmost horizontal line in Fig. 3.4. If regime II dominates, so will regime IIIa over IIIb once α' is big enough. Indeed, since $\alpha' \ll 1$, in turn $\epsilon \gg \kappa$

and thus $Y_{\gamma'} \gg Y_{\text{DM}}$, so that the dark photons have more targets to interact with.

We now would like to understand when the II-IIIa transitions happens and for that we will look at the DM– γ' equilibrium condition. We first start by assuming that the dark photons are in equilibrium with the SM at temperature T . The required coupling for DM– γ' equilibrium to occur before DM production ends is given by

$$\left. \frac{\Gamma_{\gamma' \leftrightarrow \text{DM}}^{\text{eq}}}{H} \right|_{T \simeq m_{\text{DM}}} \gtrsim 1 \quad (3.19)$$

corresponding to

$$\alpha'_{\text{th}} \approx 2 \times 10^{-9} \left(\frac{m_{\text{DM}}}{\text{GeV}} \right)^{1/2} \quad (3.20)$$

where $\Gamma_{\gamma' \leftrightarrow \text{DM}}^{\text{eq}} = \langle \sigma_{\gamma' \rightarrow \text{DM}v} \rangle n_{\gamma'}^{\text{eq}}$. It is shown as the horizontal dashed line in Figs. 3.4 and 3.5. However, if the dark photons have been frozen-in from the SM, the condition changes to

$$\left. \frac{\langle \sigma_{\gamma' \rightarrow \text{DM}v} \rangle n_{\gamma'}}{H} \right|_{T \simeq m_{\text{DM}}} \gtrsim 1. \quad (3.21)$$

where the γ' abundance is suppressed compared to the equilibrium case, $n_{\gamma'} = (\epsilon/\epsilon_{\text{th}})^2 n_{\gamma'}^{\text{eq}}(T)$. The coupling inferred from this condition is thus simply

$$\alpha'_{\text{IIIa}} = \frac{\epsilon_{\text{th}}}{\epsilon} \alpha'_{\text{th}}. \quad (3.22)$$

and corresponds to the α' for which the transition from II to IIIa regimes occurs, *i.e* a dark sector thermalization at a, yet undetermined, $T' < T$. Note that unlike the previous quantities labelled with a subscript referring to a specific regime, α'_{IIIa} does not relate to the observed relic density. It is represented as the continuation of the horizontal dashed line “ α'_{th} ” in Figs. 3.4 and 3.5.

Turning to the description of the γ' and DM particles production, the set of Boltzmann equations that has to be taken into account is

$$\begin{aligned} \text{Regime IIIa : } zHs \frac{dY_{\gamma'}}{dz} &= \gamma_{\text{SM} \leftrightarrow \gamma'}^{\text{eq}}(z) \\ &- \gamma_{\gamma' \leftrightarrow \text{DM}}^{\text{eq}}(z') \left[1 - \left(\frac{Y_{\text{DM}}}{Y_{\text{DM}}^{\text{eq}}(z')} \right)^2 \right], \end{aligned} \quad (3.23)$$

$$\begin{aligned} zHs \frac{dY_{\text{DM}}}{dz} &= \gamma_{\gamma' \leftrightarrow \text{DM}}^{\text{eq}}(z') \\ &\times \left[1 - \left(\frac{Y_{\text{DM}}}{Y_{\text{DM}}^{\text{eq}}(z')} \right)^2 \right]. \end{aligned} \quad (3.24)$$

where $z' = m_{\text{DM}}/T'$. This set of equation has to be supplemented by the Boltzmann equation describing the SM to hidden sector energy transfer [71]

$$\begin{aligned} zH \frac{d\rho'}{dz} + 4H(\rho' + p') &= (n_{\text{SM}}^{\text{eq}}(z))^2 \langle \sigma_{\text{SM} \rightarrow \text{DM}} v \Delta E \rangle \\ &+ (n_{\text{SM}}^{\text{eq}}(z))^2 \langle \sigma_{\text{SM} \rightarrow \gamma'} v \Delta E \rangle. \end{aligned} \quad (3.25)$$

where the second term dominates in regime IIIa, and the first one in regime IIIb.

Once the equation of state of the dark sector fluid has been plugged into Eq. (3.25), *i.e.* $p'(\rho')$, $\rho'(z)$ is known and one can extract $T'(z)$ as the solution of

$$\rho' = \rho_{\gamma'}^{\text{eq}}(z') + \rho_{\text{DM}}^{\text{eq}}(z'). \quad (3.26)$$

For instance, when $T' \lesssim m_{\text{DM}}$, the equation of state is

$$p' = (\rho' - m_{\text{DM}} Y_{\text{DM}} s) / 3 \quad (3.27)$$

$$\rho_{\text{DM}}(z') = \rho_{\text{DM}}^{\text{eq}}(z) Y_{\text{DM}} / Y_{\text{DM}}^{\text{eq}}(z). \quad (3.28)$$

The density parameter Ω_{DM} will depend ultimately on the combination $\log(\langle\sigma_{\text{eff}}v\rangle)/\langle\sigma_{\gamma'\rightarrow\text{DM}}v\rangle$ (for the effective cross section $\langle\sigma_{\text{eff}}v\rangle \equiv \sqrt{\langle\sigma_{\text{SM}\rightarrow\gamma'v}\rangle\langle\sigma_{\text{DM}\rightarrow\gamma'v}\rangle}$). In turn, the coupling dependence becomes $\Omega_{\text{DM}} \propto \log(\alpha'\epsilon)/\alpha'^2$, and results in an approximately horizontal line, see the ‘‘IIIa’’ line in Fig. 3.4.

3.6 Secluded freeze-out: regimes IVa and IVb

When the dark sector has a different temperature T' than the SM thermal bath, the energy source can either be active or inactive at the time of DM freeze-out in the dark sector, $T' \sim m_{\text{DM}}$. The former case is reannihilation, discussed above, and the latter is a ‘‘secluded freeze-out’’. Meaning that, necessarily, the DM depletion will be into dark sector particles (in this case, the mediator γ') and the dark sector dynamics are largely independent of the SM ones, up to small changes in the Hubble parameter.

In the case of the phase diagram presented in Figs. 3.4 and 3.5, regimes IV do not occur. Indeed, since $m_{\gamma'} < m_{\text{DM}}$ and $T' < T$, the connection $\text{SM} \rightarrow \gamma'$ will only turn off after DM has freeze-out. Nevertheless, if $m_{\gamma'} < m_{\text{DM}} < m_{e^-}$, any SM source will shut off after the electron annihilation catastrophe, which can possibly happen before $T' < m_{\text{DM}}$ (for example, if the dark sector thermalizes only after some time). The candidate will find itself in regime IVa or IVb based on the dominant dark sector energy source channel, *i.e.* $\text{SM} \rightarrow \text{DM}$ or $\text{SM} \rightarrow \gamma'$. In this regime, the relic density of DM is dependent on α' .

3.7 Freeze-out: regimes Va and Vb

Starting from the reannihilation regime, as the couplings that govern the energy transfer from the SM to the dark sector, κ and ϵ , are taken larger and larger, energy from the SM population is more efficiently transferred into DM or γ' and the dark sector temperature reaches $T' = T$, *i.e.* all the populations have reached equilibrium. For this to happen, one needs either $\kappa > \kappa_{\text{th}}$ or both $\epsilon > \epsilon_{\text{th}}$ and $\alpha' > \alpha'_{\text{th}}$. The latter condition only arises when regime Ib exists.

The DM abundance can be depleted either through $\text{DM} \rightarrow \gamma'$, therefore fixing α' (called regime Va, see the horizontal line in Fig. 3.4) or $\text{DM} \rightarrow \text{SM}$ annihilations, therefore fixing κ (*i.e.* regime Vb, the vertical line in Fig. 3.4). One transitions from regime Va to regime Vb when the DM annihilation rate into SM becomes larger than the one into γ' , *i.e.* when $\Gamma_{\text{DM}\leftrightarrow\text{SM}}^{\text{eq}} = \Gamma_{\text{DM}\leftrightarrow\gamma'}^{\text{eq}}$. In other words, this corresponds to the ϵ at which the DM–SM and the DM– γ' connection reach equilibrium at the same time. We find that the transition from freeze-out into dark photons to freeze-out into SM particles occurs at

$$\epsilon_{\text{Va-Vb}} \equiv \kappa_{\text{th}} \sqrt{\frac{\alpha_{\text{em}}}{\alpha'_{\text{th}}}} = 7 \times 10^{-4} \left(\frac{m_{\text{DM}}}{\text{GeV}} \right)^{1/4} \quad (3.29)$$

For the sake of completeness, we give the values that we found for the freeze-out couplings in regime Va and Vb respectively

$$\alpha'_{\text{Va}} = 8 \times 10^{-5} \left(\frac{m_{\text{DM}}}{\text{GeV}} \right) \quad (3.30)$$

$$\kappa_{\text{Vb}} = 5.6 \times 10^{-3} \left(\frac{m_{\text{DM}}}{\text{GeV}} \right) \quad (3.31)$$

We have assumed for those figures that the DM candidates have masses away from the Z -resonance. The funnel region corresponding to a dominant annihilation into on-shell Z 's, $\chi\bar{\chi} \rightarrow Z$ can be seen in Fig. 3.8.

In the freeze-out regime, the light mass of the dark photon, $m_{\gamma'} \ll m_{\text{DM}}$, has negligible effects on the annihilation cross section through the kinematics and the amplitude of the annihilation processes. This results in the freeze-out parameter space not depending on $m_{\gamma'}$. However, when the mass mixing δ is taken to be non-zero, destructive interferences in the annihilation amplitudes could potentially give rise to a slightly different phenomenology. Let us denote the DM annihilation cross section into massless SM particles computed in the $\epsilon - \delta$ model of Eq. (2.1) by $\sigma^{\epsilon, \delta}$. In the same model, taking the massless dark photon limit amounts to recovering the millicharged case and the corresponding DM annihilation cross section is noted $\sigma_{m_{\gamma'} \rightarrow 0}$. A small computation shows that the ratio of both quantities is

$$\frac{\sigma^{\epsilon, \delta}}{\sigma_{m_{\gamma'} \rightarrow 0}} = \frac{\mathfrak{s}^2 \left(\frac{C}{\mathfrak{s}} - 1 \right)^2}{(R^2 - \mathfrak{s})^2} \quad (3.32)$$

where $\mathfrak{s} = s/4m_{\text{DM}}$ is the energy in the center-of-mass frame, $R = m_{\gamma'}/2m_{\text{DM}}$ is the ratio between the dark photon and DM mass and $C = \delta/\epsilon \times R^2$ is the parameter that governs the amount of interference.

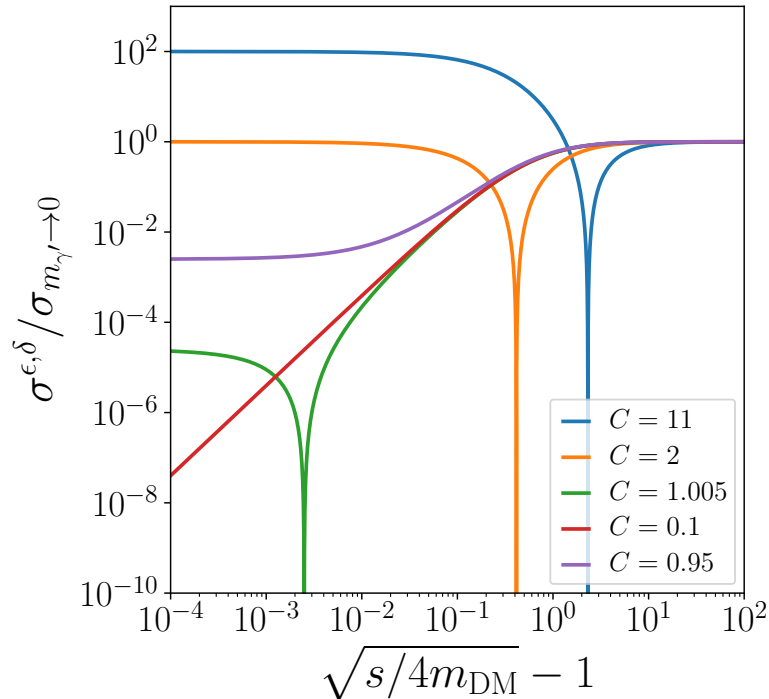


Figure 3.7: Effects of the interferences between the s -channel exchange of a photon and a dark photon in the $\epsilon - \delta$ model as a function of the kinetic energy in the center-of-mass frame. The dark photon–dark matter mass ratio is fixed at $R = 10^{-2}$. Each line corresponds to a different ratio δ/ϵ .

In Fig. 3.7 is given the cross section ratio of Eq. (3.32) as a function of the kinetic energy in the center-of-mass frame for several interference parameter C . At high energy, the dark photon mass is negligible and the ratio tends to 1, that is we recover the case of a millicharged fermion with a kinetic mixing ϵ . However, at low energies, when $m_{\gamma'}\delta - 4m_{\text{DM}}^2\epsilon \sim 0$ or equivalently $C \sim 1$, the annihilation can become suppressed. When $C \gg 1$, the amplitude proportional to δ dominates over the one proportional to ϵ at low energies. The annihilation cross section is therefore comparatively larger than in the $\delta = 0$ case but will nevertheless hit a destructive interference at high energy and reduce to the simple millicharged case (*i.e.* the mediator is the photon and the coupling is proportional to $\sim \epsilon\epsilon'$). For DM candidates, the impact of the amplitude interferences in the case $C \sim 1$ will be that the annihilation processes at freeze-out will be less efficient, since they happen non-relativistically. In the same vein, their signal in indirect detection experiments will be suppressed.

3.8 The parameter space of DM candidates

It is very illustrative to project the mesa diagrams in the $m_{\text{DM}} - \kappa$ plane, while choosing α' such that the DM relic abundance is reproduced, see Fig. 3.8.

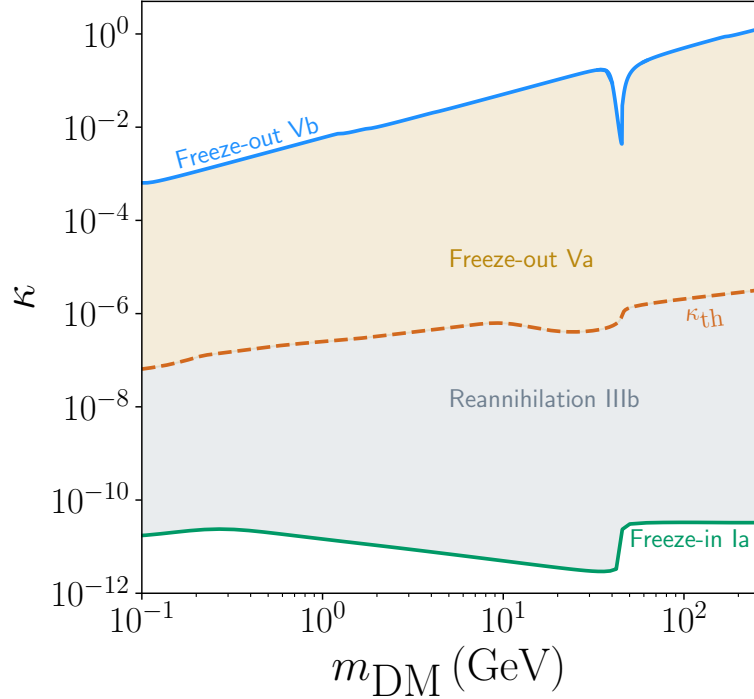


Figure 3.8: Regions where the observed DM relic abundance can be accounted for in a scenario with a kinematically mixed massless dark photon. At each (m_{DM}, κ) couple, α' has been chosen as such. The continuous line closest to the top (bottom) gives the freeze-out (freeze-in) into (from) SM parameter space, *i.e.* regime Vb (Ia). Above (below) the dashed line, DM is in (out of) equilibrium with the SM thermal bath. The dip at $m_{\text{DM}} = 45$ GeV corresponds to the Z resonance. Across 10 order of magnitude in millicharge, DM candidates are found.

For the sake of clarity, we have restricted ourselves to models where the SM- γ' connection is inactive. This picture is realistic for models with $m_{\gamma'} \ll m_{\text{DM}}$, see Chapter 4.

If the DM particle only possesses a minicharge (*i.e.* directly charged under $U(1)_Y$), candidates can only be found on the freeze-out into SM (Vb) and freeze-in from SM (Ia) lines. We see that the introduction of a new degree of freedom, the dark photon, and its coupling e' to the DM allow for many new candidates, whose abundance is set by many different dynamical mechanisms and across many orders of magnitude in coupling, shown in the blue and brown shaded region of Fig. 3.8. A small pocket of secluded freeze-out IVb is actually active between the reannihilation and freeze-out into mediator regions for DM masses between 45 GeV and 1 GeV (*i.e.* candidates which thermalize between themselves after being efficiently produced by Z -decays and for which other SM-DM processes are subdominant) but it is not shown. We note that the dip in κ_{th} is also due to the Z resonance.

Chapter 4

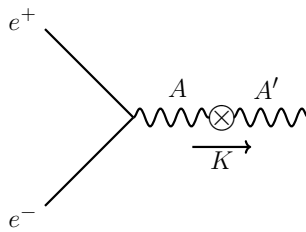
Inclusion of thermal effects

The previous discussions, while illustrated in the ϵ model of Eq. (2.1), paints a generic picture that can obviously be found in other DM models that share the three sectors–three connections structure. However, in the kinetic mixing portal model, there exists important, even though specific, thermal corrections. It is easy to understand that the previous treatment of the dark photon production is not complete. If $m_{\gamma'} = 0$, one can rotate it away and the SM does not couple to the dark photon. On the other hand, we have seen that $m_{\gamma'} \neq 0$ allows for γ' being produced by the SM. However, this begs the question of what happens when $m_{\gamma'}$ is small compared to all the other scales, for example $T \gg m_{\gamma'}$ in the Early Universe. It is expected that the production of dark photon from SM particles will be suppressed once they are relativistic, which is not reflected in the previous treatment, see Eq. (2.8). In this Chapter, we thus aim at describing the thermal effects that can appear in models with dark photon–photon mixing and assessing quantitatively their impact on the production of dark sector particles at early times. We will end the Chapter by giving the correct parameter space and describing how each regime changes once these effects are taken into account.

4.1 On-shell production

The question of dark photon production in a medium has historically been studied in the following references [91, 92, 93, 94, 95, 96], and we aim at describing these phenomena in the hot, Early Universe, within the context of DM production. In the following, we will treat the mixing as perturbations by assuming $\epsilon, \delta \ll 1$.

We will first focus on the emission, from SM particles, of a massive dark photon (possibly transverse or longitudinal) that mixes with a dressed photon propagating in a medium at temperature T . Following closely the treatment of Ref. [94], the emission amplitude reads



$$\mathcal{M}_{i \rightarrow f + \gamma'_{T/L}} = [e J_{\text{em}}^\mu] \langle A_\mu A_\nu \rangle \left(\epsilon \{ K^2 g^{\nu\alpha} - K^\nu K^\alpha \} - \delta m_{\gamma'}^2 g^{\nu\alpha} \right) \epsilon_\alpha^{T/L} \quad (4.1)$$

where e is the electric charge and $J_{\text{em}}^\mu = i\bar{e}\gamma^\mu e$ is the electromagnetic current. $K = (\omega, \vec{k})$ is the four-momentum of the (on-shell) dark photon. In the parenthesis, the first terms proportional to the mixing parameter ϵ come from the kinetic mixing and the second term, proportional to

δ , arises from the mass mixing. The last factor of the amplitude is the transverse/longitudinal polarization vector $\epsilon_\mu^{T/L}$. Assuming that the dark photon is emitted in the z direction, ϵ_μ^T are space-like unit vectors in the x and y direction and the longitudinal vector is slightly more complicated, $\epsilon_\mu^L = (|\vec{k}|, 0, 0, \omega)/\sqrt{\omega^2 - |\vec{k}|^2}$. Finally, $\langle A_\mu A_\nu \rangle$ is the dressed photon propagator. The computation proceeds most easily in the Lorentz gauge $\partial_\mu A^\mu = 0$, in which the photon propagator in a medium is given by [97]

$$\langle A_\mu A_\nu \rangle = \frac{P_{\mu\nu}^T}{K^2 - \Pi_\gamma^T} + \frac{P_{\mu\nu}^L}{K^2 - \Pi_\gamma^L} \quad (4.2)$$

where $P_{\mu\nu}^T = \sum_{i=2} \epsilon_\mu^{T,i} \epsilon_\nu^{T,i}$ and $P_{\mu\nu}^L = \epsilon_\mu^L \epsilon_\nu^L$ are the transverse and longitudinal projectors respectively. The transverse projector has $P_{ij}^T = \delta_{ij} - k_i k_j / |\vec{k}|^2$ and all the other components are 0. The projector on the longitudinal direction has $P_{00}^L = (\omega^2 - K^2)/K^2$, $P_{0i}^L = -\omega k_i / K^2$ and $P_{ij}^L = (1/K^2 + 1/|\vec{k}|^2) k_i k_j$. $\Pi_\gamma^{T/L}$ are the transverse and longitudinal polarization tensors of the photon, which have to be computed at finite-temperature by considering self-energy diagram such as Fig. (4.1) (left). In the vacuum, $\Pi_\gamma^T = \Pi_\gamma^L = 0$ and a quick computation shows that $P_{\mu\nu}^T + P_{\mu\nu}^L = -g^{\mu\nu} + K^\mu K^\nu / K^2$, *i.e.* one recovers the massless propagator for the photon in vacuum. From the poles of the propagators, we gather the dispersion relations of longitudinal and transverse photons, $\omega_{T/L}(k)$,

$$K^2 = \omega_{T/L}(k)^2 - k^2 = \text{Re } \Pi_\gamma^{T/L}(\omega_{T/L}(k), k) \quad (4.3)$$

and conclude that the real part of the transverse/longitudinal self-energy acts as the in-medium (momentum dependent) ‘‘mass’’ of the transverse/longitudinal photon. It is easy to check that $P^{T/L} \epsilon_{T/L} = \epsilon_{T/L}$, $P^{T/L} \epsilon_{L/T} = 0$ and the amplitude of emission can be directly rewritten in the compact form

$$\mathcal{M}_{i \rightarrow f + \gamma'_{T/L}} = [e J_{\text{em}}^\mu] \epsilon_\mu^{T/L} \frac{(\epsilon - \delta) m_{\gamma'}^2}{K^2 - \Pi_\gamma^{T/L}} \quad (4.4)$$

with the outgoing momentum $K^2 = m_{\gamma'}^2$, since the dark photon is emitted on-shell.

Therefore, the on-shell production rate of a dark photon from the SM thermal bath is equivalent to the production rate of a photon, with a fiducial mass $m_\gamma = m_{\gamma'}$, but with an effective in-medium coupling given by

$$\Gamma_{\text{SM} \rightarrow \gamma'_{T/L}} / \Gamma_{\text{SM} \rightarrow \gamma_{T/L}}^{m_\gamma \rightarrow m_{\gamma'}} = \frac{(\epsilon - \delta)^2 m_{\gamma'}^4}{\left(m_{\gamma'}^2 - \text{Re } \Pi_\gamma^{T/L}\right)^2 + \left(\text{Im } \Pi_\gamma^{T/L}\right)^2} \quad (4.5)$$

because of the thermal effects. The same development can be done for the case of dark matter emitting on-shell photons with, in this case, $K^2 = \text{Re } \Pi_\gamma$ acting as the fiducial dark photon mass. We find

$$\Gamma_{\text{DM} \rightarrow \gamma_{T/L}} / \Gamma_{\text{DM} \rightarrow \gamma'_{T/L}}^{m_{\gamma'} \rightarrow m_\gamma} = \frac{\left(\epsilon \text{Re } \Pi_\gamma^{T/L} - \delta m_{\gamma'}^2\right)^2}{\left(\text{Re } \Pi_\gamma^{T/L} - m_{\gamma'}^2\right)^2 + \left(\text{Im } \Pi_\gamma^{T/L}\right)^2} \quad (4.6)$$

4.2 Self-energy

The on-shell production of γ' from the SM and γ from the DM, at finite temperature, requires us to determine the real and imaginary part of the (dark-)photon self energies. Focusing on the dark photon production rate for the time being, it is possible to also illustrate the fact that they will inherit some thermal features due to their mixing with the photon and its interaction with real particles from the thermal bath (see above) through the diagrams of Fig. 4.1. The single wiggly line is a photon and the double wiggly line is a dark photon. The cross represents mixing. The fermion loops corresponds to all the on-shell (dashed cutting line) particles in the medium, taken here to be a relativistic plasma, that interact with the photon. Since the photon self-energy appears in the dark photon self-energies, it is indeed expected for the dark photon to be also affected by thermal effects.

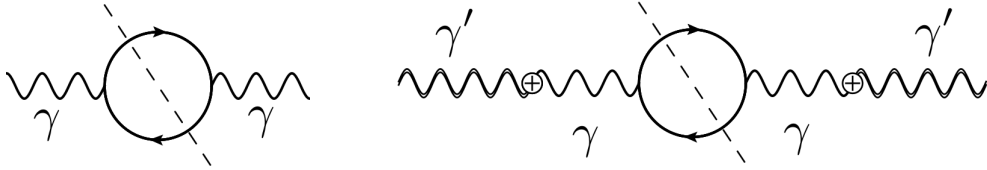


Figure 4.1: Left : The photon self-energy in a medium made of electrically charged fermion, or, in other words, the γ thermal mass. Right : Leading contribution to the dark photon production, through mixing with the photon, by SM fermions.

In vacuum, the imaginary part of the self-energy (represented by diagrams similar to those of Fig. 4.1) is simply interpreted as the decay rate of the particle. It is found that, at finite temperature, one instead interprets it as the difference (sum) between the emission and the absorption rate of the bosonic (fermionic) particle from the medium [98]

$$\text{Im } \Pi = -\omega\Gamma = -\omega(\Gamma_{\text{em}} - \Gamma_{\text{abs}}). \quad (4.7)$$

where ω is the energy of the emitted/absorbed particle.

Detailed balance informs us that emitting a particle with energy ω will come at the cost of a Boltzmann factor when compared to its absorption rate ¹,

$$\Gamma_{\text{em}} = \exp(-\omega/T) \Gamma_{\text{abs}}, \quad (4.8)$$

The emission rate of a dark photon of energy ω from the SM thermal bath will thus be rewritten as

$$\Gamma_{\text{SM} \rightarrow \gamma'_{T/L}} = \frac{(\epsilon - \delta)^2 m_{\gamma'}^4}{\left(m_{\gamma'}^2 - \text{Re } \Pi_{\gamma}^{T/L}\right)^2 + \omega^2 (e^{\omega/T} - 1)^2 \Gamma_{\text{SM} \rightarrow \gamma_{T/L}}^2} \Gamma_{\text{SM} \rightarrow \gamma_{T/L}}^{m_{\gamma} \rightarrow m_{\gamma'}} \quad (4.9)$$

and a similar expression is valid for photon emission from dark matter particles. For completeness, an expression of the absorption rate is given in Appendix B.

¹From this expression, it is seen that when taking $T \rightarrow 0$, the emission rate of the dark photon from the medium becomes negligible. In that limit, the absorption rate is reinterpreted. The only processes contributing to dark photon absorption by the medium at very low temperature (*i.e.* the reverse processes that were considered in the emission rate) are “inverse coalescence” of the type $\gamma' \rightarrow e^+e^-$, or, in other words, decays and the vacuum case is smoothly recovered.

We now turn to a more detailed description of $\Pi_\gamma^{T/L}$. The photon transverse modes acquire a thermal mass given by

$$\text{Re } \Pi_\gamma^T \equiv (m_\gamma^T)^2 = \begin{cases} \omega_P^2 = \sum_i q_i^2 T^2/9 & \text{low } k \\ 3/2 \omega_P^2 & \text{large } k \end{cases}, \quad (4.10)$$

where in the first line the plasma frequency ω_P has been defined [99]. The sum over i runs over all the relativistic electrically charged species of charge q_i in the thermal bath. As can be seen, the thermal mass slightly depends on the photon impulsion and, in the following, we will approximate $m_\gamma^T \approx \omega_P$ for all k . We can now summarize the low and high temperature behaviour of the in-medium couplings of transverse mode emission in the following Table.

Transverse modes	$T \ll m_{\gamma'}$	$T \gg m_{\gamma'}$	$T \approx T_{\text{res}} \leftrightarrow m_\gamma \approx m_{\gamma'}$
$\Gamma_{\text{SM} \rightarrow \gamma'_T} / \Gamma_{\text{SM} \rightarrow \gamma_T}^{m_{\gamma'} \rightarrow m_{\gamma'}}$	$(\epsilon - \delta)^2$	$(\epsilon - \delta)^2 \left(\frac{m_{\gamma'}^2}{m_\gamma^T} \right)^2$	$\approx (\epsilon - \delta)^2 \left(\frac{m_{\gamma'}}{\Gamma_{\text{SM} \rightarrow \gamma_T}} \right)^2$
$\Gamma_{\text{DM} \rightarrow \gamma_T} / \Gamma_{\text{DM} \rightarrow \gamma'_T}^{m_{\gamma'} \rightarrow m_\gamma}$	δ^2	ϵ^2	$(\epsilon - \delta)^2 \left(\frac{m_{\gamma'}^2}{\text{Im } \Pi_{\gamma'}^T} \right)^2$

Table 4.1: Efficiency of production of transverse dark photon from SM (first row) and photon from DM (second row) with respect to the production of a photon with $m_\gamma = m_{\gamma'}$ from the SM and the production of a dark photon with $m_{\gamma'} = m_\gamma$ from the DM. The second, third and fourth columns correspond to production at low, high and at the resonance temperature. In each regime, the parametric dependence of the efficiency changes.

We mention that similar results could be also derived if working at finite density. From this table, we read that at low temperature, emissions proceed as in vacuum, at high temperature γ' emission from the SM is suppressed and that the production boost at the resonance is important. Due to the more complicated dispersion relation of longitudinal modes, their treatment cannot be summarized as such, we discuss them below. The dispersion relation of a longitudinal photon is given by [99]

$$\Pi_\gamma^L(\omega, k) = 3\omega_P^2 \frac{K^2}{k^2} \left(\frac{\omega}{2k} \log \left(\frac{\omega + k}{\omega - k} \right) - 1 \right). \quad (4.11)$$

We note that different definitions are used for this quantity in the literature, and we choose to follow Refs. [94, 95], *i.e.* $\Pi_L \equiv \Pi_L^{\text{APP}}$, which differ from the one of [99] by a energy and momentum dependent factor, $\Pi_L^{\text{BS}} = k^2/K^2 \Pi_L^{\text{APP}}$. The thermal mass of longitudinal mode is found to be

$$\text{Re } \Pi_\gamma^L \equiv (m_\gamma^L)^2 = \begin{cases} \omega_P^2 K^2 / \omega^2 & k \sim 0 \\ \sim 0 & k \gtrsim \omega_P \end{cases}. \quad (4.12)$$

In Fig. 4.2, we show the transverse and longitudinal dispersion relation as a function of momentum. As k grows, the longitudinal modes indeed quickly become massless, their dispersion relation converging to $\omega(k) = k$.

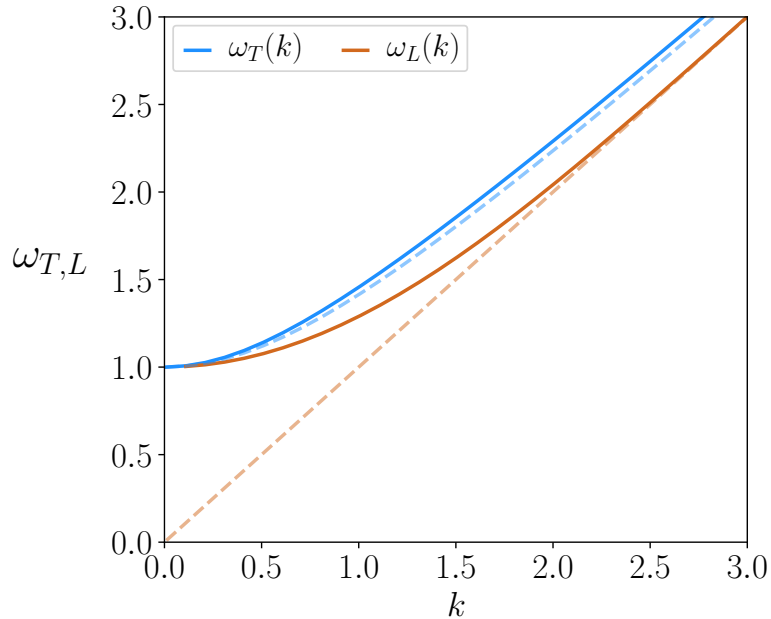


Figure 4.2: Dispersion relation for the transverse (longitudinal) photon mode in solid blue (solid orange) as a function of momentum in a relativistic thermal bath, $T \gg m_e$. The normalization is $\omega_P = 1$. In dashed blue and orange are given the dispersion relation for a massive particle of mass ω_P and a massless particle respectively. For small momentum, $\omega_{T,L} = \omega_P$. At high momentum, $\omega_T \approx \sqrt{3/2\omega_P^2 + k^2}$ and the longitudinal modes quickly become massless, $\omega_L \approx k$.

The emission rates of longitudinal (dark-)photon modes are parametrically different from the transverse ones and we will now describe their behaviour and compare their relevance for production at low and high energies. On the one hand, at high temperature, $T \gg m_{\gamma'}^T$, transverse photons effectively induce a contact interaction between dark photon and the SM, whose strength can be read from Table 4.1. On the other hand, for longitudinal modes, the strength of interaction will depend on the impulsion. This can be seen by inserting their dispersion relation in the amplitude of Eq. 4.1. Then, taking the limit of a relativistic dark photon emitted with impulsion k , away from the resonance, the photon propagator can be rewritten as

$$\frac{1}{K^2 - \Pi_L} \stackrel{k \gg T}{\approx} \frac{-1}{m_{\gamma'}^2} \quad (4.13)$$

$$\stackrel{k \sim T}{\approx} \frac{-1}{\omega_P^2} \quad (4.14)$$

The longitudinal to transverse emission rates ratio at high temperature, *i.e.* $\omega_P \gg m_{\gamma'}$, is thus

$$\frac{\Gamma_{\gamma', \text{em}}^L}{\Gamma_{\gamma', \text{em}}^T} \approx \frac{\omega_P^4}{m_{\gamma'}^4} \frac{\Gamma_{\gamma, \text{em}}^L}{\Gamma_{\gamma, \text{em}}^T}. \quad (4.15)$$

Note that as $m_{\gamma'}^L$ rapidly goes to 0 when $k \gtrsim \omega_P$, the large impulsion limit that has been used in this step of the calculation is valid for most of the dark photon being produced.

Focusing now on the emission rate of longitudinal modes, the relevant amplitude scales like $\propto m_{\gamma'}$, as it vanishes when the fiducial mass is taken to be 0. Therefore, we expect the above ratio to be overly proportional to $\omega_P^2/m_{\gamma'}^2 \gg 1$. We conclude that at high temperature, $\omega_P \gtrsim m_{\gamma'}$, most of the dark photons being produced from SM particles are longitudinal [94, 95].

At lower temperatures, $T < T_{\text{res.}}$, emission proceeds with couplings equal to the vacuum case but with a non-zero photon fiducial mass. By the same arguments,

$$\frac{\Gamma_{\gamma',\text{em}}^L}{\Gamma_{\gamma',\text{em}}^T} \approx \frac{\Gamma_{\gamma,\text{em}}^L}{\Gamma_{\gamma,\text{em}}^T} \sim \frac{m_{\gamma'}}{\omega_P} \ll 1, \quad (4.16)$$

Therefore, when $\omega_P < m_{\gamma'}$, it is thus transverse dark photons that are dominantly produced [94, 95].

4.3 Dark photon abundance

As we are now interested in the phenomenological effects of the thermal corrections on the dark sector particles abundance in the Early Universe, we will restrict ourselves to the ϵ model whose production phases have been studied previously. In summary, taking $\delta = 0$ ², the production rates of T/L on-shell dark photons in the Early Universe is the same as at zero temperature, but where the mixing parameter is replaced by an effective coupling that is

$$\epsilon \rightarrow \epsilon_{\text{eff}}^2 \approx \frac{\epsilon^2 m_{\gamma'}^4}{\left(m_{\gamma'}^2 - m_{\gamma,T/L}^2\right)^2 + \omega^2 \left(e^{\omega/T} - 1\right)^2 \Gamma_{\text{SM} \rightarrow \gamma_{T/L}}^2} \quad (4.17)$$

The effective coupling is particularly suited for understanding the qualitative behaviour of the production of longitudinal and transverse mode as a function of temperature.

In Fig. 4.3, we show the importance of each dark photon production channel from the SM as a function of temperature. In dashed is shown the abundance derived with vacuum coupling $\epsilon_{\text{eff}} = \epsilon$ and the continuous lines have been computed with thermal corrections. As can be seen, at high temperature, the overall production is suppressed by thermal effects and mainly longitudinal modes are produced, cf. Eq. (4.15). Conversely, at low temperature, the transverse mode production dominates, cf. Eq. (4.16). At intermediate temperature, when the thermal mass of the photon crosses $m_{\gamma'}$, dark photons are resonantly and massively produced, with an abundance several orders of magnitude bigger than the case of no thermal corrections. This contribution dominates the abundance until coalescence processes become effective at lower temperature. Here, we only considered resonant production of the T mode but a similar effect occurs during L mode production, albeit with a smaller impact [96, 100]. Thermal effects can boost and suppress the abundance of dark photon at different times in the evolution of the hot Early Universe.

²If $\delta \neq 0$, the effective coupling would simply be shifted $(\epsilon - \delta) \rightarrow \epsilon'$, see the first line of Table 4.1. The DM production of photon would however change at low temperature (second line of Table 4.1) but this would be a negligible effect in the Early Universe, for example opening a very suppressed DM annihilation cross section into photons (for feebly coupled models).

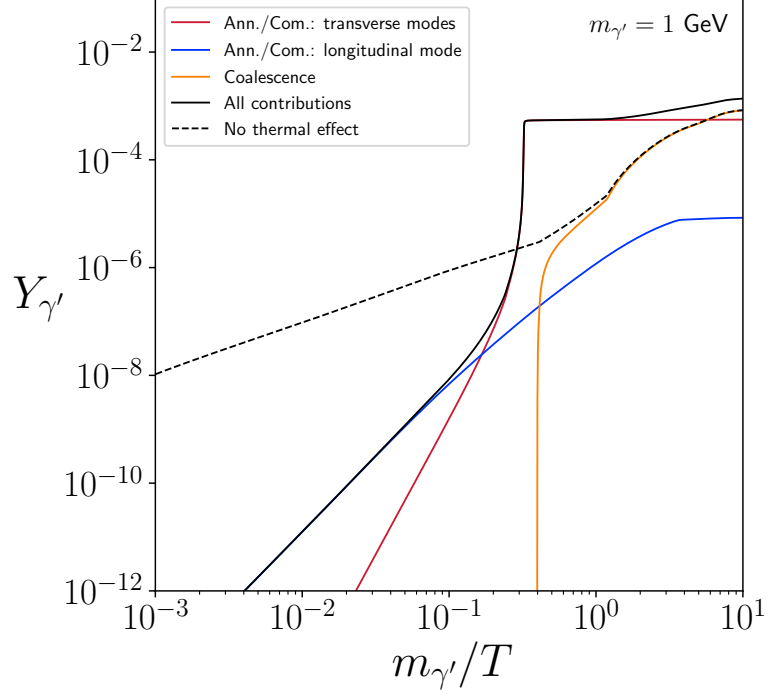


Figure 4.3: For $\epsilon = 10^{-9}$ and $m_{\gamma'} = 1$ GeV, all contributions to the dark photon yield $Y_{\gamma'}$ as a function of the inverse temperature. For the continuous lines, thermal effects have been taken into account. The dashed line gives the total abundance of dark photons when thermal effects are neglected. The transverse and longitudinal production from $2 \rightarrow 2$ processes are given respectively in red and blue. In orange is given the coalescence process. For the $2 \rightarrow 1$ processes, at high temperature, the thermal mass of the SM particles forbids the production of dark photons, purely by kinematics and the two bumps corresponds to the production by leptons and quarks. Note that the γ' never reach equilibrium ($Y_{\gamma'} \sim 1$).

In Fig. 4.3, the solid black line gives the dark photon abundance as a function of inverse temperature with the full finite temperature treatment. On the one hand, in the limit of effectively massless dark photon, $m_{\gamma'} \gg T$, the connection between the SM and the γ' is inactive, since very few dark photons are produced from SM processes such as $e^- \gamma \rightarrow e^- \gamma'$. This amounts to have $\epsilon_{\text{eff}} \rightarrow 0$ and the structure of the connections between each population is that of the right panel of Fig. 2.1, *i.e.* the $m_{\gamma'} = 0$ case. On the other hand, at low temperature, neglecting the resonant production, the abundance of dark photons is set by coalescence processes (solid orange) and $Y_{\gamma'}$ is the same as that of the dashed curve, for which thermal effects are neglected. This indicates that when $T \lesssim m_{\gamma'}$, we recover the vacuum case, that is $\epsilon_{\text{eff}} \rightarrow \epsilon$ and the coupling follows the structure of the left panel of Fig. 2.1 (taking $\delta = 0$).

The origin of the mass of the dark photon can impact the history of its production. If the $U(1)'$ is broken spontaneously, the additional scalar degrees of freedom can possibly give rise to new production channels, for example through decay $h' \rightarrow \gamma' \gamma'$, see the short discussion in [5]. If the mass arise from the Stückelberg mechanism, the previous discussion applies as such.

4.4 Impact on Dark Matter Production

The above refined treatment of the production of the dark photons from SM will mainly impact the new regimes that appear when $m_{\gamma'} \neq 0$, *i.e.* the Ib freeze-in from dark photons, the sequential freeze-in II, the reannihilation regime sourced by dark photons IIIa and the secluded freeze-out regime IVa.

In the early universe, the γ' creation from SM is resonantly enhanced (compared to the production rate without thermal effects) when the plasma frequency crosses the dark photon mass $\omega_T \approx m_{\gamma'}$, corresponding to temperature $T_{\text{res}} \simeq (\text{a few}) m_{\gamma'}$ and is strongly suppressed at higher temperature. Therefore, for DM candidates with masses $m_{\text{DM}} \gg T_{\text{res}}$, the abundance of dark photon will be irrelevant at the time of DM freezing-in or -out and one recovers the mesa diagram of DM production with a massless photon [71]. The DM phase diagram will thus only comprise only of the 4 basic ways (Ia, IIIb, IVb, Va and Vb).

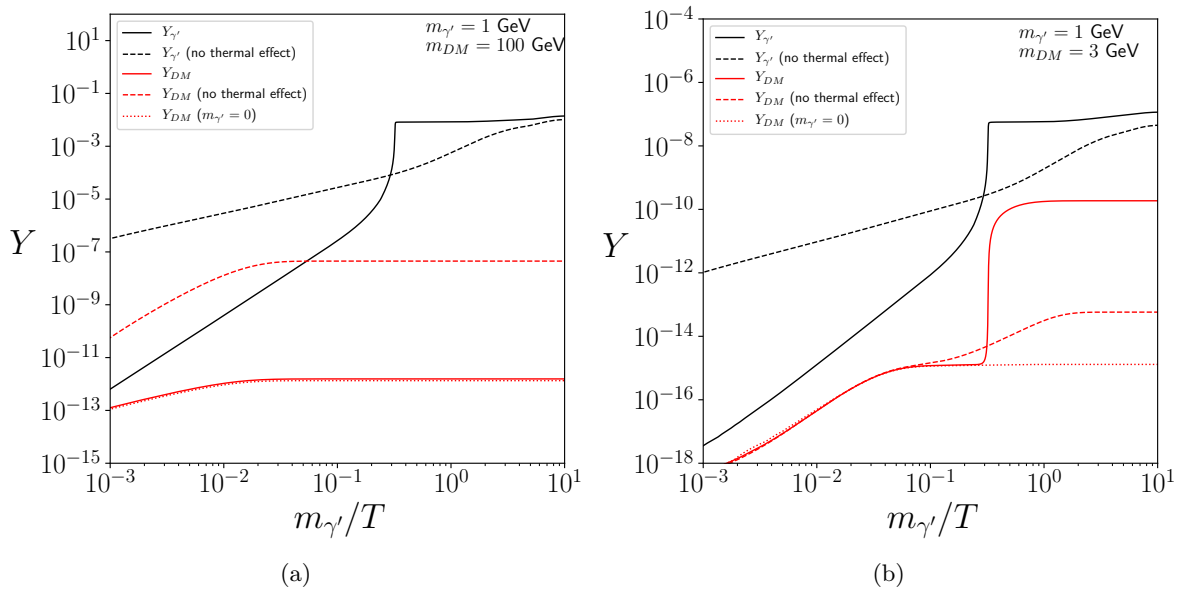


Figure 4.4: Comparison between the evolution of the dark photon (black lines) and DM (red lines) yields. For the solid curves, thermal effects are taken into account whereas for the dashed curves they are neglected. The dotted red lines give the DM abundance in the $m_{\gamma'} = 0$ limit and the extra production compared to this baseline is due to dark photon production of dark matter. Panel (a) and (b) differ by the choices of dark matter and dark photon masses. In both panels couplings are such that DM relic abundance is reproduced once thermal effects are taken into account (red lines). In panel (a), $(\kappa, \epsilon) = (2 \times 10^{-11}, 5.6 \times 10^{-9})$ and in panel (b), $(\kappa, \epsilon) = (3.6 \times 10^{-14}, 10^{-11})$

In Fig. 4.4 are shown the abundances $Y_{\gamma'}$ and Y_{DM} as a function of $z_{\gamma'} = m_{\gamma'}/T$ for a fixed $m_{\gamma'} = 1$ GeV, a heavy candidate $m_{\text{DM}} = 100$ GeV and one close in mass, $m_{\text{DM}} = 3$ GeV. In solid (dashed) black is depicted the total abundance of dark photons as a function of time with (without) thermal effects, and is the same for the two figures. They are described in details in Fig. 4.3. The dotted red line corresponds to the abundance of DM in the massless dark photon limit. The red dashed line takes into account the mass of the dark photon but not the thermal effects and the continuous red line incorporates them.

In panel (a), DM freezes-in at $T \sim m_{\text{DM}}/3$ and thus at $z_{\gamma'} \sim 3/100$. When thermal effects are neglected, dark photons are sizeably created at high temperature (dashed black) and in turn produce most of the dark matter (dashed red). Taking into account the suppression of transverse and longitudinal modes production when relativistic (continuous black), at the time of freeze-in, the dark photon sector is not populated with enough dark photons in order to affect the DM production (continuous red). Therefore, when $m_{\text{DM}} \gg m_{\gamma'}$ one recovers indeed regime Ia, where DM is only produced by SM annihilations (dotted red). As explained above, the reannihilation and secluded freeze-out phases of this candidate will therefore also proceed through regimes where the dark photon production of dark matter is inconsequential, *i.e.* IIIb and IVb.

In panel (b), we show a candidate whose production is dominated by dark photon annihilations. For the choice of DM mass, when the dark photons have been negligibly created, DM is mostly produced by Z boson decay at $z_{\gamma'} \sim m'_{\gamma'}/m_Z$. At lower temperature, the rate of production through dark photon increases and we see that both the dashed and continuous red line are above the dotted one. At the time of freeze-in, most dark photons have been produced through the resonance, hence why the abundance of DM is much bigger than in the case with no thermal effects. This panel illustrates the production history of the model in its regime II (sequential freeze-in). Since thermal effects boost the γ' production for temperature just below the resonant temperature, DM production at those temperature is more efficient. If the majority of the DM abundance is set around the resonant temperature, feebler couplings between the DM and the SM is expected when compared to the case of no thermal effects.

However, in both panel, we have implicitly assumed the dark photon momentum distribution to be well described by Boltzmann statistics, up to a normalisation factor $n_{\gamma'}/n_{\gamma'}^{\text{eq}}$, when treating a DM candidate in its sequential freeze-in regime, see the Boltzmann equations of Eq. (3.15). In Fig. 4.5, we show the momentum probability distribution of dark photon produced by a $2 \rightarrow 2$ process, say $e^- \gamma \rightarrow e^- \gamma'$, at high temperature, $T \gg m_{e^-}$. We choose the temperature to be $T = m_{\gamma'}/3$, *i.e.* when freeze-in production of dark photon stops.

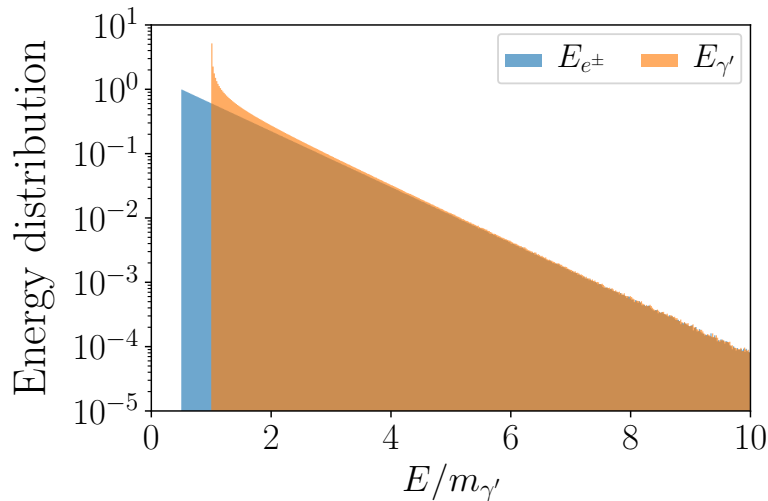


Figure 4.5: Energy distribution of SM particles (orange) in a thermal bath at temperature $T \sim m_{\gamma'} \gg m_{\text{SM}}$. The energy distribution of dark photon produced from the $\text{SM} + \text{SM} \rightarrow \text{SM} + \gamma'$ process is given in blue. The minimum energy of the initial particle participating in the process is $m_{\gamma'}/2$ and dark photons have a minimum energy of $m_{\gamma'}$. In the last freeze-in production stage, the dark photon distribution can be very different from thermal.

When dark photons are produced relativistically, their energy is half of the center-of-mass energy and, since $m_{\gamma'}$ plays little role, their impulsion p follows the initial impulsion distribution, that is the Boltzmann distribution. However, at low temperature, a fraction of the energy is converted into rest mass and the assumption fails. The failure is even more severe for coalescence processes, say $e^+ + e^- \rightarrow \gamma'$, since the dark photons are necessarily produced at rest. In the following, this problem is set aside as it would require to solve the unintegrated Boltzmann equation and would only affect DM candidates close in mass with the dark photon, $m_{\text{DM}} \gtrsim m_{\gamma'}$. For a more careful treatment of this aspect of the sequential processes, that is a freeze-in of the mediator which subsequently freezes-in the dark matter, see [90].

Now turning to the phase diagrams, we first take a look at the thermalization between dark photons and the SM when taking into account thermal effects. Because of the resonance, the simple criterion $\Gamma/H > 1$, which assumes that the dark photon production rate monotonically increases with time until $T \sim m_{\gamma'}$, does not hold anymore. The thermalization critical coupling will be inferred from the explicit solution of the dark photon Boltzmann equation. We find that for candidates close in mass with the γ' , $n_{\gamma'}$ reaches its equilibrium value $n_{\gamma'}^{\text{eq}}$ at $T = m_{\text{DM}}$ for

$$\epsilon \gtrsim \epsilon_{\text{th}} \equiv 6 \times 10^{-9} \left(\frac{m_{\text{DM}}}{\text{GeV}} \right)^{1/2}. \quad (4.18)$$

and thermalization is therefore more efficient, see Eq. (3.7) for a comparison.

The phase diagrams for the couples $(m_{\text{DM}}, m_{\gamma'}) = (3 \text{ GeV}, 1 \text{ GeV})$, $(100 \text{ GeV}, 10 \text{ GeV})$, including thermal effects are given in Figs. 4.6 and 4.7 respectively and can be compared with Fig. 3.4, Fig. 3.5.

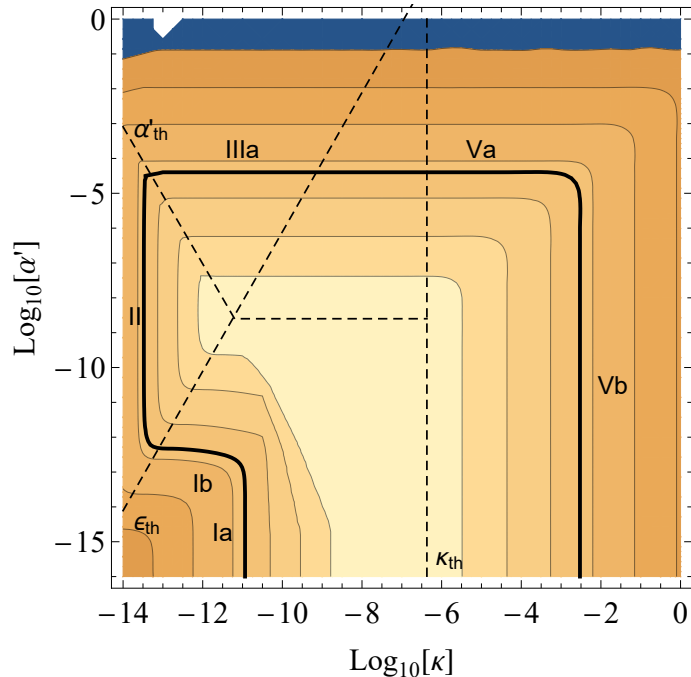


Figure 4.6: Contours of the DM relic density for $m_{\text{DM}} = 3 \text{ GeV}$ and $m_{\gamma'} = 1 \text{ GeV}$ with the thermal effects on the dark photon production taken into account. When compared with Fig. 3.4, due to the resonant production of dark photons, regime Ib extends to lower κ .

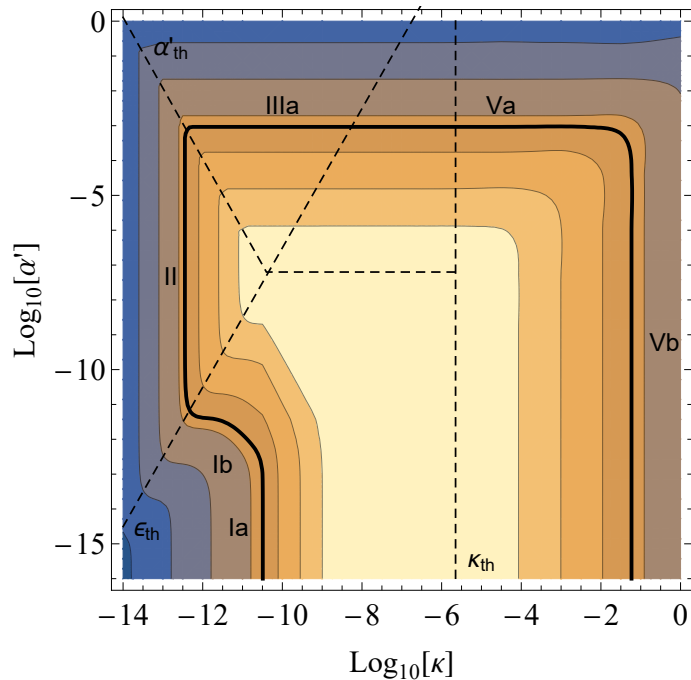


Figure 4.7: Contours of the DM relic density for $m_{\text{DM}} = 100$ GeV and $m_{\gamma} = 10$ GeV with the thermal effects on the dark photon production taken into account. When compared with Fig. 3.5, due to the resonant production of dark photons, regime Ib extends to lower κ .

We now turn to describe the impact of thermal corrections for each regime in details, with Figs. 4.6 and 4.7 as references.

Freeze-in regimes: In regime Ia, since dark photons play no roles in the determination of the abundance of DM, thermal effects are small and therefore negligible. We also expect that regime Ib will be relevant for smaller coupling when $m_{\text{DM}} \approx m_{\gamma'}$, due to the resonant enhancement of γ' production at those temperatures.

Sequential freeze-in: Since regime II follows the end point of regime Ib, for $m_{\gamma'} \lesssim m_{\text{DM}}$, as in Figs. 4.6 and 4.7, thermal effects will allow for smaller values of κ . This regime also merges more quickly with regime Ia, *i.e.* when $m_{\text{DM}} \gtrsim m_{\gamma'}$, due to the suppressed abundance of relativistic γ' .

Therefore, for these 2 regimes, the parameter space of the model will quantitatively change, but nevertheless retains the features that we have discussed previously when neglecting thermal effects. In Fig. 4.8, we show the millicharge κ for the three regime Ia, Ib and II for different candidates once thermal effects have been taken into account (continuous lines and shaded area). For comparison, we reproduce in dashed lines the regime II that is obtained without thermal effects on the γ' production.

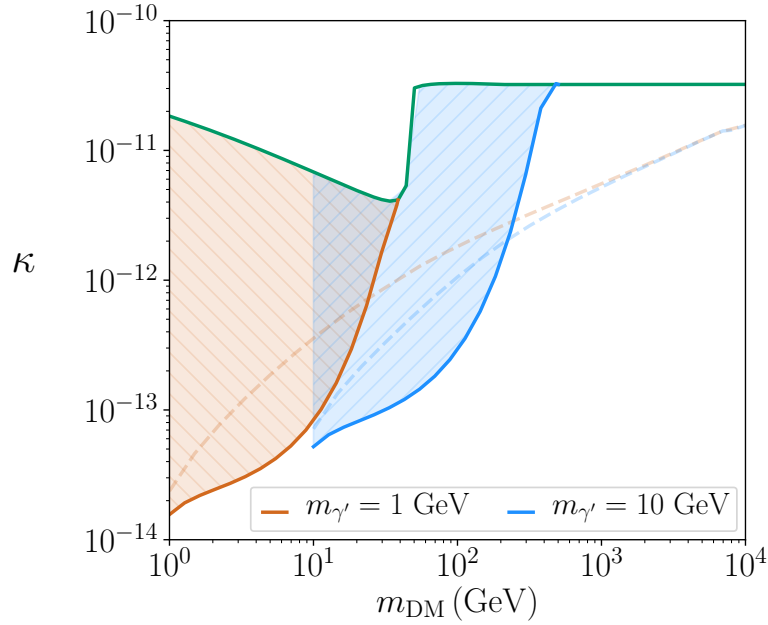


Figure 4.8: Same as Fig. 3.6 but with the thermal effects on dark photon production taken into account. In dashed is given the sequential freeze-in coupling κ_{II} of Fig. 3.6 for both dark photon masses.

Reannihilation regimes: As the $\text{SM} \rightarrow \gamma'$ source term depends also on ϵ_{eff} , regime IIIa will dominate at lower couplings when the relevant dark photon production proceeds through the resonance ($m_{\gamma'} \lesssim m_{\text{DM}}$) and merge with regime IIIb rapidly as DM candidates become heavy with respect to the dark photon, *i.e.* when the SM energy injection into dark photon become suppressed.

Secluded freeze-out: Due to thermal effects, regime IVa (*i.e.* when the secluded dark sector has been sourced by γ' production) disappears from the DM production phases. Even though applicable for candidates with $m'_{\gamma'} < m_{\text{DM}} < m_e$ when thermal effects are neglected, the dark photon production at $T \sim m_e \gg m_{\gamma'}$ is in fact highly suppressed. At a later time $T = T_{\text{res.}} \sim m_{\gamma'} < m_e$, the γ' production due to the resonance is also negligible since the production by electron is in any case Boltzman-suppressed. Therefore, the energy injection from the visible sector through dark photon is cut-off and regime IVa disappears.

Freeze-out regimes: Regime Va appears once the DM annihilation rate into dark photons dominates over other processes and either $\kappa > \kappa_{\text{th}}$ or $\epsilon > \epsilon_{\text{th}}$ and $\alpha' > \alpha_{\text{IIIa}}$. If regime Ib exists for the given set of parameters, the second condition can be fulfilled for $\kappa < \kappa_{\text{th}}$ and in this limit, thermal effects can have an impact. If dark photons thermalization with the SM is more (less) efficient due to thermal effects at low (high) temperature, regime Va will be reached for lower (higher) coupling with respect to the case where thermal corrections are neglected. For regime Vb, since dark photons play no role, thermal effects will have a negligible impact.

Chapter 5

Constraints

The model of Eq. (2.1) provides many DM candidates, across a wide range of mass and couplings. This is most easily seen in Fig. 3.8, for the case where $m_{\gamma'} \ll m_{\text{DM}}$ and $\delta = 0$. As discussed at length in Chapter 3 and more specifically Section 3.3, many more new DM candidates are found when $m_{\gamma'} \lesssim m_{\text{DM}}$, and they are shown in Fig. 4.8. In this Chapter, we aim at assessing the viability and detection potential of the DM candidates. First, we review the state of the art on dark photon coupling constraints for the case where it is massive and acts as the mediator in the kinetic mixing portal. Since the millicharge κ and dark fine structure α' fixed by the DM relic abundance can span a vast range of values (see for example the mesa diagram of Fig. 4.6, for which $m_{\text{DM}} = 3$ GeV and $3 \times 10^{-14} < \kappa < 3 \times 10^{-3}$, $10^{-15} < \alpha' < 10^{-4}$), the kinetic mixing coupling will also take a wide range of values (for the same mesa, $m_{\gamma'} = 1$ GeV and $5 \times 10^{-13} < \epsilon < 1$). Therefore, irrespectively of the possibility to detect DM, constraints on the kinetic mixing parameter ϵ and the dark photon mass $m_{\gamma'}$ must be taken into account in a full phenomenological study of the model. We then turn to the constraints on the DM with a kinematically mixed massless and massive dark photon as mediator. In particular, we detail and update our work [4] in light of the new constraints on dark photons and argue that our recast procedure is well suited for the estimation of direct detection limits when in the case of light mediators ($m_{\gamma'} < 40$ MeV).

5.1 Constraints on Dark Photons

The dark photon is a very attractive extension of the Standard Model and much work has been devoted to constraining its mass and kinetic mixing parameter with laboratory, astrophysical and cosmological observables. Since the main focus of the previous discussions has been about using the dark photon as a portal between the SM and dark matter, we will first treat the mediator mass and kinetic mixing parameter range that can be found in Figs. 4.6 and 4.7.

Constraints in the $\epsilon - m_{\gamma'}$ plane are set by considering two different physical processes. The first uses the dark photon coupling to electrically charged SM fermions (typically being of the first generation) and the subsequent alteration of an observable following γ' production through $2 \rightarrow 2$ annihilations, coalescence or Bremsstrahlung processes. The second one uses instead the mixing between γ and γ' states and constraints the energy exchange between the 2 reservoir of particles. Both categories of constraints can be relaxed at the price of some tuning, by taking $\epsilon - \delta \approx 0$. This fact is most easily seen in Eq. (2.3) and will hold even at finite temperature, see Table 4.1.

Since the dark photon phenomenology is extremely rich, a given work of the broad literature tends to analyse one particular aspect. This translates into a focus on a particular mass range for the dark photon, or the assumption that the γ' compose 100% of the DM or that the dark sector fermions play an important role. To this day, a comprehensive list of constraints for (*i*) a massive

dark photon (*ii*) which is not the DM and (*iii*) for which the dark sector degrees of freedom are irrelevant, does not exist. In Fig. 5.1, we have produced the exclusion plot of this particular dark photon scenario, which is the most relevant case for the model under consideration in this thesis. For the sake of summary, let us list some references covering the state of the art of dark photon constraints, that we hope covers as much as the γ' parameter space as possible. The most recent compilation of constraints on the dark photon parameter space in the low mass, $m_{\gamma'} < 0.1$ MeV, region can be found at [101]¹. We complement the solar constraints by direct detection constraints on γ' of solar origin, denoted XENON_⊙ [102]. For higher masses, we have gathered the following references. Between 0.1 and 1 MeV, [93, 103] provides astrophysical and cosmological constraints, which have been refined [104] for the largest value of ϵ . For even higher masses, [105] focuses on accelerator-based constraints on large ϵ values. CMB and BBN bounds in this mass region for very feeble couplings have been recently reevaluated by [106] (though we recasted and reported the weaker, more conservative bounds of [107]) and [108] derives the bounds on N_{eff} from BBN when dark photons are frozen-in from the SM thermal bath. [109, 110] gives a collection of bounds from supernovae. These bounds have been extracted from each references and reproduced in Fig. 5.1.

¹Some constraints, denoted by “DPDM”, those listed in Table II of [101] as well as DAMIC, SEINSEI and XENON, assume the dark photon to compose 100% of the dark matter and do not apply in our analysis. Also, see <https://cajohare.github.io/AxionLimits/docs/dp.html> for an easy-to-use repository of constraints on dark photon and axion.

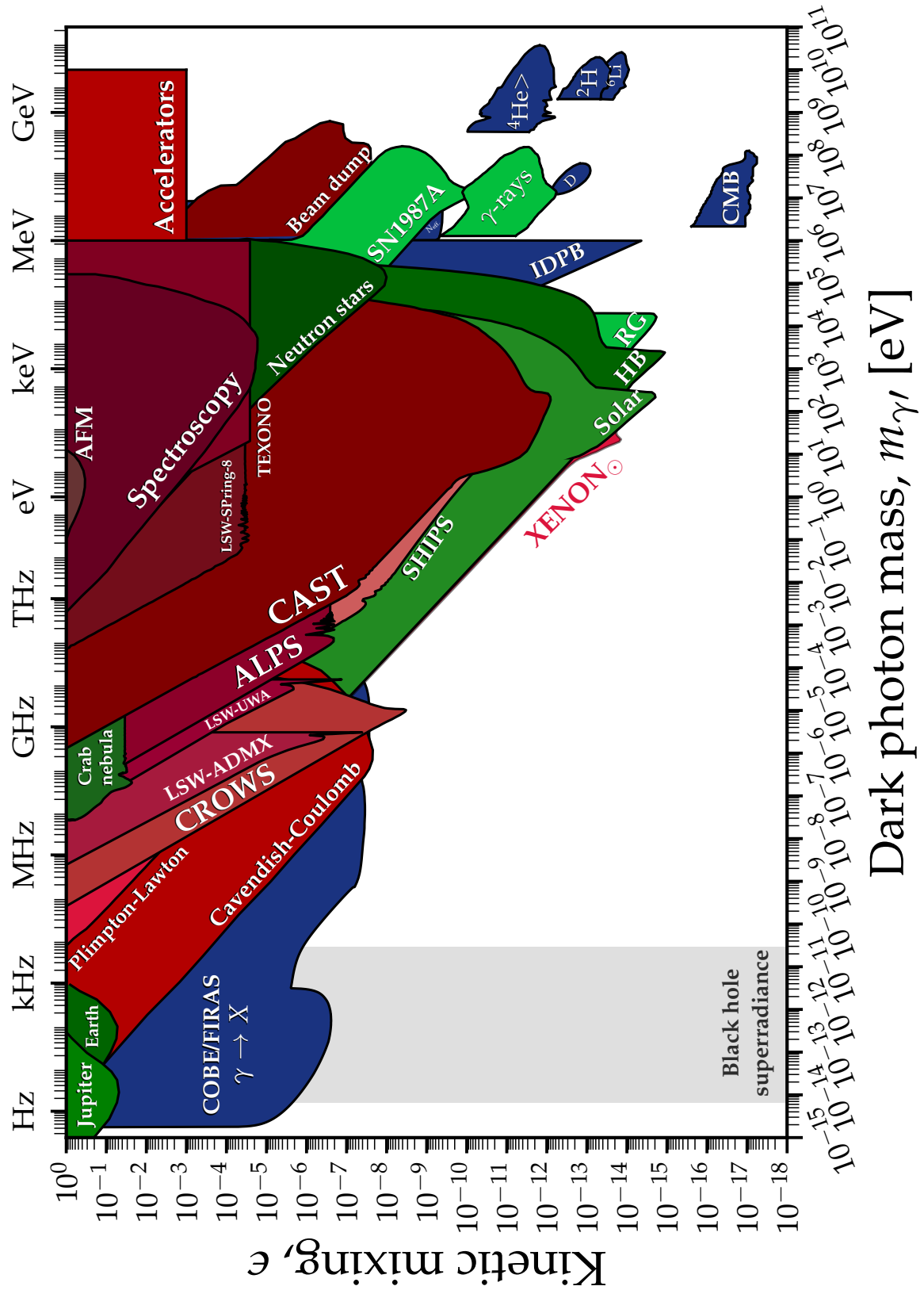


Figure 5.1: Non-exhaustive summary of current constraints on the dark photon mass and its kinetic mixing parameter with the SM photon, not assuming γ' to be the DM. The color scheme is that blue, red and green area correspond to cosmological, experimental and astrophysical exclusion limits. Adapted from [101] with the help of the publicly available code of <https://cajohare.github.io/AxionLimits/docs/dp.html>. See text for details on the constraints on masses above 0.1 MeV.

5.1.1 Cosmological constraints

Our knowledge of the thermal history of the Early Universe is exquisite up to temperature of a few MeV. The cosmological abundance of light elements has been very well understood² for decades [112] and the study of the Cosmic Microwave Background radiation has provided us with a very precise determination of the 6 free parameters that seem to describe the evolution of our Universe [113]. Since all of these cosmological measurements agree very well with computations if the particle content of the Universe at those time is that of the SM – up to error bars – any beyond the SM physics should not spoil these results. In the following, we will assume that the dark photon abundance in the Early Universe has its origin in production from thermal processes, had no significant abundance after inflation ($Y_{\gamma'}(T = T_{\text{RH}}) = 0$) and describe how to constrain its parameter space³.

Neutrinos decouple relativistically from the thermal bath at $T = \mathcal{O}(1)$ MeV and subsequently redshift as radiation, making the effective number of neutrinos $N_{\text{eff}} \propto \sum_{i=e,\mu,\tau} \rho_{\nu_i}(T_{\nu_i}) / \rho_{\gamma}(T_{e\gamma})$ constant once the electron annihilation catastrophe happened. N_{eff} can then be measured in the recombination era through analysis of the CMB multipoles. The presence of dark photons can affect this observable. For $m_{\gamma'} < 2m_{\pi}$, the γ' decay predominantly electromagnetically⁴ and can increase the electron-photon bath temperature $T_{e\gamma}$, therefore decreasing N_{eff} . Such effect constraints dark photon between 1 and 10 MeV to have a lifetime $\tau_{\gamma'} > 1 - 10$ sec or $\epsilon \lesssim 10^{-9} - 10^{-9.5}$ [108, 107]. Thermal effects have not been included in these analysis (the latter not being focused on dark photons) but since the production of dark photons is followed down to $T = m_{\gamma'} > m_{e^-}$, most of the production will be through coalescence processes and resonant production at higher temperature might only contribute to a small addition to the dark photon abundance (see Fig. 4.3 and [96] for an analytical estimation).

Any (sizeable enough) energy injected during primordial nucleosynthesis will alter the abundance of light elements. For dark photons decaying into 2 electrons, the impact on the photodissociation of ${}^4\text{He}$ and destruction of D depend strongly on the assumptions made on the evolution of the electromagnetic cascade. [96] assumed that the lepton pairs produced after the decay of a γ' undergoes inverse Compton scattering on the thermal bath photon. The boosted photon would then subsequently produce e^{\pm} pairs on the background photons until reaching the threshold energy $E_c = m_e^2/22T$. If the lifetime of the dark photon is long enough, E_c can be bigger than the photodissociation energy of light elements and alter BBN. However, [115] pointed out that within the dark photon model, e^{\pm} scatterings on photon actually proceeds in the Thomson regime, leading to many soft photons and a small effect of photodissociation. Recently, additional effects such as final state radiation have been taken into account by [106] and a much larger parameter space is now constrained by photodissociation of light elements. Even though not focused on dark photons, [107] finds similar, albeit weaker bounds⁵. Larger masses (with smaller lifetime) are constrained by hadrodissociation, since for $m_{\gamma'} > 300$ MeV the decay channel into pion opens, and overproduction

²Except for ${}^7\text{Li}$ [111].

³If $m_{\gamma'} \ll m_{e^-}$, dark photons cannot be produced in the Early Universe due to thermal effects and therefore cannot be constrained through early Universe observables such as CMB or BBN. In this mass regime one can however set the dark photon relic abundance through non thermal effect such as the misalignment mechanism [114] which in turn allows for observable consequences of dark photon dark matter. Section 5.1.3 will clarify the physics related to these constraints.

⁴The decay into neutrino, even though kinematically allowed, is suppressed by a factor $(m_{\gamma'}/m_Z)^4$ as it needs to proceed through mixing with the Z .

⁵Since [106] does not take into account thermal effects, their results can therefore be compared to [107] as both model behave effectively the same.

of ${}^4\text{He}$.

For even longer-lived dark photons ($\tau > 10^{12}$ s), CMB observations can constraint the lower mass region ($\gtrsim 1$ MeV) [96, 115, 106]. During recombination, products of the γ' decay can deposit electromagnetic energy into the plasma permeating the Universe. In turn, light elements heat up and/or undergo ionization. This additional ionized fraction will broaden the time it takes for the Universe to become transparent to photon, *i.e.* the last scattering surface, and therefore blur the small scales details or in other words suppress the high l power spectrum.

Dark photons with mass much smaller than the electron will not be produced from thermal processes in the Early Universe, due to finite temperature effects. Just below the decay threshold, for $m_{\gamma'} \lesssim 2m_{e^-}$, some production through resonant annihilation is possible and the γ' will dominantly decay into 3 photons at 1 loop (the 1 photon channel being forbidden by momentum conservation and the decay into 2 photons by spin conservation), although with a very suppressed rate, $\Gamma_{\gamma' \rightarrow \gamma\gamma\gamma} \sim \epsilon^2 \alpha^4 m_{\gamma'}^9 / m_{e^-}^8$ [104]. Nevertheless, close to threshold, mixing parameter down to $\epsilon \sim 10^{-14}$ can be excluded by the diffuse X-ray background [93, 116, 103]. Note however that because the decay is 3 body, one cannot search for a line in the photon decay spectrum of a dark photon with $m_{\gamma'} \lesssim 2m_{e^-}$. The resulting photon spectrum should however not be completely featureless and it would be interesting to assess if more stringent, updated bounds in this region of the parameter space can be found. This task might be difficult however since little detailed data is available from experiments that are sensitive to ~ 100 keV photons.

5.1.2 Stars, supernovae constraints

A star is roughly a spherically symmetric self-gravitating globally neutral plasma object sustained by thermonuclear reactions. The volume of the star is optically thick to photons and it cools through photon emission at its surface. If new, light ($m < T_\star$), feebly interacting (mean free path $\gtrsim R_\star$) particles couple to the electron, proton or neutron, they can open new cooling channels. In turn, the evolution of the star will be altered from the standard evolution model and constrained can be put on those new degrees of freedom⁶ [118]. A conservative estimate of the constraints is that the excess “dark” luminosity should be small compared to the luminosity of the star through SM processes, $L_{\text{dark}} < L_\star$. For the Sun, measurement of the neutrino flux constraints any new energy loss mechanism to be 10% of the Sun’s photon luminosity [119]. In the case of the Sun, it is possible to further constrain dark photons by looking for them in dark matter experiments after their solar production [120] or in helioscopes [91]. Other populations of stars, namely red giants and stars from the horizontal branch of stellar evolutions are hotter and the same energy loss argument lead to constraints at higher dark photon masses [95]. Notably, within the context of solar constraints on dark photons, [94] brought to light the correct treatment of the production of transverse and longitudinal dark photons at finite temperature and the bounds from cooling of stars are now settled [94, 95].

Supernovae can also provide complementary constraints. In the standard picture of the core-collapse of a progenitor star, almost all of the gravitational energy of the outer envelope of the star is shed by neutrino emission, since they can more easily escape the medium. The outer-most neutrino shell is composed of very energetic neutrino at $T \sim \text{MeV}$ and has thickness ct_{cool} where the typical time of cooling is $\mathcal{O}(1)$ s. If the supernovae is close (*i.e.* galactic) to Earth-based detector, a burst

⁶It is of course impossible to track the different stages of evolution of one star (one exception being the neutron star). It is nevertheless possible to infer the physics of stellar evolution by studying a large number of star evolving together with a similar chemical composition, in a globular cluster for example [117].

of neutrino could be detected by large, sensitive volume in underground experiments. Inside this outer shell are neutrinos produced by other cooling processes, therefore making a neutrino sphere centred on the star, but they are not energetic enough to be detected. Such an event happened in recent cosmological history somewhere in the Large Magellanic Cloud and the energetic neutrino shell reached Earth in 1987. The time scale of the cooling of the star, inferred from the neutrino burst duration, as well as many other observables, agrees with the physics thought to occur during the supernovae [121]. Akin to cooling of stars, new light, feebly coupled degrees of freedom can provide additional cooling channels and reduce the duration of the neutrino burst, therefore opening the possibility of constraining them [118]. More quantitatively, the ‘‘Raffelt criterion’’ states that the excess luminosity in the dark channels should be $\lesssim 2 \times 10^{52} \text{ erg s}^{-1}$ where $1 \text{ erg} = 10^{-7} \text{ J}$. In 10 seconds, the duration of the neutrino burst, the total gravitational binding energy of the neutron star, $3 \times 10^{53} \text{ erg}$, is shed and any dark luminosity bigger than this figure would therefore reduce neutrino emission.

For SN1987A, the Raffelt criterion was correctly evaluated (*i.e.* with thermal corrections) in [122, 123]. The measured explosion energy could also be increased by efficient transport of energy from the core to the envelope through dark photon production, decay and redistribution of energy [110]. For even feebler coupling, dark photons can escape the supernovae, though not in sufficient amount to cool it significantly, and subsequently decay into e^\pm pairs. Positrons can annihilate with e^- at the site of supernovae and increase the gamma-ray flux concomitantly with photons produced during the SN or, after propagating in the galaxy, they can annihilate with electrons and produce a detectable line at 511 keV [109]. However, if the dark photon couples to a dark fermion of similar mass, then, after both type of dark sector particles have been produced during the collapse of the star, even small interactions can lead to self-trapping and therefore alleviate constraints [124], which then become model-dependent. Nonetheless, the mergers of such objects would provide a hotter and denser environment for the production of γ' , thus allowing to reach higher masses. Their decay could then similarly be constrained by gamma-ray burst observations at the time of merger [125], though with the difficulty that the photon signal lack distinctive features. It has been recently put forward that the remnant of SN1987A is indeed compatible with a 30 years old neutron star, therefore dubbed NS1987A [126]. This particular observation would therefore exclude parameters inducing rapid cooling in such young neutron stars [127]. Recently, doubts have been cast on the validity of the dark luminosity computations. [128] argues that some basic assumptions about the dynamics of the collapse might not be valid and would relax supernovae bounds on light particles.

5.1.3 $\gamma \leftrightarrow \gamma'$ transitions

In addition to being crucial for the correct computation of the production rate of dark photon from SM particles, thermal corrections brings a new efficient mechanism than can be used to constraint dark photons, resonant $\gamma \leftrightarrow \gamma'$ conversion. As the plasma frequency of some regions of space and time in the Universe crosses the dark photon mass, photons are resonantly converted into dark photons, so visible energy is transferred to the dark sector and can lead to observable signatures. For higher temperatures, oscillations are suppressed by $(m_{\gamma'}/m_\gamma)^2$ due to thermal effects and at lower temperature, they proceed as in vacuum and are suppressed by the small mixing angle ϵ^2 . Once resonant conversion happens, the CMB could have its power spectrum distorted by dips at energies where photons were pumped into dark photons, due to their late time propagation in the reionized Universe [129, 130]. For heavier (but still very light) dark photons, it is possible to convert photons before CMB decoupling into a ‘‘hidden CMB’’, therefore decreasing the SM energy density and increase N_{eff} as well as the baryon to photon ratio η [92]. For the late time conversion of photons into dark photons, inhomogeneities and reionization can greatly affect the plasma frequency distribution and estimations of the $\gamma \rightarrow \gamma'$ conversion rate becomes more involved [131]. On the other

hand, if dark photons are numerous in the Universe at late time, perhaps if dark photons constitute the DM, the reverse resonant conversion into photons can also lead to constraints [132, 101, 133]. In a medium, the rate of resonant conversion can be straightforwardly computed using QFT tools [134]. A similar quantum mechanical treatment can describe both the resonant and non-resonant cases [92].

In vacuum, oscillations between active, sterile, photon and dark photon states is however treated in a similar fashion to 2 neutrino species oscillations [135]. In the interaction basis, when kinetic and mass mixing have been eliminated, electromagnetic currents source the combination $\mathcal{A} = A - \epsilon A'$ (“active”) whereas the orthogonal state $\mathcal{S} = \epsilon A + A'$ does not interact with SM matter (“sterile”). Assuming that the active component is emitted with definite energy $\omega \gg m_{\gamma'}$, because of the non zero dark photon mass, the evolution of the A and A' states will introduce a phase shift qr where $q = k - k' \approx m_{\gamma'}^2/2\omega$, r is the distance travelled from the source of emission and k, k' are the momentum of A and A' respectively. The relative intensity of \mathcal{S} at a distance r will therefore be given by $\rho_{\mathcal{S}} = 4\epsilon^2 \sin^2 qr/2$ with a corresponding dimming – inside a detector of SM particles – of the active component. However, the dimming of far away light sources is suppressed by ϵ^2 and will not exclude a wide range of parameters [136]. Conversely, a dark current would source \mathcal{S} and a small \mathcal{A} component would appear along the evolution of the wave. In principle, DM from the halo annihilating into light γ' could faintly shine into photons. However, complementary studies should vastly exclude the range of parameter space where such effect would be observable. Finally, if $m_{\gamma'} = 0$, no phase shifts occur during the spatial evolution between A and A' and the active component \mathcal{A} is simply called the photon. The intensity measured by SM detectors would be constant over distance to the source. An observer with a DM detector would register an intensity proportional to $e'\epsilon$, *i.e.* the millicharge. In Fig. 5.1 are presented experiments that take advantage of vacuum oscillations. For example, CAST and SHIPS are helioscope experiments, ALPS is a Light Shining through Walls (**LSW**) that uses instead a laser source, LSW-SPring-8 is similar but uses a more energetic synchrotron source and LSW-UWA, LSW-ADMX and CROWS use resonant cavities.

5.1.4 Colliders and beam dump experiments

Generally, dark photons can decay visibly (into SM particles) or invisibly (into, for example, the dark matter). Since our purpose was the study of the light mediator limit, $m_{\gamma'} < m_{\text{DM}}$, of the production phases of kinetic mixing portal DM, this discussion will be focused on visibly decaying γ' . Dark photons can be copiously produced at colliders provided the kinetic mixing is not too small and their mass not too big. The branching ratio of dark photons into SM particles is that of an e^+e^- annihilation at $\sqrt{s} = m_{\gamma'}$. Di-electrons and di-muon resonant searches can therefore reconstruct the invariant mass of the leptonic final state (which could not necessarily come from a $2 \rightarrow 2$ process, but also possibly from initial and final state γ' -strahlung or Compton-like scattering) and hunt for a bump, which would be due to on-shell production of the dark photon. The sensitivity of each experiment would then be limited at high mass by its beam energy, at low mass by the efficiency of reconstructing the final states energy (and by $m_{\gamma'} > 1$ MeV) and at low coupling by its luminosity. However, in such pure bump-hunt searches, the SM background is irreducible and new strategies would be required to push the limits on ϵ further down. Beam dump experiments can however probe smaller couplings as they are sensitive to the lifetime of the dark photon, $\propto 1/(\epsilon m_{\gamma'})$. If produced by a, say, γ' -strahlung process or in the decay of a meson coming from interactions between the beam and the fixed target, the dark photon would necessarily be boosted. If the lifetime in the laboratory frame is long enough, the dark photon can exit the beam dump, travel past the shielding and decay into a electron or muon pair, which can then be counted and compared to the expected backgrounds. Their sensitivity is limited to dark photons having a decay length longer than the beam target to shielding distance but smaller than the target material to detector distance, the

kinematics of production and the expected numbers of γ' produced. For fixed target collisions, the center of mass energy is $\propto \sqrt{E_{\text{beam}}}$ and it is thus harder to reach higher dark photon masses.

5.1.5 The dark photon as a mediator for feebly coupled DM set by freeze-in

The DM candidates treated above and whose abundance is set by (sequential) freeze-in from mediator are unconstrained from DM searches (see next section). However, the dark photon parameters required in these regimes might be in tension with the constraints described above. Taking the example of Fig. 4.6, a dark photon mass of $m_{\gamma'} = 1$ GeV is excluded by BBN for kinetic mixing values between $10^{-12} < \epsilon \lesssim 10^{-10}$ and by accelerators searches for $\epsilon > 10^{-3}$ (the excluded regions would be represented as oblique bands in the mesa diagram). For the sequential freeze-in phase of the accompanying DM candidate, ϵ_{II} spans the range $[10^{-12}, 3 \times 10^{-7}]$, higher ϵ values corresponding to regimes Ib and Ia. Therefore, a wide range of the DM parameter space allows for setting the DM relic density by regimes Ia, Ib and, in particular, sequential freeze-in. Similar conclusions can be reached for the case of Fig. 4.7. Interestingly, the reach of planned beam dump experiments such as SHiP would probe, for $m_{\gamma'} = 1$ GeV, ϵ between 10^{-8} and 10^{-6} [137], which would therefore test the mediator required for a $m_{\text{DM}} = 3$ GeV candidate to be in its Ib regime. Since, as will be seen in the next section, DM searches are not expected to be able to test DM in its Ib (and II) regime, such mediator searches might be the only way of testing the Ib or II regime of dark matter, at least in the kinetic mixing picture.

5.2 Constraining kinetic mixing portal DM

The existence of mini-charged fermions (in the strict sense) is *a priori* not forbidden by theoretical arguments. Such particles can be produced in a variety of manners from SM processes and can be constrained by observations. However, one must not be too careless when considering bounds on such new particles from the literature since they might depend on the assumptions made on the origin of the small electric charge carried by the fermion, *i.e.* be model-dependent. Collider, beam dumps and astrophysical constraints are mostly model independent and are sketched in [138]. Cosmological constraints can however be strongly model-dependent. This can be easily seen in Fig. 3.8: if the mini-charge is provided by a kinematically mixed dark photon, its interactions with the DM, proportional to α' , can change drastically the DM relic abundance as compared to a fermion directly charged under $U(1)_{\text{em}}$. One concrete example of a cosmological model-dependent bound comes from N_{eff} [139]. Indeed, if the dark sector can thermalize with itself (which necessarily need 2 different species, *i.e.* a mini-charged fermion and a massless dark photon) and enter a dark freeze-out regime (*i.e.* regime IVb), the millicharged particle relic abundance will necessarily be inversely proportional to α'^2 ⁷. It is therefore stressed that the focus of the following discussion will be on the DM scenario and assume, as before, that the dark photon (potentially massive) mixes with the photon.

Due to the broad range of the parameter space provided by the model, we expect a wide variety of constraints, that will complement each others when exploring the feeble to weakly coupled and light to heavy DM corners. In their work [140], Dunsky *et al.* assumed that DM is a mini-charged particle, thus interacting with the SM only through the massless photon, and explored at length its impact on cosmology and astrophysics, but without taking into account the production of DM. Given the model of Eq. (2.1) in its massless dark photon limit and the corresponding parameter space seen in Fig. 3.8, this concrete particle physics realisation of CHAMP DM would have most of

⁷A corollary is that taking $\alpha' = \alpha_{\text{em}}$ does not reduce models containing a kinematically mixed massless dark photon to a mini-charge one. This limit simply reduces the dark sector to a literal dark QED.

its production mechanism tested or constrained by observations. In the following, we will summarize how the candidates under scrutiny in this work can be constrained, the dependence of those constraints on the dark photon mass and recast more carefully the direct detection constraints on spin-independent DM-nucleon interactions, which will turn out to be the strongest constraints on the freeze-in parameter space.

5.2.1 Astrophysical and cosmological constraints of CHAMP DM

In the scenario where the dark photon is massless, DM interacts with ordinary matter by exchange of a massless photon and self-interacts by exchange of the massless dark photon. Such long range forces may impact drastically the dynamics of the Bullet Cluster or modify galaxy dynamics [64, 62]. Of particular importance for the following Section is the fact that the magnetic fields of our Galaxy could reduce the number density of DM near Earth [141]. More generally, this can happen in galaxies [141, 142, 143] or clusters [144]. A large component of DM particles in the disk could be accelerated due to supernovae shock, which could in turn impact the direct detection limits [140]. Recently, these bounds have been reassessed [145, 146]. If CHAMP DM is produced thermally in the Universe, it can very efficiently reach equilibrium with the baryons around the era of recombination, which would be in tension with the observation of the CMB fluctuations [147, 148]. However, if the dark photon is massive, SM–DM and DM–DM interactions now proceed by exchange of γ' , which can drastically reduce the impact on the DM halos of the magnetic fields and the supernovae shock. In [71] it was argued that giving an $\mathcal{O}(\text{MeV})$ mass to the dark photon should relax all these potential shortcomings of CHAMP DM. It might be interesting to systematically study the impact of the dark photon mass on those bounds.

5.3 A particular look at direct detection constraints

The sensitivity of current dark matter direct detection experiments is such that they are able to probe very feeble DM-nucleon interactions. As of today, the most constraining bounds on DM–nucleon spin-independent scattering cross section has been set by the XENON1T collaboration with the data released in 2018 [149]. The data comprises of a 1 tonne \times year exposure and disfavors, for example, a 30 GeV DM particle scattering with a nucleon for a value of the (spin independent) cross section bigger than $\sigma_{\text{SI}} \approx 7 \times 10^{-47} \text{cm}^2$. This figure is indeed impressive, since it would correspond to an interaction rate that is only 2 order of magnitude more important than what is expected for neutrinos produced in the Sun. For a 1 GeV mediator, this would require the DM–nucleon coupling to be smaller than $\mathcal{O}(10^{-11})$. The reach of current direct detection limits will prove to be actually sensitive enough to test the freeze-in regime of kinetic mixing portal DM with a light dark photon.

5.3.1 With a light mediator

As explored at length previously, there exist fermionic DM candidates whose interactions with the SM electrically charged fermions are mediated through a light(er) vector particle, namely the photon or the dark photon. If very feeble, this interaction can be responsible for the production of all the dark matter along, for example, the freeze-in phase of the model. This connection will in turn also give rise to interactions between the DM and a given nucleus N. In particular, the t -channel propagator of the light mediator γ' in the DM–N scattering amplitude is

$$\frac{1}{t - m_{\gamma'}^2} = \frac{-1}{2m_N E_R + m_{\gamma'}^2} \quad (5.1)$$

where m_N is the nucleus mass (for our purpose, we will take N to be $^{132}_{54}\text{Xe}$). In the center of mass frame, E_R is the recoil energy of the nucleus N . In nuclear-recoil direct detection detectors, given their sensitivity, we have typically that $E_R \gtrsim \mathcal{O}(1)$ keV. Therefore, if the mediator mass is small enough

$$m_{\gamma'} < \sqrt{2m_N E_R} \sim \mathcal{O}(40\text{MeV}) \quad (5.2)$$

the interaction is effectively long-ranged and the DM–N scattering differential cross section will be proportional to $1/E_R^2$, giving thus a large enhancement at small recoils. Therefore, with light mediators, there exists the possibility of counterbalancing at low recoils the feeble coupling required for producing freeze-in DM in order to make a discovery at direct detection experiments.

However, due to the change in the distribution of events as a function of the recoil because of the long-range interaction (*i.e.* as compared to the distribution for a contact interaction), the results of XENON1T – and other direct detection experiments – cannot be directly applied to models that interact through a light mediator.

Nonetheless, it is possible to recast the experimental constraints obtained under the assumption of an E_R independent scattering cross section into constraints that are valid for a light mediator exchange. For this purpose, we will use the differential rate of scatterings (*i.e.* the number of scattering events per second per unit of recoil energy) as a proxy. Its definition is

$$\frac{dR_\chi}{dE_R} = N_T n_\chi \int \frac{d\sigma_\chi}{dE_R} v f_\oplus(\vec{v}) d^3v \quad (5.3)$$

where N_T is the number of target nuclei and $d\sigma_\chi/dE_R$ is the DM–N differential cross section for a given recoil energy E_R . We take n_χ , the DM local number density, and $f_\oplus(\vec{v})$, the DM velocity distribution in the Earth frame, to be the common values taken from the Standard Halo Model [150], meaning $m_\chi n_\chi = \rho_\chi = 0.3$ GeV/cm³ and a Maxwellian velocity distribution with r.m.s velocity $\sigma_v = 270$ km/s in the Galactic reference frame. We then integrate over all DM particle velocities that can give rise to an event with recoil E_R , *i.e.* $v \geq v_{\min} = \sqrt{m_N E_R / 2\mu_{\chi N}^2}$ where we have introduced the DM–N reduced mass $\mu_{\chi N}$. We then parametrize the differential scattering cross section on a nucleus by

$$\frac{d\sigma_\chi}{dE_R} = \frac{m_N}{2\mu_{\chi p}^2} \frac{1}{v^2} \sigma_{\chi p}(E_R) Z^2 F^2(q r_A) \quad (5.4)$$

where $\mu_{\chi p}$ is the DM–proton reduced mass and Z the nucleus atomic number. The form factor of the nucleus $F(q r_A)$ [151, 152] takes into account finite size and substructure effects that arise at high momentum transfer. Implicitly, we have assumed that the DM only interacts with protons coherently⁸. The DM–proton scattering cross sections mediated by a dark photon of mass $m_{\gamma'}$ is

$$\sigma_{\chi p}(E_R) = \frac{16\pi\mu_{\chi p}^2 \alpha^2 \kappa^2}{\left(2m_N E_R + m_{\gamma'}^2\right)^2} \quad (5.5)$$

where α is the QED fine structure constant. Note that in the $\epsilon - \delta$ model, the expression of the scattering cross section would be more complicated due to the exchange of both the massless photon and massive dark photon.

⁸In the case of a spin-independent interaction with no isospin violation between the DM and the nucleons, one instead has $\sigma_{\chi p} \equiv \sigma_{\chi n} = \sigma_{\text{DM},n}$ and would then replace Z by the mass number A .

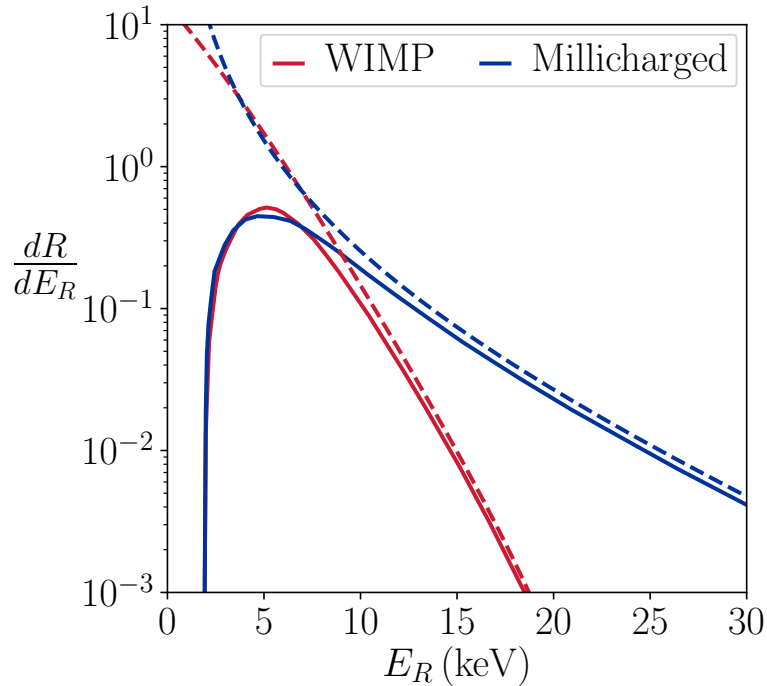


Figure 5.2: Red solid: differential rate for a WIMP candidate on the XENON1T exclusion limit with $(m_{\text{DM}}, \sigma_{\text{DM},n}) = (15 \text{ GeV}, 10^{-46} \text{ cm}^2)$. Blue solid: best fit for a millicharged DM candidate interacting with a light mediator with $(m_\chi, \kappa) = (70 \text{ GeV}, 3.1 \times 10^{-11})$. The error between those two curves is $\Delta_{\text{DR}} \approx 25\%$. For the dashed lines, the XENON1T detector efficiency has been neglected.

The shape of the differential rates of events for light and massive mediator are different for DM candidates of the *same* mass, but nevertheless can be similar for *distinct* DM masses (within a given range). In addition, because of the detection efficiency cutting low recoil events and nuclear form factor, velocity distribution, suppressing events with high recoil (regardless of type of interactions), only a small range of possible recoil ($\sim 1 - 70 \text{ keV}$) has to be taken into account for each candidate⁹. Using these facts, our recast procedure is as follows.

Given a DM candidate mass m_{DM} and the upper bound on its scattering cross section with a nucleon, $\sigma_{\text{DM},n}$, taken from the XENON1T limits, we compute the following differential rate as a proxy for the signal in the detector,

$$\left(\frac{dR_{\chi,\text{DM}}}{dE_R}\right)_{\text{exp}} = \epsilon(E_R) \frac{dR_{\chi,\text{DM}}}{dE_R}, \quad (5.6)$$

where $\epsilon(E_R)$ is detector efficiency from Fig. 1 in [149]. dR_{DM}/dE_R is computed using Eqs. (5.3) and (5.4) with the substitution $\sigma_{\chi p}(E_R) \rightarrow \sigma_{\text{DM},n}$ and $Z \rightarrow A$. We then determine the couple (m_χ, κ) that has a similar observable differential rate $(dR_\chi/dE_R)_{\text{exp}}$ with respect to the $(m_{\text{DM}}, \sigma_{\text{DM},n})$ couple. In practice, we choose the (m_χ, κ) couple that minimizes the quadratic error between the

⁹The maximum momentum exchanged in a DM–Xenon nucleus head-on collision is $q_{\text{max}} = 2m_N v = 250 \text{ MeV}$ which in turn gives a recoil energy $E_R^{\text{max}} = q_{\text{max}}^2/2m_N = 250 \text{ keV}$. For a Xenon atom, the form factor suppresses the interaction rate for exchanged momentum above 10 MeV and at q_{max} is $\sim 10^{-4}$.

differential rates

$$\Delta_{\text{DR}}^2 = \frac{1}{R_{\text{DM,exp}}^2} \int dE \epsilon(E)^2 \left(\left(\frac{dR_{\text{DM}}}{dE} \right) - \left(\frac{dR_{\chi}}{dE} \right) \right)^2 \quad (5.7)$$

where $R_{\text{DM,exp}}$ is the total measurable rate from (5.6) for the ‘‘DM’’ candidate, dR_{DM}/dE_R its differential rate assuming an E_R independent scattering and dR_{χ}/dE_R is the one corresponding to a χ interacting through a light mediator.

Our procedure is shown in Fig. 5.2 for one candidate. The dashed red curve gives the differential rate for a heavy mediator interaction with constant cross section ($\sigma_{\text{DM},n} = 10^{-46} \text{ cm}^2$) and candidate mass ($m_{\text{DM}} = 15 \text{ GeV}$) taken from the XENON1T limits. The dashed blue line represents instead the differential rate for a light mediator interaction with E_R dependent cross section (5.5). This millicharged candidate minimizes the error Δ_{DR} and corresponds to the couple $(m_{\chi}, \kappa) = (70 \text{ GeV}, 3.1 \times 10^{-11})$. In solid, we show the observable differential rates, taking into account efficiency. In this illustration, $\Delta_{\text{DR}} \approx 25\%$ and over the full range of DM masses treated here, Δ_{DR} is always smaller than 30%. In turn, the 2 candidates (70 GeV χ particle and 15 GeV XENON1T DM) share the same total number of events

$$\Delta_{\text{TR}} = \frac{N_{70}^{\chi} - N_{15}^{\text{DM}}}{N_{15}^{\text{DM}}} \approx 20\% \quad (5.8)$$

for which N_{70}^{χ} is the total number of observable events for the couple $(m_{\chi}, \kappa) = (70 \text{ GeV}, 3.1 \times 10^{-11})$ and N_{15}^{DM} the one for the candidate on the Xenon1T bound. In Table 5.1 are shown the errors on the differential and total rates of four distinct χ masses and the corresponding DM candidates. It is important to note that Δ_{TR} , the error on the total rate of event, is positive, *i.e.* the χ particle produces more event in the detector than the associated DM WIMP. It should therefore be possible, through a more refined analysis, to lower the total number of events of the χ , thus constraining κ to be smaller. Therefore, the recasted constraints obtained through our procedure is conservative.

The discussion on the recast procedure will now be closed after a short comment on the signature of DM in direct detection. It is now abundantly clear that if DM is discovered through direct detection, say just below the current constraints, arguably not much information on its nature can be obtained. Indeed, since what is observed is the number of events as a function of, in this case, nuclear recoil energy (*i.e.* dR/dE_R) and that the rate of a WIMP candidate with a mass of few tens of GeV is very similar to that of a DM particle with long range interactions of several hundreds of GeV, a precise measure of DM mass is not possible through direct detection alone, at least until the sensitivity to discriminate between the two distinct high recoil tails provided by both type of interactions is reached. Nonetheless, if detection happens through an excess of nuclear recoils, one could conclude that the DM is ‘‘heavy’’, *i.e.* with a mass at least above the GeV, since the detection sensitivity degrades very quickly for lower masses.

5.3.2 Freeze-in *vs* direct detection

Proceeding as above along the XENON1T bounds, one can build the corresponding limits on the millicharge κ in the light mediator regime, see the solid black line in Fig. 5.3. We also show on the same graph the κ_{Ia} values for which the DM abundance is reproduced by freeze-in in the kinetic mixing portal (green line). Above this line, the DM relic abundance can be accounted for in the re-annihilation regime (IIIb), and below DM is under-abundant (neglecting regime Ib and II, see further). Although not shown, for millicharge $\kappa \gtrsim 10^{-5}$, those bounds disappear due to screening effects from the overburden material above the sensitive volume [153, 140].

m_χ (GeV)	κ (10^{-11})	m_{DM} (GeV)	$\sigma_{DM,n}$ (cm^2)	Δ_{DR}	Δ_{TR}
15	3.0	10	5.6×10^{-46}	16%	15%
70	3.1	15	1.1×10^{-46}	23%	22%
200	5.2	20	5.9×10^{-47}	22%	13%
500	8.2	22	5.3×10^{-47}	26%	3%

Table 5.1: Upper bound on the millicharge κ (second column) for four χ masses (first column) obtained after recasting the corresponding WIMP XENON1T exclusion limits (third and fourth column). The differential rate and total rate error is given in the last two column. The constraints on millicharged DM solely comes from the lighter masses constrained by XENON1T, for which sensitivity is very good.

In Fig. 5.3, it is seen that XENON1T is currently testing the freeze-in parameter space of the well motivated kinetic mixing portal DM scenario, excluding candidates with millicharge $\kappa_{Ia} = 3 \times 10^{-11}$ in the range $m_Z/2 < m_{DM} < 100$ GeV. We also show the recasted limits, using the procedure outlined above, of the 2017 PANDAXII results [154]. Finally, we give the expected limits for XENON1T after 4 years of data taking and for LZ [155] (1000 days of exposure). In the near future, XENON1T should therefore probe the freeze-in phase of this scenario for the range of masses of 45 GeV up to ~ 400 GeV, and LZ could potentially probe a wider range of $m_{DM} \sim 15$ GeV to ~ 4 TeV, testing freeze-in from the decay of Z bosons. Below we comment on the validity of these bounds.

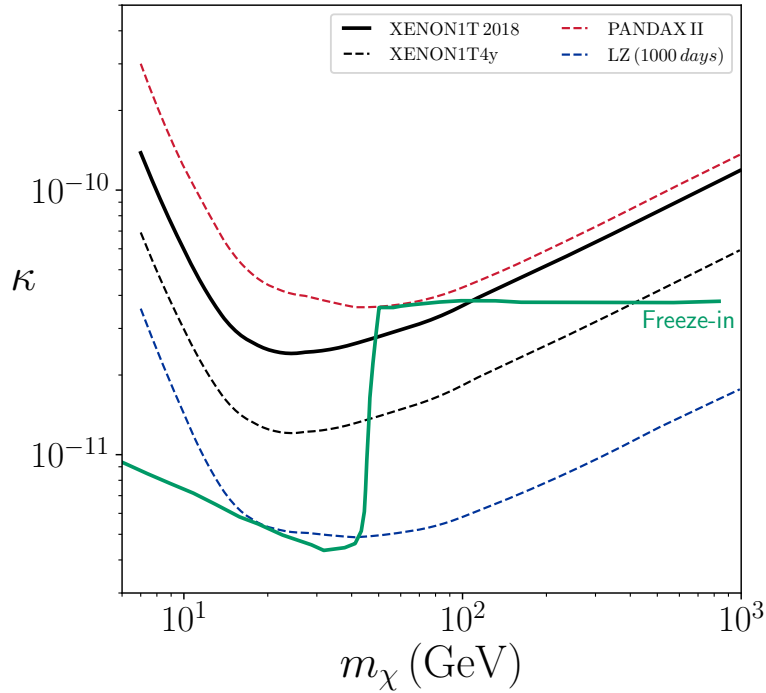


Figure 5.3: In the millicharge–DM mass plane, for candidates interacting through a light dark photon ($m_{\gamma'} \ll 40$ MeV), the exclusion limits from various current and future direct detection experiments are given, following the recast procedure outlined in the text. Black : XENON1T. Black dashed : Expected sensitivity of XENON1T after 4 years of exposure. Red dashed : PandaX II. Blue dashed : LZ for 1000 days forecast. The solid green line corresponds to the millicharge κ_{Ia} required by the freeze-in mechanism.

When compared to what has been reported in [140], the constraints of Fig. 5.3 are overall stronger (for a 30 GeV candidate, the bounds derived above using our recasting constrain the DM millicharge to be smaller by a factor 5 and, for heavier masses, by at least a factor 2). Notice that a more refined long range interaction recast that takes into account the acceptance of the detector and cuts has since been implemented in micrOMEGAs [156]. For the Xenon1T limits, the derived constraints are 20% stronger for dark matter masses above 10 GeV when compared to our results. Nevertheless, a dedicated light mediator analysis by direct detection collaboration is required to derive the most realistic bounds. In the following Figure, we show both the bounds derived above and the bounds obtained by the PandaX-II light mediator analysis with the 2018 and 2021 data [157, 158].

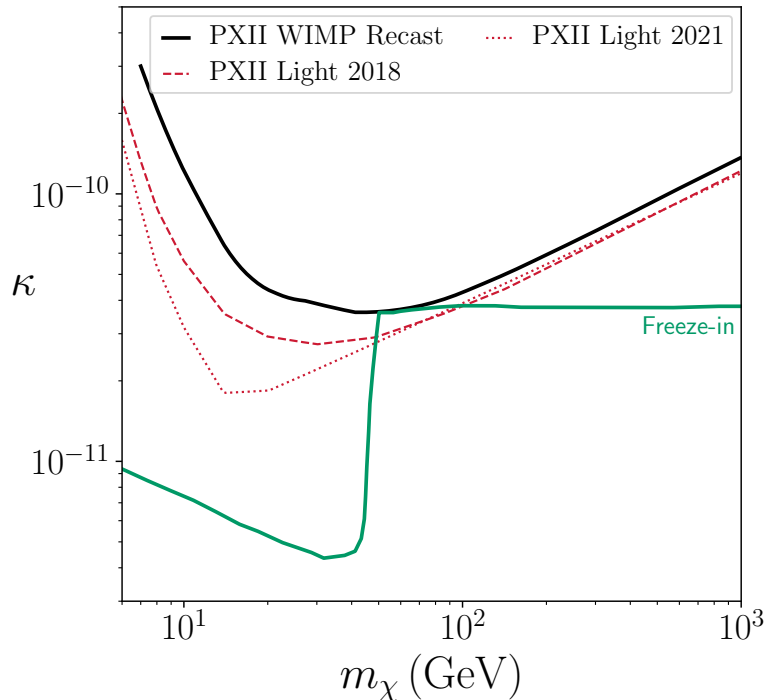


Figure 5.4: Comparison between the light mediator recast of the WIMP exclusion limit of PandaX-II of 2017 [154] (solid black) with the dedicated 2018 light mediator analysis of PandaX-II [157] (dashed red). In red dotted is given for completeness the 2021 light mediator analysis of PandaX-II [158]. This displays that the recast procedure gives quantitatively good and conservative exclusion limits.

It is seen that while the error introduced by our procedure grows for low mass candidates, it never exceeds 60% and is conservative over the whole range of DM mass. We therefore conclude that the discrepancy between the dedicated analysis by the PandaX-II experimental collaboration and our recast of their heavy mediator limits is small. Similarly, it is expected that the same will apply for the other detectors treated in Fig. 5.3. Finally, the dedicated 2021 analysis of PandaX-II constrains low mass candidates down to $\kappa = 2 \times 10^{-12}$, indicating that, in the future, dedicated light mediator limits could probe much of the range of millicharged DM produced from Z -decay.

Since the procedure outlined above has been confronted to several cross-checks, it therefore can be interesting to apply it to examples that explore avenues that are not analysed by the experimental collaborations. Of particular interest will be the consideration of the dependence of the limits on the mass of the mediator¹⁰, which could be neither light nor heavy, $m_{\gamma'} \gtrsim \sqrt{2m_N E_R} \sim 40$ MeV. For a MeV-range dark photon, the bounds on κ will not change, as the interaction is still long ranged. However, taking $m_{\gamma'} \gtrsim 40$ MeV will reduce the enhancement of forward scatterings, meaning that the bounds become less constraining. In turn, the weakened bound will mark the impossibility to test the freeze-in of these models at direct detection experiments¹¹. Nevertheless, the bounds when $m_{\gamma'} \gtrsim 40$ MeV should be close to what could be derived by the experimental collaboration and could test other DM production mechanisms lying at higher millicharge.

The scattering off electrons of sub-GeV dark matter can also lead to strong constraint when the mediator is very light ($m_{\text{med.}} \sim \sqrt{2m_e E_R} \sim 1$ keV for a typical 1 eV recoil threshold). In the coming years, the feebly coupled production phase of such scenario could be tested by current direct detection [160] or future detectors using new technologies [161]. Current DM–electron scatterings exclusion limits, including overburden effects have been derived for very light dark photon mediated interactions [162].

As illustrated here with millicharged DM produced by freeze-in from SM annihilations, direct detection experiments have started to probe new, feebly coupled DM production phases. It is however not possible to probe its freeze-in from mediator (Ib) nor sequential freeze-in (II) phase. Indeed, models with $\kappa_{\text{II}}, \kappa_{\text{Ib}} \ll \kappa_{\text{Ia}}$ have mediator masses that are within one order of magnitude of the DM candidate, due to thermal corrections. The heaviest candidate that would benefit from a collinear enhancement and be set by regime II and Ib will therefore have $m_\chi \sim 0.4$ GeV, for which current direct detection experiment do not have the reach to test the Ia regime. However, the regime Ib of a $U(1)_{B-L}$ model can be constrained by direct detection and beam dump experiments [163]. DM models in which a light scalar mediator couples to quarks possess enormous scattering rates with the SM and can have their regime II constrained [90]. Interestingly, for a vector dark matter candidate whose mass arise from symmetry breaking due to a light dark scalar which then mixes with the Higgs, its freeze-in parameter space will be inevitably tested for very heavy mass, since the DM coupling with the mediator will be proportional to the DM mass [164]. Finally, the bounds of Fig. 5.3 can be interpreted outside a specific production mechanism. If millicharged particles, perhaps being fully asymmetric DM candidates or representing only a fraction f of the dark matter abundance, have been produced in the early Universe, the bounds above will apply (up to a factor f).

¹⁰It could be also interesting to treat models that go beyond a vector coupling with a light boson (dipole interactions [159], interferences in the $\epsilon - \delta$ model) or assess the impact of uncertainties in the Standard Halo Model (velocity distribution that is not Maxwellian).

¹¹The freeze-in parameter space depends very lightly on the mass of the dark photon if $m_{\gamma'} \lesssim m_{\text{DM}}$.

5.3.3 Probing self-interacting dark matter

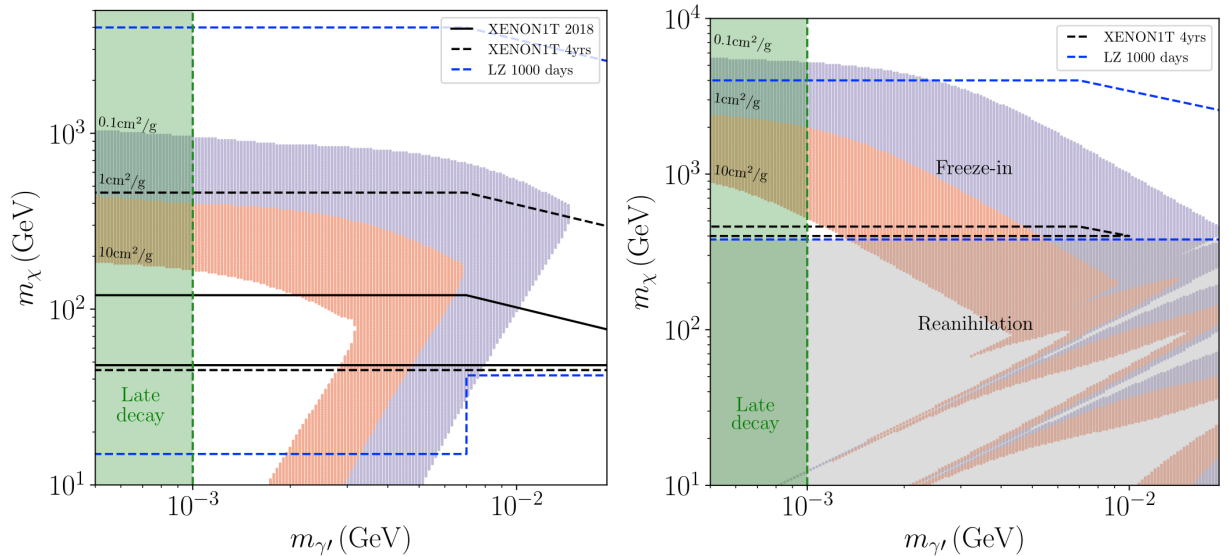


Figure 5.5: Left : For $\alpha' = 5 \times 10^{-5}$, couples of $\chi - \gamma'$ masses for which DM candidates have self-interactions that can alleviate the small-scale structure issues. Only the attractive channel is shown, the repulsive one being qualitatively similar. Red : $1 \text{ cm}^2/\text{g} \leq \sigma_T/m_\chi \leq 10 \text{ cm}^2/\text{g}$. Blue : $0.1 \text{ cm}^2/\text{g} \leq \sigma_T/m_\chi \leq 1 \text{ cm}^2/\text{g}$. Enclosed by the solid black, dashed black and dashed blue lines are the candidates that are (will be) tested by XENON1T currently, with 4 years of exposure or by the future LZ. For each DM masses, κ is chosen such that the observed relic abundance is set by the freeze-in regime Ia and is largely independent of the mediator mass. Right : same but with $\alpha' = 10^{-3}$. For light DM masses, self-interactions in the early Universe thermalize the dark sector and the DM abundance is not set by freeze-in but by the re-annihilation mechanism IIIb.

As it is necessarily light, $m_{\gamma'} \sim 1 - 40 \text{ MeV}$, the dark photon mediator might induce large enough DM self-interactions in order to reduce (possibly solve) the small scales problems of collisionless DM, such as core/cusp [46]. See the review [165] for more details. Those problems are thought to be solved if the DM–DM scattering transfer cross section σ_T is within $0.1 \text{ cm}^2/\text{g} < \sigma_T/m_\chi < 10 \text{ cm}^2/\text{g}$.

In Fig. 5.5 are shown the self-interacting DM–mediator mass couples for $\alpha' = 5 \times 10^{-5}$ in the attractive channel¹² (left) and where the velocity of DM particles has been set to the typical velocity in dwarf spheroidal galaxies, *i.e.* $v \sim 10 \text{ km/s}$. The red and blue candidates therefore should solve the core/cusp problem in dwarf galaxies [165]. The green region $m_{\gamma'} < 1 \text{ MeV}$ labelled “late decay” is constrained by intergalactic diffuse photon background [93]. Interestingly, given this α' , for all the masses we consider in this Figure, the DM candidates can be set by Ia freeze-in. Within the black solid line are feeble interacting DM candidates that are currently constrained by XENON1T. The black and blue dashed lines are prospects of XENON1T limits with 4 years of exposure and LZ for 1000 days, respectively. From this Figure, it is concluded that many freeze-in candidates can be strongly self-interacting and be within the reach of direct detection experiments.

On the right of Fig. 5.5 is instead shown the case of $\alpha' = 10^{-3}$. For low DM mass, self-interactions in the early Universe are sufficient for the dark sector to thermalize and such candidates

¹²The repulsive channel would be similar and is not shown here, see [4]

are set by reannihilation (IIb). It is clear that $\kappa_{\text{IIIb}} > \kappa_{\text{Ia}}$ and the current XENON1T bounds are therefore only probing self-interacting DM candidates in their reannihilation regime. With more exposure, XENON1T should start testing the Ia regime of those candidates after 4 years of exposure, and such is also the case of LZ. It is interesting that the PANDAX-II collaboration has also performed a similar study of self-interacting DM candidates that are tested by their experimental apparatus [157, 158], albeit with no focus on any particular production mechanism.

However, there is the additional complication that the mediator mass and α' required for having self-interacting freeze-in candidates probed by direct detection experiments might be in tension with existing constraints on dark photons. Freeze-in DM candidates with masses above $m_Z/2$ have millicharge $\kappa_{\text{Ia}} = 4 \times 10^{-12}$ and therefore have $\epsilon\sqrt{\alpha'} = 3 \times 10^{-13}$. For the dark fine structure constant chosen above, the kinetic mixing spans $1 - 5 \times 10^{-11}$ while the dark photon mass is cornered between 1 – 10 MeV in order to avoid late decays and not suppress too much self-interactions. This range of parameter has actually been recently excluded [109, 110]. Nonetheless, since this range of parameter sits close to the exclusion limits, it is possible to slightly reduced the effective γ' –SM coupling by choosing δ to be close to ϵ , perhaps at percent level. In that case, the mass region between 1 and 10 MeV becomes open and therefore the $\epsilon - \delta$ model provides self-interacting DM candidates that are within reach of current direct detection experiment. It is expected that the additional exchange of a photon with strength $e'\delta \approx e'\epsilon \ll e'$ in the self-interaction cross sections will have small effects and will thus not change Fig. 5.5 much.

5.4 Can dark stars shine bright?

The dark photon portal DM candidates treated in details above are almost prototypical of a “dark” QED sector. Even though it has been studied in a fully symmetric scenario (*i.e.* the relic abundance of DM is composed of particles and anti-particles) and even though it (self-)interacts with a massive dark photon, this setup can easily be modified to closely resemble a mirror version of QED. Owing to a gauged $U(1)'$, any asymmetry generated at early time in the dark sector will be conserved, thanks to charge conservation, even if the symmetry is broken by a Stückelberg mass or spontaneously. If, as in the SM, DM then undergoes an annihilation catastrophe, the asymmetric component could compose all of the DM. Finally, if DM possesses a kinetic mixing ϵ and a mass mixing δ (such couplings could be, for example, responsible for keeping DM in chemical equilibrium with the SM and annihilating away the entirety of the symmetric components), it will (self-)interact through an exchange of a massless photon, on top of the massive dark photon. In this realisation, the relic dark sector will be composed of dissipative asymmetric matter, hence there exists the possibility for overdensities to collapse and form compact dark stars [166, 167].

Unexpectedly, dark stars formed of millicharged DM could be bright enough for detection, through Bremsstrahlung emissions of photons thanks to $\gamma' - \gamma$ mixing [168]. Even though the flux of photons from the dark stars would be suppressed by some small mixing angle θ , the entire volume of the star (up to attenuation through reabsorption by the medium) contributes to the flux, not only the area, which would be the case for, say, a neutron star. In addition, due to gravitational redshift, the photon flux would not be thermal.

In such a medium, the dominant coupling of DM to photons is for transverse emission and proportional to δ since it is expected that DM is non-relativistic, the temperature of the dark star being low, $T \ll m_{\text{DM}}$, and the Fermi momentum being small [167], $k_F \ll m_{\text{DM}}$, see Table 4.1. The Bremsstrahlung emission of soft photon is thus proportional to δ and not ϵ , hence this could be an interesting signature of the model of Eq. (2.6) with two sources of mixing.

There also exists the possibility for dark stars to shine when $\delta = 0$, which, following the discussion of Section 4.2, requires that the photon acquires a mass. In a degenerate medium, photons acquire a density dependent mass akin to the thermal mass, $m_\gamma = g\mu/\sqrt{2\pi}$ (μ is the chemical potential, the particles of the medium are assumed to be relativistic and couple to the photon with strength g). The degenerate DM medium forming the dark star would therefore make the DM–massive photon coupling non-zero. In that case, photon emission could be possible but nevertheless with a signal suppressed by a factor of ϵ in the amplitude and by the kinematics due to the non zero photon mass.

5.4.1 Spontaneous symmetry breaking at high density

As the medium-induced mass depends solely on the photon coupling to the medium and the number density of its constituent, m_γ is completely determined and leaves very little handle in order to reduce the suppression factor $m_\gamma/m_{\gamma'}$, which could be substantial. In the following, we will propose a model which includes a spontaneous symmetry breaking of $U(1)_{\text{em}}$ at high DM chemical potential. In particular, the photon mass can be arbitrarily high, which could be of interest for making a dark star shine bright, among, perhaps, other possible phenomenological applications. The model comprises of a DM candidate ψ , taken to be a Dirac fermion, which possesses a Yukawa coupling to a scalar singlet ϕ . In turn, ϕ couples with a complex scalar σ , charged under electromagnetism. At finite density, the scalar density operator $\langle\bar{\psi}\psi\rangle$ becomes non-zero, tilts the potential of ϕ , inducing a non-zero vev v_ϕ . It is then possible for ϕ to drive σ to a $U(1)_{\text{em}}$ breaking minima, therefore making the photon massive in regions of high DM chemical potential. The scalar potential of the model is the following

$$V(\phi, \sigma) = \lambda_{\sigma_4} (\sigma^\dagger \sigma)^2 + m_\sigma^2 (\sigma^\dagger \sigma) + \lambda_{3_{\sigma-\phi}} \phi (\sigma^\dagger \sigma) + g\phi \langle\bar{\psi}\psi\rangle + \frac{1}{2} m_\phi^2 \phi^2 \quad (5.9)$$

and all other terms are taken to be 0. The quartic coupling λ_{σ_4} and the mass m_ϕ^2 are chosen positive to ensure the stability of the potential at high fields value. Assuming that both scalars get a vev, the non-trivial extremas of the potential lie at

$$v_\phi = -\frac{m_\sigma^2 + 2\lambda_{\sigma_4} v_\sigma}{\lambda_{3_{\sigma-\phi}}} \quad (5.10)$$

$$v_\sigma = \left(\frac{m_\phi^2 m_\sigma^2}{\lambda_{3_{\sigma-\phi}}} - g \langle\bar{\psi}\psi\rangle \right) / \left(\lambda_{3_{\sigma-\phi}} - 2 \frac{\lambda_{\sigma_4}}{\lambda_{3_{\sigma-\phi}}} m_\phi^2 \right) \quad (5.11)$$

where we denoted $\langle\sigma^\dagger\sigma\rangle = v_\sigma$, $\langle\phi\rangle = v_\phi$. Let us now choose the sign and magnitude of the parameters as follows

$$g > 0, \frac{m_\sigma^2}{\lambda_{3_{\sigma-\phi}}} > 0, \lambda_{3_{\sigma-\phi}} < 2 \frac{\lambda_{\sigma_4}}{\lambda_{3_{\sigma-\phi}}} m_\phi^2 \quad (5.12)$$

Below a critical value of the density, the expressions of v_σ from Eq. (5.11) would be negative, which is not possible, and the symmetry is instead restored. On the contrary, above the critical scalar density $\langle\bar{\psi}\psi\rangle_c = m_\phi^2 m_\sigma^2 / (g \lambda_{3_{\sigma-\phi}})$, v_σ is positive and electromagnetism is broken at high density. The theory possesses enough free parameters for $\langle\bar{\psi}\psi\rangle_c$ and the mass of the photon $m_\gamma = e_\sigma^2 v_\sigma$, where e_σ is the electric charge of the scalar σ , to be both chosen arbitrarily. For a concrete illustration, if one assumes all couplings to be positive, at finite density ϕ is set at some negative value $v_\phi < 0$ in field space, necessarily a minimum. If the minimum is far enough from 0, the dominant quadratic term of the σ potential is $-\lambda_{3_{\sigma-\phi}} |v_\phi| \sigma^\dagger \sigma$ and the charged scalar subsequently develops

a mexican hat potential, indeed breaking electromagnetism.

Scenarios where the photon acquire a mass in order to make asymmetric dark star bright are nonetheless less attractive, due to the suppression by the kinematics and the loss of collinear enhancement, which will make detection more challenging. Obviously, a full phenomenological study of the model would need to be pursued before using its particularities in making a dark star shine but such study is outside the scope of this thesis. This is tentative but illustrates the difficulties one has to meet for a dark star to emit photons, at least if only a kinetic mixing ϵ is present in the theory.

Part II

A spin zero portal

Chapter 6

Self-interacting asymmetric dark matter

In this second part of the thesis, we will treat a portal model similar to the kinetic mixing portal. We will consider a simple Yukawa theory where the dark matter is a fermionic singlet. In this Chapter, we aim at first motivating and describing the asymmetric dark matter scenario. In Section 6.2, we will take the first steps towards the study of collective phenomena by studying finite density in-medium effects that can arise if asymmetric DM reaches degeneracy by using well known scenarios, as an invitation for further investigation. Namely, those effects will be that of the appearance of a scalar condensate $\langle\bar{\psi}\psi\rangle$ (ψ being the dark matter) and the appearance of superfluidity, *i.e.* a non zero density of Cooper pairs $\langle\psi\psi\rangle$. Motivated by the seemingly interesting results that density effects can be important and even dominant in a very simple model like the Yukawa theory, we will argue that much work has to be done in order to treat the asymmetric DM system. We will refine and extend the computation of the superfluidity on many fronts and the results will be presented in the next Chapter. In the next to next Chapter, we will use those results for some applications that concern DM halos

6.1 Context and motivation

Today, the majority of DM is in the form of halos, which were the seeds for the large scale distribution of visible matter and which host galaxies in their center. Gravitational evidences, such as rotation curves, do not provide any direct evidence of the nature of DM, but might give some hints on its collisionful or collisionless character. The WIMP scenario, motivated by its discovery potential and its natural way of achieving the observed relic abundance by freeze-out, received much attention throughout the years. However, in the same way that self-interactions were motivated by the diversity problem, other shortcomings of the SM can motivate the study of new type of DM scenario, whose phenomenology could be very far from what is typically expected of a WIMP. One such example is the puzzle of the matter–antimatter asymmetry. In order for this problem to be solved in a satisfying manner, beyond the SM physics is needed. The dark sector could share the asymmetry of the visible sector if it is a mirror copy of the Standard Model [169]. Another possibility is that the baryon asymmetry is shared between the visible and hidden sectors so that, overall, there is no baryon asymmetry. Necessarily, the lightest particle carrying a baryon number in the hidden sector would be stable and it thus provides an excellent DM candidate. Since the density parameter of DM is about a factor 5 bigger than the one of the visible sector (which is mainly composed of protons and neutrons), this would require an asymmetric DM particle of about 5 GeV, see [170] for an explicit scenario or [171] for a more recent one. More generally, since the visible sector is asymmetric, the hidden sector need not to be symmetric and the two origins of asymmetry might not be related. From a phenomenological perspective, the asymmetric DM

scenario is attractive [172] on many fronts with, for example, its different signatures in experiments when compared to WIMPs. In this part of the thesis, we will therefore focus our attention on a spin 1/2 asymmetric candidate.

This assumption on the nature of DM has many consequences. In DM halos, if a fermionic asymmetric DM candidate is very light, its number density can be high enough for Pauli blocking effects to become important. This effect is generic for typical DM profiles [173]. The inner part of the halo is degenerate and the degeneracy pressure can support a core for the DM halo [174] (see Section. 8.2.1 for details). Moving to smaller scales, exotic DM effects can also be different between the symmetric and asymmetric cases. Interestingly, planets, stars and other compact astrophysical objects such as white dwarfs and neutron stars (**NS**) can host a huge amount of DM particles, as has been realized for a long time [175, 176, 177, 178]. When DM interacts with, say, the constituents of a neutron star, and loses some energy due to scattering, the DM particle will become gravitationally bound to the star. As the DM passes again and again through the star, if DM scatters enough on the star material, the DM can sink to the center of the star and thermalize with the NS core. If DM is light, the thermal motion of the NS constituents can give energy to the DM and unbound it from the star’s gravitational field, which is called the evaporation process [179, 180]. If DM is symmetric, annihilations of DM deplete the number of DM particles accumulated in the center of the star, hence a steady state in which capture, evaporation and annihilation compensate each other can be reached. If DM is asymmetric, no annihilation processes occur and capture can only be compensated by evaporation. In the asymmetric case, if DM is heavier than, say, the temperature of the star ¹, no evaporation occurs and DM accumulates at the center of the neutron star throughout its lifetime, which for the oldest ones are typically billions of years. As asymmetric DM capture in NS is one of the motivation for looking at finite-density effects arising due to asymmetric DM self-interactions, let us describe the capture process and its signatures in more details. Ultimately, the quantity that will be of interest will be the typical number density of DM, since it will tell us if the DM cloud behaves as a free gas or as a degenerate medium.

6.1.1 DM capture in NS

Let us assume that an asymmetric DM candidate has its mass m_χ between 1 GeV and 1 TeV. For lower masses, evaporation might be important in some cases. The highest mass considered here is because it is theoretically challenging to annihilate away the symmetric component in scenarios with very heavy DM due to the unitary limit. If the DM–nucleon cross section is above a certain critical value, all of the DM passing through the NS² will get captured³. Since the energy density of DM is fixed to the observed relic abundance, the energy flux $\rho_\chi v = m_\chi n_\chi v$ (n_χ the DM number of density) is independent of the DM mass m_χ and the total amount of DM captured is preferably expressed in terms of the total mass accreted. For a NS of mass M_\star and radius R_\star that has been accreting DM for a time t_\star in an environment with a DM energy density ρ_χ , the total DM mass in the NS is given by [182]

$$M_\chi^{\text{tot}} = 1.1 \times 10^{-14} M_\odot \left(\frac{M_\star}{1.52 M_\odot} \right)^2 \left(\frac{\rho_\chi}{\text{GeV cm}^{-3}} \frac{11.6 \text{ km}}{R_\star} \frac{t_\star}{10 \text{ Gyr}} \right) \quad (6.1)$$

where M_\odot is the mass of the Sun. We have assumed a scattering cross section above the critical value, hence 100% of the DM passing by the NS is captured. For symmetric candidates, a similar

¹Note that this statement is very naïve and off by a factor 30, due to the high momentum tail of the thermal distribution of both the DM and the constituent of the star [181].

²Due to gravitational focusing, the effective cross section of the NS is slightly larger than its effective area πR_\star^2 .

³Typically, one needs $\sigma_{\text{crit}} \sim 10^{-45} \text{ cm}^2$. As this is small, many models with, say, light mediators, saturate this value very easily.

analysis that takes into account capture and annihilations can be made, however the picture is slightly more complicated [176, 180]. The subsequent thermalization of the DM with the NS constituents⁴ confines all of the DM to be within the so called “thermal radius” r_{th} [184]

$$r_{\text{th}} = 0.1 \text{ m} \left(\frac{\text{GeV}}{m_\chi} \frac{T_\star}{10^3 \text{ K}} \right)^{1/2} \quad (6.2)$$

where T_\star is the temperature of the NS and $10^3 \text{ K} = 0.1 \text{ eV}$ is the typical value of the temperature of the core for old NS ($t_\star = 10 \text{ Gyr}$). This is obtained by equating the kinetic energy of the constituents of the DM cloud ($3k_B T$, k_B being the Boltzmann constant) to the gravitational potential of a DM particle ($GM(r_{\text{th}})m/r_{\text{th}}$ where $M(r_{\text{th}})$ is the enclosed mass of the core).

6.1.2 Signatures of DM capture in compact objects

Once DM has been captured, many interesting signatures can arise such as the gravitational collapse of the DM cloud, DM–DM annihilations or DM scatterings on the NS constituents. As an aside, we will now briefly be discussing such effects.

Asymmetric bosons captured by NS with a mass between 2 keV and 16 GeV can form a cloud at the core of the star which self-gravitates, collapses into a black hole and transmutes the entire star [185]. The lowest mass is set by evaporation consideration. For higher masses, the DM cloud has interesting dynamics during collapse that ultimately forbid transmutation [186].

For asymmetric fermions, the collapse of the DM cloud is hindered by the Fermi pressure. The maximum stable mass for a cloud of free degenerate fermions supported by Fermi pressure, namely the Chandrasekhar limit⁵, is given by

$$M_{\text{Ch}} = 0.62 \left(\frac{\text{GeV}}{m_\chi} \right)^2 M_\odot \quad (6.3)$$

Taking the typical parameters for the NS and its environment, *i.e.* saturating the parenthesis of Eq. (6.1) to 1, the gravitational collapse of the cloud can only happen for asymmetric fermions of mass 8 PeV and above. As mentioned before, obtaining an asymmetric candidate of such mass is theoretically challenging. It is interesting to note that for a 1 GeV fermion (*i.e.* the proton and the neutron) the typical stellar evolution process leads to a degenerate free⁶ fermion gas with enough particles to collapse, whereas standard DM capture by NS makes it very difficult. However, if such heavy candidate were to be motivated, its signatures in NS would be similar of that of its bosonic counterpart.

The full collapse of the DM cloud is expected to lead to a small black hole that can accrete all of the NS material⁷. It would therefore result in the transmutation of the NS into a solar mass black hole, whose mass would be below the minimal mass allowed by standard star evolution [188]. Mergers of lighter primordial black holes can also lead to solar mass black holes [189]. Such objects

⁴Thermalization is however not necessarily reached for all DM candidates [183] and some conditions needs to be fulfilled.

⁵Historically, the Chandrasekhar limit was derived for the case of white dwarfs, where the pressure is given by the electron degeneracy and the energy density by the neutron mass times their number density. This results in a fluid with a polytropic index of 4/3 for dwarfs, whereas the collapse of a NS is different, see Eq. (8.14).

⁶Neglecting the complicated QCD interactions in NS leads to a not-so-drastic change in the radii and masses of the configurations of order 1.

⁷There exists a small caveat for fast spinning and hot NS, for which, due to angular momentum conservation, accretion might be inefficient [187]. This can lead to the BH to disappear by Hawking radiation before it has the time to accrete all of the NS.

have interesting properties. For both origins (either primordial or from transmutation) the mergers of solar mass black holes can be distinguished from mergers of NS of the same mass and from the mergers of the lightest black holes originating from the standard star evolution process [188]. Such a detection would result in an undeniable proof of beyond the SM physics seen in gravitational wave observatories. In addition, the merger rate of transmuted NS would track the star formation history and, with enough data, it would be possible to distinguish this scenario with the expected merger rate of primordial black holes with a similar mass [190].

There exists also other very impressive signatures of the capture of DM by compact objects. The surface temperature of old NS could be modified by, for example, DM annihilations [191], inelastic scatterings [192] or elastic scatterings [193]. A type Ia supernovae⁸ could be triggered in a white dwarf by DM. More precisely, during collapse of the DM cloud, scatterings with the core can give enough energy to launch the runaway fusion process [194]. This energy source could also be provided by the Hawking radiation of a black hole too small to accrete all of the white dwarf [195] or simply DM annihilations [196].

6.2 Density effects

As motivated in the previous section, asymmetric fermionic DM can be degenerate in at least two scenarios. If it is light, the high density regions of DM halos can reach degeneracy. If it is heavy enough not to evaporate, degeneracy can also exist at the center of NS, where DM has been captured. Let us now discuss the possible change in the behaviour of the DM in a degenerate medium.

We will illustrate the effects of collective phenomena in a specific model for the remaining part of this thesis. We will consider the following Yukawa theory

$$\mathcal{L} = \bar{\psi}(i\not{\partial} + \gamma^0\mu - m)\psi + \frac{1}{2}(\partial^2\phi - m_\phi\phi^2) - g\bar{\psi}\psi\phi \quad (6.4)$$

Here, ψ is the DM candidate and has mass m . ϕ is the scalar mediator, has mass m_ϕ and has a Yukawa interaction with ψ of strength g . This model corresponds to the 1 colour, 1 flavour limit of QCD and shares with it similar features in a degenerate medium [197, 198]. The chemical potential μ of the fermion⁹ describe the possible density effects¹⁰. This model, augmented by a SM portal (such as Higgs mixing) and some source of asymmetry, would be a concrete realisation of the fermionic scenarios discussed in Section 6.1.

Let us interpret a few of the quantities in Eq. (6.4) as it will be very useful in the following. The operator $\langle\Psi|\bar{\psi}\psi|\Psi\rangle$ counts the number of particles and anti-particles in the state $|\Psi\rangle$ each with a weight that is m/ω , where ω is the energy of the fermion. This is easily seen by writing the ψ in terms of creation and destruction operators and then creating the state $|\Psi\rangle$ with the same creation

⁸More specifically, a type Ia supernova is the explosion of a white dwarf in a binary system. The white dwarf accretes matter from its companion and heats up. Once sufficient, the increase in temperature triggers fusion reactions, a large amount of energy is released in the form of radiation and unbinds the star. The runaway fusion process occurs at a specific white dwarf mass, hence their classification as “standard siren”. More massive stars can explode on their own in what is called a type II supernovae. They are hotter than white dwarf progenitors and can fuse elements up to iron in their core, after which fusion abruptly stops. Once this happens, the outer layers are not supported by radiation pressure anymore and collapse on the dense core, after which it bounces outward due to neutrino produced during the collapse.

⁹As will be explained in the text, $\bar{\psi}\gamma^0\psi$ corresponds to the number density of fermions. In the Hamiltonian, the presence of a chemical potential μ is taken into account by the substitution $H \rightarrow H - \mu N$ for N the number of fermions, hence the inclusion of a specific term proportional to μ in the lagrangian.

¹⁰In the following, we will work at zero temperature. For fermions, if $\mu < m$ and $T = 0$, the theory behaves exactly as in vacuum.

operators of particles and anti-particles. For a system of fermions at equilibrium at temperature T and chemical potential μ , we have that

$$n_s \equiv \langle \bar{\psi}\psi \rangle = 2 \int \frac{d^3k}{(2\pi)^3} \frac{m}{\omega_k} \left(\frac{1}{e^{\beta(\omega_k - \mu)} + 1} + \frac{1}{e^{\beta(\omega_k + \mu)} + 1} \right) \quad (6.5)$$

where we have introduced the symbol n_s , the scalar density. Inside the integral are the Fermi-Dirac distribution, for particle (minus sign) and anti-particle (plus sign), $f_{\text{FD}}(k) = (\exp(\beta(\omega_k \pm \mu)) + 1)^{-1}$ where $\omega_k = \sqrt{m^2 + k^2}$ is their energy and $\beta = 1/T$ is the inverse temperature. The operator $\langle \Psi | \bar{\psi}\gamma^0\psi | \Psi \rangle = \langle \Psi | \psi^\dagger\psi | \Psi \rangle$ is simply the number density of fermions

$$n \equiv \langle \bar{\psi}\gamma^0\psi \rangle = 2 \int \frac{d^3k}{(2\pi)^3} \left(\frac{1}{e^{\beta(\omega_k - \mu)} + 1} + \frac{1}{e^{\beta(\omega_k + \mu)} + 1} \right) \quad (6.6)$$

denoted n . When the system is composed of non-relativistic fermions (*i.e.* when $T \ll m$ and $\mu \approx m$), we have that $n_s \approx n$. In the relativistic limit, $n_s \ll n$. In a purely degenerate medium, the Fermi-Dirac distribution is a step function and the number density of particles is

$$n = \frac{k_F^3}{3\pi^2} \quad (6.7)$$

where the Fermi momentum k_F is given by $\mu = \sqrt{m^2 + k_F^2}$.

6.2.1 The scalar condensate at finite density

When the scalar density is non zero, the fermions ψ will impact the mediator ϕ which will backreact on n_s . To explicitly see that, we write the equations of motions for both the dark matter and the mediator [199]

$$[\partial^2 + m_\phi^2] \phi = g\bar{\psi}\psi \quad (6.8)$$

$$[i\cancel{\partial} - m] \psi = -g\phi\psi \quad (6.9)$$

and notice that they are coupled. In infinite matter that is static and translationally invariant, as is the case for, say, DM halos, the equations of motions transform into an algebraic equation

$$\phi = \frac{g}{m_\phi^2} \bar{\psi}\psi \quad (6.10)$$

which, when put back into Eq. (6.9), gives an effective Dirac mass m_* for the DM ψ ,

$$m_* = m - \frac{g^2}{m_\phi^2} \bar{\psi}\psi \quad (6.11)$$

For ease, we will define $G = g^2/m_\phi^2$ the ‘‘Fermi constant’’ of the theory (6.4) and define the condensate $\Sigma \equiv G\bar{\psi}\psi = Gn_s$, such that $m_* = m - \Sigma$. It is convenient to adimensionalise it by dividing with the bare mass, $\varphi \equiv \Sigma/m$, and the effective mass is then simply $m_* = m(1 - \varphi)$. The condensate φ can be obtained by noticing that the scalar condensate also depends on φ such that

$$\varphi = \frac{G}{m} \int \frac{d^3k}{(2\pi)^3} \frac{m}{\omega_k^*} \left(\frac{1}{e^{\beta(\omega_k^* - \mu)} + 1} + \frac{1}{e^{\beta(\omega_k^* + \mu)} + 1} \right) \quad (6.12)$$

where $\omega_k^* = \sqrt{m_*^2 + k^2}$ is the in-medium energy of the DM. This is a self-consistent equation for φ and has to be solved for every m , G , β and μ . For the sake of comparison with the results of the next sections, we give the equation for φ in the limit where $T \rightarrow 0$

$$\frac{\varphi}{C_\phi^2} = 3 \int_0^{k_F/m} x^2 \frac{1 - \varphi}{\sqrt{x^2 + (1 - \phi)^2}} dx \quad (6.13)$$

where

$$C_\phi^2 \equiv m^2 G / 3\pi^2 = 4\alpha_\phi / 3\pi \times (m/m_\phi)^2 \quad (6.14)$$

and $x = k/m$. Under the integral sign, we recognize the weight m/ω_k and the effects of the FD distribution was to cut the integral over momentum up to $x = k_F/m$ where $k_F = \sqrt{\mu^2 - m_*^2}$ is the Fermi momentum.

We see that something as simple as the Yukawa theory of Eq. (6.4) exhibits very peculiar properties in a medium, that is the appearance of an effective mass m_* which is smaller than the bare mass m . This is very much the opposite of what we encountered in Chapter 4, where the photon acquired a (positive) mass through medium effect. In the same way that Fig. 4.1 depicts the corrections to the (dark) photon self-energy due to the hot plasma, we can represent the effects of the degenerate medium on the dark matter, see the left diagram of Fig. 6.1. If looked at from bottom to top, we see that the propagation of a ψ (solid line) is affected by its interactions. As we have seen from its equation of motion Eq. (6.8), ϕ (dashed line) is sourced by $g \langle \bar{\psi}\psi \rangle$, which is nothing else than a tadpole diagram. Since there is no momentum flowing in the propagator, the interaction is effective and therefore must only depend on g^2/m_ϕ^2 .

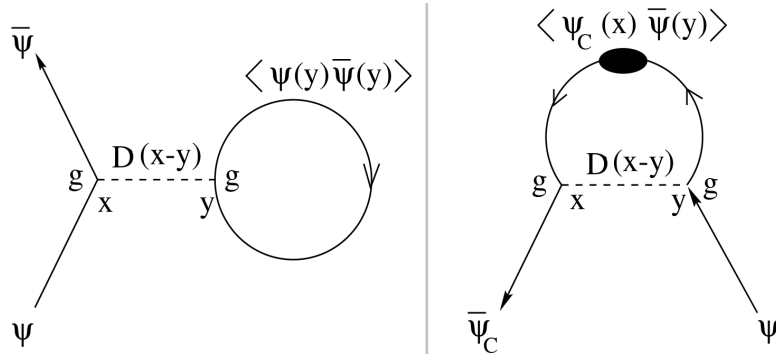


Figure 6.1: Diagrammatic representations of the scalar condensate (left) and Cooper pairing (right). Adapted from [197].

In Fig. 6.2, the numerical solutions φ of Eq. (6.13) are given as a function of the Fermi momentum divide by the bare mass for different values of C_ϕ^2 .

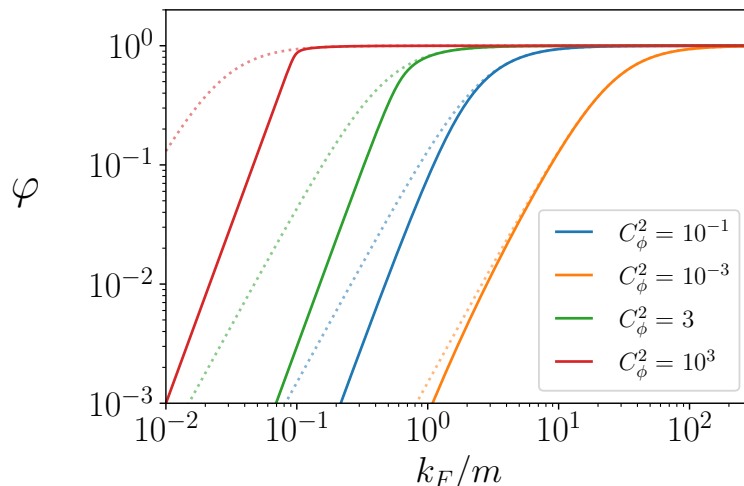


Figure 6.2: Condensate $\varphi = \Sigma/m$ as a function of Fermi momentum k_F divided by the bare mass m for different values of the effective coupling constant $C_\phi^2 = m^2 G/3\pi^2 = 4\alpha_\phi/3\pi \times (m/m_\phi)^2$ (solid lines). In dashed is given the approximate solution of Eq. (6.15). The condensate saturates to $\varphi = 1$ (or equivalently $\Sigma = m$) so that the effective mass $m_* = m(1 - \varphi) = m - \Sigma$ is zero in a very dense degenerate medium.

For “large” Fermi momentum, the condensate asymptotes $\varphi = 1$, making the fermion effectively massless in the medium. If C_ϕ^2 is small, the condensate becomes sizeable only at values of the density at which the Fermi surface is relativistic (orange curve) and the medium is expected to behave essentially like a free gas. In the opposite limit, when $C_\phi^2 \gg 1$, which could happen if, for example, the mediator is very light compared to the fermion, the effective mass $m_* = m(1 - \varphi)$ can become effectively zero at low densities where $k_F/m \ll 1$ (red curve) and the interacting medium will be very different from the free theory. It is possible to obtain an approximated analytical solution to the condensate equation in the high density limit [200]

$$\varphi \stackrel{k_F/m \gg 1}{=} \left(1 + \left[\frac{3}{2} C_\phi^2 \left(\frac{k_F}{m} \right)^2 \right]^{-1} \right)^{-1} \quad (6.15)$$

and such solutions have been presented in Fig. 6.2 in dotted lines. As can be seen, the approximation fails to reproduce correctly the low density slope and the k_F at which φ starts to saturate when $C_\phi^2 \gg 1$. In the following, the numerical solutions, and not the analytical approximation, will preferably be used. One should note that Σ is not strictly the scalar condensate but it is common to describe it as such. The actual scalar density $n_s = \langle \bar{\psi}\psi \rangle$ is instead given by $n_s = \Sigma/G$.

6.2.2 Bardeen–Cooper–Schrieffer superfluidity

The appearance of a scalar condensate is not the only density effect that arises in a medium of interacting fermions. For theories with an attractive potential between fermions, and the very simple Yukawa theory of Eq. (6.4) is one of them, superfluidity is a consequence of degeneracy [201]. Let us start by building the argument for the appearance of pairing instabilities before treating the BCS condensate in more technical details.

For a degenerate free fermion gas at zero temperature, states are filled up to a certain momentum

and empty for all momentum above

$$f_{\text{FD}}(k) = \begin{cases} 1 & k < k_F \\ 0 & k > k_F \end{cases} \quad (6.16)$$

where k_F is the momentum at the Fermi surface, $\mu = \omega_{k_F}$. Turning on interactions, the fermions in the bulk of the Fermi sea are forbidden to scatter : take k, k' both in the Fermi sea, any scattering $\psi(k) + \psi(k') \rightarrow \psi(k_f) + \psi(k'_f)$ with $k + k' = k_f + k'_f$, for example $k_f = 0$ and $k'_f = k + k'$, will be Pauli blocked since one (or the two) of the final states will already be occupied. In the example at hand the state $k_f = 0$ would already be occupied and also k'_f if $k + k' < k_F$. The only possible interaction in the bulk is back to back scattering, where the fermions simply exchange their respective momentum and reverse their direction. At the Fermi surface, the situation can be different. First neglecting interactions, the free energy Ω of the system is given by $\Omega = E - \mu N$, where E is the energy of the particles $E = \int d^3k / (2\pi)^3 \omega_k f_{\text{FD}}(k)$ and N the total number of particles. Adding one particle at the Fermi surface requires an energy μ and the change in the free energy $\Omega = (E + \mu) - \mu(N + 1) = E - \mu N$ is therefore zero. Turning interactions back on, any pair of particles added to the system will, on top of their rest mass and kinetic energies, have some potential energy due to their interactions. If the interaction is repulsive, the energy of the pair is bigger than, say, 2μ and the free energy of the system increases. However, if the potential is attractive, their energy is lowered by the potential energy of their attraction, hence the free energy is also lowered. Therefore, many such pairings will happen near the Fermi surface as long as there is a small attractive interactions between the fermions, since it is energetically favourable [202]. This, in essence, is the process of Cooper pairing.

We will now sketch the treatment of Cooper pairing in the language of QFT [203], which will be the first step in understanding superfluidity (and, by extension, superconductivity). We will assume the fermions to be massless, $m = 0$, and ϕ in the lagrangian of Eq. (6.4) to be very heavy, so that it can be integrated out¹¹. This leads to a 4 fermion interaction

$$\mathcal{L} \stackrel{m_\phi \rightarrow \infty}{=} \bar{\psi}(i\not{\partial} + \gamma^0\mu)\psi + G\bar{\psi}\bar{\psi}\psi\psi \quad (6.17)$$

where $G = g^2/m_\phi^2$ is the effective coupling, analogous to the Fermi constant in the case of electroweak interactions. As argued above, in a degenerate medium with attractive interactions, particle–particle pairings occur and their number density $\langle\psi\psi\rangle$ is non-zero. We define the gap¹² $\langle\psi\psi\rangle \equiv \Delta$, where we omit writing the fermionic indices for clarity. We will now neglect the excitations above this vev, *i.e.* we will work in the so-called mean-field approximation. Contracting the 4 fermion operator according to Wick theorem

$$\bar{\psi}\bar{\psi}\psi\psi \sim \Delta\psi\psi + \text{h.c.} \quad (6.18)$$

we have, at leading order, that

$$\mathcal{L} = (\bar{\psi} \quad \bar{\psi}_C) \begin{pmatrix} \not{k} + \mu\gamma^0 & \Delta \\ \Delta & \not{k} - \mu\gamma^0 \end{pmatrix} \begin{pmatrix} \psi \\ \psi_C \end{pmatrix} \quad (6.19)$$

where the charge conjugate $\psi_C = C\bar{\psi}^T$, T denoting transposition and $C = i\gamma^2\gamma^0$ being the charge conjugation matrix, has been introduced. We have also Fourier transformed the fields.

¹¹Even though not transparent in the derivation that is presented in this section, many difficulties arise when the fermion mass cannot be neglected and when interactions are long-ranged. We have treated in Appendix C all these complications and refer the reader to the appendix for a detailed derivation of the pairing in these cases. This more general setup is motivated by DM phenomenology and will be treated in details in Chapter 7. For interesting phenomenological applications of the BCS pairing and the scalar condensate, see Chapter 8.

¹²This terminology will soon become transparent.

The theory described by the lagrangian of Eq. (6.19) is very different from the Yukawa theory of Eq. (6.4). We now have at hand a theory of free quasi-particles (sometimes called “Bogoliubons”) propagating in a background field $\langle\psi\psi\rangle$ which is itself determined by the underlying attractive interaction. The off-diagonal term corresponds to pairing and are analogous to a Majorana mass for ψ and ψ_C . The dispersion relations of the ψ and ψ_C are found by inverting the quadratic form of the lagrangian and are given by

$$\epsilon_{\pm}(k)^2 = (k \pm \mu)^2 + \Delta^2 \quad (6.20)$$

We see that Δ indeed acts like a mass. In the same sense that the rest mass of particles is only felt near zero momentum, the effect of the mass Δ for particles (minus sign) is only felt near the Fermi surface.

A parallel is often made between spontaneous symmetry breaking of a local symmetry and superconductivity (which, for our purpose, is treated in the same way as superfluidity). In both the Brout-Englert-Higgs mechanism and the Meissner effect, a gauge boson acquires a mass because a condensate, either the vev of the Higgs $\langle H \rangle$ or the gap $\langle\psi\psi\rangle$ is non zero and charged under the gauge symmetry. It might not be obvious from the present derivation, but once we obtain a solution to the gap equation, we will have reached the same step in the study of symmetry breaking¹³ as simply finding the minimum of the potential of the Higgs (which is arguably simpler). It is then interesting to ponder if it is also possible to use the gap to give mass to fermions inside a superconductor [204]. Because of the Cooper pairing, $\bar{\psi}\bar{\psi}\psi\psi \sim \langle\bar{\psi}\bar{\psi}\rangle\psi\psi$ see Eq. (6.18). Therefore, in a superconductor, spontaneous symmetry breaking generates a Majorana mass for fermions. Let us now briefly describe where superfluidity is hiding in our description. As the gap is non-zero, the ground state of the theory is charged under a global symmetry, “dark lepton number”. Therefore, the condensate $\langle\psi\psi\rangle$ breaks a global symmetry, there exists a Nambu-Goldstone boson and this gives rise to the free transport of mass in the system, *i.e.* superfluidity. In the mean-field calculation above, the Goldstone boson do not appear explicitly since it would be excitations above the mean field, $\psi\psi - \langle\psi\psi\rangle$, which we have neglected.

The effect of the gap on the propagation of the fermions can also be illustrated by a diagram, see Fig. 6.1 (right). The $\bar{\psi}_C\psi$ propagator is changed by the gap (black blob) due to its interaction with the ϕ (dashed line). In the heavy mediator limit, *i.e.* m_{ϕ} much bigger than the typical momentum in the loop, $k \sim \mu$, the ϕ propagator becomes an effective interaction and the amplitude is simply proportional to G .

Let us now come to the determination of the gap Δ . In the same way that we obtained a self-consistent equation for the condensate, see Eq. (6.12), we can write down a self-consistent equation for the gap. It can be obtained by noticing that the right panel of Fig. 6.1, which contains the gap inside the loop, is itself equal to the gap $\Delta \sim \bar{\psi}_C\psi \sim \psi\psi$. This is called a Schwinger-Dyson equation and it can be derived diagrammatically (under the condition that we use appropriate Feynman rules) or by inverting the quadratic form of the action. In the theory of Eq. (6.17), the gap equation will be given by [203]

$$\Delta = G \int^{\Lambda} \frac{d^3k}{(2\pi)^3} \frac{\Delta}{2\sqrt{(k-\mu)^2 + \Delta^2}} \tanh \frac{\sqrt{(k-\mu)^2 + \Delta^2}}{2T} \quad (6.21)$$

where the momentum integral comes from the loop. Note that we only integrate up to some cut-off Λ , due to the obvious UV divergence of the integral $\Delta \sim \Lambda^2$.

¹³For the case that interests us, superfluidity, it is a global symmetry, lepton number, that is broken.

Under some additional assumptions, it is possible to obtain an analytical solution to the gap equation. We will assume Δ to be momentum independent. In the theory where the full momentum dependence of the mediator is kept, the integral will be finite but solving the gap equations becomes much more complicated, see Appendix C. We will also work in the zero temperature limit, such that the hyperbolic tangent goes to 1 and the gap equation becomes simpler. If $\Delta \ll \mu$, the integral is dominated by the resonant behaviour of the inverse of the dispersion relation around $k = \mu$. Assuming that only fermions in a small vicinity around the Fermi surface participates in the pairing, we are allowed to integrate only between $k = \mu - \delta$ and $k = \mu + \delta$ for δ the reach of the interactions, which we assume to be such that $\Delta \ll \delta \ll \mu$. If δ is very small, note that it is then a good approximation for Δ not to depend on momentum, since only $\Delta(k = \mu)$ will be relevant. Setting $\zeta = k - \mu$, the gap equation becomes

$$\Delta \approx \frac{\mu^2 G}{2\pi^2} \int_0^\delta \frac{\Delta}{\sqrt{\zeta^2 + \Delta^2}} \quad (6.22)$$

where we have set $k^2 dk \approx \mu^2 dk$ since $k \approx \mu$. Note that however small $\mu^2 G$ is, there will always be a non-zero solution Δ , due to the infrared divergence of the denominator near the Fermi surface $\zeta \approx 0$ that is regulated by Δ . This shows that Cooper pairing near the Fermi surface is unstable as long as a small attractive interaction exists, as we had argued by looking at the free energy above. The gap equation Eq. (6.22) can now be solved analytical and its solution, namely the BCS gap in the heavy mediator and ultra relativistic limit, is

$$\Delta \approx 2\delta \exp\left(-\frac{2\pi^2}{G\mu^2}\right) = 2\delta \exp\left(-\frac{4\pi^2}{g^2} \frac{m_\phi^2}{\mu^2}\right) \quad (6.23)$$

Interestingly, the gap is a non-perturbative quantity : it is not possible to expand Δ in power of g around $g = 0$. Due to the approximations made to obtain the BCS gap, this expression is *a priori* only valid when the exponential suppresses the gap. Indeed, in order to write Eq. (6.17) we have assumed to be in the heavy mediator limit. Furthermore, we have also assumed that m_ϕ was much bigger than μ , $m_\phi^2/\mu^2 \gg 1$, in order for the ϕ exchange to proceed as a contact interaction and the propagator of ϕ to not depend on momentum in Eq. (6.22). The coupling g must also be small. All in all, this means that the argument of the exponential is much bigger than unity, $4\pi^2/g^2 \times m_\phi^2/\mu^2 \gg 1$, and that $\Delta \ll 2\delta$, which is self-consistent with our assumption on the range of the interactions in the Fermi sea. We end this Section by stressing that our ignorance about δ does not give the overall normalization of Δ . However, we will show in Chapter 7 that our more careful treatment allows for the determination of δ .

6.2.3 Superfluid dark matter in neutron stars : first steps

Now that we have developed some intuition about density effects, it is interesting to apply it to the case of DM captured in NS. Assuming as before DM to be an asymmetric fermion with a Yukawa interaction, as in the model of Eq. (6.4), then it would necessarily be, by the BCS argument, superfluid inside NS. Owing to its very peculiar transport properties, the fact that a dark matter model as simple as the Yukawa theory could exhibit such an exotic state of matter is interesting. In this section, we aim at estimating the superfluid content of the DM cloud.

As is evident from the Wick contraction in Eq. (6.18), in principle, all possible channels should be taken into account. Since the BCS theory is a theory of relativistic particles, the scalar condensate $\Sigma \sim \bar{\psi}\psi$ was neglected. In that context it is a good approximation since, as was shown in Section 6.2.1, the condensate would saturate to the mass of the fermion which in any case is very small with respect to the Fermi energy. Nevertheless, for a non-relativistic system of fermions, such

as asymmetric DM captured in NS, both the scalar condensate and the BCS gaps are therefore expected to play a role.

Then density of the DM cloud inside a NS can be estimated by taking the maximum number of DM particles that can be captured given by Eq. (6.1) and squeezing it within the thermal radius of Eq. (6.2). Saturating all the parenthesis to 1 and keeping the DM mass free, we find that

$$\frac{n_\chi}{m_\chi^3} = \frac{M_\chi^{\text{tot}}/m_\chi}{\frac{4}{3}\pi (r_{\text{th}}m_\chi)^3} = 2 \times 10^{-2} \left(\frac{\text{GeV}}{m_\chi} \right)^{5/2} \quad (6.24)$$

We will take a typical benchmark model with $m_\chi = 1$ TeV, $m_\phi = 1$ MeV and $\alpha_\phi \equiv g^2/4\pi = 10^{-3}$ [188]. For such masses, the Fermi momentum obtained from Eq. (6.24) using Eq. (6.7) is $k_F/m_\chi \approx 3 \times 10^{-3}$ and DM is non relativistic. The effective coupling governing the scalar condensate is $C_\phi^2 = 4 \times 10^8$ and by extrapolating the results of Fig. 6.2, it is very clear that density effects are important in that scenario and make DM effectively massless in the medium. Using the BCS ansatz of Eq. (6.23), we find that it results in the gap being

$$\Delta \approx 2\delta \quad (6.25)$$

Even though the model under consideration do not respect strictly the underlying assumptions made to obtain the BCS ansatz (that is, light mediator), this result is puzzling. Clearly, Δ should be small with respect to δ for the BCS ansatz to be applicable. We see that the benchmark model used in this section is such that, inside NS, the typical BCS treatment is not valid and therefore much informations about the properties and dynamics of the DM cloud cannot be extracted with the level of refinement used in deriving the gap in Section 6.2.2. It is very interesting that DM phenomenology calls for a more careful treatment of superfluidity and also shows the possible interplay between the scalar condensate and the gap. In addition, for applications, Eq. (6.23) is arguably not very useful, since the overall normalization of the gap, δ , is not known. Moreover, if long-range interactions are to be studied, we should expect that the method used to obtained the gap equation will be more involved than what has been presented in Section 6.2.2. It is also expected that this regime should interconnect with the regularization of the UV divergences of the gap equations as well as the momentum dependence of the gap, since the interactions will not be effective in that case.

Motivated by this puzzle, the next Chapter will be dedicated to refining the treatment of the gap and the condensate in order to be able to understand the consequences of density effects in the degenerate DM medium that are expected to be encountered in the Universe.

Chapter 7

A theory of condensed dark matter

In this Chapter, we aim at describing and solving a consistent set of gap and scalar condensate equations. We will treat the general case of a degenerate fermion gas, in both the relativistic and non-relativistic regime, with attractive interactions which can be short or long-ranged. This general scenario goes beyond what is generally treated in the literature : Superfluidity is often restricted to the BCS regime, that is relativistic fermions with a short-ranged interaction, and the effects of the gaps on the scalar condensate (and the condensate on the gaps) have been neglected so far. In order to study long-range interactions, we will keep the full momentum dependence of the mediator propagator and the gaps, but neglect their energy dependence. This will complicate tremendously the derivation of the gap equations with respect to what is sketched in Section 6.2.2 and the numerical methods for solving them will be involved. The steps needed to derive the gap equations and the description of the numerical methods used for solving the gap equations are relegated to Appendix C in order not to clutter the discussion of the physics of the system. In particular, we mention that we have obtained the system of gap equations by two different method: using the minimization of the free energy and by writing a Schwinger-Dyson equation for the gaps.

7.1 The consistent system of gap equations

Within an interacting theory of fermion, Eq. (6.4) being one of them, superfluidity can manifest itself in many channels. The most general expression of the gap that is translation invariant is [197]

$$\Delta = \langle \psi_c \bar{\psi} \rangle = \Delta_1 \gamma_5 + \Delta_2 \vec{\gamma} \cdot \vec{k} \gamma_0 \gamma_5 + \Delta_3 \gamma_0 \gamma_5 + \Delta_4 + \Delta_5 \vec{\gamma} \cdot \vec{k} \gamma_0 + \Delta_6 \vec{\gamma} \cdot \vec{k} \quad (7.1)$$

with \vec{k} being the unit vector in the direction of the momentum \vec{k} . If the fermions have some internal degrees of freedom, such as colours or flavours, then the terms $\Delta_7 \vec{\gamma} \cdot \vec{k} \gamma_5$ and $\Delta_8 \gamma_0$ need to be added to Δ . This expression can be made explicitly Lorentz covariant by introducing u^μ , the four-velocity of the medium. However, since the questions that we will try to answer are not Lorentz invariant by nature, it is preferable to work in the special frame that is the rest frame of the medium and take $u^\mu = (1, \vec{0})$. Even though it has not explicitly been shown, the BCS treatment of Section 6.2.2 only takes into account the Δ_1 term and we will see that other terms are important when going beyond the assumptions of the BCS scenario. However, the expression for the gaps in Eq. (7.1) is very complicated and when considering the Yukawa theory of Eq. (6.4), not every Dirac structure is relevant. By virtue of Fermi statistics, the wave function of the Cooper pair should be antisymmetric by exchange of the two fermions. In addition, our theory is parity conserving since g is taken to be real. Note that this is not the case for electron superconductors, since weak interactions by Z boson exchange is parity violating (the effects, hence parity violating gaps, are however small) [205]. Also, the dark matter does not have any internal indices (as opposed to the case of quark matter, where flavours and colours are essential). Therefore, the Cooper pairs can

have a total spin equal to zero, $J = 0$, and even parity, $P = +$, and the wavefunction will be overall antisymmetric. In Eq. (7.1), only the terms that contains $\Delta_{1,2,3}$ have even parity, the others being odd. Therefore, for the case that is going to be most relevant for dark matter phenomenology, we have Cooper pairing with $J^P = 0^+$, and the most general gap reduces to the first three terms [205, 197]

$$\Delta = \langle \psi_c \bar{\psi} \rangle = \Delta_1 \gamma_5 + \Delta_2 \vec{\gamma} \cdot \vec{k} \gamma_0 \gamma_5 + \Delta_3 \gamma_0 \gamma_5 \quad (7.2)$$

The mean-field approximation of the condensed degrees of freedom and the QFT language and tools allow the tracking each condensation channel in a consistent manner. The reader is warmly invited to look at Appendix C for the interesting technical details on how to go from the lagrangian to the gap. Within the main text, mathematical details will be kept at the bare minimum and the focus will be on the physical interpretation.

The presence of gaps will necessarily modify the dispersion relations of particles and antiparticles propagating in the medium. In addition, the presence of the condensate will amount to replace the bare mass m with a density dependent effective mass of the medium $m_* = m - \Sigma$. With the ansatz of Eq. (7.2), the dispersion relation takes the form

$$\begin{aligned} \epsilon_{\pm}^2 = & \mu^2 + \omega^2 + \Delta_1^2 + \Delta_2^2 + \Delta_3^2 + \\ & \pm 2 \left(\mu^2 \omega^2 + 2\mu k \Delta_1 \Delta_2 + m_*^2 \Delta_2^2 + \Delta_1^2 \Delta_2^2 + 2m_* \mu \Delta_1 \Delta_3 - 2m_* k \Delta_2 \Delta_3 + k^2 \Delta_3^2 + \Delta_1^2 \Delta_3^2 \right)^{1/2}. \end{aligned} \quad (7.3)$$

Here, the $-$ sign refers to particles and the $+$ signs to anti-particles. If $\Delta_2 = 0$ and $\Delta_3 = 0$, we recover Eq. (6.20). The system of gap equations for $\Delta_{1,2,3}$ and Σ will be obtained after taking derivatives of the free energy, which amounts to take derivatives of the dispersion relations. This dispersion relation is very complicated and will result in as complicated gap equations. However, the expression of ϵ_{\pm} can take simple forms in different limits of the system, which suggests that the dynamics can be well encoded by a simpler expression that interpolates smoothly between the different regimes. For example, in the relativistic and non-relativistic limits, we have respectively that

$$\epsilon_{\pm}^2 \stackrel{m \rightarrow 0}{\approx} (k \pm \mu) + (\Delta_1 \pm \Delta_2)^2 \quad (7.4)$$

and

$$\epsilon_{\pm}^2 \stackrel{k \rightarrow 0}{\approx} (m \pm \mu) + (\Delta_1 \pm \Delta_3)^2 \quad (7.5)$$

where, for consistency, Δ_3 (Δ_2) has been taken to be 0 in the relativistic (non-relativistic) limit. The justification for these choice will be transparent once the gap equations will have been written. In addition, for weakly coupled system, we expect that the gaps should be small deviations around the Fermi surface, and should therefore not be larger than the chemical potential [197]. The dispersion relations are thus expanded in $\Delta_i/\sqrt{\mu\omega}$ and become

$$\epsilon_{\pm}^2 \approx (\omega \pm \mu)^2 + \left(\Delta_1 \pm \left(\frac{k}{\omega} \Delta_2 + \frac{m_*}{\omega} \Delta_3 \right) \right)^2 + \left(\frac{m_*}{\omega} \Delta_2 - \frac{k}{\omega} \Delta_3 \right)^2 \pm \frac{(m_* \Delta_2 - k \Delta_3)^2}{\mu\omega} \quad (7.6)$$

$$\approx (\omega \pm \mu)^2 + \tilde{\Delta}_{\pm}^2 + \left(1 \pm \frac{\omega k}{\mu} \right) \tilde{k}^2 \quad (7.7)$$

where we have defined

$$\tilde{\Delta}_{\pm} = \Delta_1 \pm \left(\frac{k}{\omega} \Delta_2 + \frac{m_{\star}}{\omega} \Delta_3 \right), \quad (7.8)$$

$$\tilde{\kappa} = \frac{m_{\star}}{\omega} \Delta_2 - \frac{k}{\omega} \Delta_3. \quad (7.9)$$

Furthermore, the last term vanish when either $k \rightarrow 0$ or $m \rightarrow 0$. It is then assumed that taking into account only the first two terms will encompass most of the relevant dynamics and interpolates smoothly between the different regimes. The dispersion relations for particles ($-$) and antiparticles ($+$) now become the much simpler expressions that are

$$\epsilon_{\pm}^2 \approx (\omega \pm \mu)^2 + \left(\Delta_1 \pm \left(\frac{k}{\omega} \Delta_2 + \frac{m_{\star}}{\omega} \Delta_3 \right) \right)^2 = (\omega \pm \mu)^2 + \tilde{\Delta}_{\pm}^2 \quad (7.10)$$

so that, in each regime, there's effectively one gap. The form of $\tilde{\Delta}_{\pm}$ is a direct generalization to all momenta of the gap used in [205]. In the latter reference, it is argued that the only combination of gap that is relevant at the Fermi surface is $d = \Delta_1 - \frac{k_F}{\mu} \Delta_2 - \frac{m}{\mu} \Delta_3$ (see Eq. (1.52) in [205]). Evaluated at $k = k_F$, Eq. (7.10) reproduces the expression for d . Finally, the approximations made above will be a-posteriori checked and will turn out to be very good across the entire range of values that will be considered in the following.

Using the three gaps of Eq. (7.2) and the dispersion relation of Eq. (7.10), we use a Hubbard-Strantanovich transformation in order to obtain a theory of quasi-particles propagating in the interacting medium. This allows for the computation of the partition function Z of the system by path integrals. For a system of volume \mathcal{V} and temperature T , the free-energy is given by $\Omega = -\frac{T}{\mathcal{V}} \log Z$, and contains all the information about the thermodynamics of the system. Within the mean-field approximation, we obtain a full set of consistent gap equations by minimization of Ω with respect to the gaps and the condensate (see Appendix C). The system is the following

$$\Delta_1(p_0, p) = \frac{T}{\mathcal{V}} \sum_k \sum_{\eta=\pm} V(p-k) \frac{\tilde{\Delta}_{\eta}(k)}{k_0^2 - \epsilon_{\eta}^2(k)}, \quad (7.11)$$

$$\Delta_2(p_0, p) = -\frac{T}{\mathcal{V}} \sum_k \sum_{\eta=\pm} \eta V(p-k) \hat{\mathbf{k}} \cdot \hat{\mathbf{p}} \frac{k}{\omega_k} \frac{\tilde{\Delta}_{\eta}(k)}{k_0^2 - \epsilon_{\eta}^2(k)}, \quad (7.12)$$

$$\Delta_3(p_0, p) = \frac{T}{\mathcal{V}} \sum_k \sum_{\eta=\pm} \eta V(p-k) \frac{m_{\star}}{\omega_k} \frac{\tilde{\Delta}_{\eta}(k)}{k_0^2 - \epsilon_{\eta}^2(k)}, \quad (7.13)$$

$$\Sigma(p_0, p) = \frac{T}{\mathcal{V}} \sum_k \sum_{\eta=\pm} 2 \frac{V(p)}{k_0^2 - \epsilon_{\eta}^2(k)} \left(\frac{m_{\star}}{\omega_k} (\mu + \eta \omega_k) - \eta \frac{k}{\omega_k} \frac{\tilde{\kappa}(k)}{\omega_k} \tilde{\Delta}_{\eta}(k) \right). \quad (7.14)$$

In this expression, the sum over k runs over all $k_0 = \pi i (2n + 1) T$ (the Matsubara frequencies¹) and all 3-momenta. The attractive interactions is hidden in $V(k) = g^2 D(k)$ for g the coupling between ψ and ϕ and D the ϕ propagator. The sum over η corresponds to a sum over particles and antiparticles.

Let us now discuss this system of gap equations and condensate. Written in this form, Eqs. (7.11–7.14) are not expressed in a way that is suited for solving either analytically or numerically, and some

¹We work in Euclidean space. After the Wick rotation to imaginary time, $t \rightarrow \tau = -it$, the t integral becomes an integral over τ between 0 and β , the inverse temperature. In Fourier space, this amounts to have discrete frequencies. For fermions, the boundary conditions around τ only allow odd Matsubara frequencies, whereas for bosons only even multiples of $\pi i T$ are allowed [97].

manipulations are still required, see Appendix C for details. On the left hand-side of the equations we find the gaps Δ_i and the condensate Σ . On the right hand-side, the factors of $T/V \sum_k$ can be replaced by an integral over all k , $\int d^4k$. It corresponds to the momentum running in the loop. In the propagator V , we see the dependence on both k and p , we have thus kept the full momentum dependence of the gaps. Interestingly, for Σ , the propagator does not depend on the momentum of the loop, meaning that we can choose p_0 and $p = 0$ in Eq. (7.14). In the right hand-side of the Δ_i , the small differences in k and p dependences originates from the different Dirac structures that have been considered in Eq. (7.2). We find that all gaps Δ_i depend only on the combination of gaps $\tilde{\Delta}_\pm$ and that Σ depends on $\tilde{\Delta}_\pm$ and $\tilde{\kappa}$. This hints to the fact that a better system to consider would be one not on Δ_i but on the combination of gaps of Eq. (7.8) and Eq. (7.9).

In the heavy mediator limit, $V \rightarrow g^2/m_\phi^2$, and Eq. (7.11) will reduce to the standard BCS equation of Eq. (6.21) once the Matsubara sum has been performed². The right hand side of the equation for Δ_2 is proportional to p , hence, in the non-relativistic limit, the left hand side of the equation, *i.e.* Δ_2 , also goes to zero. For the second to last equation it is therefore also expected that Δ_3 goes to zero, this time in the relativistic limit, *i.e.* when $m/\mu \ll 1$. This proves the consistency of the choices made when writing Eq. (7.4) and Eq. (7.5) in each limit.

The system of Eq. (7.11–7.14) for the gaps Δ_i and the condensate can now be recast in a system of gap equations for $\tilde{\Delta}_\pm$ and $\tilde{\kappa}$. Performing the Matsubara sum, writing everything in terms of integrals and integrating over the angles, we find (see Appendix C) that the system for the gaps and the condensate becomes

$$\tilde{\Delta}_\pm(p) = \frac{g^2}{32\pi^2} \sum_\eta \int_0^\infty dk \frac{k}{p} \left\{ \log \frac{m_\phi^2 + (p-k)^2}{m_\phi^2 + (p+k)^2} \pm \eta \frac{kp}{\omega_p \omega_k} \left(-2 + \frac{m_\phi^2 + k^2 + p^2}{2kp} \log \frac{m_\phi^2 + (p-k)^2}{m_\phi^2 + (p+k)^2} \right) \right. \\ \left. \pm \eta \frac{m_\star^2}{\omega_p \omega_k} \log \frac{m_\phi^2 + (p-k)^2}{m_\phi^2 + (p+k)^2} \right\} \frac{\tilde{\Delta}_\eta(k)}{\epsilon_\eta(k)}, \quad (7.15)$$

$$\tilde{\kappa}(p) = \frac{g^2}{32\pi^2} \sum_\eta \int_0^\infty dk \frac{k}{p} \left\{ \eta \frac{m_\star k}{\omega_p \omega_k} \left(-2 + \frac{m_\phi^2 + k^2 + p^2}{2kp} \log \frac{m_\phi^2 + (p-k)^2}{m_\phi^2 + (p+k)^2} \right) \right. \\ \left. - \eta \frac{m_\star p}{\omega_p \omega_k} \log \frac{m_\phi^2 + (p-k)^2}{m_\phi^2 + (p+k)^2} \right\} \frac{\tilde{\Delta}_\eta(k)}{\epsilon_\eta(k)}, \quad (7.16)$$

$$\Sigma(0) = \frac{-g^2}{2m_\phi^2} \sum_\eta \int \frac{d^3k}{(2\pi)^3} \left\{ \frac{m_\star}{\omega_k} \left[\frac{\omega_k + \eta\mu}{\epsilon_\eta(k)} - 1 \right] - \eta \frac{k}{\omega_k} \frac{\tilde{\kappa}(k)}{\omega_k} \frac{\tilde{\Delta}_\eta(k)}{\epsilon_\eta(k)} \right\}. \quad (7.17)$$

A few comments are in order. When going from Eqs. (7.11–7.14) to Eqs. (7.15–7.17), we have assumed that the propagator $V(p-k)$ can be approximated by $V(\vec{k}-\vec{p})$, *i.e.* the energy dependence can be neglected. Keeping the 3-momentum dependence allows us to go further than the standard treatments [201, 197] (see Section 7.2), at the price of needing to implement complicated numerical methods in order to solve the gap equations. It is however possible to keep also the energy dependence [198] but the numerical algorithms needed for obtaining the solutions to the gap equations in that case are more involved. In each equations of the system, it is possible to neglect the contribution of anti-particles ($\eta = +$) and only keep the particles ($\eta = -$). In the right hand side, each term is proportional to $1/\epsilon_\eta$. At the Fermi surface, $\epsilon_- = \tilde{\Delta}_- \ll \epsilon_+ \approx 2\mu$ and thus the antiparticles contribution is more suppressed than the particles contribution.

²In order to reproduce the BCS equation, one need to use $T \sum_{k_0} \frac{1}{k_0^2 - a^2} = \frac{-1}{2a} \tanh\left(\frac{a}{2T}\right)$, where the sum over k_0 is a sum over all fermionic Matsubara frequencies $k_0 = (2n+1)\pi iT$.

In the relativistic and/or heavy mediator limit, this set of equations reduces to the common BCS case and therefore smoothly interpolates between the two known extremes. It also allows for the exploration of the non-relativistic and light mediator limits, both of which are not necessarily found in systems treated in nuclear or particle physics, such as nuclear matter or quark matter. It is fully consistent in the sense that it also takes into account the contribution of the scalar condensate and the impact of the gaps on Σ and vice-versa, which, to the best of our knowledge, has not been done before. It is also possible to take into account corrections to the gap equations from the higher order terms neglected in the dispersion relation of Eq. (7.10), as can be seen in Appendix C. Since the full momentum dependence has been kept at all time and the vacuum contribution to Σ has been subtracted – note the -1 in the bracket – one need not to introduce spurious cut-offs to regularize UV divergences. The solutions to the system will be UV finite by construction and this will allow for the determination of the normalization of the gaps³. Setting all the gaps to 0 in Eq. (7.17), we recover the equation for the condensate given in Eq. (6.13). We note that for some condensed matter system, the BCS description fails and calls for a better description of the attractive interactions, as we have done in this Chapter. The Eliashberg theory of superconductivity is a refinement of the BCS theory for which in Eq. (7.11) the mediator propagator is energy dependent (but momentum independent). In the same vein as our treatment, the mediator is therefore not integrated out. This additional ingredient provided a better description of strongly coupled system [206].

It is interesting to ponder what the physics of such system would be, had the Dirac structure of the interactions be different. Within this Yukawa theory, the mediator ϕ could be a pseudoscalar. In this case, the condensate Σ would be identically zero since interactions between ψ 's would be velocity suppressed and Σ is evaluated at zero momentum exchange. The gap equations would also be affected⁴ by the pseudoscalar nature of the mediator but studying pairing in such channels goes beyond the scope of this thesis. If ϕ is taken to be a vector boson (*i.e.* repulsive interactions), there are many possibilities. Assuming ϕ to arise from an abelian group, the physics of the scalar condensate can be found in Chapter 11 of [200] in the context of nuclear physics and solutions are discussed in [207]. In that case, the gaps will be zero since interactions between the fermions of the medium will be solely repulsive. If instead ϕ comes from a non abelian group, the gap physics will be akin to what happens to QCD [208].

7.2 Solutions of the gap equations

With the help of the numerical methods described in Appendix C, it is possible to solve the system of gap equations for $\tilde{\Delta}_-(k)$ and Σ once given a fermion mass m , a mediator mass m_ϕ , a Yukawa coupling g and a Fermi momentum k_F . One can measure all dimensionful quantities in units of the bare mass m and this parameter can simply be absorbed. The condensate alone has already been treated in Section 6.2.1. We will now treat the gaps $\tilde{\Delta}_\eta$, followed by the gap-condensate system. This will pave the way for the study of the thermodynamics of the medium.

³When regularizing with a counter term such as in [197], one needs to introduce a renormalization scale Λ , to which the gaps will be roughly proportional to. Otherwise interesting for analytical insight, it is not suited for this work since the aim is to obtain the size of the gaps given a set of coupling, masses and density. This can also be seen in Eq. (6.22) and its solution (6.23) for which δ , which is essentially the regulator, is unknown. Hence, in the BCS treatment, the pre-exponential factor is not known and one should keep the momentum dependence of the gaps in order to be able to determine it.

⁴If the pseudoscalar mediator is heavy, after integrating it out, the 4 fermion interactions would be of the form $G\bar{\psi}\gamma_5\psi\bar{\psi}\gamma_5\psi$, to be compared with Eq. (6.17). In the same vein, if the heavy mediator was of spin 1, the interaction would be of the form $G\bar{\psi}\gamma_\mu\psi\bar{\psi}\gamma^\mu\psi$. Both different structure of the interaction term would affect Cooper pairing.

7.2.1 The gaps $\tilde{\Delta}_-$ with heavy mediators

The parametric dependence of the gaps is more complicated than that of the scalar condensate. One should expect that fermion pairing will depend on the range of the interaction, *i.e.* short or long, with respect to the typical distance between fermions, *i.e.* $n^{-1/3} \sim 1/k_F$. The gap should also have another dependence on the strength of the interaction g , which rules the typical width of the shell in Fermi space in which pairing occurs. Finally, given some masses, coupling and density, pairing should be less and less common at scales below the typical interparticle distance, and the dependence on momentum (scale) of the gaps should tend to zero at high momentum (small scales).

We first treat the relativistic case $k_F \gg m$. This limit is well known by some of the particle physics community since it is the relevant one for color superconductivity. In Fig. 7.1 and Fig. 7.2 is given the normalization $\tilde{\Delta}_{-,F}$, defined as the value of the gap evaluated at the Fermi momentum

$$\tilde{\Delta}_{-,F} \equiv \tilde{\Delta}_-(k = k_F), \quad (7.18)$$

for different mediator mass m_ϕ and coupling g , respectively. The mediator masses are taken to be “heavy”, *i.e.* $m_\phi > m$, and the couplings are of order $\mathcal{O}(1)$. It is stressed that the overall normalization is completely determined through the numerical calculations since we have kept the 3-momentum dependence at all time. That is to be contrasted with the solutions of Eq. (6.23) which is proportional to the unknown δ .

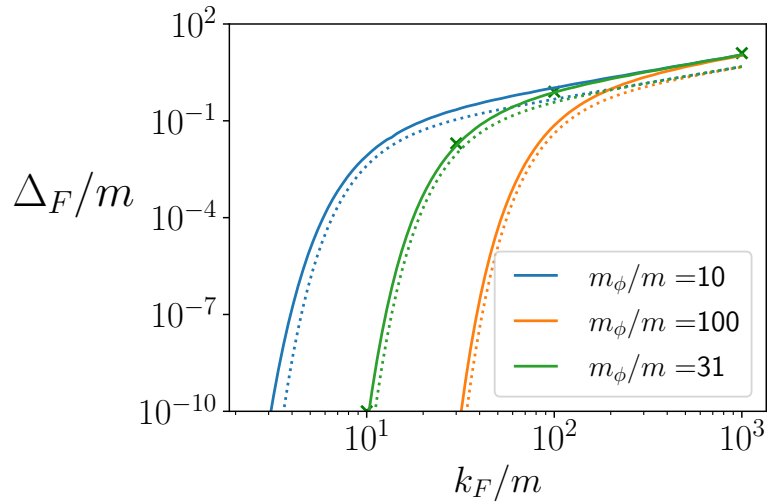


Figure 7.1: Normalization of the gap $\tilde{\Delta}_-$ at the Fermi momentum with $g = 4$. Each solid curve corresponds to different mediator mass in the heavy mediator limit, $m_\phi > m$. In dashed is given the ansatz of Eq. (7.21).

When the Fermi momentum is the biggest scale, the gap $\tilde{\Delta}_-$ in Fig. 7.1 (continuous lines) simply grows as k_F and becomes independent of the mediator mass. At low density, the gap becomes exponentially suppressed (but always non-zero) and the heavier the mediator is, the higher the density at which the gap becomes unsuppressed is. Throughout, it is important to notice that the gap is always much smaller than the energy at the Fermi surface, $\mu \approx k_F$ in this regime.

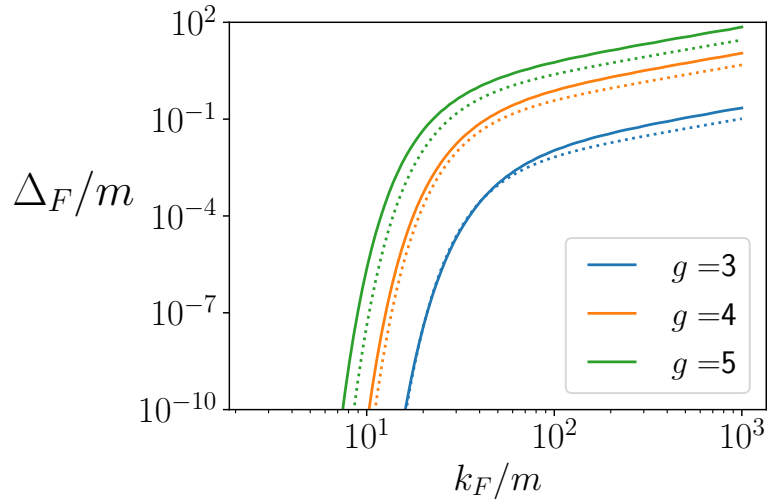


Figure 7.2: Normalization of the gap $\tilde{\Delta}_-$ at the Fermi momentum with $m_\phi = 10^{1.5}$. Each solid curve corresponds to different coupling g . In dashed is given the ansatz of Eq. (7.21).

It is seen in Fig. 7.2 (continuous lines) that as the coupling grows (is reduced), the unsuppressed density regime occurs at lower (higher) k_F . More importantly, the normalization at high Fermi momentum very steeply depends on the coupling, with bigger coupling meaning bigger gaps. As this dependence will be important in the following, in Fig. 7.3 is given $\tilde{\Delta}_{-,F}/2k_F$ for $k_F \gg m_\phi, m$ as a function of the coupling g and $\alpha_\phi \equiv g^2/4\pi$ (continuous line). The normalization is exponentially suppressed below $\alpha_\phi = 2$ and becomes roughly constant for higher α_ϕ . Even though gaps are non-perturbative quantities, their computations are only valid in the weakly coupled regime and results for $\alpha_\phi \gg 1$ should not be trusted.

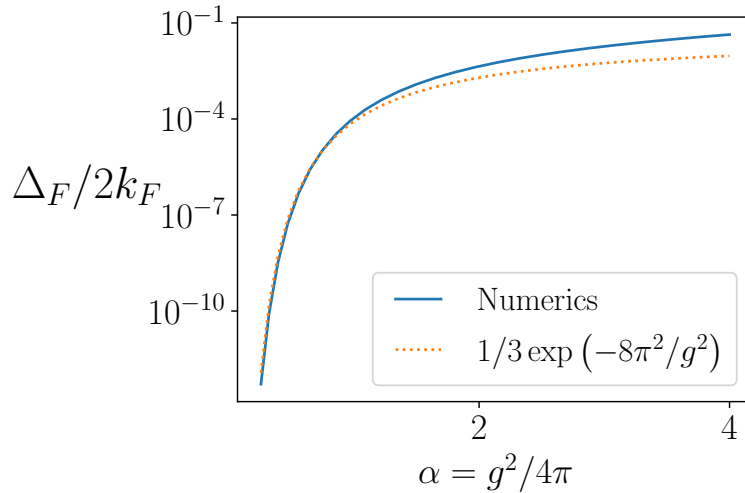


Figure 7.3: Coupling dependence of the gap $\tilde{\Delta}_-(k_F)$ in the ultra relativistic limit, $k_F \gg m, m_\phi$ (solid blue). In dashed is given the ansatz of Eq. (7.21).

In Fig. 7.4 the shape function $\chi(k) = \tilde{\Delta}_-(k)/\tilde{\Delta}_-(k_F)$ (continuous lines), is given for a choice of coupling $g = 4$, mediator mass $m_\phi/m = 10^{1.5}$ and for some representative values of the density. These parameters have been highlighted in Fig. 7.2 as little crosses. By definition, the shape function is normalized such that $\chi(k_F) = 1$. As is evident from the graph, at high momentum the gap goes to zero, showing that the computations are finite in the UV. This means that the

high momentum behaviour is under control and no additional renormalization is required for the determination of the gaps.

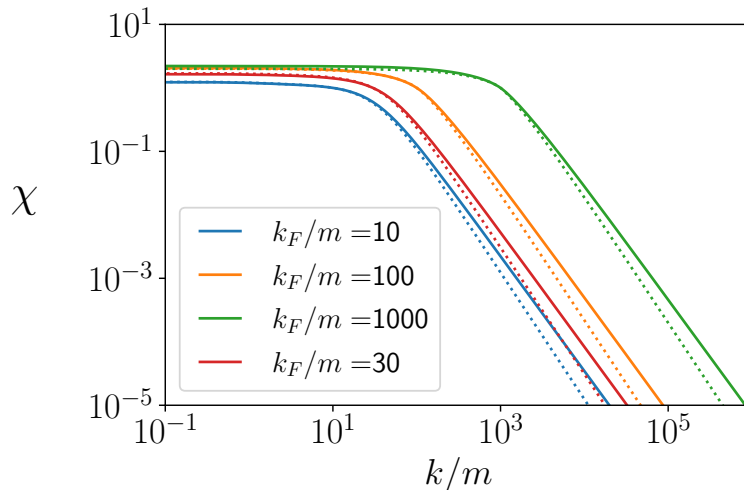


Figure 7.4: Shape function of $\tilde{\Delta}_-$ for $g = 4$ and $m_\phi/m = 30$. Different solid curve corresponds to different densities. In dashed is given $\phi(k)$, see Eq. (C.76).

Within the heavy mediator and relativistic regime, it is possible to obtain insight on the parametric dependence of the gaps through an analytical ansatz. The standard BCS treatment of the (momentum independent) gap shows that, up to a normalization that depends on the strength of pairing and an arbitrary momentum cutoff, the gap in the ultra relativistic regime should behaves as [201, 203]

$$\tilde{\Delta}_- \sim 2k_F \delta(g) \exp\left(\frac{-2\pi^2}{G_F k_F^2}\right) \quad (7.19)$$

where the 2 has been added for cosmetic purposes and the function $\delta(g)$ encompasses the ignorance about the depth at which pairing occurs in the Fermi sea. On the other hand, at very high densities and small couplings (more precisely, regions where the mediator mass is overwhelmingly given by the density corrections), the more careful treatment of [197] shows that the gap should be proportional to

$$\tilde{\Delta}_- \propto k_F \exp(-8\pi^2/g^2) \quad (7.20)$$

It is possible to guess an analytical ansatz which exploits the knowledge of both of these limits. We propose to use the following expression

$$\tilde{\Delta}_{-,F} \approx \mathcal{N} \times 2k_F \exp(-8\pi^2/g^2) \exp\left(\frac{-2\pi^2}{\frac{g^2}{2m_\phi^2} k_F^2}\right) \quad (7.21)$$

in the relativistic and weakly coupled limit. In this expression, \mathcal{N} is a normalization that must be determined numerically. We have found that $\mathcal{N} = 1/3$ provides a good fit to the numerics. Finally, the momentum dependence is approximated⁵ by $\tilde{\Delta}_-(k) = \tilde{\Delta}_{-,F} \phi(k)$, see Eq. (C.76).

⁵Conversely, one can assume the shape function χ to be given by ϕ , solve the gap equation for $\tilde{\Delta}_{-,F}$ and then try to fit some analytical expressions, and they would recover Eq. (7.21).

In Fig. 7.1, 7.2 and 7.3, the ansatz of Eq. (7.21) is given in dotted lines and reproduces correctly the qualitative behaviour of the numerical solutions. It is noted that by allowing more fitting parameter in the expression of the ansatz, the numerics can be more closely matched but it is not the purpose of this discussion. In the following, we will use the numerical solutions of the system of gap equations. In Fig. 7.4, the potential ϕ also reproduces very well the momentum dependence of the gaps in the relativistic limit. The slope of the shape function of the gap is slightly harder at $\sim k^{-1.85}$ than the high momentum tail of ϕ that behaves as k^{-2} but the agreement is very good close to the Fermi surface, around $k \approx k_F$.

One can see from these expressions that the typical Fermi momentum $k_{\text{supp.}}$ at which the gap become suppressed in the BCS limit is

$$k_{\text{supp.}} = \frac{2\pi}{g} m_\phi \quad (7.22)$$

When considering heavy mediator, *i.e.* $m_\phi > m$, the BCS treatment applies and for reasonable couplings, the exponential density suppression happens at relativistic densities, $k_{\text{supp.}} \gg m$. Going to the non-relativistic limit, $k_F \ll m$, when considering heavy mediators, it is therefore expected that the gap will be exponentially small and completely irrelevant for such scenarios. In this regime, analytical computations are possible, the overall dependence is slightly modified but as the gap will be exponentially small, no phenomenological relevance is expected and it would be extremely numerically challenging to compare the analytical solution to the numerical ones. Therefore, this regime will not be presented here. The study of the other gaps will be postponed shortly after the range in Fermi momentum has been extended to the non relativistic regime.

7.2.2 The gaps $\tilde{\Delta}_-$ with light mediators

The gap equations of Eqs. (7.15–7.17) are valid beyond the heavy mediator limit and it will be very interesting to study these regions of the parameter space. Such cases might not be encountered in practice in a laboratory or in neutron stars, nevertheless dark matter phenomenology allows very naturally for the exploration of these new, as of now uncharted, regimes. Light mediator scenarios with $m_\phi \ll m$ will now be treated.

It is expected that, given a mediator mass, pairing should vanish once the gas is so dilute that the interparticle spacing is much greater than the interaction range, $k_F^{-1} \gg m_\phi^{-1}$. In contrast with the BCS picture, the suppression could therefore happen at densities at which the fermions will be non-relativistic, hence sizeable gaps are expected even in very dilute gas. As is seen from Eq. (7.15), the shape function, *i.e.* the momentum dependence of the gap, will be non trivial in this limit. Once the Fermi momentum is such that the Fermi surface is relativistic, k_F becomes the biggest scale in the system and each quantity should therefore depend only on this parameter. In particular, the previous discussion applies and hence one should recover the ansatz of Eq. (7.21) in the unsuppressed density regime.

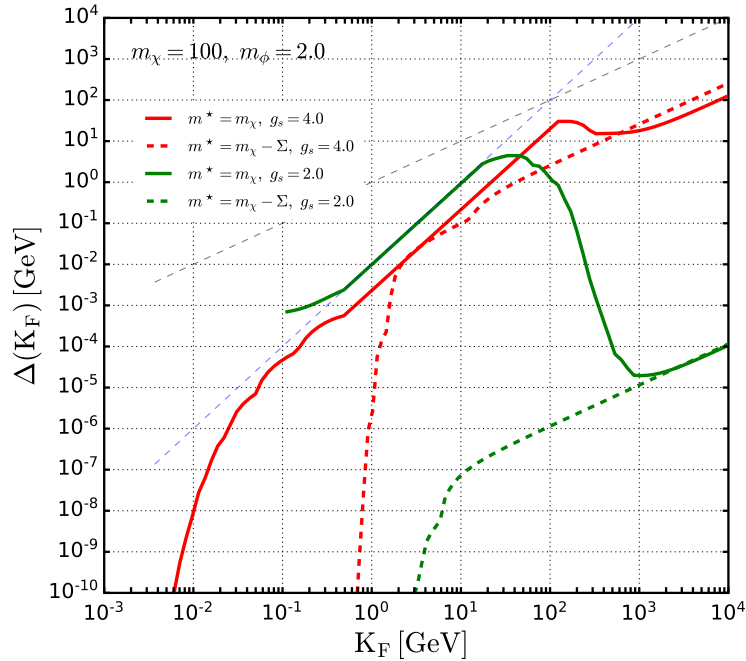


Figure 7.5: Normalization of the gap $\tilde{\Delta}_-$ in the light mediator regime. The DM mass is fixed at $m = 100$ GeV. The mediator is light, $m_\phi = 2$ GeV, such that $m_\phi/m = 0.02$. We show the cases $g = 4$ (red) and $g = 2$ without (solid) and with (dashed) the scalar condensate taken into account. The dashed grey lines are $\propto k_F$ and $\propto k_F^2$.

In Fig. 7.5, we give in solid line the normalization of $\tilde{\Delta}_-$ in the limit of light mediators, $m_\phi/m = 1/50 \ll 1$, for two different representative couplings. At high $k_F \gg m, m_\phi$, the gap is proportional to k_F and we recover the relativistic limit. However, in the non relativistic limit, light mediators allow for much bigger gaps than what the BCS treatment would typically yield. For the green curve ($g = 2$), it is interesting to note that in the ultra relativistic limit, the normalization of the gap $\tilde{\Delta}_- \propto \exp(-8\pi^2/2^2) \approx 10^{-9}$ is small but once $k_F < m$, the gap becomes comparable to the case with $g = 4$ (red line). This hints to the fact that the coupling dependence of the non-relativistic, light mediator regime is different from the ultra relativistic regime.

Let us now introduce the condensate. For $g = 2$ and $g = 4$, the coupling that enters in the condensate is $C_\phi^2 = 337$ and $C_\phi^2 = 1350$ respectively. Given these interactions strengths, the DM is effectively massless down to small k_F . In turn, the mediator is heavy when compared to m_* , and the system behaves as the BCS ansatz (dashed lines). We have checked numerically that for the parameters of Fig. 7.5, the gap had no influence on the condensate (see Eq. (7.17)). However, for $g > 7$, we have found that the gap contribution tends to boost the condensate, but we do not trust our equations in that regime.

We stress that obtaining Fig. 7.5 is numerically very challenging and much effort is left in order to fully explore the dependence of the solutions in coupling and mediator mass. In the following months, we will pursue further towards a complete understanding of the light mediator regime.

Chapter 8

Thermodynamics, phase transition and dark matter clouds

The aim of this chapter will be to compute the free energy of the system of interacting gas, in presence of the gaps and condensate, at zero temperature and finite density. Building upon the solutions to the gaps and condensate coupled equations found in the previous chapter, the free energy of the system is known and every thermodynamics quantities can be computed by taking the appropriate derivatives of it. Given the attractive interactions between the fermions, a (super-)gas to (super-)liquid transition should be expected at high densities. More precisely, the system should be seen going from a low density regime to a higher density one, which is dubbed liquid once the attractive self-interactions are strong enough to bind the fermions together. The order parameter of this transition will be the gaps and condensate, whose overall normalization will also jump from gas to liquid. Conversely, given a density, if the attractive interactions are strong enough, the liquid state should also appear. Packing further fermions together and, perhaps, compressing the system should, in principle, also give rise to a crystal-like solid phase. However, keeping in mind the context of DM, it would be difficult to have a handle on the pressure of the system, as would be done in a laboratory, and the solid state will not be discussed, even though one could in principle study it. An interesting consequence of superfluidity is its peculiar transport properties, but they will not be discussed in details within these pages.

This study of the thermodynamics of the system will pave the way for building self-gravitating DM “clouds”, which require as input the Equation of State (**EoS**) of the system, *i.e.* the pressure P as a function of the energy density ϵ , $P(\epsilon)$. If the temperature T is not negligible, one should specify the EoS at every T . This is very reminiscent of Neutron Star (**NS**) physics for which at very high densities, one develops a phenomenologically motivated EoS for nuclear matter obtained from nuclear potentials at moderate densities and then constrains it by building a mass–radius relationship that depends on the central density of the compact object (which is not accessible by observation). The origin of the constraints are, for example, the ability of the EoS to provide observed NS masses and radii and reproduce other observed characteristics such as tidal deformability. As a final comment, it is very interesting that one can probe the microphysics of nuclear matter by observing such macroscopic objects. *A priori*, DM clouds can have arbitrary sizes and one is allowed to explore other scales by simply considering other ranges of the parameters of the lagrangian. In the following, the focus will be on two different type of DM clouds that can be argued to exist in our Universe. If the galactic halos of DM reach thermodynamical equilibrium, they can be thought of as a galactic size star, supported by internal pressure against gravitational collapse. The “dark stars” mass–radius relationship will therefore need to reproduce observed DM halos and one will be able, for an example of a phenomenological application, to determine if they exhibit a cored or cuspy profile at their center. At very small scales, DM capture inside compact

objects such as neutron stars can lead to self-gravitating DM clouds of order of the centimetre. This DM cloud could, perhaps, behave very differently due to its superfluid nature, behaviour that is yet to be determined. The DM cloud could further grow through capture and, in contrast with what is expected with a DM cloud for which self-interactions are negligible, it could reach its Chandrasekar limit within the lifetime of the NS and collapse, depending on what its exotic EoS might be. From a phenomenological point of view, it is striking that the DM pervading the Universe could be in a phase that is very different from a simple free gas.

8.1 Thermodynamics, phase transition

This section is dedicated to the study of the impact of the condensate on the thermodynamic properties of the system.

The free energy of a degenerate system of spin 1/2 fermion of mass m , interacting through a Yukawa interaction of strength g thanks to a mediator ϕ of mass m_ϕ in which superfluidity is negligible (for example, if g is small) is given by [200]

$$\Omega = -2T \int \frac{d^3p}{(2\pi)^3} \left[\log \left(1 + e^{-\beta(\omega_* - \mu)} \right) + \log \left(1 + e^{-\beta(\omega_* + \mu)} \right) \right] + \frac{1}{2} m_\phi^2 \phi^2 \quad (8.1)$$

where $\omega_* = \sqrt{m_*^2 + p^2}$. The pressure P is simply minus the free energy and takes the following form in the zero temperature limit [207]

$$P = -\Omega = \frac{m^4}{3\pi^2} \left(-\frac{\varphi^2}{2C_\phi^2} + \int_0^{k_F/m} \frac{x^4}{\sqrt{x^2 + (1 - \varphi)^2}} dx \right) \quad (8.2)$$

The energy density ϵ is then found through

$$\epsilon = \mu n - P \quad (8.3)$$

$$= \frac{m^4}{3\pi^2} \left(\frac{\varphi^2}{2C_\phi^2} + 3 \int_0^{k_F/m} x^2 \sqrt{x^2 + (1 - \varphi)^2} dx \right) \quad (8.4)$$

where the number density of particles¹ is given by $n = k_F^3/3\pi^2$ for k_F the Fermi momentum. Alternatively, the energy density of the fermions is simply given by the integral over all momentum of the Fermi-Dirac distribution weighted by the energy of each mode. The chemical potential is then related to k_F by $\mu^2 = m_*^2 + k_F^2$ where m_* is the effective mass of the fermions in the medium. The adimensional condensate $\varphi = \Sigma/m$ that renormalizes the mass $m_* = m(1 - \varphi)$ is determined through the following equation

$$\frac{\varphi}{C_\phi^2} = 3 \int_0^{k_F/m} x^2 \frac{1 - \varphi}{\sqrt{x^2 + (1 - \varphi)^2}} dx \quad (8.5)$$

which is the same as Eq. (6.13). Note that it is easy to accommodate for repulsive interactions by introducing a vector boson. In that case, the thermodynamic potential will look very closely to what has been presented above. Such simplified system has been treated extensively in nuclear

¹This statement is actually a theorem, attributed to Luttinger, well known within the condensed matter community. It states that the volume of the Fermi sphere, which is nothing else than the number density of particles – up to a factor 2 for the spin factor – is a constant quantity, even in the presence of deformation due to interactions.

physics – the so-called $\sigma - \omega$ model – in order to understand the properties of nuclear matter at very high densities. Neutrons, protons interact attractively by exchange of the scalar σ meson and repulsively by exchange of the vector meson ω . Condensation of σ renormalizes the mass, condensation of ω (more precisely, the 0th component of $\langle \omega^\mu \rangle$ by virtue of rotational symmetry) renormalizes the chemical potential and by fitting the couplings $g_{\sigma, \omega}$ to measured quantities, one is able to reproduce some characteristics of nuclear matter. Interestingly, this is similar in spirit to a Lennard-Jones-type potential and some features are expected to be shared between them. For the scenario that is treated here, the same parallel can be made, with the attractive interaction rising from the exchange of the scalar mediator and the degenerate Fermi pressure at relativistic Fermi momentum balancing it. In order to know the thermodynamics of the system, given a m and a C_ϕ^2 , one solves Eq. (8.5) for φ at every k_F and then computes $P(k_F)$ and $\epsilon(k_F)$. The pressure and energy density of a free gas (no interactions) is recovered by taking the limit $C_\phi^2 \rightarrow 0$ which, in turn, sends $\varphi \rightarrow 0$ and the in-medium mass becomes the bare mass, $m_* = m$.

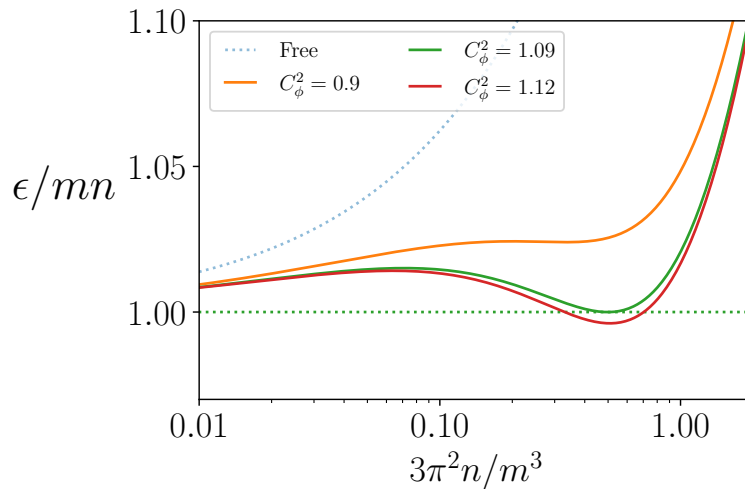


Figure 8.1: Binding energy per particle as a function of density for different coupling C_ϕ^2 . The blue dotted line corresponds to a free gas. Below $\epsilon/mn = 1$ (dashed green), matter can clump into nuggets.

It is interesting to first look at the binding energy per fermion as a function of density, which will broadly paint the behaviours of this thermodynamic system. In Fig. 8.1 is given ϵ/mn as a function of the adimensionalized density $(k_F/m)^3$. For $C_\phi^2 \ll 1$, one recovers the non-interacting case. For $C_\phi^2 > 1.09$, the binding energy becomes bigger than the rest mass of the fermions and therefore a global minima develops at high density. This signals that the matter in the system can clump into stable bound states of high densities, the so-called “nuggets” [209, 210], which are therefore in what is identified as the liquid phase.

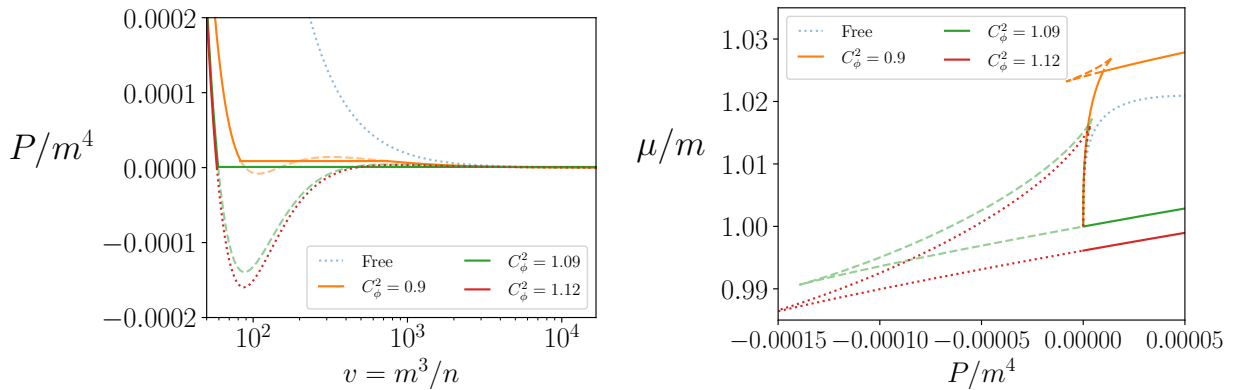


Figure 8.2: Maxwell construction of the physical equation of state. Left : Pressure as a function of volume. Right : Chemical potential as a function of pressure. The dashed and red dotted states do not correspond to equilibrium configurations.

In order to better understand the behaviour of the system at different densities and coupling, the “isothermal curves” of the pressure P as a function of volume $v = 1/n$ are shown see Fig. 8.2, as is usually done for the van der Waals equation of state in textbooks [211]. In this system, the inverse of the coupling $\tau = 1/C_\phi^2$ plays a role analogous to the temperature. Indeed, at high τ (small C_ϕ^2) the system can only be in the gas phase whereas at small τ (high C_ϕ^2) the system can be put in a high density phase, as has been argued from the binding energy. From the free energy expression, the conjugate variable to τ is identified to the square of the scalar density, φ^2 . For $C_\phi^2 > 0.841$, $P(v)$ start developing a local minima at small volume and for $C_\phi^2 > 0.885$ the minima becomes global with the pressure dropping below 0. For strong enough interactions, some portions of the $P(v)$ curves have $dP/dv > 0$, meaning that the compressibility of the system is negative and that these regions are unstable under any small perturbations. If prepared in such states, the system is expected to collapse to a mixture of state at low and high density at the same pressure. The description of these regions obtained from Eq. (8.1) is therefore unphysical and a more careful treatment which takes into account the phase transition is needed.

Building the physical EoS is a matter of finding the equilibrium states and identifying the metastable and unstable configurations. Let us now summarize how the physical EoS can be build from the standard Maxwell constructions [211]. The Gibbs-Duhem relation $d\mu = -sdT + vdP$ provides, at constant temperature (in our case, it would be constant τ), a relation between the chemical potentials between two states A and B taken to be, say, at low and high density respectively and the area under the curve $v(P)$ between those two states

$$\mu_B - \mu_A = \int_A^B v(P) dP \quad (8.6)$$

which, of course, depend on the coupling. For appropriately chosen states A and B , it possible for the chemical potential of, say, B , to be bigger, lower or equal to the chemical potential of A . As can be seen on the right of Fig. 8.2, many different state share the same equal pressure P but different volumes v . The essence of the Maxwell construction is, for an EoS $P(v)$, identifying the two states A and B such that they are at equal pressure and at the same chemical potential. Using Eq. (8.6), this amounts to look for two points on the $P(v)$ such that the areas between the curve and a constant line at constant P (which is the pressure of both the state A and B) is the same under and above. In Fig. 8.2, the orange curve ($C_\phi^2 = 0.9$) showcases such construction.

On the right of Fig. 8.2 is given $\mu(P)$ for the free case and $C_\phi^2 = 0.9, 1.09, C_\phi^2 = 1.12$. Following the standard Maxwell construction of the physical EoS, the physical iso-coupling for $C_\phi^2 = 0.9, 1.09$ have been explicitly constructed and are presented as the continuous green and red lines respectively, with the unphysical iso-coupling in dashed. For those curves, the first derivative of the pressure (and hence the free energy) with respect to the volume is discontinuous near the gas and liquid density and the system exhibits a first order phase transition. As can be seen, as the coupling grows, the gas to liquid phase transition happens at smaller and smaller densities. Interestingly, for $C_\phi^2 > 1.09$, the Maxwell construction cannot be performed since no couple of state with different densities but with same μ and P exist. Put in another way, for large enough coupling, the area between the $P < 0$ region of the curve and the $P = 0$ horizontal axis is bigger than the area under the curve of the region where $P > 0$, even if integrated up to infinite volume.

The phase diagram of the model at zero temperature is given in Fig. 8.3 and is interpreted as follows. Given a coupling C_ϕ^2 , a system prepared at density n/m^3 could be in an equilibrium configuration that is a gas, a liquid or a mixture of the two. The systems with a couple $(C_\phi^2, n/m^3)$ in the blue or orange region will be in a gas or liquid phase respectively and the systems set in the green region will exhibit a gas and liquid phase coexisting at equal pressure. As has been argued above, it is also possible for the system to not have any equilibrium configuration and only be able to set itself in metastable (perhaps very long lived) or unstable states and the region where such behaviour happens has been hashed in red. Ultimately, once gravity will be considered, those regions will not be accessible (since they are either in tension² or would collapse to the liquid phase due to chemical potential being lower in the high density phase) and they will not be studied further. At low coupling (high “temperature”, purple region), there is no phase transition and one can go smoothly from the gas to the liquid phase. This is done by dialing the coupling C_ϕ^2 and the density n (like in the case of the gas-liquid) and this region is what is commonly called a crossover. Within the coexistence region, the gas and liquid fraction can be computed and as C_ϕ^2 reaches 1.09 from below, the gas fraction tends to zero and the gaseous phase disappears. Finally, the question of the impact of the gaps on the thermodynamics of the system could be easily understood by assessing their impact on the phase diagram. The parametric dependence on the masses and coupling would however be more complicated as the gaps are sensitive to both m_ϕ and g and not only the combination C_ϕ^2 .

²Or, equivalently, at negative pressure.

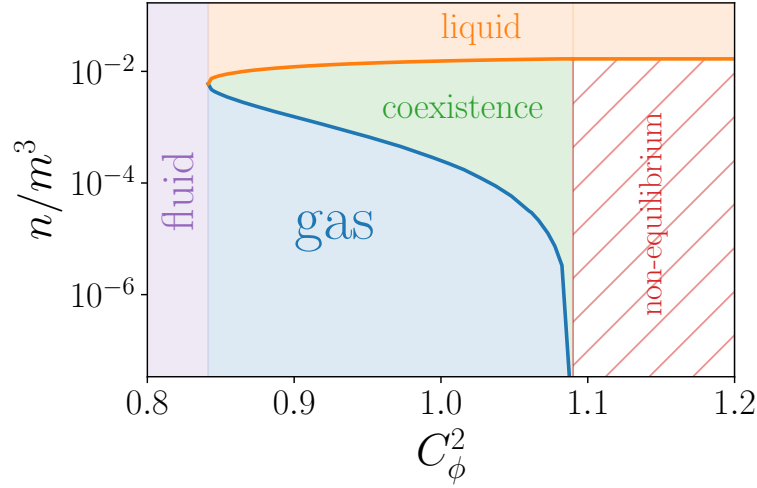


Figure 8.3: Phase diagram in the density–coupling plane of matter described by Eq. (8.1).

As mentioned before, the setup of this model closely resembles that of the Lennard-Jones potential and a similarity between both phase diagrams is expected. On the left of Fig. 8.4, the phase diagram of the Yukawa model is given in the $P-\tau$ plane, that is pressure and “temperature”, which is mimicked by the inverse coupling $\tau = 1/C_\phi^2$. Following the labelling of Fig. 8.3, for high τ (low coupling), there’s no phase transition and the phase is that of a self-interacting gas, dubbed here fluid. At moderate τ ($0.841 < C_\phi^2 < 1.09$), a stable gas phase appears at low pressure and a stable liquid phase appears at high pressure. Both phases are separated by the binodal (solid green line) and the critical point is marked by a diamond. Finally, at low τ (high C_ϕ^2), the only stable phase is the liquid. On the right of Fig. 8.4 is presented the phase diagram of ${}^4\text{He}$ in the $P-T$ plane, which share similar features.

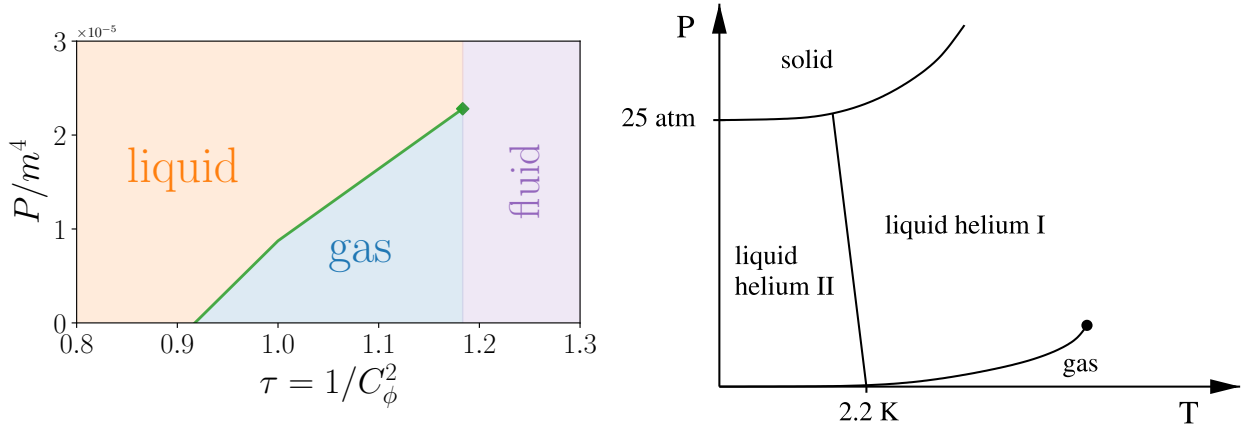


Figure 8.4: Right: Phase diagram in the pressure–inverse coupling plane of matter described by Eq. (8.1). Left: Phase diagram of ${}^4\text{He}$, taken from [203]. Both diagrams exhibit a gas-liquid phase transition.

8.2 Building clouds

Now that the thermodynamics of the system have been discussed, it is interesting to use those informations to look at what a cloud of self-interacting asymmetric fermions (which are assumed to be the DM) could be and try to understand its relevancy in DM phenomenology. Self-gravitating

spherically symmetric configurations of a perfect fluid with a given EoS $P(\epsilon)$ are obtained by solving the Tolman–Oppenheimer–Volkoff (**TOV**) system of equations [212]

$$\frac{dP(r)}{dr} = -\frac{G}{r^2} \left(\frac{P(r) + \epsilon(r)}{1 - \frac{2GM(r)}{r}} \right) (M(r) + 4\pi r^3 P(r)) \quad (8.7)$$

$$\frac{dM(r)}{dr} = 4\pi r^2 \epsilon(r) \quad (8.8)$$

where r is the distance to the center of the object and $M(r)$ is the enclosed mass within this radius, $G = 1/M_P^2$ being Newton's constant. It is readily seen that General Relativity (**GR**) corrections have been included, since the question of the collapse of the DM cloud – in other word, the Chandrasekar limit – will be of interest for the case of DM capture and gravitational collapse inside neutron stars. These equations can be solved by using the EoS to change the system into a set of equations for $\rho(r)$ and $M(r)$, set the central initial conditions to be $\rho(0) = \rho_0$ for some central density ρ_0 , $M(0) = 0$ and integrate the system up to the radius r_c at which the pressure reaches zero, $P(r_c) = 0$. It is standard for r_c to then be used as the size of the configuration. Another criteria would be to define the radius of the object as the radius which encloses, say, 90% of the total mass of the object. For every scenario that will be treated in this work, it has been checked that both criteria gives very similar radii and the former definition will be used in the following. The system can be further simplified by introducing the dimensionless Landau variables M_L, R_L [213]

$$M' = \frac{M}{M_L}, \quad r' = \frac{r}{R_L} \quad (8.9)$$

where $M_L = M_P^3/m^2$, $R_L = M_P/m^2$. These variable absorb factors of the fermion mass from the pressure $P \equiv m^4 P'$ and energy density $\epsilon \equiv m^4 \epsilon'$ such that the dependency on m disappears from the new system

$$\frac{d\epsilon'(r')}{dr'} = -\frac{1}{c_s^2 r'^2} \left(\frac{P'(\epsilon'(r')) + \epsilon'(r)}{1 - \frac{2M'(r')}{r'}} \right) (M'(r') + 4\pi r'^3 P'(\epsilon'(r'))) \quad (8.10)$$

$$\frac{dM'(r')}{dr'} = 4\pi r'^2 \epsilon'(r') \quad (8.11)$$

where $c_s^2 = dP/d\epsilon$ is the sound speed. For ease of conversion, at the galactic and neutron star scales it is convenient to know that

$$M_L = \frac{M_P^3}{m_f^2} = 1.63 \left(\frac{\text{GeV}}{m_f} \right)^2 M_{\text{sun}} \quad (8.12)$$

$$R_L = \frac{M_P}{m_f^2} = 80 \left(\frac{\text{eV}}{m_f} \right)^2 \text{ kpc} = 2.5 \left(\frac{\text{GeV}}{m_f} \right)^2 \text{ km} \quad (8.13)$$

8.2.1 Free, degenerate DM halos

The physics of halos is best understood by first considering a free and degenerate gas at zero temperature. In that case, the equation of state at both $k_F \ll m$ and $k_F \gg m$ are simply given by

$$P = \begin{cases} \epsilon/3 & k_F \gg m \\ \frac{(3\pi^2)^{2/3}}{5} \epsilon^{5/3} / m^{8/3} & k_F \ll m \end{cases} \quad (8.14)$$

and the polytropic exponent $\gamma = d \log P / d \log \epsilon$ therefore being 1 (5/3) in the (non-)relativistic limit. The case of DM halos allows for many simplifications of the EoS and TOV equations. A DM

halo is far from gravitational collapse and the GR effects in Eq. (8.7) can be neglected. Furthermore, since the density of DM halos is small, a degenerate halo is expected to be non relativistic and thus behave as a polytropic fluid with $\gamma = 5/3$. Under these assumptions, the TOV equations can be recast in a simple Lane-Emden equation which further eliminates the dependency on the central density [174].

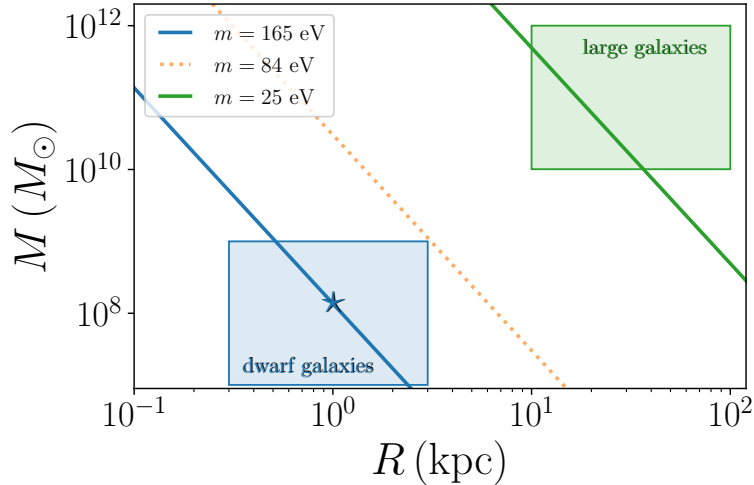


Figure 8.5: DM halo mass–radius relationship for a free degenerate gas of fermions. The different line corresponds to different values of the fermion mass. Each line is parametrized by the central density of DM, top left corresponding to higher densities and bottom right to lower densities.

In Fig. 8.5 are given the mass–radius relationship for $m = 165$ eV (solid blue), $m = 84$ eV (dashed orange) and $m = 25$ eV (green). The blue (green) shaded area is the typical range in total mass and radius of (large) dwarf galaxies. For a given cloud mass, as the fermions are taken to be lighter and lighter, their number density increases, the fermions are packed up to higher and higher Fermi momentum, resulting in a higher Fermi pressure and therefore more puffy configurations (*i.e.* larger radii). It is seen that for the scenario of degenerate DM halo, a given DM species cannot account for both a core in the dwarfs and large galaxies halos. In turn, this argues for the existence of a lower bound on the mass of a fermionic DM candidate below which it would be impossible for halos at the scales of dwarf galaxies to be compact enough. This bound is known at the Tremaine-Gunn (**TG**) bound and in the following, the physics of several approaches to it will be discussed and detailed. Once the physics of the TG bound has been established, it will be shown that the TG bound can be violated in scenarios will self-interactions and medium effects that are phenomenologically viable. For the specific scenario of a degenerate gas of free fermion, the naive TG bound is $m > 84$ eV and this candidate’s $M - R$ relationship is given in dotted lines in Fig. 8.5. This treatment can however be refined. As a final comment, we mention that the virial temperature of the halo can be higher than the degeneracy pressure at large distance from the core. The halo would then be composed of an isothermal halo with a degenerate core [173].

8.2.2 The Tremaine-Gunn bounds

Since the study of velocity dispersion of galaxies and clusters unveiled the DM problem, the nature of the constituents of DM can be constrained by the very same observations. The TG bound is a limit on the smallest allowed DM mass (in the case of fermionic candidates) such that properties of dwarf galaxies – which are thought to be DM dominated objects – are well reproduced by the DM halo.

For a fully degenerate halo, the formulation of the bound is particularly straightforward. Assuming spherical symmetry, the Fermi velocity at some point r should be less than that of the escape velocity at the same radius, $v_F(r) \leq v_{\text{esc.}}(r)$. Evaluating the bound at some very large radii which encloses the majority of the DM halo gives the lower bound [214, 215]

$$m_{\text{deg.}} \geq \mathcal{O}(100) \text{ keV} \quad (8.15)$$

This bound can be strengthened if it is evaluated at smaller radii, which however requires the additional input that is the DM profile. To that goal, one can use the full information that the measurements of velocity dispersion provides, *i.e.* including higher moments, such that the range of realistic DM profiles can be constrained [216]. It would be interesting to include the self-consistent halo profile for the case of purely degenerate fermion obtained from the TOV equations in such analyses. As it will be detailed later, this step is actually necessary once self-interactions kick in and both approaches could perhaps benefit from each other and provide the most constraining bounds (which albeit would become more model dependent). In other words, the naïve TG bound quoted in the previous section only uses the informations that are the total mass and radius at large r and it would be interesting to test if the fully degenerate DM profile might be in tension with the constraints obtained at smaller r .

However, this is not the only physical argument that one can use to give a bound on the fermion mass. Historically, the following arguments have lead to what is commonly known as the Tremain-Gunn bound [214]. For a given system of collisionless and dissipationless fermions, regardless of the potential that they find themselves in, the phase space density $f(x, p, t)$ (which gives the probability that the system will be in a given state (x, p) at time t) is constant along any trajectory (determined by the potential) in phase space. One can then choose an initial phase space density in the very Early Universe, for instance motivated by a certain DM production mechanism. By virtue of Liouville's theorem, the phase space density *today*, for example in a DM halo, should have been conserved along the history of the Universe. An important point is that due to the incompressibility of the flow of the phase space density in phase space, the maximum of f is the same at all time [214]. With this information at hand, one can then estimate from observation the maximum f_{max} of $f(x, p, t)$ today and require the maximum $f_{\text{max},0}$ of $f(x, p, t=0)$ in the Early Universe to not be smaller than f_{max} . However, we do not know $f(x, p, t)$ everywhere, only its average coarse-grained value \bar{f} over a certain volume in phase space. The maximum of \bar{f} will necessarily be smaller than f_{max} and due to the inherent errors in measurements, it is not possible to constrain the evolution of f as much as Liouville's theorem allows us. Nevertheless, a key point is that f_{max} (and equivalently \bar{f}_{max}) will depend on the DM mass, as is evident from Fig. 8.5 for instance. Using $\bar{f}_{\text{max}} \leq f_{\text{max},0}$, one is able to put a constrain on the lowest fermionic DM mass allowed. Even though both arguments presented here are based on very different physics, the TG bound is very close to Eq. (8.15).

8.2.3 Beyond Tremain-Gunn with self interactions

In this section it will be assumed that DM halos are degenerate and interact attractively, thus allowing for a scalar condensate to form. The superfluid character will be neglected and it will be seen *a posteriori* that this approximation is valid. The discussion on the phenomenological viability of the DM candidates are relegated to the end of this section.

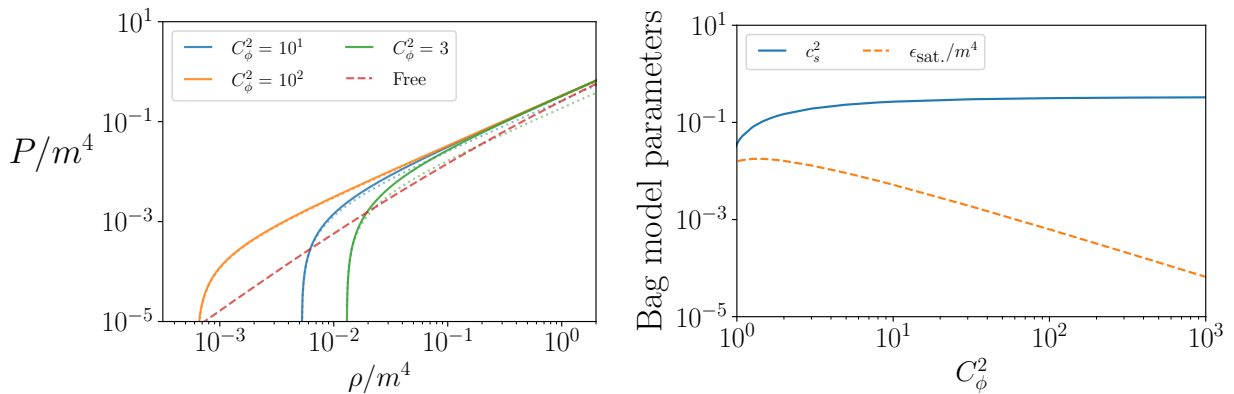


Figure 8.6: Left : Equation of state $P(\rho)$ of the liquid phase (solid lines) for a few representative coupling. In dashed is given the equation of state of a free gas of fermions and the dotted line corresponds to the bag model of Eq. (8.16). Right : Parameters of the bag model of Eq. (8.16) of the liquid phase as a function of coupling.

Given a coupling, the equation of state $P'(\rho')$ can be calculated. The scenarii that will be most relevant are those with $C_\phi^2 > 1.09$ and a few typical EoS are given in Fig. 8.6 (continuous lines). In dashed is presented the EoS for a free gas. For this curve, at low density, the slope is $\propto \rho'^{5/3}$ and as ρ' approaches 1, it smoothly transitions to the relativistic limit $P' = \rho'/3$. For the interacting liquid, as C_ϕ^2 grows, the relativistic limit can be reached at $\rho' \ll 1$, since the effective mass in the medium is small, $m_* \ll m$, and Fermi pressure takes over. For each coupling, P decreases rapidly at low density, close to their respective $\epsilon_{\text{sat.}}$. Interestingly, for the EoS presented in Fig. 8.6, their particular form is actually indicative of the appearance of something analogous to an incompressible fluid of density $\epsilon_{\text{sat.}}$. Very close to the saturation density, it is found that the EoS can be approximated by a “bag model”

$$P \stackrel{\epsilon \rightarrow \epsilon_{\text{sat.}}}{\approx} c_s^2 (\epsilon - \epsilon_{\text{sat.}}) \quad (8.16)$$

where c_s is the speed of sound. For simplicity, the speed of sound is taken here to be evaluated at saturation density and depends on the coupling, hence it has to be determined numerically. Both parameters of the EoS can be found in Fig. 8.6 as a function of coupling for completeness. In Fig. 8.6 are given in dotted line the corresponding bag EoS and qualitatively good agreement is seen close to the saturation density for each coupling. For such type of matter, the polytropic exponent is given by $\gamma = (1 - \epsilon_{\text{sat.}}/\epsilon)^{-1}$ and, at densities just above saturation, γ becomes large. This indicates that a small change in density results in a significant variation in pressure. It is tempting to qualify such fluid to be incompressible, but incompressibility would necessary violate relativity, since the sound speed would be infinite (cf rigid rod). As is evident from Figure. 8.6, the speed of sound at saturation instead asymptotes $c_s^2 = 1/3$ at high coupling. One can also compute the compressibility factor $K = p_F^2 \frac{d^2}{dp_F^2} (\epsilon/n)$ near saturation density. For a free gas, K tends to 0 both in the non-relativistic and relativistic limit, and reaches a maximum of ~ 0.3 in the intermediate regime. In the case of the bag model, at high coupling, K is instead bigger than 1. For comparison, an incompressible fluid is expected to have an infinite compressibility factor. One can therefore interpret a fluid with the EoS of Eq. 8.16 to be as incompressible as relativity allows. In nature, such fluid is realized in nuclei.

In the incompressible limit, numerical scans can be performed [209] and the mass–radius relationships of the incompressible fluid as a function of DM mass and coupling can be obtained and

is given by

$$\left(\frac{M}{10^8 M_\odot}\right) \left(\frac{\text{kpc}}{R}\right)^3 = \frac{4170}{C_\phi^2} \left(\frac{m}{\text{eV}}\right)^4 \quad (8.17)$$

where the typical values of masses and radii of a dwarf galaxies have been chosen on the left hand side. It is reminded that it is assumed that $C_\phi^2 > 1.09$ in order for the liquid phase to be dominant. It has been explicitly checked that for high coupling ($C_\phi^2 > 10$) the agreement between the mass–radius relationships obtained from the numerical EoS and the bag model of Eq. (8.16) has typically an error of less than 10% across all range in energy density.

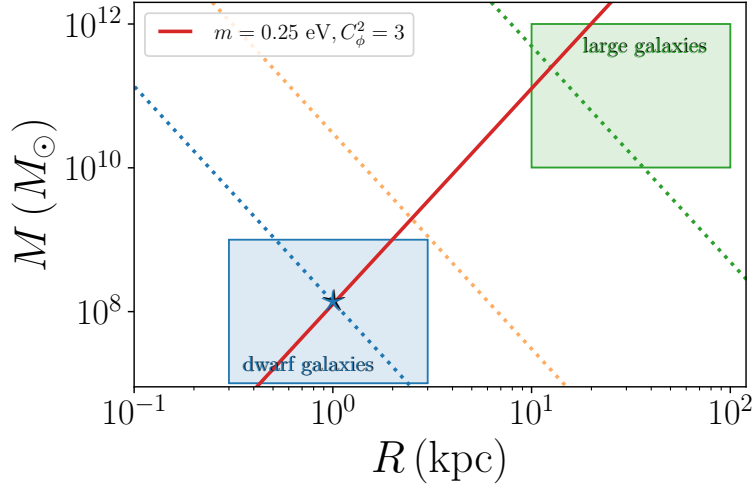


Figure 8.7: DM halo mass–radius relationship for a self-interacting degenerate gas of fermions that is dominated by the condensate (solid red). In dashed, a few mass–radius relationship for free degenerate fermions are reproduced, see Fig. 8.5.

In Fig. 8.7 the typical masses and radii of the halos of dwarf galaxies and large galaxies are given as the blue and green shaded area respectively. In the same Figure is given as the continuous line the mass–radius relationship of a candidate with $m = 0.15$ eV and $C_\phi^2 = 2$. As can be seen, due to self-interactions and medium effects, a dwarf galaxy halo mass and radius can be reproduced for very small DM masses. The benchmark point of 8.7 is much smaller than the minimum mass implied by the TG bounds. For large C_ϕ^2 , see the last row of Table 8.1 for such a candidate, the Fermi velocity of the constituent reaches 1 and the condition of Eq. (8.15) fails. This highlights the fact that for halos with non-trivial dynamics, it is necessary to self-consistently solve the TOV in order to obtain the DM profile.

As is seen in Fig. 8.7, given two different central densities, the *same* DM candidate that reproduces a dwarf galaxy halo with $M = 10^8 M_\odot$ $R = 1$ kpc can in addition reproduce a typical halo for large galaxy, with a typical radius of 10 kpc and a halo mass of $10^{11} M_\odot$. The density profile of both halos are constant with central density $\epsilon_{\text{sat.}} \sim 0.24 \text{ eV}^4$ and abruptly goes to zero once saturation density is reached. Both halos therefore exhibit a cored profile. Within the scenario where an asymmetric DM candidate has self-interactions strong enough to develop a condensate and form self-gravitating nuggets, the mechanism that solves the core-cusp problem is straightforward and very different to what has been presented in Section 1.2.

As mentioned above, at “large” radius, the virial temperature of a typical dwarf galaxy has been shown above to be higher than the free fermions degeneracy temperature³. In this case, the halo is composed of a degenerate core supported by Fermi pressure and an isothermal halo in the outer regions. Given the benchmark model shown in Fig. 8.7, a similar situation could happen, for which the core is a nugget (the liquid phase) and the rest of the halo is purely in the gas phase at temperature above the liquid–gas transition critical temperature. At high C_ϕ^2 , the nuggets are tightly bound, the binding energy being of the order of the mass of the constituent and the critical temperature is expected to be similarly high. Conversely, for $C_\phi^2 \sim 1$, the binding energy is a small fraction of the rest mass and the nuggets are therefore loosely bound. Light candidates with small C_ϕ^2 , such as in Fig. 8.7, are therefore expected to exhibit a liquid–gas transition, which could naturally provide a cored profile in the inner regions with a diffuse outer halo. Those effects have not been taken into account in this work but could result in a promising avenue for explaining the behaviour of DM halo profiles from dwarfs to clusters. Since the candidate of Fig. 8.7 can reproduce both a dwarf galaxy and a large galaxy, the core of both galaxies would necessarily be similar and provide a possible interesting signature of the model.

In Fig. 8.7, a potential DM candidate that provides a flat DM profile at the scale of dwarf galaxies and large galaxies has been identified. Since the connection between the dark sector and visible sector does not impact the EoS, the matter of assessing limits from, say, direct detection and cosmological bounds will not be studied. However, observations of the Bullet Cluster constraints the unavoidable DM self-interactions and a few paragraphs are now dedicated to confronting the benchmark point of Fig. 8.7 to this limit.

The impact of DM–DM scatterings on the Bullet Cluster observations is encompassed in an upper bound on the ratio of the transfer cross section σ_T to the DM mass m . Multiple estimations overall quote a value for the limit to be [34]

$$\sigma_T/m < 1 \text{ cm}^2/\text{g} \quad (8.18)$$

for which the relative velocity of DM particles is typically of $v = 2000\text{km/s}$ or equivalently $v/c = 6.7 \times 10^{-3}$. Throughout this analysis, those two values will be considered but it is stressed that a stricter bound on σ_T/m would not qualitatively change the results of the discussion. The scattering of two particles in an attractive potential is however not straightforward due to quantum effects and different physics are important in different regime. For the case at hand, the regime is classical and approximations are known in this regime [34].

m (eV)	C_ϕ^2	α_ϕ	m_ϕ (eV)	σ_T/m (cm ² /g)	Pass?
0.15	3	3×10^{-20}	10^{-11}	0.1	✓
0.15	3	3×10^{-19}	3×10^{-11}	7.6	✗
0.6	1000	10^{-19}	6×10^{-12}	0.16	✓

Table 8.1: Benchmark candidates that can reproduce a DM halo with $M = 10^8 M_\odot$ and $R = 1$ kpc, which is representative of DM halos in dwarf galaxies. In the second to last column is given their scattering cross section at cluster scales and the last column identifies the candidates who do not violate the bound of Eq. (8.18).

In Table 8.1 we give a few candidates that can reproduce a typical dwarf DM halo mass and radius along with their scattering cross section evaluated at the Bullet Cluster scales. The first two candidates have the same mass and C_ϕ^2 , hence their profile in dwarf is the same, but for the

³More specifically, above the degeneracy temperature of the typical candidates that reproduce the correct DM halo in the zero temperature limit, *i.e.* few tens of eV masses.

second, a slightly heavier mediator has been compensated by a bigger interaction strength so that the condensate is unaffected. However, the self-interaction cross sections of the second is bigger than that of the first and only the latter is consistent with the Bullet Cluster observations. The third candidate has a very large C_ϕ^2 , violates the TG bound and also passes the Bullet Cluster test. It is stressed that viable candidates respecting those 2 considerations are not restricted to the DM masses used in the benchmark points of Table 8.1 and the DM mass range can be extended above the GeV (with a correspondingly even lighter mediator). Finally, we mention that the mediator masses in Table 8.1 are close to the black hole superradiance bounds.

As is often the case, DM phenomenology delves in many areas of physics and other considerations might be important, for example cosmological ones. One important question that is left to answer is that of their production in the Early universe, which happens not to be straightforward. Clearly, if sub-eV mediators were ever in thermal contact with the SM heat bath at the time of DM production, they would contribute to N_{eff} both at BBN and CMB times. This is very much in tension with the standard thermal history of asymmetric DM candidates, which is now briefly described. At high temperature, a small asymmetry is generated in the dark sector through some additional physics or, less attractively, perhaps through some initial conditions. Then, the dark sector thermalizes at least with itself and DM undergoes freeze out once the dark sector temperature is low enough. With sufficiently efficient annihilation processes, the symmetric part of the DM can be annihilated away in, say, mediators and the asymmetric surplus remains. A DM candidate is then realised once the leftovers from the DM annihilation catastrophe have the right relic abundance, *i.e.* given a DM mass, the asymmetry and annihilation cross sections have been adequately chosen. It is then clear that, in such a scenario, the abundance of the light mediators would act as dark radiation throughout the evolution of the Universe and be very much in tension with every cosmological observable. The asymmetric DM relic abundance could perhaps arise from an asymmetric freeze-in, hence circumventing the problem of mediator production by some thermal bath. Such scenario faces many problems and might not be realisable [217]. Another possibility is that the lagrangian of Eq. (6.4) could only be an approximation of the model, perhaps only valid in its deconfined phase. The overall picture of the model could perhaps be that of a dark QCD sector, whose dynamics in the Early Universe might be best understood with other degrees of freedom. It was recently put forward that the degeneracy pressure of light DM candidates might be enough to impact drastically structure formations in the Early Universe [218] such that only an extremely small fraction of DM is allowed to be in the form of light fermions. Nevertheless, the situation under study is meant to be illustrative and a motivated invitation for further, more complete, study. Those problems are general for DM models with light fermions.

Chapter 9

General conclusions and perspectives

The dark matter puzzle was unveiled by the observations made by Fritz Zwicky in the 30's and, to this day, its nature still eludes us. Thanks to the tremendous efforts made by many communities across physics, we are now, today, certain that DM cannot be many things, but do not know much about what it *is*. The goal of this thesis was to continue to explore this puzzle.

In this thesis, we have explored many aspects of DM phenomenology. The richness and relevance of DM in today's scientific panorama brought us to study DM at early time, in the hot and dense primeval Universe, and at late time, *i.e.* today. In turn, this thesis touched upon many areas of physics : from high energy physics and particle physics, both from theoretical and experimental aspects, to the use of the tools of Quantum Field Theory and statistical physics for applications of condensed matter and nuclear physics phenomena and to the astrophysical aspects of DM halos. We have focused our manuscript on a very popular class of DM models which comprises of a fermionic DM candidate which interacts with a bosonic mediator, that is either of spin 1 (part I of this thesis) or spin 0 (part II of this thesis). Within this context, we have shown in particular that hot and dense media can impact drastically the behaviour of a DM candidate and unveiled new effects that were either not studied or overlooked. Throughout the thesis, we have argued that our results should not be seen as restricted to the models we have studied (except when we have explicitly stated otherwise, see Chapter 4) but are instead a general feature expected in many models that share the overall structure of the so-called “portal” interactions. It is very interesting that such simple structures can hide a great deal of physics and much is left to explore. We will now detail the results obtained in this thesis and describe possible follow-up and questions that naturally arise from our conclusions.

The first part of the thesis focused on the kinetic mixing portal and our related work [5] [4]. The model is that of a $U(1)'$ gauge group added to the SM. The associated dark photon is kinematically mixed with the SM hypercharge boson, which in turns allows for the DM candidate to interact with the SM by exchange of γ' . In Chapter 2, we presented in detail the model by considering the general case of kinetic mixing and mass mixing. In particular, we identified the coupling structure between each population (dark matter, dark photon, SM degrees of freedom) and briefly described UV completions. In Chapter 3, we set out to answer the question of DM (thermal) production in the Early Universe within this model. We thoroughly identified all possible dynamical mechanisms that can lead to the observed DM abundance: 9 distinct regimes can be operative, along 5 different dynamical mechanisms. Namely, they are the freeze-in (I), sequential freeze-in (II), reannihilation (III), secluded freeze-out (IV) and freeze-out (V) mechanisms. For each of those, except II, the main source of DM production can either come from the visible sector or from dark photons. Out of all of those, 4 regimes are new (Ib, II, IIIa, IVa) and one dynamical mechanisms (II) is also new. More generally, the common denominator of these new DM production mechanisms is that DM is

produced by on-shell mediators. In Chapter 4, we set out to tackle the peculiarities that arise from the kinetic mixing portal. We considered both the kinetic and mass mixing of the dark photon. Due to mixing with the photon, the dark photon inherits the photon’s thermal features and this quantitatively (but not qualitatively) changes the parameter space of DM candidates. We took into account the thermal effects on both the transverse and longitudinal polarization states of the dark photons and computed their abundances in the Early Universe, which can be very different when compared to their abundance when no thermal effects are taken into account. We then evaluated and discussed their impact on the production of DM and the DM candidates parameter space in each different dynamical mechanism. In Chapter 5, we pursued our phenomenological study of the DM candidates and the mediator, the dark photon, by looking at the constraints on the kinetic mixing parameter ϵ , the dark photon mass $m_{\gamma'}$ and the DM mass m_{DM} . We first presented a review of dark photon constraints under the assumptions that were relevant within the context of our scenario of DM production : the dark photon was not the DM and was lighter than the DM, $m_{\gamma'} < m_{\text{DM}}$, so that it decays visibly. We then focused on the direct detection of DM when the dark photon is light, $m_{\gamma'} < 40$ MeV. We focused on the upper bounds of the DM–nucleon spin independent cross section for WIMP candidates (short-range interactions) published by the direct detection experiments. We then described our recasting procedure of these bounds for the case of long-range interactions, which we argued is necessary for deriving the correct bounds. We also confronted our direct detection limits for long-range interactions with the light mediator bounds that were derived by the PANDAX-II experimental collaboration and by other groups using different recast method and concluded that our bounds were compatible with these results. We then identified DM candidates that were within reach of the direct detection experiments and had a self-interaction cross sections compatible with what is required for alleviating the small scale structure problems of collisionless DM. Finally, using our results on SM– γ' and DM– γ couplings in a medium shown in Table 4.1, we briefly discussed the possibility of making a dark star shine if it couples to photon through (only) a kinematically mixed dark photon, by giving a mass to the photon (breaking electromagnetism) at high DM densities.

From our description of the physics of the kinetic mixing portal, one finds many invitations to pursue its phenomenological study. Models with the 3 connections–3 sectors structure are expected to have a similar mesa diagram as what has been presented in this thesis, but there can be possibly interesting variations upon this theme. The most straightforward model to apply our findings to is the Higgs portal, where a fermionic DM candidate ψ has a Yukawa interaction with a scalar mediator ϕ which then mixes with the SM scalar through the interaction¹ $\phi^2 H^2$. If both ϕ and H have a vev, then there exists a mixing angle θ , analogous to the kinetic mixing parameter ϵ , and the phenomenology is essentially the same as the kinetic mixing portal, *i.e.* that of s –channel mediator. However, when there’s no mixing, *i.e.* $\langle \phi \rangle = 0$ and m_{DM} is bigger than the electroweak scale, we see that there exists no tree-level SM+SM \rightarrow DM+DM processes and that DM production by the SM can only proceed by the $2 \rightarrow 3$ process $HH \rightarrow \bar{\psi}\psi\phi$. In turn, this makes the DM–SM connection less efficient, pushing the freeze-in regime (Ia), thermalization (SM \leftrightarrow DM) and freeze-out (Vb) to higher coupling, hence freeze-in from mediator (Ib) is expected to dominate the phase diagram towards higher coupling. This phase of the model would therefore allow freeze-in DM candidates to be more testable. The scenario where only H or only ϕ have a non-zero vev could also be studied. It is possible to find the same kind of structure in models with effective interactions. For example, a dimension 5 operator of the form $\sim \phi(Q_L H u_R)$ would play the role of the quartic interaction between ϕ and H , except that the production of ϕ can proceed by UV freeze-in. With the phase diagram of the kinetic mixing portal in mind, it is evident from Fig. 3.8 that the reannihilation candidates are very interesting from a phenomenological point of view. They lie between the very feeble freeze-in regime and the freeze-out candidates, which makes

¹If ϕ is uncharged, a term of the form ϕH^2 should in principle be written. We will neglect it for this discussion.

them perfect targets for experiment to search for. In contrast to the more popular freeze-out and freeze-in regime, reannihilation is however not yet included in public codes that automatize the computation of the DM relic abundance, such as micrOmega. From a model building perspective, it would therefore be very interesting to include the reannihilation candidates in those codes. The $\epsilon - \delta$ model could also be studied more in-depth, with a focus on the destructive interferences in both the annihilation and scattering cross sections, which could, perhaps, give rise to a different signature in direct detection experiments when compared to a particle that is only millicharged.

In the second part of the thesis, we looked at a phenomenological model of an asymmetric fermionic DM candidate with attractive interactions, with the aim of exploring the possible density effects that can arise when DM is degenerate. Our results will be part of an upcoming article [6]. We introduced the asymmetric DM problematic in Chapter 6 and argued that such fermionic DM can form a degenerate medium, for instance at the core of the DM halos or if it is efficiently captured by NS. We then took a closer look at the possible density effects that can arise in such medium. We first described the appearance of a scalar condensate $\langle \bar{\psi}\psi \rangle$ and its renormalization of the bare mass of the DM into an effective mass $m_* < m$. The second finite-density effects that we looked at is superfluidity. We gave a brief argument for the existence of a superfluid component for degenerate fermion system with attractive self-interactions and then sketched the treatment of Cooper pairing in the language of QFT, interpreted the physics of the Bogoliubons and obtained the gap in the BCS limit. We then showed that, with the simple description of the density effects of Chapter 6, it is not straightforward to treat the phenomenologically motivated case of DM captured in NS, since many standard assumptions of the BCS treatment are violated. In Chapter 7, we presented our general treatment of superfluidity and the scalar density condensation. We aimed at providing a set of gap equations that is valid in all regimes, *i.e.* relativistic, non-relativistic and with interactions that are either short or long-ranged. The technical details have been relegated to Appendix C and the beginning of this Chapter was focused on presenting the system, assessing the qualitative improvements over the standard treatment (for example, keeping the full momentum dependence of the gaps) and recovering known limits (the BCS case). We then presented the numerical solutions to these equations. In the heavy mediator limit ($m_\phi > m$), we showed that our solutions reproduced qualitatively the results expected by the BCS argument and proposed an ansatz for the gap that is valid across all densities, which we also confronted to our solutions of our gap system. We then went on to describe the solutions in the more complicated light mediator regimes. Finally, we took into consideration the coupled system of the gaps and condensate and presented its solutions.

In Chapter 8, we focused on the effect of the scalar density on DM halos. We first studied the thermodynamics of a degenerate system with a non-zero scalar condensate, which shares features with matter described by the van der Waals equation of state, and took a particular look at the gas to liquid first order phase transition that arises in such systems. In the following, we first built free DM halos by using the hydrostatic equation and detailed the Tremaine-Gunn bounds, a lower limit on the mass of fermionic DM candidates extracted from the existence of DM halos at the scale of dwarf galaxies, which is about $\mathcal{O}(100)$ eV. We then argued that for the case of a degenerate DM halo, the existence of a scalar condensate (*i.e.* self-interactions) allows one to reproduce DM halos at the dwarf galaxies scales with asymmetric candidates that are orders of magnitude lighter than the lower limit of the Tremaine-Gunn bounds. To that end, we identified a couple of DM candidates that (*i*) have masses of order eV, (*ii*) have a DM halo that is compatible with what is typically expected for a dwarf DM halo to be and (*iii*) does not have self-interactions that are excluded by the observations of the Bullet Cluster. Those candidates have very light mediators (10^{-11} eV) and very small coupling constant ($\sim 10^{-10}$). The question of their Early Universe behaviour was left open.

A simple Yukawa model has revealed itself to show striking properties at finite density. We have not yet answered the question that piqued our interest for considering finite density effects : What is the impact of superfluidity and its transport properties on a DM cloud originating from its capture by a NS? Recently, [219] showed that there might be interesting effects of superfluidity on the transport of leptons inside a very young NS in the presence of new particles that are neutrino-philic. It would also be interesting to push further the study of DM halos that are dominated by the condensate. The virial temperature of the halo might allow the outer regions (where the temperature is higher) to be in the gas phase. The halo would therefore exhibit a liquid core and a gaseous outer envelope. This DM profile could then be confronted to the velocity dispersion in Dwarf galaxies. This can be done by bringing together the analyses of [174] and [216]. It might also be interesting to revisit the Tremaine-Gunn bounds by considering the halo obtained from the TOV equations in the case of a fully degenerate free fermion gas. Within the context of the capture of asymmetric DM by a NS, we argued that it was difficult to motivate asymmetric candidates with a mass required for gravitational collapse (mass of order of PeV). It could be interesting to explore the idea of heavy DM candidates but with only a partial asymmetry. Let us assume that it takes the symmetric component a time t to reach a steady state where capture, annihilation and evaporation compensate each other. If the asymmetry is only partial at, say, the 10% level, then within a time equal to $10t$, the asymmetric component would start to dominate the energy density of the cloud and perhaps interesting effects could be studied in such a scenario. We leave this and related questions for future studies.

Appendix A

A spin 1/2 portal

If the SM is completed by one DM candidate and another particle that is often dubbed the mediator, the structure of the model need not to follow what has been discussed previously. In broad terms, the main text has been focusing on s -channel mediator with a mass hierarchy $m_{\text{med}} < m_{\text{DM}}$. Unsurprisingly, the phenomenology of other, perhaps more complicated, structure will be very different from what has been discuss in this work. In this appendix, a short discussion on other possibilities in minimal DM models will be presented, with emphasis on works that have not been presented in the main text [1, 2].

Interactions of the form $\phi\chi\psi$ where two fermions and one scalar intervenes are renormalizable. Assuming that ψ is a fermion of the SM, one can therefore allow χ to be identified with the DM candidate, ϕ to be the mediator and then choose the spin of the DM to be either 0, 1/2 or 1, the spin being assigned to ϕ being 1/2, 0 or 1/2 respectively. Such interactions are different from those arising from the kinetic mixing portal or the Higgs portal. By gauge invariance, the representation of the product $\phi\chi$ should be such that its contraction with ψ is a singlet under all gauge groups in the model. An economical choice, requiring only the smallest representations to be present, would be to take χ to be a SM singlet, ψ to be a left-handed fermion and ϕ to share the same quantum numbers as ψ . To avoid mixing between ϕ and ψ , the dark sector can be charged under a Z_2 symmetry, which would also assure the stability of the DM (if it is lighter than the mediator). A theoretically interesting realisation of this structure can be found within the MSSM. The neutralino, a Majorana fermion, is assumed to be lightest supersymmetric particle, therefore stable, and to be the DM [52]. The mediator is then a sfermion, either a spin 0 slepton or squark. As mentioned previously, it is possible to “spin flip” this model, the DM now being a scalar and the mediator being instead a heavy fermionic partner of ψ . Owing to a great richness in its phenomenology and simplicity in its matter content, many such scenarios have been studied, for example lepto-philic dark matter [220, 221, 222], dominant coupling to light quarks [223, 224] (systematized in [225]) or heavy quarks [226, 1, 2]. For recent refinements, see [227, 228, 229, 230]. We will now focus on the (right handed-) top-philic scalar dark matter case, in which the mediator is a vector-like top partner. The relevant terms to describe the interactions of the dark matter, mediator and top are

$$\mathcal{L} \supset \tilde{y}_t S \bar{T} t_R + \text{h.c.} \quad (\text{A.1})$$

where S is the scalar dark matter, t_R the right handed top quark and T the mediator, which shares the same quantum number as t_R . S and T are also charged under a Z_2 symmetry to forbid mixing of T with t_R and stabilize the DM. This structure is quite different from the “dark” or “hidden” sector of the main text, since the mediator T , being a top partner, is charged under both $SU(3)_c$ and $U(1)_Y$.

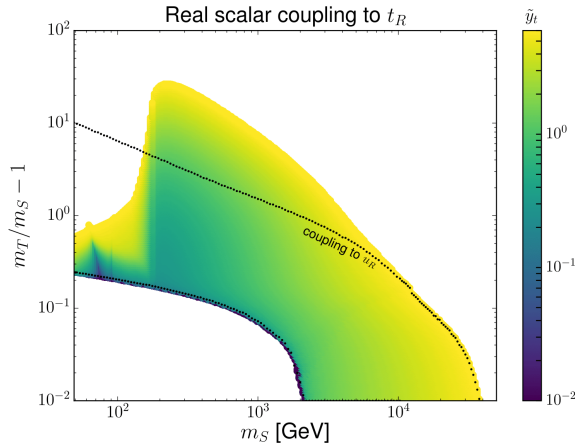


Figure A.1: Parameter space of the thermal candidates of the model of Eq. (A.1) in the $m_T/m_S - 1$ and m_S plane. The colour code gives the Yukawa coupling. The dotted lines correspond to the parameter space of the thermal candidates coupling predominantly to the up quark, for which mass effects in the final state are negligible.

Assuming the dark matter and the mediator to be in equilibrium with the SM at high temperature, the relic density of dark matter is set by a number of competing processes. Annihilations of S into $\bar{t}t$ proceeds in a d -wave, *i.e.* is suppressed at low relative velocity because of intrinsic and orbital angular momentum conservation as well as CP arguments (\tilde{y}_t being here chosen to be real) [220]. This suppression can be lifted by the additional radiation of a particle, say a gluon and the $SS \rightarrow \bar{t}tg$ can be the most efficient annihilation channels for high masses. In contrast to the case where the final state consists of massless particles, an inherent problem of the top-philic case is that infrared divergences plague the calculation of the leading annihilation cross section. Nonetheless, this problem can be tackled by using ideas imported from effective field theory methods and this particular complications was addressed in our work [2]. At low masses, $m_S < m_{\text{top}}$, annihilation into tops is forbidden and proceeds instead at 1 loop into a gluon or photon pair. Interestingly, in such models, the “heavy” mediator limit is typically required, $m_\phi > m_\chi$, for DM to be stable and, akin to the kinetic mixing portal, the mass spectrum of the dark sector can impact greatly the phenomenology¹. If T is close in mass to S , the DM production reaches a new regime dubbed “co-annihilation”. Through its interactions with the T in the thermal bath, S can be efficiently depleted by $ST \rightarrow tg$ or $St \rightarrow Tg$ processes. A compressed mass spectrum therefore allows for smaller thermal couplings, since co-annihilation is proportional to $\tilde{y}_t^2 \alpha$ where α is, say, the strong coupling constant, and not \tilde{y}_t^4 . In summary, owing to many different annihilation and conversion processes, this type of model can accommodate DM masses across many order of magnitude and coupling. The thermal candidates are depicted in Fig. (A.1) where $m_T/m_S - 1$ is the relative mass difference between the mediator and the dark matter, m_S is the dark matter mass and the color code corresponds to the required coupling for reproducing the dark matter relic abundance.

¹The necessary condition for (strict) stability is actually $m_\chi < m_\phi + m_\psi$ if ψ is stable (if not, m_ψ needs to be replaced by the smallest sum of the mass of ψ 's decay product). The region $m_\phi < m_\chi < m_\phi + m_\psi$ is however typically very small, since the stable particles of the SM are very light. In this limit, the mediator would be also stable and contribute to the DM relic abundance. Inevitably, the mediator would freeze-out by annihilating into either photons or gluon depending on its representations, which should be efficient to reduce the abundance of ϕ to a negligible (compared to the dark matter) amount, at least for low ($\ll 1$ TeV) mediator mass. However, the mediator is directly charged under the SM and stringent bounds apply. This region of parameter space is therefore not expected to be viable.

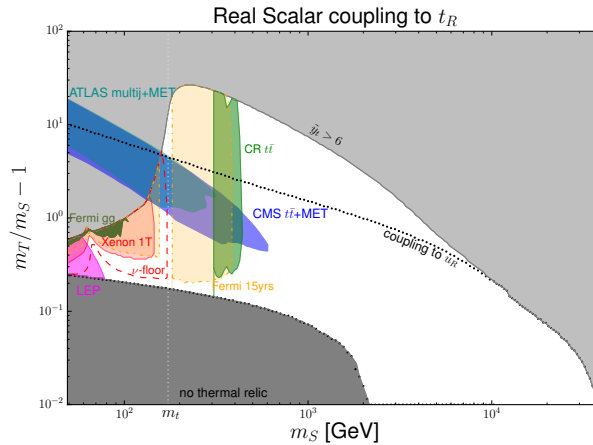


Figure A.2: Summary of constraints on the thermal DM candidates of the model of Eq. (A.1) in the $m_T/m_S - 1$ and m_S plane (color shaded regions). Viable candidates lie within the white region.

Detection prospects of this model are particularly interesting, thanks to the possible production of the coloured mediator at colliders, the appearance of smoking gun γ -ray signals in indirect detection experiments and the remarkable complementarity between colliders, indirect and direct detection experiments over a large mass range. Constraints extracted from the full phenomenological study of the model are depicted in Fig. A.2 in the $(m_T/m_S - 1, m_S)$ plane.

Scatterings on nucleons proceed through an effective coupling $S^2 G^{\mu\nu} G_{\mu\nu}$ through a box diagram of T and t , since the parton distributions of top quarks inside a nucleon is negligible. Light candidates with the highest couplings \tilde{y}_t (*i.e.* candidates with the relic density set through $SS \rightarrow gg$ and uncompressed spectrum) have the largest spin independent interaction with nucleons and are tested by the Xenon1T experiment. For larger DM masses, additional efficient annihilation channels appear (annihilations into tWb) and \tilde{y}_t quickly become too feeble for detection, with the remaining candidates well become the ν -floor.

The indirect detections prospects of such model are especially fitted for DM discovery considerations. For heavy candidates with nearly degenerate mass, annihilations in the channel $SS \rightarrow \bar{t}t\gamma$ is sizeable. The resulting spectrum of prompt photons from such processes is not featureless and has been dubbed “Virtual Internal Bremsstrahlung” (VIB) in the literature [231]. For photon energies close to the DM mass, hard emission is enhanced comparatively to the spectrum expected from the soft final state radiation ($\sim 1/E_\gamma$) and abruptly stop at $E_\gamma = m_S - m_{\text{top}}$. For light candidates, annihilation proceeds dominantly into gg but also inevitably in $\gamma\gamma$, giving therefore rise to a sharp γ -ray line at $E_\gamma = m_S$, on top of a continuum of photons coming from the hadronization of the gg shower. As such spectrum cannot be mimicked by astrophysical processes, the observation of a γ -ray line or a smeared bump coming from, say, the center of our Galaxy would be a smoking gun signal for the existence of DM and would give invaluable informations on its mass and possible nature. Experimental bounds on γ -ray lines have been assessed but the VIB channel would require dedicated model-dependent analysis since the VIB feature depends on the masses of the mediator and final states as well as the DM mass. Other indirect detection signals from S annihilating into unstable particles are expected. At low masses and away from the co-annihilation regime, the annihilation cross section in the DM halo reaches the thermal cross sections, $\sigma v_{gg} = 2 \times 10^{-26} \text{cm}^3/\text{s}$, and those candidates are constrained by the Fermi limits on the gg annihilation channel. If the annihilation channel into top is open, anti-protons can be produced in the hadronic cascade and

propagate to Earth, increasing the flux expected from standard cosmic ray propagation processes. With 15 years of accumulated data, the Fermi-LAT experiment should be able to exclude much more candidates and the bounds from annihilation into $b\bar{b}$ are shown (and have been recasted in order to be applied to an annihilations into $t\bar{t}$).

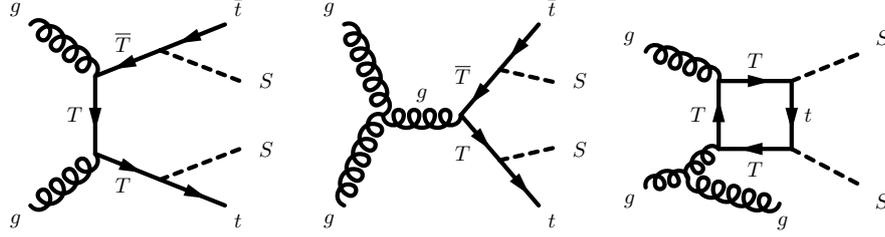


Figure A.3: Feynman diagrams depicting the main channels for the production of S and T at colliders.

At colliders, missing transverse energy and mono-X events are expected and the relevant Feynman diagrams are depicted in Fig. (A.3). Production of a $\bar{T}T$ pair would necessarily result in a $t\bar{t}$ pair being detected and DM exiting the detector as missing transverse energy. A pair of S can also be directly produced by a pair of gluon through a box diagram. The initial state radiation of a gluon would then be necessary for detection and result in a monojet event. LHC constraints on $pp \rightarrow t\bar{t} + \cancel{E}_T$ exclude the mediator to be heavier than 1 TeV when the DM mass is small enough to allow T to decay into a S and on-shell top, as can be seen in Fig. (A.4). Interestingly, for a compressed spectrum, the T will be long lived if very little phase space is left for the top to decay. Soft displaced vertices could be searched for [232] and, for longer lifetime, the top partner could hadronize and different searches could provide complementary bounds in regions of parameter space unconstrained from missing energy searches.

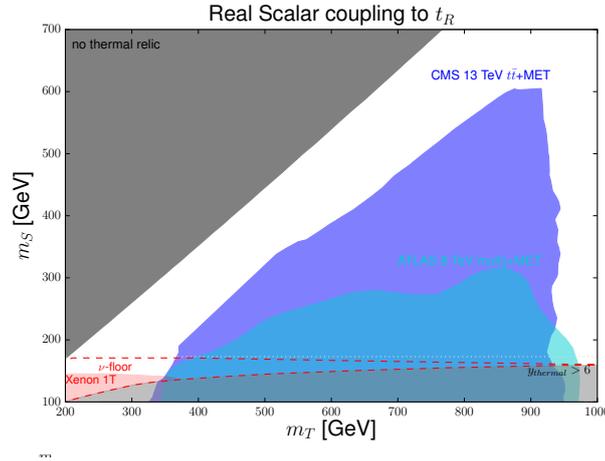


Figure A.4: LHC constraints on the top-philic scalar DM thermal candidates in the $m_S - m_T$ plane.

In summary, this very simple model with only 3 parameters (the DM, mediator mass and the Yukawa coupling \tilde{y}_t) can have a rich phenomenology at colliders and in direct, indirect dark matter detection experiments.

Appendix B

Dark photon emission rate

Until now, the emission rate of a dark photon with energy ω , *i.e.* $\Gamma_{\text{em}}(\omega)$ in the main text, has yet to be specified. For the absorption rate of a $\gamma^{(l)}2 \rightarrow 34$ process, the general expression is the following [98]

$$\Gamma_{\text{abs}} = \frac{1}{4\pi} \frac{1}{2\omega} \int d\Omega_\omega \int \frac{d^3 p_2}{2E_2} \frac{f_2}{(2\pi)^3} \int \frac{d^3 p_3}{2E_3} \frac{1 \pm f_3}{(2\pi)^3} \int \frac{d^3 p_4}{2E_4} \frac{1 \pm f_4}{(2\pi)^3} \delta^4(K^\mu + p_2^\mu - p_3^\mu - p_4^\mu) |\mathcal{M}_{12 \rightarrow 34}|^2 \quad (\text{B.1})$$

where we have labelled the absorbed particle 1 and have not integrated over its energy ω .

Assuming no Pauli-blocking in the final state ($f_3, f_4 \ll 1$) the integration of the amplitude squared of the process over the Lorentz invariant phase space of the final state is

$$\int \frac{d^3 p_3}{2(2\pi)^3 E_3} \int \frac{d^3 p_4}{2(2\pi)^3 E_4} \delta^4(K^\mu + p_2^\mu - p_3^\mu - p_4^\mu) |\mathcal{M}_{\gamma 2 \rightarrow 34}|^2 = 4F g_1 g_2 \sigma_{12 \rightarrow 34} \quad (\text{B.2})$$

where $F = \sqrt{(K \cdot p_2)^2 - m_1^2 m_2^2}$, as is describe in the seminal work of Gondolo and Gelmini. If it is assumed that the particle 2 has an equilibrium distribution, the emission rate becomes

$$\Gamma_{\text{abs}} = \frac{1}{4\pi} \int d\Omega_\omega \int \frac{d^3 p_2}{E_2} \frac{f_2^{\text{EQ}}}{(2\pi)^3} v_{\text{Mol}} \sigma_{12 \rightarrow 34} = \frac{1}{4\pi} \int d\Omega_\omega \int dn_2^{\text{EQ}} \sigma_{12 \rightarrow 34} v_{\text{Mol}} \quad (\text{B.3})$$

If the particle 2 follows a Boltzmann distribution $f_2^{\text{EQ}} \sim e^{-m_2/T}$, Γ_{abs} is

$$\Gamma_{\text{abs}} = \frac{1}{4\pi^2 \omega} \int_0^\pi d\cos\theta \int_{m_2}^\infty dE_2 p_2 e^{-E_2/T} \sigma_{12 \rightarrow 34} \frac{1}{2} \sqrt{(s - (m_1^2 + m_2^2))^2 - 4m_1^2 m_2^2} \quad (\text{B.4})$$

where $s = (K + p_2)^2 = m_1^2 + m_2^2 + 2\omega E_2 - 2\sqrt{E_1^2 - m_1^2} \sqrt{E_2^2 - m_2^2} \cos\theta$. It is preferable to integrate over the square of the center-of-mass energy s . The absorption rate of a particle of mass m_1 and energy ω in a $12 \rightarrow 34$ process, where 2 has mass and energy m_2, E_2 is

$$\Gamma_{\text{abs}} = \frac{1}{16\pi^2 \omega \sqrt{\omega^2 - m_1^2}} \int_{m_2}^\infty dE_2 e^{-E_2/T} \int_{s_-}^{s_+} ds \sigma_{12 \rightarrow 34} \sqrt{(s - (m_1^2 + m_2^2))^2 - 4m_1^2 m_2^2} \quad (\text{B.5})$$

where $s_\pm = m_1^2 + m_2^2 + 2\omega E_2 \pm 2\sqrt{\omega^2 - m_1^2} \sqrt{E_2^2 - m_2^2}$. Throughout the computation of the Boltzmann equation, the following approximated expression, valid for a relativistic plasma,

$$\Gamma_{\text{abs}} \approx \frac{q^4 \alpha^2 T^2}{\pi \omega} \log \frac{4T\omega}{m^2} \quad (\text{B.6})$$

has been used. Here, q and m are respectively the charge and mass of a particle in the plasma and a sum over each relativistic species of the thermal bath is implicit. It has been checked that for $\omega \sim T$, both expressions agree very well.

Appendix C

Obtaining the gap equations

C.1 The free energy of an interacting gas

In this section, we will detail the derivation of the gap equations, which uses the Hubbard-Strantanovich transformation, mean-field approximations and standard field theoretic techniques. Starting from a Yukawa theory with one Dirac fermion ψ and a scalar mediator ϕ , the action can be written in the following non-local form [203]

$$S = \int_{x,y} \left[\bar{\psi}(x) G_0^{-1}(x,y) \psi(y) - \frac{1}{2} \phi(x) D^{-1}(x,y) \phi(y) \right] - g \int_x \bar{\psi}(x) \psi(x) \phi(x) \quad (\text{C.1})$$

where the fermionic and scalar propagators are

$$G_0^{-1}(x,y) = \delta^4(x,y) (i\not{\partial} + \gamma^0 \mu - m) \quad (\text{C.2})$$

$$D^{-1}(x,y) = \delta^4(x,y) (\partial^2 + m_\phi^2) \quad (\text{C.3})$$

$$V^{-1}(x,y) = g^2 D^{-1}(x,y) = g^2 \delta^4(x,y) (\partial^2 + m_\phi^2) \quad (\text{C.4})$$

Without the need to assume ϕ to be heavy, it can be integrated out and give a term in the action that comprises 4 fermions and a full propagator D

$$S = \int_{x,y} \left[\bar{\psi}(x) G_0^{-1}(x,y) \psi(y) + \frac{g^2}{2} \bar{\psi}_\alpha(x) \psi_\beta(x) D_{\alpha\beta\gamma\delta} \bar{\psi}_\gamma(y) \psi_\delta(y) \right] \quad (\text{C.5})$$

where D might have a complicated Dirac structure if the underlying interaction is complicated. In order to know the thermodynamics of the system, the partition function Z

$$Z = \int \mathcal{D}\bar{\psi} \mathcal{D}\psi e^{-S} \quad (\text{C.6})$$

would need to be computed. However, since the action is not quadratic in the fields, it would be difficult. To put the action in a more manageable form, a combination of the Hubbard-Strantanovich (HS) transformation and a mean-field approximation will be invoked. Some auxiliary fields Δ , $\bar{\Delta}$ and ρ , representing condensation channels, are introduced in order to rewrite the 4 fermion interaction as a combination of contractions. With this goal in mind, two 'fat-identites' factors are added to the partition function. The $\bar{\psi}\psi$ contraction of the four fermion operator is taken care of by the "scalar condensate" ρ as follows

$$\mathbf{1} \propto \int \mathcal{D}\rho \exp \left\{ -\frac{1}{2} (\bar{\psi}\psi - \rho) \frac{V}{2} (\bar{\psi}\psi - \rho) - \frac{1}{2} (\bar{\psi}_c \psi_c - \rho) \frac{V}{2} (\bar{\psi}_c \psi_c - \rho) \right\}. \quad (\text{C.7})$$

For the fermionic HS field $\Delta, \bar{\Delta}$, corresponding to the $\psi_C \bar{\psi}$ and $\psi \bar{\psi}_C$ contractions, a different gaussian integral is instead introduced

$$\mathbb{1} \propto \int \mathcal{D}\bar{\Delta} \mathcal{D}\Delta \exp\left\{-\frac{1}{2}(\Delta - \psi_C \bar{\psi}) \frac{V}{2} (\bar{\Delta} - \psi \bar{\psi}) - \frac{1}{2}(\bar{\Delta} - \psi \bar{\psi}) \frac{V}{2} (\Delta - \psi_C \bar{\psi})\right\} \quad (\text{C.8})$$

It is then assumed that the auxiliary fields are at their vacuum expectation values, which amounts to neglecting $(\psi\psi)^2$ fluctuations. More explicitly, we take, in the spirit of the mean field approximation, the HS fields to be

$$\Delta_{\alpha\beta}(x, y) = \langle \psi_{C,\alpha}(x) \bar{\psi}_\beta(y) \rangle \quad (\text{C.9})$$

$$\bar{\Delta}_{\alpha\beta}(x, y) = \langle \psi_\alpha(x) \bar{\psi}_{C,\beta}(y) \rangle \quad (\text{C.10})$$

$$\rho_{\alpha\beta}(x) = \langle \bar{\psi}_\alpha(x) \psi_\beta(x) \rangle = \langle \bar{\psi}_{C,\alpha}(x) \psi_{C,\beta}(x) \rangle = (x \rightarrow y) = \rho_{\alpha\beta}(y) \quad (\text{C.11})$$

where ψ_C is the charge conjugate of ψ and α, β are spin indices. We also introduce the position dependent gaps Φ and the condensate Σ

$$\Phi_{\alpha\beta}^+(x, y) = g^2 D_S(x, y) \Delta_{\alpha\beta}(x, y) \quad (\text{C.12})$$

$$\Phi_{\alpha\beta}^-(x, y) = g^2 D_S(x, y) \bar{\Delta}_{\alpha\beta}(x, y) \quad (\text{C.13})$$

$$\Sigma_{\alpha\beta}(x, y) = g^2 D_S(x, y) \rho_{\alpha\beta}(x) = g^2 D_S(x, y) \rho_{\alpha\beta}(y) \quad (\text{C.14})$$

The action therefore becomes quadratic in all the fields

$$\begin{aligned} S = & \int_{x,y} \bar{\psi}_\alpha(x) [G_0^{-1}(x, y)]_{\alpha\beta} \psi_\beta(y) + \\ & + \frac{1}{2} \int_{x,y} -\frac{1}{2g^2} \frac{1}{D(x, y)} \Sigma_{\alpha\alpha}(x) \Sigma_{\beta\beta}(x) + -\frac{1}{2g^2} \frac{1}{D(x, y)} \Phi_{\alpha\delta}^+(x, y) \Phi_{\delta\alpha}^-(x, y) + \\ & + \frac{1}{2} \int_{x,y} \frac{1}{2} \{ \bar{\psi}_\alpha(x) \psi_\alpha(x) + \bar{\psi}_{C,\alpha}(x) \psi_{C,\alpha}(x) \} \Sigma_{\gamma\gamma}(y) + \\ & - \frac{1}{2} \bar{\psi}_{C,\alpha}(x) \Phi_{\alpha\delta}^+(x, y) \psi_\delta(y) - \frac{1}{2} \bar{\psi}_\alpha(x) \Phi_{\alpha\delta}^-(x, y) \psi_{C,\delta}(y) \end{aligned} \quad (\text{C.15})$$

To proceed further, we introduce the Fourier transforms of each quantity

$$\psi(x) = \frac{1}{\sqrt{V}} \sum_k e^{-ik \cdot x} \psi(k), \quad \bar{\psi}(x) = \frac{1}{\sqrt{V}} \sum_k e^{ik \cdot x} \bar{\psi}(k) \quad (\text{C.16})$$

$$\psi_C(x) = \frac{1}{\sqrt{V}} \sum_k e^{-ik \cdot x} \psi_C(k), \quad \bar{\psi}_C(x) = \frac{1}{\sqrt{V}} \sum_k e^{ik \cdot x} \bar{\psi}_C(k) \quad (\text{C.17})$$

$$\Phi^\pm(x, y) = \frac{T}{V} \sum_k e^{-ik \cdot (x-y)} \Phi^\pm(k), \quad \Sigma(x, y) = \frac{T}{V} \sum_k e^{-ik \cdot (x-y)} \Sigma(k) \quad (\text{C.18})$$

$$G_0^{-1}(x, y) = \frac{T}{V} \sum_k G_0^{-1}(k) e^{-ik \cdot (x-y)}, \quad G_0^{-1}(k) = \not{k} + \mu\gamma^0 - m \quad (\text{C.19})$$

$$D^{-1}(x, y) = \frac{T}{V} \sum_k D^{-1}(k) e^{-ik \cdot (x-y)}, \quad D^{-1}(k) = -k^2 + m_\phi^2 \quad (\text{C.20})$$

$$\frac{1}{D(x, y)} = \frac{V}{T} \sum_k \frac{1}{D(k)} e^{-ik \cdot (x-y)}, \quad \frac{1}{D(k)} = -k^2 + m_\phi^2 \quad (\text{C.21})$$

$$D(x, y) = \frac{T}{V} \sum_k D(k) e^{-ik \cdot (x-y)}, \quad D(k) = \frac{1}{-k^2 + m_\phi^2} \quad (\text{C.22})$$

where T is the temperature and \mathcal{V} is the volume. The action can now be rewritten in terms of sum over all the (positive) modes

$$S = \sum_{k>0} \frac{1}{T} (\bar{\psi}(k) \quad \bar{\psi}_C(k)) \begin{pmatrix} k + \mu\gamma^0 - m + \tilde{\Sigma}_{\alpha\alpha}(0) & \tilde{\Phi}^-(k) \\ \tilde{\Phi}^+(k) & k - \mu\gamma^0 - m + \tilde{\Sigma}_{\alpha\alpha}(0) \end{pmatrix} \begin{pmatrix} \psi(k) \\ \psi_C(k) \end{pmatrix} + \\ - \frac{\mathcal{V}}{T} \sum_{k,q} \tilde{\Sigma}_{\alpha\alpha}(k) \frac{D^{-1}(k-q)}{g^2} \tilde{\Sigma}_{\beta\beta}(q) - \frac{\mathcal{V}}{T} \sum_{k,q} \tilde{\Phi}_{\alpha\delta}^+(k) \frac{D^{-1}(k-q)}{g^2} \tilde{\Phi}_{\delta\alpha}^-(q) \quad (\text{C.23})$$

In this expression, it is easily seen that the scalar condensate renormalizes the mass and that the gaps, being an off-diagonal term, introduce anomalous propagators. The partition function is thus

$$Z = \int \mathcal{D}\bar{\Psi}\mathcal{D}\Psi\mathcal{D}\Phi^+\mathcal{D}\Phi^-\mathcal{D}\Sigma \exp(S) \\ = \left(\prod_{k>0} \text{Det} \left[\frac{\mathcal{S}^{-1}(k)}{T} \right] \right)^1 \times \exp \left(-\frac{\mathcal{V}}{T} \sum_{k,q} \tilde{\Sigma}_{\alpha\alpha}(k) \frac{D^{-1}(k-q)}{g^2} \tilde{\Sigma}_{\beta\beta}(q) \right) \times \\ \times \exp \left(-\frac{\mathcal{V}}{T} \sum_{k,q} \tilde{\Phi}_{\alpha\delta}^+(k) \frac{D^{-1}(k-q)}{g^2} \tilde{\Phi}_{\delta\alpha}^-(q) \right) \quad (\text{C.24})$$

where \mathcal{S}^{-1} is simply the quadratic form of the fermionic part of the action, see the first line of Eq. (C.23). Again, in order to compute the gaussian integral, the fact that Φ and Σ are non-dynamical and take their vacuum values (*i.e.* that the derivation assumes mean-field approximation) has been used. The free energy is extracted from the partition function

$$\Omega = -\frac{T}{\mathcal{V}} \log Z = \frac{-T}{\mathcal{V}} \sum_{k=-\infty}^{+\infty} \frac{1}{2} \log \left(\text{Det} \left[\frac{\mathcal{S}^{-1}(k)}{T} \right] \right) + \\ + \sum_{k,q} \tilde{\Sigma}_{\alpha\alpha}(k) \frac{D^{-1}(k-q)}{g^2} \tilde{\Sigma}(q) + \sum_{k,q} \tilde{\Phi}_{\alpha\delta}^+(k) \frac{D^{-1}(k-q)}{g^2} \tilde{\Phi}_{\delta\alpha}^-(q) \quad (\text{C.25})$$

For the model under study, 3 condensation channels are considered and the gap structure can therefore be specified

$$\Phi = \langle \psi_c \bar{\psi} \rangle = \Delta_1 \gamma_5 + \Delta_2 \vec{\gamma} \cdot \vec{k} \gamma_0 \gamma_5 + \Delta_3 \gamma_0 \gamma_5 \quad (\text{C.26})$$

The first term in the free energy can be manipulated as

$$\sum_{k=-\infty}^{+\infty} \frac{1}{2} \log \left(\text{Det} \left[\frac{\mathcal{S}^{-1}(k)}{T} \right] \right) = \sum_{k=-\infty}^{+\infty} \left(\log \frac{\omega_n^2 + \epsilon_+^2}{T^2} + \log \frac{\omega_n^2 + \epsilon_-^2}{T^2} \right) \quad (\text{C.27})$$

$\omega_n = (2n+1)\pi T$ being the Matsubara sum over all odd frequencies. The Matsubara sum can be performed [200]:

$$T \sum_n \log \left(\frac{\omega_n^2 + \epsilon_{\pm}^2(k)}{T^2} \right) = T \sum_n \log \left((2n+1)^2 \pi^2 + \frac{\epsilon_{\pm}^2(k)}{T^2} \right) = |\epsilon_{\pm}(k)| + 2T \log \left(1 + e^{-\frac{|\epsilon_{\pm}(k)|}{T}} \right). \quad (\text{C.28})$$

C.2 Quasiparticle dispersion relations

The determinant of the quadratic form, seen as a polynomial in impulsion, gives as its root the dispersion relations $\epsilon_{-(+)}$ of the (anti-)particles of the theory. For the specific gap structure of Eq. (C.26), one finds 8 roots, each 4 fold degenerate, which are

$$\begin{aligned} \epsilon_{\pm}^2 = & \mu^2 + \omega^2 + \Delta_1^2 + \Delta_2^2 + \Delta_3^2 + \\ & \pm 2 \left(\mu^2 \omega^2 + 2\mu k \Delta_1 \Delta_2 + m_{\star}^2 \Delta_2^2 + \Delta_1^2 \Delta_2^2 + 2m_{\star} \mu \Delta_1 \Delta_3 - 2m_{\star} k \Delta_2 \Delta_3 + k^2 \Delta_3^2 + \Delta_1^2 \Delta_3^2 \right)^{1/2}. \end{aligned} \quad (\text{C.29})$$

where we denoted the effective mass $m_{\star} = m - \Sigma$ (and the energies ω also include Σ) and dropped the indices and tilde for the condensate. It is then further approximated by expanding the dispersion relation in $\Delta_i/\sqrt{\mu\omega}$. This approximation can and will a-posteriori checked for consistency. The approximated dispersion is of the form

$$\epsilon_{\pm}^2 \approx (\omega \pm \mu)^2 + \left(\Delta_1 \pm \left(\frac{k}{\omega} \Delta_2 + \frac{m_{\star}}{\omega} \Delta_3 \right) \right)^2 + \left(\frac{m_{\star}}{\omega} \Delta_2 - \frac{k}{\omega} \Delta_3 \right)^2 \pm \frac{(m_{\star} \Delta_2 - k \Delta_3)^2}{\mu\omega}. \quad (\text{C.30})$$

It is further noted that the last two terms, as $m_{\star} \rightarrow 0$ or $|k| \rightarrow 0$, also approach 0. Further neglecting them, the dispersion relation takes a simplest form.

$$\epsilon_{\pm}^2 \approx (\omega \pm \mu)^2 + \left(\Delta_1 \pm \left(\frac{k}{\omega} \Delta_2 + \frac{m_{\star}}{\omega} \Delta_3 \right) \right)^2. \quad (\text{C.31})$$

Introducing the following handy combination of gaps

$$\tilde{\Delta}_{\pm} = \Delta_1 \pm \left(\frac{k}{\omega} \Delta_2 + \frac{m_{\star}}{\omega} \Delta_3 \right), \quad (\text{C.32})$$

$$\tilde{\kappa} = \frac{m_{\star}}{\omega} \Delta_2 - \frac{k}{\omega} \Delta_3. \quad (\text{C.33})$$

the dispersion relations at different level of approximations take the suggestive form

$$\epsilon_{\pm}^2 \approx (\omega \pm \mu)^2 + \tilde{\Delta}_{\pm}^2 + \left(1 \pm \frac{\omega k}{\mu} \right) \tilde{\kappa}^2 \quad (\text{C.34})$$

$$\approx (\omega \pm \mu)^2 + \tilde{\Delta}_{\pm}^2. \quad (\text{C.35})$$

C.3 The gap equations at zero temperature

The most convenient way to derive the gap equations is to minimize the free energy with respect to the vevs of the auxilliary fields, i.e. individual components $\Sigma_{\alpha\beta}$ and $\Phi_{\alpha\beta}^{\pm}$:

$$\frac{\delta\Omega}{\delta\Sigma_{\alpha\beta}(k)} = 0 \quad \text{and} \quad \frac{\delta\Omega}{\delta\Phi_{\alpha\beta}^{\pm}(k)} = 0. \quad (\text{C.36})$$

C.3.1 Dirac algebra and derivatives

The individual pairing channels are related to $\Phi_{\alpha\beta}^{\pm}$ as follows

$$\Delta_1 = \frac{\pm 1}{4} \text{Tr} [\Phi^{\pm} \gamma_5], \quad \Delta_2 = \frac{1}{4} \text{Tr} [\Phi^{\pm}(p) \vec{\gamma} \cdot \hat{p} \gamma_0 \gamma_5] \quad \text{and} \quad \Delta_3 = \frac{-1}{4} \text{Tr} [\Phi^{\pm} \gamma_0 \gamma_5]. \quad (\text{C.37})$$

the trace being taken in Dirac space. Consequently the dispersion relation of Eq. (C.31) can also be written as

$$\epsilon_{\pm}^2(k) \approx (\omega_k \pm \mu)^2 + \left(\frac{\text{Tr}[\Phi^+(k)\gamma_5]}{4} \pm \left(\frac{k}{\omega_k} \frac{\text{Tr}[\Phi^+(k)\hat{\gamma} \cdot \hat{k}\gamma_0\gamma_5]}{4} - \frac{m_*}{\omega_k} \frac{\text{Tr}[\Phi^+(k)\gamma_0\gamma_5]}{4} \right) \right)^2, \quad (\text{C.38})$$

with $\omega_k = \sqrt{m_*^2 + |\vec{k}|^2} = \sqrt{(m - \Sigma)^2 + |\vec{k}|^2}$. Taking the $T \rightarrow 0$ limit in Eq. (C.28) simplifies the expression of the free energy and the computation of the derivatives of the free energy with respect to the gap Φ becomes a fairly straightforward task with Eq. (C.38) at hand. After projecting the resulting equations on each separate Dirac structure of the gap Φ , one arrives at the following system of gap equation

$$\Delta_1(r) = \sum_{p,\eta} V(r-p) \frac{\tilde{\Delta}_\eta(k)}{p_0^2 - \epsilon_\eta(p)^2} \quad (\text{C.39})$$

$$\Delta_2(r) = - \sum_{p,\eta} V(r-p) \hat{r} \cdot \hat{p} \frac{\hat{\eta} p}{\omega_p} \frac{\tilde{\Delta}_\eta(k)}{p_0^2 - \epsilon_\eta(p)^2} \quad (\text{C.40})$$

$$\Delta_3(r) = \sum_{p,i} V(r-p) \frac{\eta m_*}{\omega_p} \frac{\tilde{\Delta}_\eta(k)}{p_0^2 - \epsilon_\eta(p)^2} \quad (\text{C.41})$$

$$\frac{\Sigma(r)}{V(r)} = \sum_{k,i} \frac{2}{k_0^2 - \epsilon_\eta^2(k)} \frac{1}{\omega_k} \left\{ (\omega \pm \mu) m_* - \eta \frac{k}{\omega_k} \tilde{\kappa}(k) \tilde{\Delta}_\eta(k) \right\} \quad (\text{C.42})$$

where hatted vectors are of unit length.

C.3.2 Useful integrals

As done in [197], the following integrals are defined

$$\mathcal{F}_0^\pm(r) = \frac{T}{V} \sum_p V(r-p) \frac{1}{p_0^2 - \epsilon_\pm^2} \quad (\text{C.43})$$

$$\mathcal{F}_1^\pm(r) = \frac{T}{V} \sum_p V(r-p) \frac{p}{\omega_p} \frac{\hat{r} \cdot \hat{p}}{p_0^2 - \epsilon_\pm^2} \quad (\text{C.44})$$

Such factors appear in the gap equations. In order to perform the Matsubara sum, it is assumed that no energy is exchanged in the propagator, *i.e.* $r_0 - p_0 \approx 0$. This amounts to neglecting the time dependence of the gaps (as they will not depend explicitly on the frequency). It is therefore possible to use

$$T \sum_{k_0} \frac{1}{k_0^2 - a^2} = \frac{-1}{2a} \tanh\left(\frac{a}{2T}\right) \quad (\text{C.45})$$

and compute the sum over the Matsubara frequencies. Taking the $T \rightarrow 0$ limit, as well as converting the leftover sums into integral over momentum, one obtains

$$\mathcal{F}_0^\pm(r) = -\frac{g^2}{4} \int \frac{d^3p}{(2\pi)^3} \frac{1}{m_\phi^2 + (\vec{r} - \vec{p})^2} \frac{1}{\epsilon_\pm} \quad (\text{C.46})$$

$$\mathcal{F}_1^\pm(r) = -\frac{g^2}{4} \int \frac{d^3p}{(2\pi)^3} \frac{1}{m_\phi^2 + (\vec{r} - \vec{p})^2} \frac{p}{\omega_p} \frac{\hat{r} \cdot \hat{p}}{\epsilon_\pm} \quad (\text{C.47})$$

After integrating over the angles, the expressions become

$$\mathcal{F}_0^\pm(r, g) = -\frac{g^2}{32\pi^2 r} \int dp \log \frac{m_\phi^2 + (r+p)^2}{m_\phi^2 + (r-p)^2} \frac{p}{\epsilon_\pm} g(p) \quad (\text{C.48})$$

$$\mathcal{F}_1^\pm(r, g) = -\frac{g^2}{32\pi^2 r} \int dp \left\{ \frac{m_\phi^2 + r^2 + p^2}{2rp} \log \frac{m_\phi^2 + (r+p)^2}{m_\phi^2 + (r-p)^2} - 2 \right\} \frac{p}{\omega_p} \frac{p}{\epsilon_\pm} g(p) \quad (\text{C.49})$$

where we introduced for convenience a second argument of the \mathcal{F} function. It is noted that those expressions are very similar to the massless case [197] but contains factor of the energy ω which, here, takes into account the mass of the fermions.

C.3.3 The gap equations for $\tilde{\Delta}_\eta$, $\tilde{\kappa}$

Finally, in order to put the system in a form that one can solve on a computer using standard techniques, one last manipulation must be made. One should expect the antiparticle contribution to be small (*i.e.* the $\eta = +1$ term). The physics of pairing corresponds to phenomena taking place at small energies around the Fermi surface, whereas antiparticle lie far away from it, at at least $E = 2\mu$, and should therefore not impact the dynamics much. In more technical term, the antiparticle dispersion ϵ_+ , being in the denominator, always suppresses more the integrand at the Fermi momentum $k = k_F$, $\epsilon_+ \sim 2\mu$, compared to the term $\eta = -1$ which is resonantly enhanced, $\epsilon_-(k_F) \sim \tilde{\Delta}_-$. Therefore, one can simply neglect the terms with $\eta = +1$ above. Combining the gap equations of $\Delta_{1,2,3}$ such that $\tilde{\Delta}_\eta$, $\tilde{\kappa}$ appears on the left hand side, rewriting everything in terms of the \mathcal{F} functions and keeping only the $\eta = -$ term in the sum over particles and antiparticles, the system can be very simply rewritten as

$$\tilde{\Delta}_\eta(r) = \mathcal{F}_0^-(r, \tilde{\Delta}_-) + \eta \frac{r}{\omega_r} \mathcal{F}_1^-(r, \tilde{\Delta}_-) - \eta \frac{m^2}{\omega_r} \mathcal{F}_0^-\left(r, \frac{\tilde{\Delta}_-}{\omega_p}\right) \quad (\text{C.50})$$

$$\tilde{\kappa}(r) = \frac{m}{\omega_r} \mathcal{F}_1^-(r, \tilde{\Delta}_-) + \frac{mr}{\omega_r} \mathcal{F}_0^-\left(r, \frac{\tilde{\Delta}_-}{\omega_p}\right) \quad (\text{C.51})$$

$$\Sigma(0) = \frac{-g^2}{2m_\phi^2} \int \frac{d^3k}{(2\pi)^3} \left\{ \frac{m_* \omega_k - \mu}{\omega_k \epsilon_-(k)} + \frac{k}{\omega_k} \frac{\tilde{\kappa}(k)}{\omega_k} \frac{\tilde{\Delta}_-(k)}{\epsilon_-(k)} - 1 \right\} \quad (\text{C.52})$$

It is noted that only $\tilde{\Delta}_-$ and Σ appear on the right hand side. The equations for $\tilde{\Delta}_+$ and $\tilde{\kappa}$ are therefore decoupled and one should only solve for $\tilde{\Delta}_-$ and Σ at the same time. In particular, it is very easy to see that taking $m \rightarrow 0$ reduces the system to that of the massless case, as suggested by the common notation with [197].

C.4 First corrections to the gap equations

Using the dispersion relation of Eq. (C.30) will make additional terms appear on the right hand side of the gap equations when deriving with respect to the gaps. For completeness, the resulting

more complicated gap system is given here

$$\begin{aligned} \tilde{\Delta}_\epsilon(r) = \sum_{p,\eta} V(r+p) \left\{ \left(1 + \eta\epsilon \left[-\frac{\vec{r} \cdot \vec{p}}{\omega_r \omega_p} + \frac{m_*^2}{\omega_r \omega_p} \right] \right) \frac{\tilde{\Delta}_\eta(p)}{p_0^2 - (\epsilon_p^\eta)^2} + \right. \\ \left. -\epsilon \frac{m_*}{\omega_r} \frac{\vec{r} \cdot \vec{p}}{\omega_p} + p \left(1 + \eta \frac{\omega_p}{\mu} \right) \frac{\tilde{\kappa}(p)}{p_0^2 - (\epsilon_p^\eta)^2} \right\} \end{aligned} \quad (\text{C.53})$$

$$\tilde{\kappa}(r) = \sum_{p,\eta} V(r+p) \left\{ \frac{-\eta m_*}{\omega_r} \frac{r + \vec{r} \cdot \vec{p}}{\omega_p} \frac{\tilde{\Delta}_\eta(p)}{p_0^2 - (\epsilon_p^\eta)^2} + \frac{rp - m_*^2 \vec{r} \cdot \vec{p}}{\omega_p \omega_r} \left(1 + \eta \frac{\omega_p}{\mu} \right) \frac{\tilde{\kappa}(p)}{p_0^2 - (\epsilon_p^\eta)^2} \right\} \quad (\text{C.54})$$

$$\begin{aligned} \frac{\Sigma(r)}{V(r)} = 2 \sum_{k,\eta} \left\{ \frac{m_*}{\omega_k} \frac{\omega_k + \eta\mu}{k_0^2 - \epsilon_\eta^2(k)} - \eta \frac{k}{\omega_k^2} \tilde{\kappa}(k) \frac{\tilde{\Delta}_\eta(p)}{p_0^2 - (\epsilon_p^\eta)^2}(k) + \eta \frac{m_*}{\omega_k} \frac{\tilde{\kappa}(k)}{2\mu} \frac{\tilde{\kappa}(p)}{p_0^2 - (\epsilon_p^\eta)^2} + \right. \\ \left. + \frac{k}{\omega_k^2} \frac{\tilde{\Delta}_+ - \tilde{\Delta}_-}{2} \left(1 + \eta \frac{\omega_k}{\mu} \right) \frac{\tilde{\kappa}(p)}{p_0^2 - (\epsilon_p^\eta)^2} \right\} \end{aligned} \quad (\text{C.55})$$

where one recognizes the first terms to be the gap equations treated above, other terms being corrections. Note that now, the equations for $\tilde{\Delta}_\epsilon$ and $\tilde{\kappa}$ are coupled, which makes the task of solving the system much more complicated. It is also noted that those corrections are not to be confused with *quantum* corrections. From the functional approach, it is however possible to write down loop corrections [233]. For ease of tractability, it is possible to express the gap equations in term of the $\mathcal{F}_{0,1}^\pm$ functions and integrals

$$\begin{aligned} \tilde{\Delta}_\eta(r) = \mathcal{F}_0^- \left(r, \tilde{\Delta}_- \right) + \eta \frac{r}{\omega_r} \mathcal{F}_1^- \left(r, \tilde{\Delta}_- \right) - \eta \frac{m_*^2}{\omega_r} \mathcal{F}_0^- \left(r, \frac{\tilde{\Delta}_-}{\omega_p} \right) + \\ - \eta \mathcal{F}_1^- \left(r, \frac{r}{p} \frac{m_*}{\omega_r} \left(1 - \frac{\omega_p}{\mu} \right) \tilde{\kappa} \right) - \eta \mathcal{F}_0^- \left(r, \frac{m_*}{\omega_r} \frac{p}{\omega_p} \left(1 - \frac{\omega_p}{\mu} \right) \tilde{\kappa} \right) \end{aligned} \quad (\text{C.56})$$

$$\begin{aligned} \tilde{\kappa}(r) = \frac{m}{\omega_r} \mathcal{F}_1^- \left(r, \tilde{\Delta}_- \right) + \frac{mr}{\omega_r} \mathcal{F}_0^- \left(r, \frac{\tilde{\Delta}_-}{\omega_p} \right) \\ + \mathcal{F}_0^- \left(r, \frac{rp}{\omega_r \omega_p} \left(1 - \frac{\omega_p}{\mu} \right) \tilde{\kappa} \right) - \mathcal{F}_1^- \left(r, \frac{m_*^2}{\omega_r \omega_p} \left(1 - \frac{\omega_p}{\mu} \right) \tilde{\kappa} \right) \end{aligned} \quad (\text{C.57})$$

$$\begin{aligned} \Sigma(0) = \frac{-g^2}{2m_\phi^2} \int \frac{d^3k}{(2\pi)^3} \left\{ \frac{m_*}{\omega_k} \frac{\omega_k - \mu}{\epsilon_-(k)} + \frac{k}{\omega_k} \frac{\tilde{\kappa}(k)}{\omega_k} \frac{\tilde{\Delta}_-(k)}{\epsilon_-(k)} - 1 \right. \\ \left. - \frac{m_*}{\omega_k} \frac{\tilde{\kappa}}{2\mu} \frac{\tilde{\kappa}}{\epsilon_-} + \frac{k}{\omega_k} \frac{\tilde{\Delta}_+ - \tilde{\Delta}_-}{2\omega_k} \left(1 - \frac{\omega_k}{\mu} \right) \frac{\tilde{\kappa}}{\epsilon_-} \right\} \end{aligned} \quad (\text{C.58})$$

Again, those equations are very difficult to solve and no attempt at solving them will be made. Furthermore, the solutions of this system are expected to be close to the solutions of the system where only the terms from the first line of each equation are kept.

C.5 Derivation from projectors

Complementary to the functional approach, gap equations can also be derived from a Schwinger-Dyson equation. The quadratic form \mathcal{S}^{-1} in the action is the inverse of the propagator

$$\mathcal{S}^{-1} = \begin{pmatrix} [G_0^+]^{-1} & 0 \\ 0 & [G_0^-]^{-1} \end{pmatrix} + \begin{pmatrix} 0 & \Phi^- \\ \Phi^+ & 0 \end{pmatrix} \quad (\text{C.59})$$

After obtaining \mathcal{S} , the dressed fermion propagator will be given by the diagonal entries

$$G^\pm = \left([G_0^\pm]^{-1} - \Phi^\mp G_0^\pm \Phi^\pm \right)^{-1} \quad (\text{C.60})$$

where the free propagator can be rewritten using (quasi-) projector

$$[G_0^\pm]^{-1} = (k_0 \pm \mu - \omega) \Lambda^+ \gamma_0 + (k_0 \pm \mu + \omega) \Lambda^- \gamma_0 \quad (\text{C.61})$$

where Λ^\pm are projectors onto state of positive and negative energy of free particles

$$\Lambda^\pm(k) = \frac{k_0 \pm (\gamma_0 \vec{\gamma} \cdot \vec{k} + m \gamma_0)}{2k_0} \quad (\text{C.62})$$

It is reminded that the gap Φ is chosen to be

$$\Phi^\pm = \pm \Delta_1 \gamma_5 + \Delta_2 \vec{\gamma} \cdot \hat{k} \gamma_0 \gamma_5 + \Delta_3 \gamma_0 \gamma_5 \quad (\text{C.63})$$

To obtain the gap equation, one equates the off diagonal terms, say $F^+ = -G_0^- \Phi^+ G^+$, of \mathcal{S} to the two point function, say $-\langle \psi(x) \bar{\psi}_C(y) \rangle$ in the case of F^+ , and uses the definition of the gap, $\Phi^-(x, y) = g^2 D(x, y) \langle \psi(x) \bar{\psi}_C(y) \rangle$ in this case, to write a Schwinger-Dyson equation

$$\Phi^+(p) = g^2 \frac{T}{V} \sum_k D(p-k) G_0^\mp \Phi^\pm G^\pm \quad (\text{C.64})$$

in Fourier space. Consistently with the previous approximations $\omega, \mu \gg \Delta_{1,2,3}$, the fully dressed propagator is written as

$$G^\pm = \frac{k_0 \mp (\mu - \omega_k)}{k_0^2 - (\epsilon_k^-)^2} \Lambda^\pm \gamma^0 + \frac{k_0 \mp (\mu + \omega_k)}{k_0^2 - (\epsilon_k^+)^2} \Lambda^\mp \gamma^0 \quad (\text{C.65})$$

which is nothing but the dressed propagator of the massless case where the particle and antiparticle rest mass has been included in the expression of their energy and the dispersion relation is that of Eq. (C.31). It is straightforward to compute each term of the right hand side of the gap equation

$$\Delta_1 G_0^- \gamma_5 G^+ = -\Delta_1 \left\{ \frac{\Lambda^- \gamma_5}{k_0^2 - (\epsilon_k^-)^2} + \frac{\Lambda^+ \gamma_5}{k_0^2 - (\epsilon_k^+)^2} \right\} \quad (\text{C.66})$$

$$\begin{aligned} \Delta_2 G_0^- \vec{\gamma} \cdot \hat{k} \gamma_0 \gamma_5 G^+ &= \Delta_2 \frac{k}{\omega} \left\{ \frac{\Lambda^- \gamma_5}{k_0^2 - (\epsilon_k^-)^2} - \frac{\Lambda^+ \gamma_5}{k_0^2 - (\epsilon_k^+)^2} \right\} + \\ &- \Delta_2 \frac{m}{\omega} \left\{ \frac{k_0 - \mu + \omega_k}{k_0 - \mu - \omega_k} \frac{\Lambda^+ \vec{\gamma} \cdot \hat{k} \gamma_5}{k_0^2 - (\epsilon_k^-)^2} - \frac{k_0 - \mu - \omega_k}{k_0 - \mu + \omega_k} \frac{\Lambda^- \vec{\gamma} \cdot \hat{k} \gamma_5}{k_0^2 - (\epsilon_k^+)^2} \right\} \end{aligned} \quad (\text{C.67})$$

$$\begin{aligned} \Delta_3 G_0^- \gamma_0 \gamma_5 G^+ &= \Delta_3 \frac{m}{\omega} \left\{ \frac{\Lambda^- \gamma_5}{k_0^2 - (\epsilon_k^-)^2} - \frac{\Lambda^+ \gamma_5}{k_0^2 - (\epsilon_k^+)^2} \right\} + \\ &+ \Delta_3 \frac{k}{\omega} \left\{ \frac{k_0 - \mu + \omega_k}{k_0 - \mu - \omega_k} \frac{\Lambda^+ \vec{\gamma} \cdot \hat{k} \gamma_5}{k_0^2 - (\epsilon_k^-)^2} - \frac{k_0 - \mu - \omega_k}{k_0 - \mu + \omega_k} \frac{\Lambda^- \vec{\gamma} \cdot \hat{k} \gamma_5}{k_0^2 - (\epsilon_k^+)^2} \right\} \end{aligned} \quad (\text{C.68})$$

One can safely neglect the terms from the second line of the last two equations since they are overall proportional to factors that die quickly when in both the relativistic and non relativistic limit. The gap equation therefore becomes

$$\begin{aligned} &\Delta_1 \gamma_5 + \Delta_2 \vec{\gamma} \cdot \hat{p} \gamma_0 \gamma_5 + \Delta_3 \gamma_0 \gamma_5 = \\ &= \frac{-g^2}{\mathcal{V}/T} \sum_k D(p-k) \left[\frac{\Delta_1 - \Delta_2 \frac{k}{\omega} - \Delta_3 \frac{m}{\omega}}{k_0^2 - (\epsilon_k^-)^2} \Lambda^- \gamma_5 + \frac{\Delta_1 + \Delta_2 \frac{k}{\omega} + \Delta_3 \frac{m}{\omega}}{k_0^2 - (\epsilon_k^+)^2} \Lambda^+ \gamma_5 \right] \end{aligned} \quad (\text{C.69})$$

Multiplying by each gap structure and taking the trace, one arrives at the system above. Similar developments can be made to obtain the equation for the scalar condensate.

C.6 Numerical methods for solving the gap equations

C.6.1 Gap

The gap equation is an integral equation

$$\begin{aligned} \tilde{\Delta}_-(p) = & \frac{g^2}{32\pi^2} \int_0^\infty dk \frac{k}{p} \left\{ \left(1 + \frac{m_*^2}{\omega_p \omega_k} \right) \log \frac{m_\phi^2 + (p-k)^2}{m_\phi^2 + (p+k)^2} + \right. \\ & \left. + \frac{kp}{\omega_p \omega_k} \left(-2 + \frac{m_\phi^2 + k^2 + p^2}{2kp} \log \frac{m_\phi^2 + (p-k)^2}{m_\phi^2 + (p+k)^2} \right) \right\} \frac{\tilde{\Delta}_-(k)}{\epsilon_-(k)} \end{aligned} \quad (\text{C.70})$$

It is convenient to rewrite the gap equation as

$$\Delta(k) = \frac{-1}{\pi} \int \frac{v(k, k') \Delta(k')}{\sqrt{(\omega_{k'} - \mu)^2 + \Delta^2(k')}} k'^2 dk' \quad (\text{C.71})$$

or, equivalently [234, 235]

$$\chi(k) = \phi(k) - \frac{1}{\pi} \int \frac{W(k, k') \chi(k')}{\left[(\omega_{k'} - \mu)^2 + \Delta_F^2 \chi^2(k') \right]^{1/2}} k'^2 dk' \quad (\text{C.72})$$

$$1 = -\frac{1}{\pi} v_F \int \frac{\phi(k') \chi(k')}{\left[(\omega_{k'} - \mu)^2 + \Delta_F^2 \chi^2(k') \right]^{1/2}} k'^2 dk' \quad (\text{C.73})$$

where the shape function is defined as

$$\chi(k) = \frac{\Delta(k)}{\Delta(k_F)} = \frac{\Delta(k)}{\Delta_F} \quad (\text{C.74})$$

and the potential ϕ and kernel W are

$$\phi(k) = \frac{v(k, k_F)}{v_F}, \quad W(k, k') = v(k, k') - v_F \phi(k) \phi(k') \quad (\text{C.75})$$

where we used the shorthand $v_F = v(k_F, k_F)$. In the Yukawa theory, we have that

$$\begin{aligned} v(k, k') = & \frac{-g^2}{32\pi k k'} \left[\left(1 + \frac{m_*^2}{\omega_k \omega_{k'}} \right) \log \frac{m_\phi^2 + (k+k')^2}{m_\phi^2 + (k-k')^2} + \right. \\ & \left. - \frac{k k'}{\omega_k \omega_{k'}} \left(\frac{m_\phi^2 + k^2 + k'^2}{2k k'} \log \frac{m_\phi^2 + (k+k')^2}{m_\phi^2 + (k-k')^2} - 2 \right) \right] \end{aligned} \quad (\text{C.76})$$

Let us now briefly describe the numerical method of [234] for solving the gap equation. By construction, W is zero when one of its argument is on the Fermi surface. Therefore, Eq. (C.72) should not be very sensitive to the value of $\tilde{\Delta}_{-,F}$ and one can solve this equation by first inputting a small, constant value for the gap in the denominator. After obtaining a first approximation to χ by using, for example, matrix inversion, one can now input the shape function in Eq. (C.73). The equation for the normalization of the gap at the Fermi surface, $\tilde{\Delta}_{-,F}$, now becomes algebraic and

can be easily solved. The first approximation solution can now be used in Eq. (C.72) as input in the denominator and the procedure repeated until convergence of the solution. As a final comment, we stress that in the Yukawa theory, it is numerically challenging for W to vanish identically at the Fermi surface due to the many logs in Eq. (C.76) and analytical limits should preferably be used when possible. Also, when defining a momentum grid to discretize Eq. (C.72–C.73), one should make sure that the grid is very fine around $k = k_F$ in order not to miss the effect of the gap in the denominator.

C.6.2 An approximated solution to the gap equation

As suggested by the integral equation for χ , if W plays little role, one could take $\chi \approx \phi$ as the shape function and then solve the much simpler algebraic equation for the normalization Δ_F

$$1 \approx -\frac{1}{\pi} v_F \int \frac{\phi^2(k')}{\left[(\omega_{k'} - \mu)^2 + \Delta_F^2 \phi^2(k')\right]^{1/2}} k'^2 dk' \quad (\text{C.77})$$

This equation has the benefit of being UV finite and happens to reproduce very well the relativistic limit $k_F \gg m$, be it in the heavy mediator or light mediator regime. In particular, this allows for an extremely easy and straightforward way of generalizing the numerical results at zero temperature of [197].

C.6.3 Condensate - gap coupled system

When dealing with the coupled gap - scalar condensate system

$$\begin{aligned} \tilde{\Delta}_-(p) = & \frac{g^2}{32\pi^2} \int_0^\infty dk \frac{k}{p} \left\{ \left(1 + \frac{m_*^2}{\omega_p \omega_k} \right) \log \frac{m_\phi^2 + (p-k)^2}{m_\phi^2 + (p+k)^2} + \right. \\ & \left. + \frac{kp}{\omega_p \omega_k} \left(-2 + \frac{m_\phi^2 + k^2 + p^2}{2kp} \log \frac{m_\phi^2 + (p-k)^2}{m_\phi^2 + (p+k)^2} \right) \right\} \frac{\tilde{\Delta}_-(k)}{\epsilon_-(k)} \end{aligned} \quad (\text{C.78})$$

$$\Sigma(0) = \frac{-g^2}{2m_\phi^2} \int \frac{d^3k}{(2\pi)^3} \left\{ \frac{m_* \omega_k - \mu}{\omega_k \epsilon_-(k)} + \frac{k \tilde{\kappa}(k)}{\omega_k \omega_k \epsilon_-(k)} \tilde{\Delta}_-(k) - 1 \right\} \quad (\text{C.79})$$

an iterative procedure is used for solving, which usually converges within a few iterations. The first equation is solved with $m_* = m$ using the techniques described above. The solution $\tilde{\Delta}_-(k)$ is then fed in the second equation and one solves for Σ . The procedure is repeated after having updated $m_* = m - \Sigma$ until the solutions $\tilde{\Delta}$ and Σ are stable upon going through the procedure. In principle, both equations should be solved at the same time but this is of course impossible analytically and challenging numerically.

Bibliography

- [1] S. Colucci, B. Fuks, F. Giacchino, L. Lopez Honorez, M. H. G. Tytgat and J. Vandecasteele, *Top-philic Vector-Like Portal to Scalar Dark Matter*, *Phys. Rev. D* **98** (2018) 035002, [1804.05068].
- [2] S. Colucci, F. Giacchino, M. H. G. Tytgat and J. Vandecasteele, *Radiative corrections to vectorlike portal dark matter*, *Phys. Rev. D* **98** (2018) 115029, [1805.10173].
- [3] F. Giacchino, *A Dark Matter through the Vector-like Portal*, .
- [4] T. Hambye, M. H. G. Tytgat, J. Vandecasteele and L. Vanderheyden, *Dark matter direct detection is testing freeze-in*, *Phys. Rev.* **D98** (2018) 075017, [1807.05022].
- [5] T. Hambye, M. H. G. Tytgat, J. Vandecasteele and L. Vanderheyden, *Dark matter from dark photons: a taxonomy of dark matter production*, *Phys. Rev. D* **100** (2019) 095018, [1908.09864].
- [6] R. Garani, M. H. G. Tytgat and J. Vandecasteele, *In preparation, A theory of condensed dark matter*, 21xxx.xxxxx.
- [7] F. Zwicky, *Die Rotverschiebung von extragalaktischen Nebeln*, *Helv. Phys. Acta* **6** (1933) 110–127.
- [8] F. Zwicky, *On the Masses of Nebulae and of Clusters of Nebulae*, *APJ* **86** (Oct., 1937) 217.
- [9] E. W. Kolb and M. S. Turner, *The early universe*. Frontiers in physics. Westview Press, Boulder, CO, 1990. 10.1201/9780429492860.
- [10] S. D. M. White, C. S. Frenk and M. Davis, *Clustering in a neutrino-dominated universe*, *APJL* **274** (Nov., 1983) L1–L5.
- [11] KATRIN collaboration, M. Aker et al., *Improved Upper Limit on the Neutrino Mass from a Direct Kinematic Method by KATRIN*, *Phys. Rev. Lett.* **123** (2019) 221802, [1909.06048].
- [12] J. Lesgourgues and S. Pastor, *Neutrino mass from Cosmology*, *Adv. High Energy Phys.* **2012** (2012) 608515, [1212.6154].
- [13] G. R. Farrar, *Stable Sexaquark*, 1708.08951.
- [14] V. C. Rubin, J. Ford, W. K. and N. Thonnard, *Rotational properties of 21 SC galaxies with a large range of luminosities and radii, from NGC 4605 ($R=4kpc$) to UGC 2885 ($R=122kpc$).*, *APJ* **238** (June, 1980) 471–487.
- [15] Y. Sofue, Y. Tutui, M. Honma, A. Tomita, T. Takamiya, J. Koda et al., *Central rotation curves of spiral galaxies*, *The Astrophysical Journal* **523** (sep, 1999) 136–146.
- [16] Y. Sofue, *Rotation curve of the milky way and the dark matter density*, *Galaxies* **8** (2020) .

- [17] S. McGaugh, *Milky Way Mass Models and MOND*, *Astrophys. J.* **683** (2008) 137–148, [0804.1314].
- [18] J. F. Navarro, C. S. Frenk and S. D. M. White, *The Structure of cold dark matter halos*, *Astrophys. J.* **462** (1996) 563–575, [astro-ph/9508025].
- [19] M. Mateo, *Dwarf galaxies of the Local Group*, *Ann. Rev. Astron. Astrophys.* **36** (1998) 435–506, [astro-ph/9810070].
- [20] N. A. Bahcall and X. Fan, *The Most Massive Distant Clusters: Determining Ω and σ_8* , *APJ* **504** (Sept., 1998) 1–6, [astro-ph/9803277].
- [21] R. G. Carlberg, H. K. C. Yee and E. Ellingson, *The Average mass and light profiles of galaxy clusters*, *Astrophys. J.* **478** (1997) 462, [astro-ph/9512087].
- [22] L. Bergström, *Nonbaryonic dark matter: Observational evidence and detection methods*, *Rept. Prog. Phys.* **63** (2000) 793, [hep-ph/0002126].
- [23] G. Bertone, D. Hooper and J. Silk, *Particle dark matter: Evidence, candidates and constraints*, *Phys. Rept.* **405** (2005) 279–390, [hep-ph/0404175].
- [24] *Particle Dark Matter: Observations, Models and Searches*. Cambridge University Press, 2010. 10.1017/CBO9780511770739.
- [25] PARTICLE DATA GROUP collaboration, P. A. Zyla et al., *Review of Particle Physics*, *PTEP* **2020** (2020) 083C01.
- [26] M. Milgrom, *A modification of the Newtonian dynamics as a possible alternative to the hidden mass hypothesis.*, *APJ* **270** (July, 1983) 365–370.
- [27] R. B. Tully and J. R. Fisher, *Reprint of 1977AA....54..661T. A new method of determining distance to galaxies.*, *AAP* **500** (Feb., 1977) 105–117.
- [28] M. Milgrom, *The MOND paradigm*, 0801.3133.
- [29] J. S. Heyl, S. Cole, C. S. Frenk and J. F. Navarro, *Galaxy formation in a variety of hierarchical models*, *MNRAS* **274** (June, 1995) 755–768, [astro-ph/9408065].
- [30] S. S. McGaugh and W. J. G. de Blok, *Testing the dark matter hypothesis with low surface brightness galaxies and other evidence*, *Astrophys. J.* **499** (1998) 41, [astro-ph/9801123].
- [31] D. Clowe, A. Gonzalez and M. Markevitch, *Weak-Lensing Mass Reconstruction of the Interacting Cluster 1E 0657-558: Direct Evidence for the Existence of Dark Matter*, *APJ* **604** (Apr., 2004) 596–603, [astro-ph/0312273].
- [32] M. Markevitch, A. H. Gonzalez, D. Clowe, A. Vikhlinin, W. Forman, C. Jones et al., *Direct Constraints on the Dark Matter Self-Interaction Cross Section from the Merging Galaxy Cluster 1E 0657-56*, *APJ* **606** (May, 2004) 819–824, [astro-ph/0309303].
- [33] M. Markevitch, A. H. Gonzalez, D. Clowe, A. Vikhlinin, L. David, W. Forman et al., *Direct constraints on the dark matter self-interaction cross-section from the merging galaxy cluster 1E0657-56*, *Astrophys. J.* **606** (2004) 819–824, [astro-ph/0309303].
- [34] S. Tulin, H.-B. Yu and K. M. Zurek, *Beyond Collisionless Dark Matter: Particle Physics Dynamics for Dark Matter Halo Structure*, *Phys. Rev.* **D87** (2013) 115007, [1302.3898].

- [35] D. Harvey, R. Massey, T. Kitching, A. Taylor and E. Tittley, *The non-gravitational interactions of dark matter in colliding galaxy clusters*, *Science* **347** (2015) 1462–1465, [1503.07675].
- [36] N. C. Amorisco, A. Agnello and N. W. Evans, *The core size of the Fornax dwarf Spheroidal*, *Mon. Not. Roy. Astron. Soc.* **429** (2013) L89–L93, [1210.3157].
- [37] D. J. Sand, T. Treu, G. P. Smith and R. S. Ellis, *The dark matter distribution in the central regions of galaxy clusters: Implications for CDM*, *Astrophys. J.* **604** (2004) 88–107, [astro-ph/0309465].
- [38] K. A. Oman et al., *The unexpected diversity of dwarf galaxy rotation curves*, *Mon. Not. Roy. Astron. Soc.* **452** (2015) 3650–3665, [1504.01437].
- [39] M. Kaplinghat, T. Ren and H.-B. Yu, *Dark Matter Cores and Cusps in Spiral Galaxies and their Explanations*, *JCAP* **06** (2020) 027, [1911.00544].
- [40] M. Boylan-Kolchin, J. S. Bullock and M. Kaplinghat, *Too big to fail? The puzzling darkness of massive Milky Way subhaloes*, *MNRAS* **415** (July, 2011) L40–L44, [1103.0007].
- [41] S. Garrison-Kimmel, M. Boylan-Kolchin, J. S. Bullock and E. N. Kirby, *Too big to fail in the Local Group*, *MNRAS* **444** (Oct., 2014) 222–236, [1404.5313].
- [42] PLANCK collaboration, N. Aghanim et al., *Planck 2018 results. VI. Cosmological parameters*, *Astron. Astrophys.* **641** (2020) A6, [1807.06209].
- [43] P. J. E. Peebles, *The large-scale structure of the universe*. 1980.
- [44] I. Ferreras, *Fundamentals of Galaxy Dynamics, Formation and Evolution*. UCL Press, 2019.
- [45] T. K. Chan, D. Kereš, J. Oñorbe, P. F. Hopkins, A. L. Muratov, C. A. Faucher-Giguère et al., *The impact of baryonic physics on the structure of dark matter haloes: the view from the FIRE cosmological simulations*, *Mon. Not. Roy. Astron. Soc.* **454** (2015) 2981–3001, [1507.02282].
- [46] D. N. Spergel and P. J. Steinhardt, *Observational evidence for selfinteracting cold dark matter*, *Phys. Rev. Lett.* **84** (2000) 3760–3763, [astro-ph/9909386].
- [47] P. Gondolo and G. Gelmini, *Cosmic abundances of stable particles: Improved analysis*, *Nucl. Phys.* **B360** (1991) 145–179.
- [48] L. Husdal, *On Effective Degrees of Freedom in the Early Universe*, *Galaxies* **4** (2016) 78, [1609.04979].
- [49] N. Bernal, M. Heikinheimo, T. Tenkanen, K. Tuominen and V. Vaskonen, *The Dawn of FIMP Dark Matter: A Review of Models and Constraints*, *Int. J. Mod. Phys.* **A32** (2017) 1730023, [1706.07442].
- [50] F. Elahi, C. Kolda and J. Unwin, *Ultraviolet freeze-in*, *Journal of High Energy Physics* **2015** (2015) 48.
- [51] L. Forestell and D. E. Morrissey, *Infrared Effects of Ultraviolet Operators on Dark Matter Freeze-In*, 1811.08905.
- [52] G. Jungman, M. Kamionkowski and K. Griest, *Supersymmetric dark matter*, *Phys. Rept.* **267** (1996) 195–373, [hep-ph/9506380].

- [53] G. Steigman, B. Dasgupta and J. F. Beacom, *Precise Relic WIMP Abundance and its Impact on Searches for Dark Matter Annihilation*, *Phys. Rev. D* **86** (2012) 023506, [1204.3622].
- [54] B. Patt and F. Wilczek, *Higgs-field portal into hidden sectors*, hep-ph/0605188.
- [55] J. Abdallah et al., *Simplified Models for Dark Matter Searches at the LHC*, *Phys. Dark Univ.* **9-10** (2015) 8–23, [1506.03116].
- [56] A. Albert et al., *Towards the next generation of simplified Dark Matter models*, *Phys. Dark Univ.* **16** (2017) 49–70, [1607.06680].
- [57] J. Jaeckel and A. Ringwald, *The Low-Energy Frontier of Particle Physics*, *Ann. Rev. Nucl. Part. Sci.* **60** (2010) 405–437, [1002.0329].
- [58] R. Essig et al., *Working Group Report: New Light Weakly Coupled Particles*, in *Proceedings, 2013 Community Summer Study on the Future of U.S. Particle Physics: Snowmass on the Mississippi (CSS2013): Minneapolis, MN, USA, July 29-August 6, 2013*, 2013. 1311.0029.
- [59] J. Alexander et al., *Dark Sectors 2016 Workshop: Community Report*, 1608.08632.
- [60] A. De Rujula, S. L. Glashow and U. Sarid, *CHARGED DARK MATTER*, *Nucl. Phys. B* **333** (1990) 173–194.
- [61] R. Foot and S. Vagnozzi, *Dissipative hidden sector dark matter*, *Phys. Rev.* **D91** (2015) 023512, [1409.7174].
- [62] L. Ackerman, M. R. Buckley, S. M. Carroll and M. Kamionkowski, *Dark Matter and Dark Radiation*, *Phys. Rev.* **D79** (2009) 023519, [0810.5126].
- [63] J. L. Feng, H. Tu and H.-B. Yu, *Thermal Relics in Hidden Sectors*, *JCAP* **0810** (2008) 043, [0808.2318].
- [64] J. L. Feng, M. Kaplinghat, H. Tu and H.-B. Yu, *Hidden Charged Dark Matter*, *JCAP* **0907** (2009) 004, [0905.3039].
- [65] T. Hambye, *On the stability of particle dark matter*, *PoS IDM2010* (2011) 098, [1012.4587].
- [66] B. Holdom, *Two $U(1)$'s and Epsilon Charge Shifts*, *Phys. Lett.* **166B** (1986) 196–198.
- [67] E. C. G. Stueckelberg, *Interaction energy in electrodynamics and in the field theory of nuclear forces*, *Helv. Phys. Acta* **11** (1938) 225–244.
- [68] F. Englert and R. Brout, *Broken Symmetry and the Mass of Gauge Vector Mesons*, *Phys. Rev. Lett.* **13** (1964) 321–323.
- [69] P. W. Higgs, *Broken Symmetries and the Masses of Gauge Bosons*, *Phys. Rev. Lett.* **13** (1964) 508–509.
- [70] R. Foot, *Experimental signatures of a massive mirror photon*, hep-ph/9407331.
- [71] X. Chu, T. Hambye and M. H. G. Tytgat, *The Four Basic Ways of Creating Dark Matter Through a Portal*, *JCAP* **1205** (2012) 034, [1112.0493].
- [72] K. S. Babu, C. F. Kolda and J. March-Russell, *Implications of generalized $Z - Z'$ mixing*, *Phys. Rev. D* **57** (1998) 6788–6792, [hep-ph/9710441].

- [73] S. A. Abel, M. D. Goodsell, J. Jaeckel, V. V. Khoze and A. Ringwald, *Kinetic Mixing of the Photon with Hidden $U(1)$ s in String Phenomenology*, *JHEP* **07** (2008) 124, [0803.1449].
- [74] B. Holdom, *Searching for ϵ Charges and a New $U(1)$* , *Phys. Lett. B* **178** (1986) 65–70.
- [75] N. Arkani-Hamed and N. Weiner, *LHC Signals for a SuperUnified Theory of Dark Matter*, *JHEP* **12** (2008) 104, [0810.0714].
- [76] G. Barello, S. Chang and C. A. Newby, *Correlated signals at the energy and intensity frontiers from non-Abelian kinetic mixing*, *Phys. Rev. D* **94** (2016) 055018, [1511.02865].
- [77] D. Feldman, Z. Liu and P. Nath, *The Stueckelberg Z -prime Extension with Kinetic Mixing and Milli-Charged Dark Matter From the Hidden Sector*, *Phys. Rev. D* **75** (2007) 115001, [hep-ph/0702123].
- [78] Y. Farzan and M. Rajaei, *Pico-charged particles explaining 511 keV line and XENON1T signal*, *Phys. Rev. D* **102** (2020) 103532, [2007.14421].
- [79] B. Kors and P. Nath, *A Stueckelberg extension of the standard model*, *Phys. Lett. B* **586** (2004) 366–372, [hep-ph/0402047].
- [80] B. Kors and P. Nath, *Aspects of the Stueckelberg extension*, *JHEP* **07** (2005) 069, [hep-ph/0503208].
- [81] M. Fabbrichesi, E. Gabrielli and G. Lanfranchi, *The Dark Photon*, 2005.01515.
- [82] T. G. Rizzo, *Dark Moments for the Standard Model ?*, 2106.11150.
- [83] C. M. Ho and R. J. Scherrer, *Anapole Dark Matter*, *Phys. Lett. B* **722** (2013) 341–346, [1211.0503].
- [84] E. Bernreuther, S. Heeba and F. Kahlhoefer, *Resonant sub-GeV Dirac dark matter*, *JCAP* **03** (2021) 040, [2010.14522].
- [85] C.-Y. Xing and S.-H. Zhu, *Dark Matter Freeze-Out via Catalyzed Annihilation*, *Phys. Rev. Lett.* **127** (2021) 061101, [2102.02447].
- [86] G. Bélanger, F. Boudjema, A. Goudelis, A. Pukhov and B. Zaldivar, *micrOMEGAs5.0 : Freeze-in*, *Comput. Phys. Commun.* **231** (2018) 173–186, [1801.03509].
- [87] L. J. Hall, K. Jedamzik, J. March-Russell and S. M. West, *Freeze-In Production of FIMP Dark Matter*, *JHEP* **03** (2010) 080, [0911.1120].
- [88] G. L. Kane, P. Kumar, B. D. Nelson and B. Zheng, *Dark matter production mechanisms with a nonthermal cosmological history: A classification*, *Phys. Rev.* **D93** (2016) 063527, [1502.05406].
- [89] M. Klasen and C. E. Yaguna, *Warm and cold fermionic dark matter via freeze-in*, *JCAP* **1311** (2013) 039, [1309.2777].
- [90] G. Bélanger, C. Delaunay, A. Pukhov and B. Zaldivar, *Dark matter abundance from the sequential freeze-in mechanism*, *Phys. Rev. D* **102** (2020) 035017, [2005.06294].
- [91] J. Redondo, *Helioscope Bounds on Hidden Sector Photons*, *JCAP* **0807** (2008) 008, [0801.1527].
- [92] J. Jaeckel, J. Redondo and A. Ringwald, *Signatures of a hidden cosmic microwave background*, *Phys. Rev. Lett.* **101** (2008) 131801, [0804.4157].

- [93] J. Redondo and M. Postma, *Massive hidden photons as lukewarm dark matter*, *JCAP* **0902** (2009) 005, [0811.0326].
- [94] H. An, M. Pospelov and J. Pradler, *New stellar constraints on dark photons*, *Phys. Lett.* **B725** (2013) 190–195, [1302.3884].
- [95] J. Redondo and G. Raffelt, *Solar constraints on hidden photons re-visited*, *JCAP* **1308** (2013) 034, [1305.2920].
- [96] A. Fradette, M. Pospelov, J. Pradler and A. Ritz, *Cosmological Constraints on Very Dark Photons*, *Phys. Rev.* **D90** (2014) 035022, [1407.0993].
- [97] M. L. Bellac, *Thermal Field Theory*. Cambridge Monographs on Mathematical Physics. Cambridge University Press, 2011. 10.1017/CBO9780511721700.
- [98] H. A. Weldon, *Simple Rules for Discontinuities in Finite Temperature Field Theory*, *Phys. Rev.* **D28** (1983) 2007.
- [99] E. Braaten and D. Segel, *Neutrino energy loss from the plasma process at all temperatures and densities*, *Phys. Rev.* **D48** (1993) 1478–1491, [hep-ph/9302213].
- [100] J.-T. Li, G. M. Fuller and E. Grohs, *Probing dark photons in the early universe with big bang nucleosynthesis*, *JCAP* **12** (2020) 049, [2009.14325].
- [101] A. Caputo, A. J. Millar, C. A. J. O’Hare and E. Vitagliano, *Dark photon limits: a cookbook*, 2105.04565.
- [102] H. An, M. Pospelov, J. Pradler and A. Ritz, *New limits on dark photons from solar emission and keV scale dark matter*, *Phys. Rev. D* **102** (2020) 115022, [2006.13929].
- [103] J. H. Chang, R. Essig and S. D. McDermott, *Revisiting Supernova 1987A Constraints on Dark Photons*, *JHEP* **01** (2017) 107, [1611.03864].
- [104] S. D. McDermott, H. H. Patel and H. Ramani, *Dark Photon Decay Beyond The Euler-Heisenberg Limit*, *Phys. Rev. D* **97** (2018) 073005, [1705.00619].
- [105] A. Filippi and M. De Napoli, *Searching in the dark: the hunt for the dark photon*, *Rev. Phys.* **5** (2020) 100042, [2006.04640].
- [106] J. Coffey, L. Forestell, D. E. Morrissey and G. White, *Cosmological Bounds on sub-GeV Dark Vector Bosons from Electromagnetic Energy Injection*, *JHEP* **07** (2020) 179, [2003.02273].
- [107] P. F. Depta, M. Hufnagel and K. Schmidt-Hoberg, *Updated BBN constraints on electromagnetic decays of MeV-scale particles*, *JCAP* **04** (2021) 011, [2011.06519].
- [108] M. Ibe, S. Kobayashi, Y. Nakayama and S. Shirai, *Cosmological constraint on dark photon from N_{eff}* , *JHEP* **04** (2020) 009, [1912.12152].
- [109] W. DeRocco, P. W. Graham, D. Kasen, G. Marques-Tavares and S. Rajendran, *Observable signatures of dark photons from supernovae*, *JHEP* **02** (2019) 171, [1901.08596].
- [110] A. Sung, H. Tu and M.-R. Wu, *New constraint from supernova explosions on light particles beyond the Standard Model*, *Phys. Rev. D* **99** (2019) 121305, [1903.07923].
- [111] B. D. Fields, *The primordial lithium problem*, *Ann. Rev. Nucl. Part. Sci.* **61** (2011) 47–68, [1203.3551].

- [112] R. A. Alpher, H. Bethe and G. Gamow, *The origin of chemical elements*, *Phys. Rev.* **73** (1948) 803–804.
- [113] PLANCK collaboration, N. Aghanim et al., *Planck 2018 results. VI. Cosmological parameters*, *Astron. Astrophys.* **641** (2020) A6, [1807.06209].
- [114] A. E. Nelson and J. Scholtz, *Dark Light, Dark Matter and the Misalignment Mechanism*, *Phys. Rev. D* **84** (2011) 103501, [1105.2812].
- [115] J. Berger, K. Jedamzik and D. G. E. Walker, *Cosmological Constraints on Decoupled Dark Photons and Dark Higgs*, *JCAP* **1611** (2016) 032, [1605.07195].
- [116] R. Essig, E. Kuflik, S. D. McDermott, T. Volansky and K. M. Zurek, *Constraining Light Dark Matter with Diffuse X-Ray and Gamma-Ray Observations*, *JHEP* **11** (2013) 193, [1309.4091].
- [117] G. G. Raffelt, *Astrophysical methods to constrain axions and other novel particle phenomena*, *Phys. Rept.* **198** (1990) 1–113.
- [118] G. G. Raffelt, *Astrophysical axion bounds*, *Lect. Notes Phys.* **741** (2008) 51–71, [hep-ph/0611350].
- [119] P. Gondolo and G. G. Raffelt, *Solar neutrino limit on axions and keV-mass bosons*, *Phys. Rev. D* **79** (2009) 107301, [0807.2926].
- [120] H. An, M. Pospelov and J. Pradler, *Dark Matter Detectors as Dark Photon Helioscopes*, *Phys. Rev. Lett.* **111** (2013) 041302, [1304.3461].
- [121] T. J. Loredo and D. Q. Lamb, *Bayesian analysis of neutrinos observed from supernova SN-1987A*, *Phys. Rev. D* **65** (2002) 063002, [astro-ph/0107260].
- [122] E. Hardy and R. Lasenby, *Stellar cooling bounds on new light particles: plasma mixing effects*, *JHEP* **02** (2017) 033, [1611.05852].
- [123] J. H. Chang, R. Essig and S. D. McDermott, *Supernova 1987A Constraints on Sub-GeV Dark Sectors, Millicharged Particles, the QCD Axion, and an Axion-like Particle*, *JHEP* **09** (2018) 051, [1803.00993].
- [124] A. Sung, G. Guo and M.-R. Wu, *Supernova Constraint on Self-Interacting Dark Sector Particles*, *Phys. Rev. D* **103** (2021) 103005, [2102.04601].
- [125] M. D. Diamond and G. Marques-Tavares, *Gamma-Ray Flashes from Dark Photons in Neutron Star Mergers*, 2106.03879.
- [126] D. Page, M. V. Beznogov, I. Garibay, J. M. Lattimer, M. Prakash and H.-T. Janka, *NS 1987A in SN 1987A*, *Astrophys. J.* **898** (2020) 125, [2004.06078].
- [127] D. K. Hong, C. S. Shin and S. Yun, *Cooling of young neutron stars and dark gauge bosons*, 2012.05427.
- [128] N. Bar, K. Blum and G. D’Amico, *Is there a supernova bound on axions?*, *Phys. Rev. D* **101** (2020) 123025, [1907.05020].
- [129] A. Mirizzi, J. Redondo and G. Sigl, *Microwave Background Constraints on Mixing of Photons with Hidden Photons*, *JCAP* **03** (2009) 026, [0901.0014].

- [130] A. Caputo, H. Liu, S. Mishra-Sharma and J. T. Ruderman, *Dark Photon Oscillations in Our Inhomogeneous Universe*, *Phys. Rev. Lett.* **125** (2020) 221303, [2002.05165].
- [131] A. Caputo, H. Liu, S. Mishra-Sharma and J. T. Ruderman, *Modeling Dark Photon Oscillations in Our Inhomogeneous Universe*, *Phys. Rev. D* **102** (2020) 103533, [2004.06733].
- [132] S. D. McDermott and S. J. Witte, *Cosmological evolution of light dark photon dark matter*, *Phys. Rev. D* **101** (2020) 063030, [1911.05086].
- [133] M. A. Fedderke, P. W. Graham, D. F. J. Kimball and S. Kalia, *The Earth as a transducer for dark-photon dark-matter detection*, 2106.00022.
- [134] H. An, F. P. Huang, J. Liu and W. Xue, *Radio-frequency Dark Photon Dark Matter across the Sun*, *Phys. Rev. Lett.* **126** (2021) 181102, [2010.15836].
- [135] L. B. Okun, *LIMITS OF ELECTRODYNAMICS: PARAPHOTONS?*, *Sov. Phys. JETP* **56** (1982) 502.
- [136] H.-S. Zechlin, D. Horns and J. Redondo, *New Constraints on Hidden Photons using Very High Energy Gamma-Rays from the Crab Nebula*, *AIP Conf. Proc.* **1085** (2009) 727–730, [0810.5501].
- [137] SHiP collaboration, M. Anelli et al., *A facility to Search for Hidden Particles (SHiP) at the CERN SPS*, 1504.04956.
- [138] J. Redondo and A. Ringwald, *Light shining through walls*, *Contemp. Phys.* **52** (2011) 211–236, [1011.3741].
- [139] H. Vogel and J. Redondo, *Dark Radiation constraints on minicharged particles in models with a hidden photon*, *JCAP* **02** (2014) 029, [1311.2600].
- [140] D. Dunskey, L. J. Hall and K. Harigaya, *CHAMP Cosmic Rays*, *JCAP* **07** (2019) 015, [1812.11116].
- [141] L. Chuzhoy and E. W. Kolb, *Reopening the window on charged dark matter*, *JCAP* **0907** (2009) 014, [0809.0436].
- [142] S. D. McDermott, H.-B. Yu and K. M. Zurek, *Turning off the Lights: How Dark is Dark Matter?*, *Phys. Rev.* **D83** (2011) 063509, [1011.2907].
- [143] F. J. Sanchez-Salcedo, E. Martinez-Gomez and J. Magana, *On the fraction of dark matter in charged massive particles (CHAMPs)*, *JCAP* **1002** (2010) 031, [1002.3145].
- [144] K. Kadota, T. Sekiguchi and H. Tashiro, *A new constraint on millicharged dark matter from galaxy clusters*, 1602.04009.
- [145] J.-T. Li and T. Lin, *Dynamics of millicharged dark matter in supernova remnants*, *Phys. Rev. D* **101** (2020) 103034, [2002.04625].
- [146] A. Stebbins and G. Krnjaic, *New Limits on Charged Dark Matter from Large-Scale Coherent Magnetic Fields*, *JCAP* **12** (2019) 003, [1908.05275].
- [147] S. L. Dubovsky, D. S. Gorbunov and G. I. Rubtsov, *Narrowing the window for millicharged particles by CMB anisotropy*, *JETP Lett.* **79** (2004) 1–5, [hep-ph/0311189].

- [148] A. D. Dolgov, S. L. Dubovsky, G. I. Rubtsov and I. I. Tkachev, *Constraints on millicharged particles from Planck data*, *Phys. Rev. D* **88** (2013) 117701, [1310.2376].
- [149] XENON collaboration, E. Aprile et al., *Dark Matter Search Results from a One Ton-Year Exposure of XENON1T*, *Phys. Rev. Lett.* **121** (2018) 111302, [1805.12562].
- [150] C. Savage, G. Gelmini, P. Gondolo and K. Freese, *Compatibility of DAMA/LIBRA dark matter detection with other searches*, *JCAP* **0904** (2009) 010, [0808.3607].
- [151] N. Fornengo, P. Panci and M. Regis, *Long-Range Forces in Direct Dark Matter Searches*, *Phys. Rev.* **D84** (2011) 115002, [1108.4661].
- [152] R. H. Helm, *Inelastic and elastic scattering of 187-mev electrons from selected even-even nuclei*, *Phys. Rev.* **104** (Dec, 1956) 1466–1475.
- [153] C. Kouvaris and I. M. Shoemaker, *Daily modulation as a smoking gun of dark matter with significant stopping rate*, *Phys. Rev. D* **90** (2014) 095011, [1405.1729].
- [154] PANDAX-II collaboration, X. Cui et al., *Dark Matter Results From 54-Ton-Day Exposure of PandaX-II Experiment*, *Phys. Rev. Lett.* **119** (2017) 181302, [1708.06917].
- [155] LUX-ZEPLIN collaboration, D. S. Akerib et al., *Projected WIMP sensitivity of the LUX-ZEPLIN dark matter experiment*, *Phys. Rev. D* **101** (2020) 052002, [1802.06039].
- [156] G. Belanger, A. Mjallal and A. Pukhov, *Recasting direct detection limits within micrOMEGAs and implication for non-standard Dark Matter scenarios*, *Eur. Phys. J. C* **81** (2021) 239, [2003.08621].
- [157] PANDAX-II collaboration, X. Ren et al., *Constraining Dark Matter Models with a Light Mediator at the PandaX-II Experiment*, *Phys. Rev. Lett.* **121** (2018) 021304, [1802.06912].
- [158] PANDAX-II collaboration, J. Yang et al., *Constraining self-interacting dark matter with the full dataset of PandaX-II*, 2104.14724.
- [159] B. J. Kavanagh, P. Panci and R. Ziegler, *Faint Light from Dark Matter: Classifying and Constraining Dark Matter-Photon Effective Operators*, *JHEP* **04** (2019) 089, [1810.00033].
- [160] R. Essig, T. Volansky and T.-T. Yu, *New Constraints and Prospects for sub-GeV Dark Matter Scattering off Electrons in Xenon*, *Phys. Rev. D* **96** (2017) 043017, [1703.00910].
- [161] S. Knapen, T. Lin, M. Pyle and K. M. Zurek, *Detection of Light Dark Matter With Optical Phonons in Polar Materials*, *Phys. Lett. B* **785** (2018) 386–390, [1712.06598].
- [162] T. Emken, R. Essig, C. Kouvaris and M. Sholapurkar, *Direct Detection of Strongly Interacting Sub-GeV Dark Matter via Electron Recoils*, *JCAP* **09** (2019) 070, [1905.06348].
- [163] S. Heeba and F. Kahlhoefer, *Probing the freeze-in mechanism in dark matter models with $U(1)$ ' gauge extensions*, *Phys. Rev. D* **101** (2020) 035043, [1908.09834].
- [164] M. Duch, B. Grzadkowski and D. Huang, *Strongly self-interacting vector dark matter via freeze-in*, *JHEP* **01** (2018) 020, [1710.00320].
- [165] S. Tulin and H.-B. Yu, *Dark Matter Self-interactions and Small Scale Structure*, *Phys. Rept.* **730** (2018) 1–57, [1705.02358].
- [166] C. Kouvaris and N. G. Nielsen, *Asymmetric Dark Matter Stars*, *Phys. Rev. D* **92** (2015) 063526, [1507.00959].

- [167] J. H. Chang, D. Egana-Ugrinovic, R. Essig and C. Kouvaris, *Structure Formation and Exotic Compact Objects in a Dissipative Dark Sector*, *JCAP* **03** (2019) 036, [1812.07000].
- [168] A. Maselli, C. Kouvaris and K. D. Kokkotas, *Photon spectrum of asymmetric dark stars*, *Int. J. Mod. Phys. D* **30** (2021) 2150003, [1905.05769].
- [169] R. Foot, *Mirror matter-type dark matter*, *Int. J. Mod. Phys.* **D13** (2004) 2161–2192, [astro-ph/0407623].
- [170] D. E. Kaplan, M. A. Luty and K. M. Zurek, *Asymmetric Dark Matter*, *Phys. Rev. D* **79** (2009) 115016, [0901.4117].
- [171] G. Alonso-Álvarez, G. Elor and M. Escudero, *Collider Signals of Baryogenesis and Dark Matter from B Mesons: A Roadmap to Discovery*, 2101.02706.
- [172] K. M. Zurek, *Asymmetric Dark Matter: Theories, Signatures, and Constraints*, *Phys. Rept.* **537** (2014) 91–121, [1308.0338].
- [173] L. Randall, J. Scholtz and J. Unwin, *Cores in Dwarf Galaxies from Fermi Repulsion*, *Mon. Not. Roy. Astron. Soc.* **467** (2017) 1515–1525, [1611.04590].
- [174] V. Domcke and A. Urbano, *Dwarf spheroidal galaxies as degenerate gas of free fermions*, *JCAP* **01** (2015) 002, [1409.3167].
- [175] W. H. Press and D. N. Spergel, *Capture by the sun of a galactic population of weakly interacting massive particles*, *Astrophys. J.* **296** (1985) 679–684.
- [176] K. Griest and D. Seckel, *Cosmic Asymmetry, Neutrinos and the Sun*, *Nucl. Phys. B* **283** (1987) 681–705.
- [177] A. Gould, *WIMP Distribution in and Evaporation From the Sun*, *Astrophys. J.* **321** (1987) 560.
- [178] A. Gould, *Resonant Enhancements in WIMP Capture by the Earth*, *Astrophys. J.* **321** (1987) 571.
- [179] D. N. Spergel and W. H. Press, *Effect of hypothetical, weakly interacting, massive particles on energy transport in the solar interior*, *Astrophys. J.* **294** (1985) 663–673.
- [180] T. K. Gaisser, G. Steigman and S. Tilav, *Limits on Cold Dark Matter Candidates from Deep Underground Detectors*, *Phys. Rev. D* **34** (1986) 2206.
- [181] R. Garani and S. Palomares-Ruiz, *Evaporation of dark matter from celestial bodies*, 2104.12757.
- [182] R. Garani, Y. Genolini and T. Hambye, *New Analysis of Neutron Star Constraints on Asymmetric Dark Matter*, *JCAP* **05** (2019) 035, [1812.08773].
- [183] R. Garani, A. Gupta and N. Raj, *Observing the thermalization of dark matter in neutron stars*, *Phys. Rev. D* **103** (2021) 043019, [2009.10728].
- [184] B. Bertoni, A. E. Nelson and S. Reddy, *Dark Matter Thermalization in Neutron Stars*, *Phys. Rev. D* **88** (2013) 123505, [1309.1721].
- [185] C. Kouvaris and P. Tinyakov, *Excluding Light Asymmetric Bosonic Dark Matter*, *Phys. Rev. Lett.* **107** (2011) 091301, [1104.0382].

- [186] C. Kouvaris and P. Tinyakov, *(Not)-constraining heavy asymmetric bosonic dark matter*, *Phys. Rev. D* **87** (2013) 123537, [1212.4075].
- [187] C. Kouvaris and P. Tinyakov, *Growth of Black Holes in the interior of Rotating Neutron Stars*, *Phys. Rev. D* **90** (2014) 043512, [1312.3764].
- [188] C. Kouvaris, P. Tinyakov and M. H. G. Tytgat, *NonPrimordial Solar Mass Black Holes*, *Phys. Rev. Lett.* **121** (2018) 221102, [1804.06740].
- [189] M. Raidal, C. Spethmann, V. Vaskonen and H. Veermäe, *Formation and Evolution of Primordial Black Hole Binaries in the Early Universe*, *JCAP* **02** (2019) 018, [1812.01930].
- [190] B. Dasgupta, R. Laha and A. Ray, *Low Mass Black Holes from Dark Core Collapse*, *Phys. Rev. Lett.* **126** (2021) 141105, [2009.01825].
- [191] C. Kouvaris, *WIMP Annihilation and Cooling of Neutron Stars*, *Phys. Rev. D* **77** (2008) 023006, [0708.2362].
- [192] N. F. Bell, G. Busoni and S. Robles, *Heating up Neutron Stars with Inelastic Dark Matter*, *JCAP* **09** (2018) 018, [1807.02840].
- [193] N. F. Bell, G. Busoni and S. Robles, *Capture of Leptophilic Dark Matter in Neutron Stars*, *JCAP* **06** (2019) 054, [1904.09803].
- [194] J. Bramante, *Dark matter ignition of type Ia supernovae*, *Phys. Rev. Lett.* **115** (2015) 141301, [1505.07464].
- [195] J. F. Acevedo and J. Bramante, *Supernovae Sparked By Dark Matter in White Dwarfs*, *Phys. Rev. D* **100** (2019) 043020, [1904.11993].
- [196] P. W. Graham, R. Janish, V. Narayan, S. Rajendran and P. Riggins, *White Dwarfs as Dark Matter Detectors*, *Phys. Rev. D* **98** (2018) 115027, [1805.07381].
- [197] R. D. Pisarski and D. H. Rischke, *Superfluidity in a model of massless fermions coupled to scalar bosons*, *Phys. Rev. D* **60** (1999) 094013, [nucl-th/9903023].
- [198] M. G. Alford, K. Pangeni and A. Windisch, *Color superconductivity and charge neutrality in Yukawa theory*, *Phys. Rev. Lett.* **120** (2018) 082701, [1712.02407].
- [199] G. J. Stephenson, Jr., J. T. Goldman and B. H. J. McKellar, *Neutrino clouds*, *Int. J. Mod. Phys. A* **13** (1998) 2765–2790, [hep-ph/9603392].
- [200] J. I. Kapusta and C. Gale, *Finite-temperature field theory: Principles and applications*. Cambridge Monographs on Mathematical Physics. Cambridge University Press, 2011. 10.1017/CBO9780511535130.
- [201] J. Bardeen, L. N. Cooper and J. R. Schrieffer, *Theory of superconductivity*, *Phys. Rev.* **108** (1957) 1175–1204.
- [202] M. G. Alford, A. Schmitt, K. Rajagopal and T. Schäfer, *Color superconductivity in dense quark matter*, *Rev. Mod. Phys.* **80** (2008) 1455–1515, [0709.4635].
- [203] A. Schmitt, *Introduction to Superfluidity: Field-theoretical approach and applications*, vol. 888. 2015. 10.1007/978-3-319-07947-9.
- [204] F. Wilczek, *Superfluidity and Symmetry Breaking — An Anderson Living Legacy*, PWA90: A Lifetime of Emergence.

- [205] D. Bailin and A. Love, *Superfluidity and Superconductivity in Relativistic Fermion Systems*, *Phys. Rept.* **107** (1984) 325.
- [206] F. Marsiglio, *Eliashberg theory: A short review*, *Annals of Physics* **417** (Jun, 2020) 168102.
- [207] M. I. Gresham and K. M. Zurek, *Asymmetric Dark Stars and Neutron Star Stability*, *Phys. Rev. D* **99** (2019) 083008, [1809.08254].
- [208] K. Rajagopal and F. Wilczek, *The Condensed matter physics of QCD*, hep-ph/0011333.
- [209] M. I. Gresham, H. K. Lou and K. M. Zurek, *Early Universe synthesis of asymmetric dark matter nuggets*, *Phys. Rev. D* **97** (2018) 036003, [1707.02316].
- [210] M. I. Gresham, H. K. Lou and K. M. Zurek, *Nuclear Structure of Bound States of Asymmetric Dark Matter*, *Phys. Rev. D* **96** (2017) 096012, [1707.02313].
- [211] H. B. Callen, *Thermodynamics and an introduction to thermostatistics; 2nd ed.* Wiley, New York, NY, 1985.
- [212] C. W. Misner, K. S. Thorne and J. A. Wheeler, *Gravitation*. W. H. Freeman, San Francisco, 1973.
- [213] G. Narain, J. Schaffner-Bielich and I. N. Mishustin, *Compact stars made of fermionic dark matter*, *Phys. Rev. D* **74** (2006) 063003, [astro-ph/0605724].
- [214] S. Tremaine and J. E. Gunn, *Dynamical Role of Light Neutral Leptons in Cosmology*, *Phys. Rev. Lett.* **42** (1979) 407–410.
- [215] A. Boyarsky, O. Ruchayskiy and D. Iakubovskiy, *A Lower bound on the mass of Dark Matter particles*, *JCAP* **03** (2009) 005, [0808.3902].
- [216] J. Alvey, N. Sabti, V. Tiki, D. Blas, K. Bondarenko, A. Boyarsky et al., *New constraints on the mass of fermionic dark matter from dwarf spheroidal galaxies*, *Mon. Not. Roy. Astron. Soc.* **501** (2021) 1188–1201, [2010.03572].
- [217] A. Hook, *Unitarity constraints on asymmetric freeze-in*, *Phys. Rev. D* **84** (2011) 055003, [1105.3728].
- [218] M. Carena, N. M. Coyle, Y.-Y. Li, S. D. McDermott and Y. Tsai, *Cosmologically Degenerate Fermions*, 2108.02785.
- [219] S. Reddy and D. Zhou, *Dark Lepton Superfluid in Proto-Neutron Stars*, 2107.06279.
- [220] F. Giacchino, L. Lopez-Honorez and M. H. G. Tytgat, *Scalar Dark Matter Models with Significant Internal Bremsstrahlung*, *JCAP* **10** (2013) 025, [1307.6480].
- [221] F. Giacchino, L. Lopez-Honorez and M. H. G. Tytgat, *Bremsstrahlung and Gamma Ray Lines in 3 Scenarios of Dark Matter Annihilation*, *JCAP* **08** (2014) 046, [1405.6921].
- [222] A. Ibarra, T. Toma, M. Totzauer and S. Wild, *Sharp Gamma-ray Spectral Features from Scalar Dark Matter Annihilations*, *Phys. Rev. D* **90** (2014) 043526, [1405.6917].
- [223] F. Giacchino, A. Ibarra, L. Lopez Honorez, M. H. G. Tytgat and S. Wild, *Signatures from Scalar Dark Matter with a Vector-like Quark Mediator*, *JCAP* **02** (2016) 002, [1511.04452].
- [224] A. Ibarra, M. Totzauer and S. Wild, *High-energy neutrino signals from the Sun in dark matter scenarios with internal bremsstrahlung*, *JCAP* **12** (2013) 043, [1311.1418].

- [225] C. Arina, B. Fuks, L. Mantani, H. Mies, L. Panizzi and J. Salko, *Closing in on t -channel simplified dark matter models*, *Phys. Lett. B* **813** (2021) 136038, [2010.07559].
- [226] T. Bringmann, A. J. Galea and P. Walia, *Leading QCD Corrections for Indirect Dark Matter Searches: a Fresh Look*, *Phys. Rev. D* **93** (2016) 043529, [1510.02473].
- [227] T. Bringmann, F. Calore, A. Galea and M. Garny, *Electroweak and Higgs Boson Internal Bremsstrahlung: General considerations for Majorana dark matter annihilation and application to MSSM neutralinos*, *JHEP* **09** (2017) 041, [1705.03466].
- [228] A. S. Cornell, A. Deandrea, T. Flacke, B. Fuks and L. Mason, *Contact interactions and top-philic scalar dark matter*, 2104.12795.
- [229] L. Calibbi, F. D’Eramo, S. Junius, L. Lopez-Honorez and A. Mariotti, *Displaced new physics at colliders and the early universe before its first second*, *JHEP* **05** (2021) 234, [2102.06221].
- [230] M. Cermeño, C. Degrande and L. Mantani, *Circular polarisation of gamma rays as a probe of dark matter interactions with cosmic ray electrons*, 2103.14658.
- [231] T. Bringmann, L. Bergstrom and J. Edsjo, *New Gamma-Ray Contributions to Supersymmetric Dark Matter Annihilation*, *JHEP* **01** (2008) 049, [0710.3169].
- [232] H. An, Z. Hu, Z. Liu and D. Yang, *Exploring Uncharted Soft Displaced Vertices in Open Data*, 2107.11405.
- [233] D.-H. RISCHKE and W. GREINER, *A functional integral approach to the thermodynamics of the sigma-omega model*, *International Journal of Modern Physics E* **03** (1994) 1157–1194, [<https://doi.org/10.1142/S0218301394000358>].
- [234] V. A. Khodel, V. V. Khodel and J. W. Clark, *Solution of the gap equation in neutron matter*, *Nucl. Phys. A* **598** (1996) 390–417.
- [235] G. De Rosi, *Superfluidity in neutron star matter*, .